Generators, Calorimeter Trigger and J/ψ production at LHCb

P. Robbe

LAL-12-08

Mars 2012

Laboratoire de l'Accélérateur Linéaire

Habilitation à diriger des recherches

présentée à l'Université Paris-Sud XI

par

Patrick ROBBE

Generators, Calorimeter Trigger and J/ψ production at LHCb

Soutenue le 12 mars 2012 devant le jury composé de :

Mme. Nora BRAMBILLA	
M. Olivier CALLOT	
M. Ginés MARTÍNEZ	Rapporteur
M. Anders RYD	Rapporteur
M. Olivier SCHNEIDER	Rapporteur
M. Achille STOCCHI	Président

Contents

Introduction

The LHCb experiment [1] is one of the four experiments installed at the Large Hadron Collider (LHC) at CERN. It is designed for the study of *CP* violation in *B* and *D* decays and for the study of rare decays of beauty and charm hadrons from the pp collisions delivered by the LHC. The LHCb detector is shown in Fig. 1.

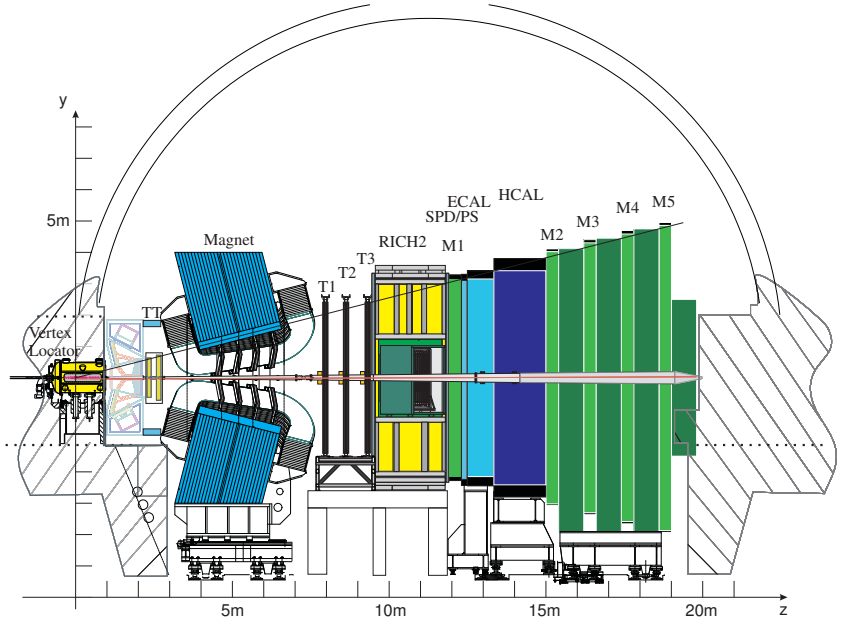

Figure 1 – *Side view of the LHCb detector showing the Vertex Locator (VELO), the dipole magnet, the two RICH detectors, the four tracking stations TT and T1−T3, the Scintillating Pad Detector (SPD), Preshower (PS), Electromagnetic (ECAL) and Hadronic (HCAL) calorimeters, and the five muon stations M1−M5.*

The detector covers the forward region with respect to pp collisions that occur inside the Vertex Locator (VELO). It contains the necessary sub-detectors to achieve the physics goals of the experiment. A 4 Tm dipole magnet whose field is oriented vertically bends the trajectories of charged particles. Precise tracking and vertexing is obtained combining the information from the Vertex Locator (VELO) and four tracking stations, one before the magnet (TT) and three after the magnet (T1−T3). Charged hadron identification is obtained with Cherenkov Detectors

(RICH1 and RICH2). An electromagnetic calorimeter system (ECAL, Preshower –PRS– and Scintillating Pad Detector – SPD) is used for photon detection and electron identification. An hadron calorimeter (HCAL) provides information for triggering interesting events. The muon detection consists in five muon stations (MUON, M1−M5). The LHCb coordinate system is a right-handed Cartesian system where the y axis is vertical and pointing upwards, and the z axis is parallel to the beam axis and oriented from the VELO to the MUON.

The goals of the LHCb experiment are to test the Standard Model in the flavour sector, through precision measurements of CP violation in weak interactions and measurements of rare D and B decay properties. Within the Standard Model, CP violation in weak interactions appears in quark flavour changing processes, described by the Cabbibo-Kobayashi-Maskawa (CKM) matrix [2, 3],

$$V_{\text{CKM}} = \begin{pmatrix} V_{ud} & V_{us} & V_{ub} \\ V_{cd} & V_{cs} & V_{cb} \\ V_{td} & V_{ts} & V_{tb} \end{pmatrix}. \tag{1}$$

The amplitude of the transition from a quark q_j to a quark q_i through weak interaction and the emission of a W ($q_j \to q_i W^-$) is proportional to the matrix element V_{ij}. The same transition between the anti-quarks ($\bar{q}_j \to \bar{q}_i W^+$) has an amplitude proportional to the complex conjugate of this matrix element, V_{ij}^*. Since there are 3 quark families, the CKM matrix is a 3×3 unitary matrix which can be parameterised by four numbers: three modules and one phase. Because of this phase which appears in decay amplitudes, CP violation can arise from quantum mechanics interference effects when summing several amplitudes with different relative phases.

The unitarity condition of the CKM matrix can be graphically represented with triangles in the complex plane which illustrate relations between the elements of the matrix. The most commonly used triangle is called the "Unitarity Triangle" and is shown in Fig. 2.

A large number of phenomena are explained by the CKM mechanism and depend only on the four free parameters of the matrix. Combining the different experimental measurements related to the CKM matrix provides a powerful test of the validity of the CKM formalism and of the Standard Model, verifying that all these measurements are consistent between them. The combination of the experimental data can be obtained with different methods, such as the one presented in Ref. [4] or the one presented in Ref. [5], which give similar results. Figure 3 represents the result of the combination of existing experimental data, obtained from Ref. [5]. On this figure, the fit to the different constraints is represented by the ellipses around the triangle apex, showing that all experimental measurements

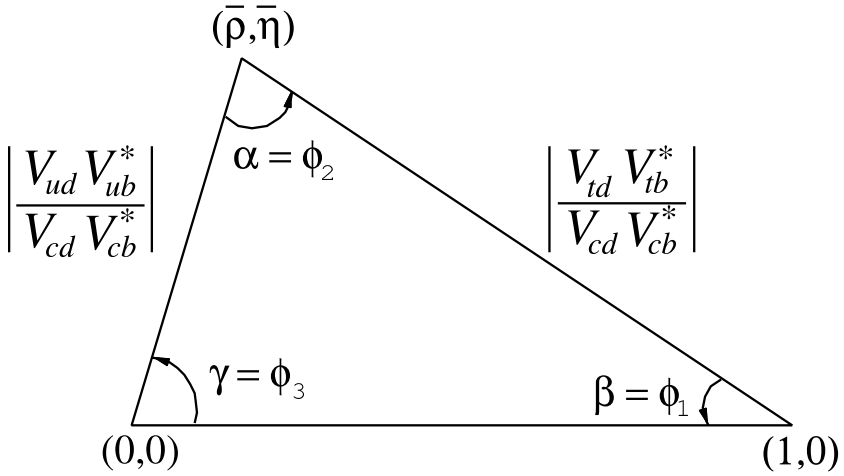

Figure 2 – *Unitarity triangle.*

are compatible with the Standard Model description of the *CP* violation through the CKM matrix.

A large number of the precise experimental constraints used in Fig. 3 were obtained from analyses done at *B*-factories (asymmetric e^+e^- colliders at a center-of-masse energy of 10.6 GeV, BABAR [6] and BELLE [7]) during the last 12 years, mainly using B^0 and B^+ meson decays.

The data recorded at the LHCb experiment will allow to increase the number

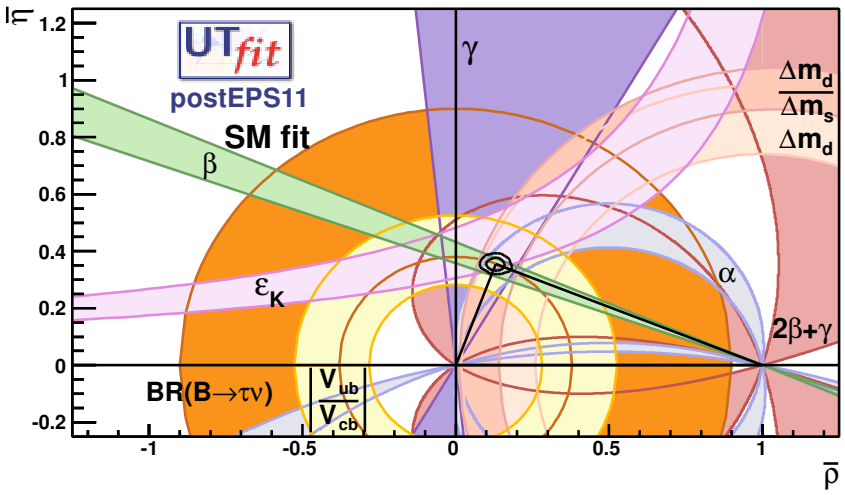

Figure 3 – *Global fit of the Unitarity triangle.*

of independent measurements related to the CKM matrix, in particular studying decays of B_s^0 mesons which were not produced at B-factories because of their too low collision energy. In addition, because of the large B production cross-section at the LHC collision energy, precision measurements of the CKM parameters will be obtained. Their comparisons may reveal discrepencies that could be interpreted as being due to the presence of new particles (New Physics) modifying the expectations from the Standard Model.

I have been working in the LHCb Collaboration for the last 9 years and this document presents results related to the preparation of the physics program of LHCb to which I contributed. *CP* violation measurements are usually involving complex analyses like measurements of asymmetries as a function of the decay time and flavour of the B hadron. A detailed simulation is mandatory to develop the analysis tools needed for this. In particular, B meson production and decay properties need to be modelled acurately and a detailed generator framework has been implemented which describes for example B mixing and *CP* violation in B decays in the LHCb hadronic environment.

As can be seen from Fig. 3, the unitarity triangle angle known with the worse precision is the γ angle. The most promising methods to measure this angle involve the analysis of $B \to D^0 K$ or $B \to D^0 K^*$ decay modes, with D^0 decaying to the $K\pi$, KK and $\pi\pi$ final states, for example. These decay modes containing only hadrons in the final state, are particularly challenging to study at hadron colliders because they have small branching fractions and suffer from the large QCD background processes that also produce hadrons. To overcome these difficulties, a complex trigger system is mandatory and has been designed. For hadronic decay modes such as the ones mentioned above, this trigger is based at the first level (Level 0) on information provided by the calorimeters, and in particular the hadronic calorimeter. Trigger lines based on the hadronic calorimeters are now the ones with higher rates in the experiment.

Important measurements, such as the measurement of the *CP* violating phase ϕ_s, are based on decay modes containing a J/ψ in the final state, like $B_s^0 \to J/\psi\phi$ [8]. An important first step for these measurements is to understand detector performances concerning $J/\psi \to \mu^+\mu^-$ reconstruction. The measurement of the J/ψ production cross-section constitutes one of these steps. It also allows to measure the $b\bar{b}$ production cross-section which is an important input parameter of branching fraction limits or measurements of rare B decays, $B_s^0 \to \mu^+\mu^-$ for example [9].

Chapter 1 describes the generator part of the LHCb simulation software. This chapter is meant as a documentation of how the generators are implemented in LHCb and applies to all Monte Carlo simulation samples produced for the anal-

yses performed at LHCb. This could also be a support for LHCb collaborators wanting to add new features to the generation software in the future.

Chapter 2 describes the final implementation of the calorimeter trigger, the way it was installed in the LHCb cavern. In contains technical details that I found useful to know when working on the system or that have been modified or added with respect to the original design. It could hopefully also be useful for L0 piquets in charge of the daily operation of the trigger, to know better the system.

Chapter 3 is the description of the analysis leading to the measurement of the J/ψ production cross-section performed with the first data recorded by LHCb in 2010. This analysis was published in Ref. [10].

CHAPTER 1

LHCb Monte Carlo Event Generation

The LHCb simulation application, Gauss, consists of two independent phases: the generation of the primary event and the tracking of the particles produced in the experimental setup. For the LHCb experimental program it is particularly important to model B meson decays: the EvtGen [11] code developed in CLEO and BABAR has been chosen and customized for non-coherent B production as occuring in pp collisions at the LHC. The initial proton-proton collision is provided by a different generator engine, currently PYTHIA 6 [12] for massive production of signal and generic pp collisions events. Beam gas events, background events originating from proton halo, cosmics and calibration events for different detectors can be generated in addition to pp collisions. Different generator packages are available in the physics community or specifically developed in LHCb, and are used for the different purposes. Running conditions affecting the events generated such as the size of the luminous region, the number of collisions occuring in a bunch crossing and the number of spill-over events from neighbouring bunches are modeled via dedicated algorithms appropriately configured. The design of the generator phase of Gauss will be described: a modular structure with well defined interfaces specific to the various tasks, e.g. pp collisions, particles' decays, selections, etc. has been chosen. Different implementations are available for the various tasks allowing selecting and combining them as most appropriate at run time as in the case of PYTHIA 6 for pp collisions or HIJING for beam gas. The advantages of such structure, allowing for example to adopt transparently new generators packages will be discussed.

1.1 Introduction

The LHCb simulation application, Gauss [13, 14], consists of two independent phases:

1. the generation of the primary event,
2. the tracking of the particles produced in the experimental setup (detector).

The first step can be further divided into two important main parts, both using external generator packages. The first one is the production of particles coming out of the primary *pp* collision of the LHC beams. This is usually realized by the PYTHIA general purpose event generator. The second one is the decay and time evolution of the produced particles. EvtGen is usually used to perform this step. The simulation software application, Gauss, is interfaced to these two external generators, and provides the necessary algorithms to steer the execution of the different generation sequences, and to ensure the coherence between them.

A very generic framework has been designed. The resulting application is flexible enough to be able to generate a very large variety of event types, from beam gas events up to very rare decays of *B* mesons. Thus different generator packages available in the high-energy physics community have been interfaced to Gauss.

1.2 General Software Structure

The structure of the LHCb simulation software is represented in Fig. 1.1, where the two main phases are represented: event generation and detector simulation. The simulation part is based on the GEANT4 package [15] and is described in details in Ref. [14]. The generation step deals with the generation of physics events and uses several generic tools to perform the necessary actions.

1.2.1 Main generation algorithm

The generation of the events is realized in one Gaudi algorithm [16, 17] which implements three main actions:

a) Initialization

This step mainly deals with the configuration of the algorithms which are obtained from “configurables”. The "configurables" are files written in Python language which compute from user inputs the value of the parameters to be used by the generation software. These values can be for example the energy of the proton

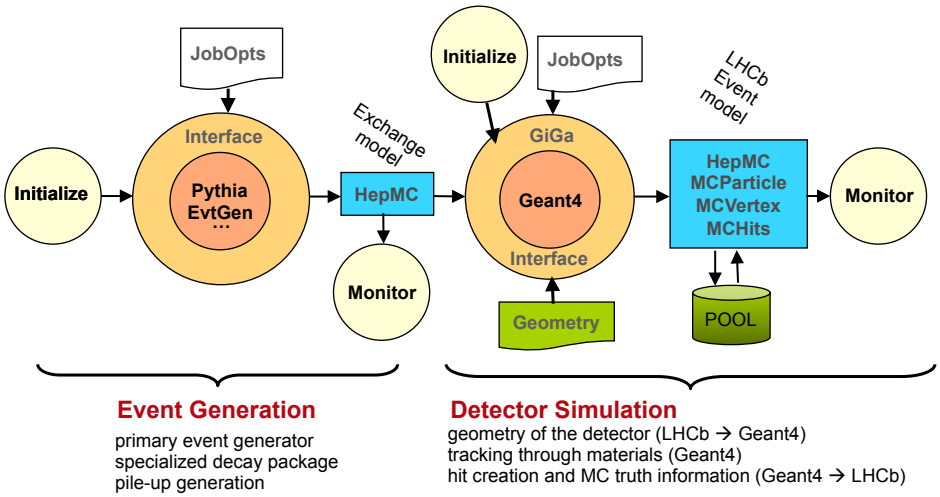

Figure 1.1 – *Structure of the LHCb simulation software, Gauss.*

beam to consider for the generation, since the LHC can operate at various center-of-mass energies (900 GeV, 7 TeV, 14 TeV), or the crossing angle between the beams.

b) Event loop execution

The result of this step is the generation of one physics event corresponding to the criteria defined at the initialization (for example events containing a b quark). The generated event is stored in HepMC format [18] and can optionally be saved on disk to be analyzed in detail later. The generator event in HepMC format is then transferred to the simulation step, as illustrated in Fig. 1.1.

In order to realize all the computations needed for the generation of one event, several tools are called by the execution function. Each tool has a generic interface and several concrete implementations which are chosen depending on the configuration of the algorithm. This choice of generic tools allows to easily substitute inside the algorithm a method by another method. For example, the generation of beam parameters is usually describing the head-on collision of two proton beams but can be substituted by the description of the collision of one proton beam with one gas molecule in order to simulate beam-gas events. All the available tools will be decribed in details in the next paragraph.

c) Finalization

Monitoring counters are printed at this stage. They allow to count the efficiency of the various generator-level selections applied during the event generation, and to know the cross-sections of the generated processes. These counters are available from the log files of the massive production simulation jobs. A script extracts from these log files the interesting information and compute numerical results which are available in web pages for the physicists analysing the simulated data.

The generation algorithm also access generic services. A random generator service provides all tools and algorithms with a common random number generator, including external libraries which are interfaced in such a way that their internal random number generator is replaced by the one of the service. In order to ensure that any event in a sequence of events (a production job for example) can be reproduced without generating all preceeding events, the random generator seed is set before generating any new event. The seed is set according to an unique combination of integers (run and event numbers) which identify uniquely each event.

A particle property service is used to define properties of particles (mass, lifetime, spin, charge and width). This ensures that all parts of the software (including also the reconstruction and the analysis software) use the same particle properties. The source of data for the particle properties is the review of particle physics of the Particle Data Group (PDG) [19].

1.2.2 Tools for the generation algorithm

The algorithm described in Sec. 1.2.1 calls various tools to realize specific computations. These tools are described in the following.

a) Sample Generation Tool

Several categories of event samples are of interest for the LHCb physics program:

Minimum Bias All events generated by the production generator, with no requirement about their content.

Inclusive Events containing a particle out of a configurable list of particle types. This category is mainly composed of inclusive c and b events, defined as

events containing at least one charm hadron or one beauty hadron respectively.

Signal All events containing a particle of a given type (the "signal"), like $B_s^0/\overline{B_s}^0$ for example. In each event, one of the "signal" particle is forced to decay by the decay generator to a predefined decay mode, such as $B_s^0 \to J/\psi\phi$. In order to speed-up the generation of B events for relatively rare signal hadrons (B_s^0 or Λ_b compared to B^+ and B^0 for example), the following method is applied: once an event with a b quark is obtained, the same event is re-hadronized several times until the correct type of B meson is found. This is implemented only when using the PYTHIA 6 production generator, and will be explained in details in Sec. 1.3.3.

Special events Events defined with special generator settings, usually for processes with very low cross-sections, such as Z^0 production.

The "Sample Generation Tool" implements the sequence of actions required to generate these types of events, calling at the appropriate time the functions of the "Production Tool" and "Decay Tool" that are described below. Inclusive and Signal events have a rather large cross-section, they are then extracted from Minimum Bias and do not need extra special settings of the production generator.

b) Production Tool

The "Production Tool" takes care of the primary pp collision generation: hard process, evolution of the partons up to the formation of hadrons and generation of multiple parton-parton interactions. This is usually realized calling an external generator, such as the general purpose event generators PYTHIA 6 [12], PYTHIA 8 [20], HERWIG [21], Herwig++ [22] or SHERPA [23]. In this case, the tool is an interface with the generator (which can be either written in FORTRAN or in C++ language). The tool also provides the possibility to configure the external generator in various ways, transferring the configuration commands given by the Gauss user through "Configurables" into the format needed by the external generator. The main external generator used is PYTHIA 6, whose interface in Gauss will be detailed in the next section Sec. 1.3.

Other implementations are provided in Gauss for specific purposes: an interface to BCVEGPY [24] for the production of the B_c meson or an interface to HIJING [25] for the simulation of beam-gas events. The possibility to use text files as input is also provided, either containing fully generated events, or containing parton level events to be hadronized by another generator. The supported file

format are the HepMC ASCII file format or PYTHIA Les Houches Event (LHE) files [26].

A "Production Tool" must implement the following functions which are called by the framework to use correctly the external generator:

1. `generateEvent(Event)`: calls the external generator to generate a single primary interaction (usually a pp collision) and translates the event produced by the generator into the HepMC format.
2. `setStable(ParticleProperty)`: declares a particle as stable for the production generator. During the initialization, the framework will call this function to set stable all particles which are known to the "Decay Tool". The purpose of this is to ensure that particles will be decayed always with the same method: by the "Decay Tool" if it knows how to handle it or by the "Production Tool" if not.
3. `updateParticleProperties(ParticleProperty)`: modifies the particle properties of the generator so that they are identical to the LHCb ones to ensure coherence between all the parts of the software.
4. `initializeGenerator`: performs the necessary actions to initialize properly the generator.

c) Decay Tool

The "Decay Tool" is used to decay hadrons produced by the “Production Tool”. The primary event generation stops after the hadronization, and then delegates to the decay tool the generation of decays. The decay chains obtained are then transmitted to GEANT4 to simulate their interactions in the detector. The "forced decay chain" feature of GEANT4 is used, meaning that the decay modes generated by the decay tool will be kept during the simulation phase. If a particle is modified when it travels through the detector material, its decay product will be re-generated by GEANT4 but keeping the same final states (except when the particle is destroyed because of material interactions).

Because the LHCb experiment focuses on flavour physics and in particular B physics, it needs a very detailed simulation of B decays, taking into account CP violation effects or angular correlations in decay chains. The EvtGen generator [11] is very well suited for this purpose since it was developped at CLEO and BABAR, experiments also devoted to B physics. The use of EvtGen in LHCb will be described in details in Sec. 1.4.

The SHERPA generator is also interfaced to Gauss as a “Decay Tool” since it also provides the possibility to implement detailed description of decay properties. One important task of the “Decay Tool” is to generate signal decay, i.e. to force the “signal” particle to decay into the decay mode of interest. This allow Gauss users to obtain samples containing only the decay mode under study to be able to determine their reconstruction efficiencies or the biases introduced by the experimental setup.

A "Decay Tool" must implement the following functions:

1. `generateDecay(MotherParticle)`: calls the external generator to generate the decay of the mother particle up to stable particles that will be then tracked in the detector's material by the simulation phase.
2. `generateSignalDecay(MotherParticle)`: calls the external generator to generate the decay of the mother particle according to a predifined "signal" decay mode. The mother particle is always decayed unpolarized, setting its helicity density matrix to a diagonal matrix where all the elements are equal.
3. `generateDecayWithLimit(MotherParticle,pdgId)`: does the same as the function `generateDecay` but stops the decay chain and leave undecayed particles with a PDG number [19] equal to `pdgId`. This is useful when generating "signal" events, because a "signal" can be a decay product of a heavier particle (for example a B coming from a B^*) which is undecayed after the event is produced (because it was set stable in the production generator). Without this feature, only "signal" particle produced directly by the pp collision would be visible.
4. `isKnownToDecayTool(ParticleProperty)`: checks if the particle is known and can be handled by the decay generator. If yes, the particle will be set as stable in the production generator.

d) Pile-Up Tool

More than one interaction can occur in one individual event. Additional interactions with respect to the interaction containing the process of interest are called “Pile-Up Interactions”. They are also generated by Gauss, adding Minimum Bias interactions generated by the production generator on top of the main interaction.

The “Pile-Up Tool” is used to provide the distribution of the number of interactions in one event, N_{int}. The default and main usage is to generate N_{int} following a

Poisson law with mean value ν. In this case, the probability that an event contains i interactions is equal to

$$P(N_{\text{int}} = i) = \frac{e^{-\nu}\nu^i}{i!}. \tag{1.1}$$

The value of ν depends on the total cross-section of the pp collision (including elastic and diffractive processes), σ_{tot}, the instantaneous luminosity, $\mathscr{L}$ and the collision frequency of the LHC bunches, f. The value of ν is equal to

$$\nu = \frac{\mathscr{L}\sigma_{\text{tot}}}{f}. \tag{1.2}$$

The user can give as input to the software the values of the luminosity and of the cross-section but the revolution frequency is fixed to $f = 11.245\,\text{kHz}$. For the simulation of events corresponding to the data recorded in 2011, ν is set to 2.

For the generation of rare processes, since they have very low cross-sections, they cannot be extracted out of Minimum Bias because this would take a large amount of CPU time. A different pile-up scheme has to be adopted then to generate directly the correct N_{int} distribution. If the production cross-section σ_{rare} of the rare process is small compared to σ_{tot}, the probability to find the rare process in an event with two pile-up interactions is twice the probability to find it in an event with only one interaction, and so on for events with 3, 4, ... interactions. The probability that an event has i interactions out of which at least one contains the rare process is then equal to

$$P(N_{\text{int}} = i) = i\,\frac{\sigma_{\text{rare}}}{\sigma_{\text{tot}}}\,\frac{e^{-\nu}\nu^i}{i!} = \frac{\sigma_{\text{rare}}}{\sigma_{\text{tot}}}\,\nu\frac{e^{-\nu}\nu^{i-1}}{(i-1)!}. \tag{1.3}$$

In this case, it is $(N_{\text{int}} - 1)$ that follows a Poisson distribution with the same mean value ν as described in Eq. (1.2). The mean number of interactions per event containing the rare process is then $< N_{\text{int}} >= \nu + 1$.

The possibility to generate single interaction events, for beam-gas for example, is also available, together with the possibility to generate a fixed number of interactions for specific studies. The only function that must provide a "Pile Up tool" is the function `numberOfPileUp` which gives for each event the number of interactions to generate.

e) Beam Tool

The "Beam Tool" generates the kinematics of the proton beams, in the LHCb coordinate system. The main usage is to describe two colliding proton beams, with a crossing angle. The angle between the two beams is the sum of two contributions:

1. the angle between the LHCb axis and the angle between the LHC beam line,
2. the angle between the beam circulating in one direction and the angle between the beam circulating in the other direction. This angle is the sum of an **external** crossing angle which is the angle defined by the LHC beam optics and that is applied in order to separate beams outside the interaction region to avoid long range collisions, and an **internal** crossing angle due to the effect of the LHCb dipole magnet that has to be compensated.

All the angles can be defined separately in the horizontal plane and in the vertical plane. For the simulation of events corresponding to the data collected in 2011, the angle of the beam line was set to $-75\,\mu$rad in the horizontal plane and to $35\,\mu$rad in the vertical plane. The angle between the beams is equal to 0 in the vertical plane. In the horizonal plane it is equal to $-520\,\mu$rad for one magnet polarity (up) and $20\,\mu$rad for the other polarity (down).

The crossing angle is smeared by a Gaussian function with σ equal to

$$\sigma = \sqrt{\frac{\varepsilon_{\mathrm{N}}}{\beta\,\gamma\beta^{*}}}, \tag{1.4}$$

where ε_{N} is the normalized beam emittance, β and γ are the protons' speed and Lorentz factor, respectively, and β^{*} is the beam β-function at the collision point. For simulation of 2011 data, the following values are used: $\varepsilon_{\mathrm{N}} = 2.2\,\mu$m and $\beta^{*} = 3\,$m.

An implementation of the "Beam Tool" also provides the possibility to generate a single beam against a fixed target. This is used for the simulation of beam-gas events, where the fixed target is a molecule of the residual gas in the beam-pipe of the experiment. The only required function that the "Beam Tool" implements is `getBeams` which returns the two colliding proton parameters for each event.

f) Vertex Smearing Tool

The "Vertex Smearing Tool" implements the generation of the luminous region of the LHC collisions at the LHCb Interaction Point. By default, the position of the interaction point is smeared around the mean collision point by Gaussian distributions in x, y and z (and truncated at 4σ from the central value). The values of the σ of the Gaussian are

$$\sigma_{x,y} = \sqrt{\frac{\beta^{*}\varepsilon_{\mathrm{N}}}{\beta\gamma}}, \tag{1.5}$$

for the x and y directions and

$$\sigma_z = \frac{\sigma_S}{\sqrt{2}}, \tag{1.6}$$

for the z direction, where σ_S is the RMS of the proton bunch length (set to 57 mm). This gives $\sigma_x = \sigma_y = 30\,\mu$m and $\sigma_z = 40.3$ mm for simulation of 2011 events. The center of the luminous region is set to $x = 0,\ y = 0,\ z = 0.9$ mm.

For the generation of beam-gas events, only the x and y positions are smeared and the z coordinate has a flat distribution. The only function implemented for a "Vertex Smearing Tool" is the function `smearVertex` which computes the position of the primary vertex and moves the generated event to it.

g) Cut Tool

The full simulation of the interactions of the generated events in the LHCb detector material, their digitization and their reconstruction is time consuming. In order to reject as early as possible in the simulation process the events which would anyway not be selected by the analysis, cuts at the generator level are implemented. The most simple cut applied to events is to require that the particles of interest travel in direction of the LHCb detector which has a limited acceptance, i.e. that particles have an angle with respect to the beam direction less than 400 mrad, with $p_z > 0$. This cut is the default cut for the generation of inclusive c and b events.

A more efficient cut that can be applied on “signal” particles is to require that all stable decay products have an angle θ with respect to the beam axis between $10 < \theta < 400$ mrad for charged particles and $5 < \theta < 400$ mrad for neutral particles (tracking detectors and calorimeters do not have the same angular acceptance) and that the "signal" particle has $p_z > 0$. To save also time, if the "signal" particle has $p_z < 0$, the transformation $z \mapsto -z$ is applied to the whole interaction containing. The decay products of Λ, $\overline{\Lambda}$ and K^0_S are excluded from this cut because they can fly long distances and the polar angle of their decay products would not be correctly defined. Photons not coming from a π^0 or η decay are also not considered for the cuts because they may be radiative photons (generated by PHOTOS [27] as described below). In this case, they are not really part of the decay chain but since they cannot be distinguished at this level from a real photon, the only possibility is to ignore them.

A lot of other different implementations are available or can be added easily. Kinematic properties of all the particles generated in the event can be used to apply generator level cuts in the Gauss generation phase. The function that a "Cut Tool" must implement is the function `applyCut(particle, event)` deciding if

the `particle` or the `event` should pass the cut or not.

1.2.3 Sequencing of the generation algorithm

The actions done by each tool are steered from the main generation algorithm. Figure 1.2 represents the order in which tools are called, and shows schematically what they realize.

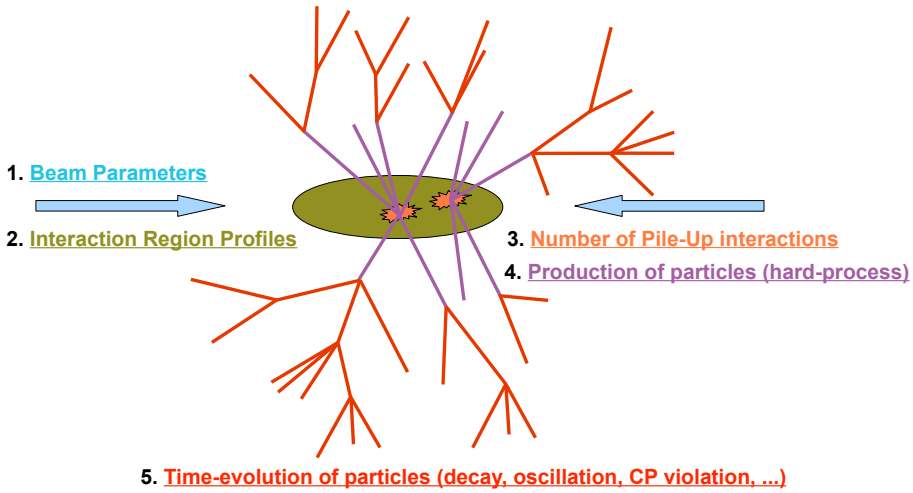

Figure 1.2 – *Sequence of actions for the generation of events*

In more details, the logic of "signal" sample generation is the following to obtain one event:

1. Compute the number N_{int} of pile-up interactions for this event, calling the "*Pile-Up Tool*".

2. Produce N_{int} interactions of type "Minimum Bias" with the "*Production Tool*". For each interaction, the beam parameters (4-momentum) are obtained from the "*Beam Tool*".

   (a) Decay all the produced hadrons that are heavier than the "signal" hadron using the "*Decay Tool*" (for example decay $B^{*(*)}$ hadrons).

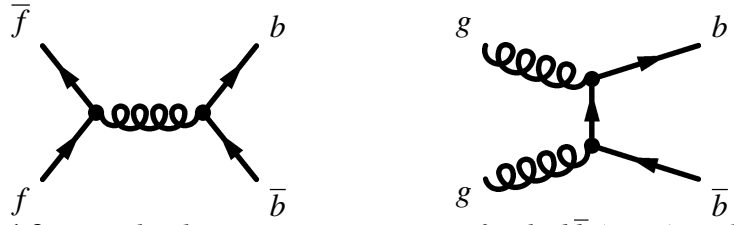

Figure 1.3 – *Tree-level pair-creation processes for the $b\overline{b}$ (or $c\overline{c}$) production.*

(b) Check if one of the interactions contains the signal hadron. If not, go back to 2). This step is arranged by the "*Sample Generation Tool*".

(c) Force the signal particle to decay into the "signal" requested final state, also using the "*Decay Tool*".

(d) Check if the signal particle meets the requirements of the generator level selection, calling the "*Cut Tool*". If not, go back to 2).

(e) Determine the spatial position of each N_{int} interactions with the "*Vertex Smearing Tool*".

(f) Decay all hadrons left undecayed using the "*Decay Tool*".

The generation of other types of events (Minimum Bias, Inclusive or Special samples) are simplified adaptations of the scheme described above.

1.3 Use of PYTHIA 6 in LHCb

The main production generator used in LHCb is PYTHIA, version 6.4. It is a general purpose event generator widely used in high-energy physics collaborations and written in FORTRAN. Thanks to a very large number of steering parameters, PYTHIA can be configured in many different ways. This section describes the settings chosen for the LHCb generation and the interface of Gauss to PYTHIA 6.

1.3.1 Physics processes

The LHCb experiment is dedicated to the study of rare D and B decays. These hadrons are produced at the Leading Order (tree-level) in $2 \to 2$ QCD processes by the creation of $c\overline{c}$ or $b\overline{b}$ pairs from interactions between light quarks and gluons of the protons. These processes are the pair creation processes whose diagrams are shown in Fig. 1.3.

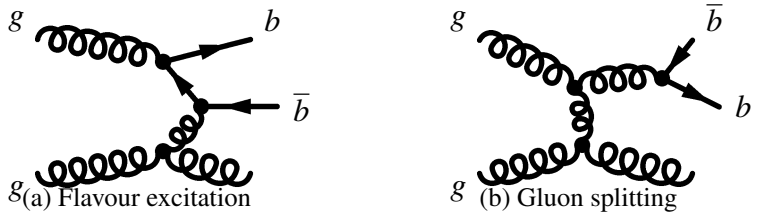

Figure 1.4 – *Higher order processes for the $b\bar{b}$ (or $c\bar{c}$) production.*

B and D production can also emerge from b and c quarks being picked up in the parton distributions of the proton (flavour excitation). They can also be produced by gluon splitting in initial or final state gluon emission. These two processes, represented in Fig. 1.4, are not negligible at LHC energies even though they are of higher orders that the pair-creation processes. They have to be taken into account for a correct generation of heavy flavours. This is why additional $2 \to 2$ QCD processes are activated in Gauss, as can be seen in Tab. 1.1.

In addition to these processes, single diffractive, double diffractive and elastic processes are also added to obtain a realistic description of "Minimum Bias" events. On top of these processes, the production of prompt charmonium and prompt bottomonium states is also activated, since the detailed study of these particles is also part of the LHCb physics program.

Other processes (W, Z or Higgs production) can be activated for specific studies. Since the cross-section of these processes is very small, they are not part of the "Minimum Bias" definition, a special configuration of the software is needed to obtain them. The Gauss software provides the possibility to change the value of any of the PYTHIA 6 configuration switches, through Python configurable files.

1.3.2 PYTHIA 6 tuning

a) Charged track multiplicity

The principle of the PYTHIA tuning for the LHCb simulation is to extrapolate to the LHC energies [28, 29], charged track multiplicities observed at experiments running at lower energies . In PYTHIA, the charged track multiplicity is mainly controlled by the $p_{\mathrm{T}\,\mathrm{min}}$ parameter (`PARP(82)`) which is the minimal transverse momentum of the parton-parton collision in multiple interactions. The LHCb simulation software uses the so-called new interleaved multiple interaction model of PYTHIA 6.4 (`MSTP(81)=21`), with multiple interactions assuming a varying impact parameter and a hadronic matter following a Gaussian matter distribution

(`MSTP(82)=3`).

The mean charged track multiplicity in the central region $\frac{dn_{ch}}{d\eta}|_{\eta=0}$ has been measured by the UA5 [30, 31] and CDF [32] experiments at pp or $p\overline{p}$ collisions for various center-of-mass energies, $\sqrt{s}$. Using the LHCb PYTHIA configuration (i.e. with the parameters given in Table 1.6, in particular using the CTEQ6ll Parton Density Function [33]), values of the $p_{\mathrm{T}\,\mathrm{min}}$ parameter (`PARP(82)`) are deter-

Table 1.1 – *LHCb* PYTHIA *6 Minimum Bias processes*

Process Number	Descripton
11	$f+f' \to f+f'$(QCD)
12	$f+\overline{f} \to f'+\overline{f'}$
13	$f+\overline{f} \to g+g$
28	$f+g \to f+g$
53	$g+g \to f+\overline{f}$
68	$g+g \to g+g$
91	Elastic scattering
92	Single diffractive ($AB \to XB$)
93	Single diffractive ($AB \to AX$)
94	Double diffractive
95	Low-p_{T} scattering
421 - 439	Prompt charmonium
461 - 479	Prompt bottomonium

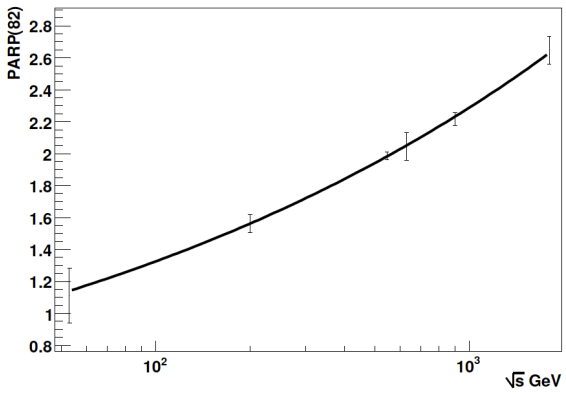

Figure 1.5 – $p_{\mathrm{T}\,\mathrm{min}}$ *=PARP(82) as a function of* $\sqrt{s}$

mined to reproduce the measured multiplicities. The obtained values are shown in Fig. 1.5, as a function of the different experiment energies. In order to be closer to the experimental setups, elastic and single-diffractive events are excluded when computing multiplicities. The evolution of $p_{\mathrm{T}\,\mathrm{min}}$ as a function of $\sqrt{s}$ is then fitted with the function:

$$p_{\mathrm{T}\,\mathrm{min}} = p_{\mathrm{T}\,\mathrm{min}}^{\mathrm{LHC}} \left(\frac{\sqrt{s}}{\sqrt{s_0}} \right)^{2\varepsilon} \tag{1.7}$$

where $p_{\mathrm{T}\,\mathrm{min}}^{\mathrm{LHC}}$ is the extrapolated $p_{\mathrm{T}\,\mathrm{min}}$ at the reference energy $\sqrt{s_0} = 14\,\mathrm{TeV}$. The result of this fit [34] is shown in Fig. 1.5 and is used to determine the multiple interaction PYTHIA parameters:

$$\begin{aligned} PARP(82) &= p_{\mathrm{T}\,\mathrm{min}}^{\mathrm{LHC}} = 4.28\,\mathrm{GeV}/c, \\ PARP(90) &= 2\varepsilon = 0.238. \end{aligned}$$

b) Excited states fraction

A large part of the LHCb physics program is dedicated to *CP* violation studies. These analyses need b flavour tagging to know the flavour of the studied B hadron at production. Some of the tagging techniques use the sign of the charge of particles produced in excited B decays. It is thus very important to describe precisely the fractions of excited $B^{*(*)}$ produced in pp collisions. These fractions are set in order to be compatible with the B^* fraction measured at LEP and CDF [35–37], to preserve spin counting rules for B^{**} states and to give B hadronization fractions in agreement with the measurement averages [38], i.e. $f(B) = 21\%$, $f(B^*) = 63\%$ and $f(B^{**}) = 16\%$ for the excited states fractions, and $f_u = f_d = 40.5\%$, $f_s = 10\%$ and $f_{\mathrm{baryon}} = 9\%$ for the b hadronization fractions into B^+, B^0, B_s^0 and b-baryons respectively. As it can be seen in Fig. 1.6, the production (by PYTHIA) and the decay (by EvtGen) of the excited B states are linked together for the generation of correct hadronization fractions.

In addition, the PYTHIA parameters governing the production of high spin states are determined to also reproduce the production rates measured at LEP of the following resonances: $\rho(770)^0$, $\omega(782)$, $\phi(1020)$, $K^*(892)^{\pm}$ and $D^*(2010)^{\pm}$

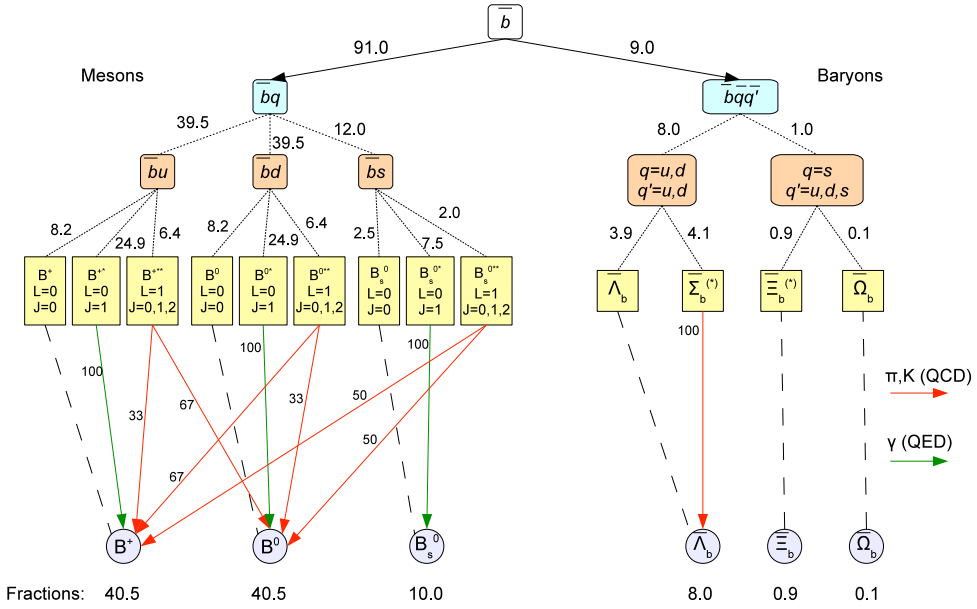

Figure 1.6 – *b hadron production mechanisms: the first level indicates the hadronization of the* $\overline{b}$ *quark into mesons and baryons of the different flavors, the second level is the repartition of the hadrons into the different excited states, and the third level shows the decay of the excited states into weakly decaying b-hadrons, via electromagnetic decays (*green *arrows) or strong decays (*red *arrows).*

[39]. This procedure leads to [40]

$$\begin{aligned} PARJ(11) &= 0.4, \\ PARJ(12) &= 0.4, \\ PARJ(13) &= 0.769, \\ PARJ(14) &= 0.09, \\ PARJ(15) &= 0.018, \\ PARJ(16) &= 0.0815, \\ PARJ(17) &= 0.0815, \end{aligned}$$

where the `PARJ` parameters are PYTHIA configuration parameters determining the proportions of excited states. Namely,

- PARJ(11) is the probability that a light meson has spin $S = 1$,
- PARJ(12) is the probability that a strange meson has spin $S = 1$,
- PARJ(13) is the probability that a c or b meson has spin $S = 1$,

- PARJ(14) is the probability that a spin $S = 0$ meson is produced with an angular momentum $L = 1$ for a total spin $J = 1$,
- PARJ(15) is the probability that a spin $S = 1$ meson is produced with an angular momentum $L = 1$ for a total spin $J = 0$,
- PARJ(16) is the probability that a spin $S = 1$ meson is produced with an angular momentum $L = 1$ for a total spin $J = 1$,
- PARJ(17) is the probability that a spin $S = 1$ meson is produced with an angular momentum $L = 1$ for a total spin $J = 2$,

Depending on the meson content ($i = 11$, 12 or 13), the probabilities to obtain the different states are equal to

$$\begin{aligned}
P(S=0,L=0,J=0) &= (1-PARJ(i))\,(1-PARJ(14)),\\
P(S=0,L=1,J=1) &= (1-PARJ(i))\,PARJ(14),\\
P(S=1,L=0,J=1) &= PARJ(i)\,(1-PARJ(15)-PARJ(16)-\\
&\qquad PARJ(17)),\\
P(S=1,L=1,J=0) &= PARJ(i)\,PARJ(15),\\
P(S=1,L=1,J=1) &= PARJ(i)\,PARJ(16) \text{ and}\\
P(S=1,L=1,J=2) &= PARJ(i)\,PARJ(17).
\end{aligned}$$

Important parameters that also affect the production of excited states are their masses and branching fractions to the ground states. The later are defined in the main decay file of EvtGen (`DECAY.DEC`). These parameters are summarized in Tables 1.2 and 1.3 for b-meson excited states. The result of this tuning is that the hadronization fractions of a b quark into a B^0, B^+, B_s^0 meson or into a b-baryon are equal to

$$\begin{aligned}
f_d &= 40.5\%,\\
f_u &= 40.5\%,\\
f_s &= 10.0\% \text{ and}\\
f_{\text{baryon}} &= 9.0\%.
\end{aligned}$$

This is also illutrated in Fig. 1.6 which gives the fractions of the different states produced at the fragmentation level, and after strong and electromagnetic decays of excited states.

Table 1.2 – *B_u and B_d meson parameters in the LHCb software (charge conjugaison is implied): mass, width and branching fractions.*

	S	L	J	Mass (GeV/c^2)	Width (MeV)
B^0	0	0	0	5.280	0
$B_1(L)^0$	0	1	1	5.723	21
		$\to B^{*+}\pi^-$ (2/3)			
		$\to B^{*0}\pi^0$ (1/3)			
B^{*0}	1	0	1	5.325	6.6×10^{-3}
		$\to B^0\gamma$			
B_0^{*0}	1	1	0	5.738	150
		$\to B^+\pi^-$ (2/3)			
		$\to B^0\pi^0$ (1/3)			
$B_1(H)^0$	1	1	1	5.757	250
		$\to B^{*+}\pi^-$ (2/3)			
		$\to B^{*0}\pi^0$ (1/3)			
B_2^{*0}	1	1	2	5.743	23
		$\to B^+\pi^-$ (30%)		$\to B^{*+}\pi^-\pi^0$(13%)	
		$\to B^0\pi^0$ (15%)		$\to B^{*0}\pi^-\pi^+$ (6%)	
		$\to B^{*+}\pi^-$ (16%)		$\to B^+\pi^-\pi^0$ (8%)	
		$\to B^{*0}\pi^0$ (8%)		$\to B^0\pi^-\pi^+$ (4%)	
B^+	0	0	0	5.279	0
$B_1(L)^+$	0	1	1	5.723	21
		$\to B^{*0}\pi^-$ (2/3)			
		$\to B^{*+}\pi^0$ (1/3)			
B^{*+}	1	0	1	5.325	6.6×10^{-3}
		$\to B^+\gamma$			
B_0^{*+}	1	1	0	5.738	150
		$\to B^0\pi^+$ (2/3)			
		$\to B^+\pi^0$ (1/3)			
$B_1(H)^+$	1	1	1	5.757	250
		$\to B^{*0}\pi^+$ (2/3)			
		$\to B^{*+}\pi^0$ (1/3)			
B_2^{*+}	1	1	2	5.743	23
		$\to B^0\pi^+$ (30%)		$\to B^{*0}\pi^+\pi^0$(13%)	
		$\to B^+\pi^0$ (15%)		$\to B^{*+}\pi^-\pi^+$ (6%)	
		$\to B^{*0}\pi^+$ (16%)		$\to B^0\pi^+\pi^0$ (8%)	
		$\to B^{*+}\pi^0$ (8%)		$\to B^+\pi^-\pi^+$ (4%)	

Table 1.3 – *B_s meson parameters in the LHCb software (charge conjugaison is implied): mass, width and branching fractions.*

	S	L	J	Mass (GeV/c^2)	Width (MeV)
B_s^0	0	0	0	5.366	0
$B_{s1}(L)^0$	0	1	1	5.829	1
		$\rightarrow B^{*+}K^-$ (1/2)			
		$\rightarrow B^{*0}\overline{K}^0$ (1/2)			
B_s^{*0}	1	0	1	5.413	6.6×10^{-3}
		$\rightarrow B_s^0\gamma$			
B_{s0}^{*0}	1	1	0	5.841	150
		$\rightarrow B^+K^-$ (1/2)			
		$\rightarrow B^0\overline{K}^0$ (1/2)			
$B_{s1}(H)^0$	1	1	1	5.859	250
		$\rightarrow B^{*+}K^-$ (1/2)			
		$\rightarrow B^{*0}\overline{K}^0$ (1/2)			
B_{s2}^{*0}	1	1	2	5.840	1
		$\rightarrow B^+K^-$ (30%)		$\rightarrow B^{*+}K^-$(20%)	
		$\rightarrow B^0\overline{K}^0$ (30%)		$\rightarrow B^{*0}\overline{K}^0$ (20%)	

c) Inclusive quarkonium spectrum

One other important aspect of the tuning consists in obtaining a realistic momentum spectrum of J/ψ for analyses such as the one described in Chapter 3. The prompt J/ψ production processes activated in PYTHIA are the Leading Order Colour Singlet and Colour Octet processes. Their implementation and the parameters used are described in detail in Ref. [41]. In particular the long-distance matrix elements controlling the behaviour of the model are obtained from a fit to the CDF data for J/ψ and Υ cross-sections [42, 43] The production of $\psi(2S)$ is also activated, using only the Colour Singlet processes.

Decays of the charmonium states are generated with the EvtGen package. All charmonium states produced are considered for decay by EvtGen with a diagonal spin density matrix where all elements on the diagonal are equal (i.e. they are decayed unpolarised) when they are forced to decay (into $\mu^+\mu^-$ for the simulated events used in the analysis described in Chapter 3). The relevant branching fractions generated with EvtGen are shown in Table 1.4.

Inclusive decays of b-hadrons to J/ψ are also generated using EvtGen. A large fraction of decay modes is described by a list of exclusive channels contained in the decay table used by LHCb [44] and EvtGen delegates to PYTHIA the gener-

ation of the other unspecified decay modes. The inclusive branching fractions for the different b-hadrons to decay modes with a J/ψ in the final state are shown in Table 1.5.

J/ψ production is not well described by the current LHCb simulation. The inclusive branching fractions of b-hadrons to J/ψ given in Table 1.5 are significantly larger than the experimental measurements, namely the branching fraction of the inclusive decay of the B^- and B^0 mixture to J/ψ measured at BABAR [45],

$$\frac{1}{2}\left[\mathscr{B}\left(B^-/B^+ \to J/\psi\, X\right) + \mathscr{B}\left(\overline{B}^0/B^0 \to J/\psi\, X\right)\right] = (1.057 \pm 0.012 \pm 0.04)\,\%$$

and CLEO [46]

$$\frac{1}{2}\left[\mathscr{B}\left(B^-/B^+ \to J/\psi\, X\right) + \mathscr{B}\left(\overline{B}^0/B^0 \to J/\psi\, X\right)\right] = (1.121 \pm 0.013 \pm 0.040 \pm 0.013)\,\%.$$

The branching fraction of the inclusive decay $\mathscr{B}(b \to J/\psi\, X)$ is also overestimated in the LHCb simulation compared to the experimental measurements at DELPHI [47]

$$\mathscr{B}(b \to J/\psi\, X) = (1.12 \pm 0.12 \pm 0.10)\,\%,$$

at L3 [48]

$$\mathscr{B}(b \to J/\psi\, X) = (1.16 \pm 0.16 \pm 0.14)\,\%$$

and at ALEPH [49]

$$\mathscr{B}(b \to J/\psi\, X) = (1.21 \pm 0.13 \pm 0.08)\,\%.$$

Table 1.4 – *Charmonium branching fractions of decays to J/ψ assumed in the LHCb generation software.*

decay mode	branching fraction
$\chi_{c0} \to J/\psi\,\gamma$	1.28 %
$\chi_{c1} \to J/\psi\,\gamma$	36 %
$\chi_{c2} \to J/\psi\,\gamma$	20 %
$\psi(2S) \to J/\psi\, X$	52.7 %

Table 1.5 – *Branching fractions of inclusive b-hadron decays to J/ψ in the LHCb simulation.*

b-hadron	branching fraction
$\overline{B}^0$	$\mathscr{B}\left(\overline{B}^0/B^0 \to J/\psi\, X\right) = (1.59 \pm 0.04)\%$
B^-	$\mathscr{B}\left(B^-/B^+ \to J/\psi\, X\right) = (1.48 \pm 0.04)\%$
$\overline{B}_s^0$	$\mathscr{B}\left(\overline{B}_s^0/B_s^0 \to J/\psi\, X\right) = (1.39 \pm 0.04)\%$
Λ_b^0	$\mathscr{B}\left(\Lambda_b^0/\overline{\Lambda}_b^0 \to J/\psi\, X\right) = (0.81 \pm 0.03)\%$

1.3.3 Repeated hadronization

In order to have a more efficient generation of B events, a special method called "Repeated Hadronization" has been designed. This method consists in looking for events with b quarks, and then keep the parton level event and repeat the hadonization step until the hadron of interest, or "signal hadron" (B^0, B^+, B_s or Λ_b) has been obtained.

In more details, the sequence of actions performed by this method is:

1. Generate "Minimum Bias" events until one with a b quark has been found, save the parton level event (`CALL PYEDIT(21)`).
2. Check if the "signal hadron" is present in the event. If yes, go to 4).
3. Repeat the PYTHIA hadronization on the same parton event (`MSTJ(1)=1`; `CALL PYEDIT(22)`; `CALL PYEXEC`; `MSTJ(1)=0`) , decay all excited B hadrons with EvtGen, and go to 2).
4. Check if the "signal hadron" passes the generator level cuts, if not go back to 1). Note that a completely new event has to be regenerated in order to avoid biases.

The non-default PYTHIA parameters used in the LHCb generation software are summarized in Table 1.6. They imply that the α_s value used in PYTHIA is computed at the second order and depends on the energy scale, and that the parton density function is the CTEQ6LL [33] PDF taken from the LHAPDF library [50].

With these settings, the total pp cross-section at $\sqrt{s} = 7\,\text{TeV}$ (including inelastic and diffractive processes) is found to be $91.2 \pm 0.5\,\text{mb}$, the prompt J/ψ produc-

Table 1.6 – *LHCb* PYTHIA *6 parameters*

Parameter	Value	Parameter	Value
CKIN(41)	3.0	PARP(86)	0.66
MSTP(2)	2	PARP(89)	14000
MSTP(33)	3	PARP(90)	0.238
MSTP(81)	21	PARP(91)	1.0
MSTP(82)	3	PARP(149)	0.02
MSTP(52)	2	PARP(150)	0.085
MSTP(51)	10042	PARJ(11)	0.4
MSTP(142)	2	PARJ(12)	0.4
PARP(67)	1	PARJ(13)	0.769
PARP(82)	4.28	PARJ(14)	0.09
PARP(85)	0.33	PARJ(15)	0.018
MSTJ(26)	0	PARJ(16)	0.0815
PARJ(33)	0.4	PARJ(17)	0.0815

tion cross-section is $102 \pm 12\,\mu$b, the $b\bar{b}$ production cross-section is $454 \pm 2\,\mu$b, and the J/ψ from b production cross-section $13.8 \pm 1\,\mu$b.

1.4 Use of EvtGen in LHCb

EvtGen [11] is the main decay engine used in LHCb. It is a package developped in CLEO and BABAR and it is particularly interesting for what concerns B decays because it implements a very large number of B decay modes studied at LHCb, and it can also take care of angular distribution correlations in complex subsequent decays or of time-dependant CP violation in B decays.

1.4.1 Implementation of incoherent B mixing

EvtGen was however developped for the $\Upsilon(4S)$ B-factories environment and had to be adapted to incoherent B production like the one seen at the LHC pp collisions. The main difference concerns B mixing. Contrary to $B\overline{B}$ pairs produced at the $\Upsilon(4S)$ which evolve coherently, the B mesons from the $b\bar{b}$ pairs produced at

hadron collisions evolve independantly one from the other. In the EvtGen version adapted by LHCb, a B meson produced as a B^0 (or B_s^0) and evolving into a $\overline{B}^0$ (or $\overline{B_s}^0$) at the time of its decay, is implemented as a decay $B^0 \to \overline{B}^0$ (or $B_s^0 \to \overline{B_s}^0$). The mixing probability is generated for a B initial state as:

$$P_{\text{mix}} = \frac{x^2+y^2}{x^2+y^2+\alpha^2(2+x^2-y^2)}, \tag{1.8}$$

and for a $\overline{B}$ initial state:

$$P_{\text{mix}} = \frac{x^2+y^2}{x^2+y^2+\alpha^{-2}(2+x^2-y^2)}, \tag{1.9}$$

where $x = \Delta m$, $\alpha = \left|\frac{q}{p}\right|$ and $y = \frac{\tau_{\text{H}}-\tau_{\text{L}}}{\tau_{\text{H}}+\tau_{\text{L}}}$.

The mixing parameters Δm and $\left|\frac{q}{p}\right|$ are transmitted to EvtGen through the main decay configuration file [44] with the following syntax:

```
Define qoverp_incohMix_B0 1.0
Define dm_incohMix_B0 0.507e12
Define qoverp_incohMix_B_s0 1.0
Define dm_incohMix_B_s0 17.8e12
```

meaning that $\Delta m_d = 0.507 \times 10^{12}\,\hbar\text{s}^{-1}$ and $\Delta m_s = 17.8 \times 10^{12}\,\hbar\text{s}^{-1}$. The lifetime of the heavy and light mass eigenstates, τ_{H} and τ_{L} respectively, are defined in the EvtGen particle list through four extra particles, B_{H}, B_{L}, $B_s\text{H}$ and $B_s\text{L}$.

Then the lifetime distribution of the neutral B mesons is generated proportional to:

$$f(t) = e^{-(\Gamma_{\text{H}}+\Gamma_{\text{L}})t}\left(\cosh\left(\frac{(\Gamma_{\text{L}}-\Gamma_{\text{H}})t}{2}\right)+\cos(\Delta m t)\right), \tag{1.10}$$

for unmixed states, and

$$f(t) = e^{-(\Gamma_{\text{H}}+\Gamma_{\text{L}})t}\left(\cosh\left(\frac{(\Gamma_{\text{L}}-\Gamma_{\text{H}})t}{2}\right)-\cos(\Delta m t)\right), \tag{1.11}$$

for mixed states, where $\Gamma_{\text{H}} = 1/\tau_{\text{H}}$ and $\Gamma_{\text{L}} = 1/\tau_{\text{L}}$.

1.4.2 Implementation of *CP* violation

Time dependant *CP* violation implementation in the original EvtGen version is also based on the fact that the B mesons are produced coherently from the $\Upsilon(4S) \to B^0\overline{B}^0$ decay and thus cannot be applied directly to the LHC environment. Correct generation of time dependant *CP* violation also requires a special interface with the generation steering framework. A consequence of *CP* violation is that the time-integrated *CP* asymmetry of B decays into *CP* eigenstates is different from 0, when the B are produced incoherently. For example, the decay rate of a B produced as a B^0 and decaying into $J/\psi K_S$ as a function of the time, t, is equal to

$$\Gamma(B^0 \to J/\psi K_S) = \frac{\Gamma_B}{4} e^{-\Gamma_B t}[1 + \sin(2\beta)\,\sin(\Delta m t)], \tag{1.12}$$

where β is one angle of the Unitarity Triangle and Δm is the B^0 oscillation frequency. For a B produced in the state $\overline{B}^0$, it is equal to

$$\Gamma(\overline{B}^0 \to J/\psi K_S) = \frac{\Gamma_B}{4} e^{-\Gamma_B t}[1 - \sin(2\beta)\,\sin(\Delta m t)]. \tag{1.13}$$

The integrated *CP* asymmetry between B^0 and $\overline{B}^0$ is the equal to

$$A = \frac{\int_0^{+\infty} \Gamma(B^0 \to J/\psi K_S, t)\mathrm{d}t - \int_0^{+\infty} \Gamma(\overline{B}^0 \to J/\psi K_S, t)\mathrm{d}t}{\int_0^{+\infty} \Gamma(B^0 \to J/\psi K_S, t)\mathrm{d}t + \int_0^{+\infty} \Gamma(\overline{B}^0 \to J/\psi K_S, t)\mathrm{d}t}. \tag{1.14}$$

The value of A is approximately equal to 33% using world averages of the parameters [38].

Since neutral B and $\overline{B}$ mesons are produced in equal amount by the production generator, PYTHIA (apart from small production asymmetries), forcing each B meson to decay into a *CP* violating decay mode to obtain a "signal" sample, will result also in a sample with equal amount of B and $\overline{B}$ mesons, thus not respecting the correct integrated *CP* asymmetry.

To overcome this problem, a dedicated interface between EvtGen and Gauss has been designed [51]. The principle of this interface is that the flavour at production of the "signal" b-hadron is generated randomly by EvtGen, depending on the generated B lifetime, t: i.e. EvtGen can request the flavour of the B produced by PYTHIA to be flipped. The B and $\overline{B}$ decay amplitudes are normalized such that they are equal at $t = 0$. In the final sample, only events for which the B flavour generated by EvtGen matches the flavour produced by PYTHIA are kept. This allows not only to generate the correct *CP* integrated asymmetry, but also to keep possible production asymmetries.

1.4.3 Interface with PYTHIA 6 and PHOTOS

Particle decays are configured in EvtGen by a decay file which contains a list as complete as possible of possible decay modes for all particles [44]. This decay file is inherited from the BABAR decay file and it contains very precise description and modelling of B^0, B^+ and D decays. The branching fractions of the decay modes are updated regularly using the more and more precise measurements. The B_s^0 and b-baryon decay description has been improved adding new decay modes that are important for the LHCb physics program. Eventually, branching fraction measurement made at LHCb will be imported to the decay file.

However, a lot of decay modes have not been measured and the listed decay modes do not saturate the particle decay widths. The decays to these unknown modes are delegated by EvtGen to JETSET (the ancestor of PYTHIA) in the original version of EvtGen: the quarks of the hadron are given to the JETSET program to be hadronized and to form the final states.

Since in LHCb PYTHIA 6 is also used as production generator, the interface to JETSET has been replaced by an interface to PYTHIA 6. Gauss uses a single instance of PYTHIA 6, that must be shared between the production generator and EvtGen. PYTHIA settings have been chosen not to have any interference between the two usages. In particular, particle properties are set from the Gauss framework in PYTHIA and EvtGen with exactly the same values, to ensure coherence inside the entire generation process. Decay modes generated inside EvtGen are removed from the PYTHIA decay table so that a given decay mode is always generated either only by EvtGen, or only by PYTHIA.

The interface of EvtGen to PYTHIA 6 mainly consists in transforming the internal EvtGen event records into PYTHIA event record (FORTRAN common blocks), in calling the necessary PYTHIA routines to handle particle decays, and then in retrieving and transfering the result of the decay from PYTHIA event record to the EvtGen format.

QED radiative corrections to the charged decays are generated using the PHOTOS package [27], where the so-called exponentiation method is activated, which is in agreement with $O(\alpha^2)$ Matrix Element computations. PHOTOS is called internally by EvtGen, and is configured in LHCb to be applied on all decays with charged tracks in the final state.

1.4.4 Signal decays

EvtGen offers the possibility to force decays of particles to predefined "signal" modes, using aliases. This possibility is used in the Gauss software to produce "signal" samples. However, again because of complications due to the hadronic environment, a special interface had to be designed to use this feature correctly. The main reason for that is that when generating "signal" samples, only one of the B hadrons produced in the event has to be forced to decay to the signal mode, and there are at least two B hadrons produced per $b\overline{b}$ event. For the generation of a signal B^0 sample for example, an event with both a B^0 and a $\overline{B}^0$ will have twice more probability to decay to the signal mode than an event with only one B^0. Then, in order to establish the correct proportion of $B^0\overline{B}^0$ compared to $B^0\overline{B_x} + \overline{B}^0 B_x$, where B_x is a b-hadron which is not a B^0, events where only one B^0 and no $\overline{B}^0$ or only one $\overline{B}^0$ and no B^0 are rejected with probability $\frac{1-\mathscr{B}}{2-\mathscr{B}}$, where $\mathscr{B}$ is the branching fraction of the signal decay mode. Only one of the B^0 or $\overline{B}^0$ will be forced to the signal decay.

1.5 Conclusion

The logic and implementation of the generation of physics events for the LHCb simulation software has been described. It allows to interface different generators available within the high-energy physics community and also provides tools to generate events in conditions as close as possible to the real conditions seen in the LHCb experimental setup. The major ongoing developments are to use the new generation of generators, written in C++ and aiming at replacing older FORTRAN generators, like PYTHIA 8 and PYTHIA 6. An interface between Gauss and PYTHIA 8 for the production part, and between EvtGen and PYTHIA 8 for the decay part are being studied. This will simplify the structure of the software, since several instances of PYTHIA 8 could be used, with different settings but not interfering between each other (for example one for the signal process, and a different one for the Minimum Bias pile-up).

CHAPTER 2

Level 0 Calorimeter Trigger

For a process with cross-section σ, the rate of pp interactions from the LHC collisions giving this process is equal to

$$R = \mathscr{L}\sigma, \tag{2.1}$$

where $\mathscr{L}$ is the instantaneous luminosity. When the LHC rings are filled with N proton bunch pairs colliding at the LHCb interaction point, the average number of interactions per bunch crossing containing the process is equal to

$$\mu = \frac{R}{fN} = \frac{\mathscr{L}\sigma}{fN}, \tag{2.2}$$

where $f = 11.25\,\text{kHz}$ is the LHC revolution frequency.

The distribution of the number of interactions per bunch crossing containing the process is a Poisson distribution of mean μ, $\mathscr{P}(n) = \frac{\mu^n e^{-\mu}}{n!}$ and the probability that a bunch crossing gives at least one interaction containing the process is

$$\mathscr{P}_{n>0} = 1 - \mathscr{P}(0) = 1 - e^{-\mu}. \tag{2.3}$$

The rate of bunch crossings containing at least one process of interest is thus

$$F = (1 - e^{-\mu})fN = \left(1 - e^{-\frac{\mathscr{L}\sigma}{fN}}\right) fN \tag{2.4}$$

The typical running conditions at LHCb during the year 2011 were:

- instantaneous luminosity: $\mathscr{L} = 3.5 \times 10^{32}\,\text{cm}^{-2}\text{s}^{-1}$
- number of colliding bunch pairs: $N = 1\,296$

The visible pp collision cross-section at LHCb was measured equal to $\sigma_{\text{visible}} = 58.8 \pm 2.0\,\text{mb}$ [52], where a visible pp collision is defined as an interaction giving at least two tracks in the VELO. The rate of visible collisions is then equal to $F_{\text{visible}} = 11\,\text{MHz}$.

The available computing resources set a limit on the data rate that can be written on tape at 2 kHz. Moreover, the visible rate of decay modes interesting for the physics program of LHCb (excluding the study of CP violation in charm decays which have a higher rate) is also very small. For example, the visible cross-section of $B^0 \to \pi^+\pi^-$ production is equal to

$$\sigma_{B\to\pi\pi} = 2\,\sigma_{b\bar{b}}\, f_{b\to B^0}\, \varepsilon_{\text{geom}}\, \mathscr{B} = 0.21\,\text{nb} \tag{2.5}$$

where $\sigma_{b\bar{b}} = 288 \pm 48\,\mu\text{b}$ [10] is the $pp \to b\bar{b}X$ production cross-section, $f_{b\to B^0} = 0.404 \pm 0.012$ is the hadronisation fraction of a b quark into a B^0 meson [38], $\varepsilon_{\text{geom}} = 18\%$ is the probability that both pions from the B^0 decay are inside the LHCb detector acceptance and $\mathscr{B}$ is the branching fraction of the decay $B^0 \to \pi^+\pi^-$ [19]. The rate of collisions containing a $B^0 \to \pi^+\pi^-$ decay in the LHCb acceptance is then equal to 73.5 mHz.

The LHCb experiment needs a selective trigger system to be able to obtain the necessary reduction factors. This system is organized in three successive levels:

1. Level 0 (L0), a hardware trigger which uses information from the Calorimeters, the MUON and the Pile-Up detectors. Events containing high transverse momentum (p_{T}) particles are kept since they are the sign of the possible presence of a b-hadron in the event. At this level, multiplicity counters are also available in order to reject events with a large activity which would be very long to process at the following steps. At the output of the L0, the rate is reduced to a maximum of 1.1 MHz.

2. High Level Trigger 1 (HLT1), a software trigger which runs on CPUs of an event filter farm. It uses information from the tracking detectors to form tracks and to apply impact parameter and transverse momentum selections on them, in order to detect events with secondary vertices because of the relatively long lifetimes of the B and D mesons.

3. High Level Trigger 2 (HLT2), also a software trigger which applies selection cuts similar to the ones used in the offline analysis: invariant mass selections, muon and electron identification, decay length cuts.

In this chapter, the details of the implementation of the part of the L0 related to the Calorimeters (L0CALO) will be described. The L0CALO was designed at

LAL [53] and is implemented in different electronics boards developped in different LHCb groups: Orsay (LAL), Clermont-Ferrand (LPC), Annecy (LAPP), Barcelona and Bologna. The functionalities of these different boards will be described in this chapter together with their integration in the global LHCb acquisition and control system.

2.1 Usage of the Calorimeters in the L0 trigger

The role of the calorimeter L0 trigger is to detect, at the LHCb clock frequency (40 MHz), high p_{T} objects amongst the particles produced by collisions. The L0CALO is designed to determine the hadron, electron, photon, and π^0 candidates of highest p_{T}. The presence of a high p_{T} particle allows to discriminate between events containing a b-hadron and minimum-bias events.

2.1.1 Calorimeter hardware

Identification of hadrons, electrons, photons and π^0 for the L0 trigger is realized using the Calorimeter system, formed of four subsystems, a scintillator pad detector (SPD), a preshower detector (PS), an electromagnetic calorimeter (ECAL) and a hadronic calorimeter (HCAL). These four subdetectors are stacked along the collision axis (z axis of the LHCb coordinate system) as shown in Fig. 2.1.

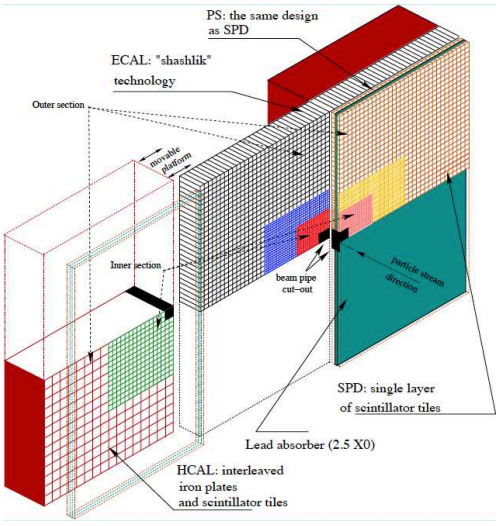

Figure 2.1 – *Structure of the Calorimeter system*

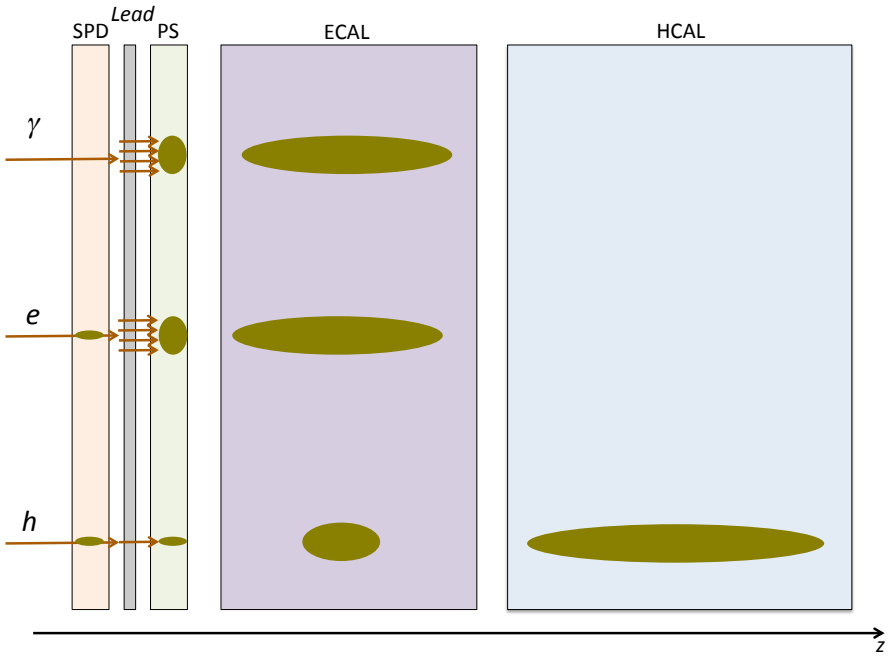

Figure 2.2 – *Structure of the Calorimeter system*

The SPD and PS, two planes of scintillating pads, are separated by a lead converter wall of 15 mm thickness, corresponding to 2.5 X_0 radiation length. The longitudinal segmentation of the calorimeter into these four pieces (SPD, PS, ECAL and HCAL) provides enough information to distinguish between charged and neutral particles (using SPD information) and between hadronic and electromagnetic shower types, as illustrated in Fig. 2.2.

In order to obtain a good energy and a good position resolution on individual particles, the calorimeters are segmented in the plane transverse to the beam axis into square "cells", in three zones of different granularities (two zones for the HCAL). Since the particle density is larger close to the beam axis, the size of the cells is the smallest in the center (Inner area) and increases as a function of the distance to the beam axis (Middle and Outer areas for SPD, PS and ECAL, Outer area for the HCAL). In order to ease the processing of the subdetector informations, especially for the L0 trigger, the transverse segmentation is projective between SPD, PS and ECAL, i.e. the cell boundaries are aligned between the SPD, PS and ECAL, and the cell sizes are adjusted to take into account their different positions in z. The HCAL cells are larger than the cells in the other sub-detectors but their sizes have been chosen to be a multiple of the sizes of the SPD, PS and ECAL sizes also to simplify computations. Figures 2.3 show the structure of the

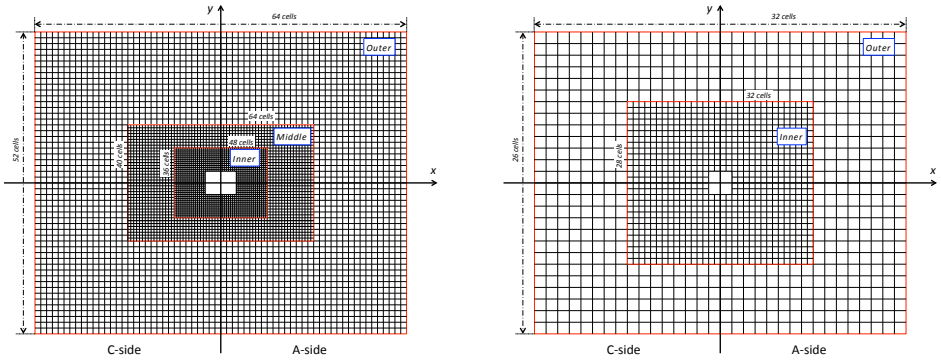

Figure 2.3 – *Organisation of the SPD, PS and ECAL (left) and of the HCAL (right)*

calorimeters in the transverse plane, seen from the Muon detectors towards the interaction point. The calorimeters are also separated into two halves that can be independently moved in a direction perpendicular to the z axis in order to allow maintenance of the hardware. These halves are referred to as A-side ($x > 0$) and C-side ($x < 0$).

The four sub-detectors use the same principle: the light produced in scintillator tiles by the charged particles contained in the shower developing from the incoming particle is collected by wave-length shifting fibers, is transported to photomultiplier tubes (PMT) connected to the read-out front-end electronics and is sampled at a rate of 40 MHz equal to the LHC bunch crossing frequency. The absorber material is lead for SPD, PS and ECAL and iron for HCAL.

a) Scintillating Pad Detector (SPD) and Preshower (PS)

The SPD and PS are planes of scintillator pads located before and after the $2.5\,X_0$ lead converter wall. The dimension of the sensitive area of the SPD is 7.57 m along the x axis and 6.17 m along the y axis. The dimensions of the PS is slightly larger to respect the projectivity between the detector cells with respect to the interaction point and are equal to 7.6 m along the x axis and 6.2 m along the y axis.

The photomultiplier tubes used to read out the detector are Multi Anode Photo-Multiplier Tubes (MAPMT) which can handle 64 channels (cells). The SPD is a binary detector which gives a hit when the energy deposited in the cell is larger than a threshold. The PS measures an energy, however for the trigger, it converts it into a single bit, also comparing with a threshold.

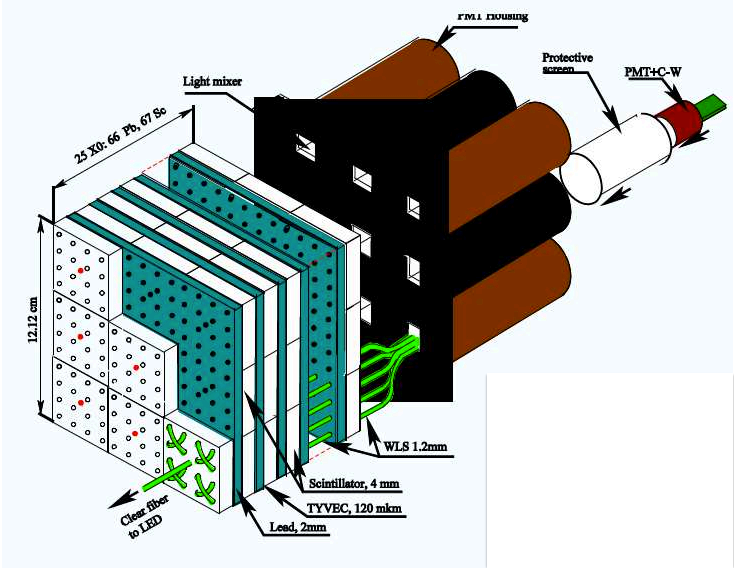

Figure 2.4 – *Schematics of one Inner ECAL Module.*

b) Electromagnetic Calorimeter (ECAL)

The ECAL is a shashlik sampling calorimeter consisting of plates of lead and scintillators stacked perpendicular to the z axis. The plates are organized in modules of the equal sizes, each module being divided into cells: 1 cell for the Outer Area, 4 cells for the Middle Area and 9 cells for the Inner Area. Fig. 2.4 shows the schematics of one Inner Area module, consisting of 66 lead plates of 2 mm width and 67 scintillator plates of 4 mm width.

The depth of the sampling volume of the ECAL (the lead/scintillator plates) is equal to 42 cm corresponding to $25\,X_0$ and $1.1\,\lambda_I$. The Moliere radius of the ECAL is equal to 3.5 cm and the energy resolution obtained is equal to

$$\sigma_E = a\sqrt{E} \oplus bE, \tag{2.6}$$

where a is equal to 8% to 10% depending on the area (Inner, Middle or Outer), $b = 0.9\%$ and E is expressed in GeV.

c) Hadronic Calorimeter (HCAL)

The HCAL is also a sampling calorimeter composed of tiles of scintillator and iron parallel to the z axis. The tiles are grouped into large modules as shown in Fig. 2.5. The depth of the sampling volume is equal to 1.2 m corresponding to $5.6\,\lambda_I$.

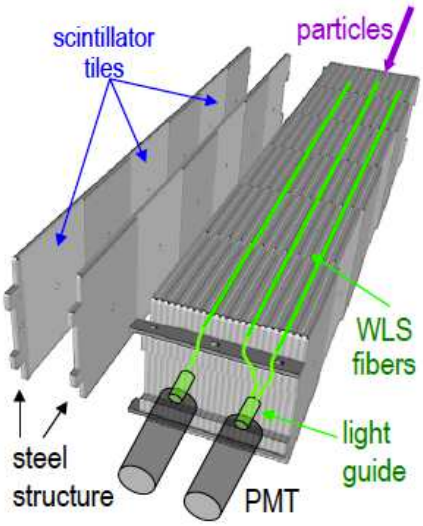

Figure 2.5 – *Schematics of the HCAL tile assembly.*

2.1.2 Trigger design

The goal of the L0 calorimeter trigger is to detect particles with relatively larger transverse momentum. The information from the four calorimeter sub-detectors

Table 2.1 – *Summary of the calorimeter parameters*

	SPD	PS	ECAL	HCAL
z position (m)	12.3	12.3	12.5	13.33
Cell size (cm)				
Inner	3.96	3.98	4.04	13.1
Middle	5.95	5.98	6.06	
Outer	11.9	11.95	12.12	26.2
Number of cells				
Inner	1536	1536	1536	880
Middle	1792	1792	1792	
Outer	2688	2688	2688	608
Total depth (cm)	7.5	7.5	83.5	123.3

is combined to identify three types of particles: electrons, photons and hadrons, and to estimate their transverse energy, E_{T}. The E_{T} of the candidates is compared to a threshold and the event is triggered if at least one candidate has E_{T} larger than the threshold.

The transverse energy measured in one calorimeter cell is defined as

$$E_{\mathrm{T}} = E \sin\theta, \tag{2.7}$$

where E is the energy collected in the cell, and θ is the polar angle between the beam line and a line joining the origin of the LHCb coordinate system (close to the interaction point) and the cell, $C(x_C, y_C, z_C)$. x_C and y_C are the coordinates of the center of the cell in the $x-y$ plane and z_C is chosen to correspond to the position of the maximum extension of the shower. This definition of the transverse energy is natural for neutral particles but ignores the bending of the trajectory in the experiment magnet for charged tracks and differs in this case from the track transverse momentum.

The transverse energy of L0 calorimeter candidates is computed in square clusters made of 4 adjacent cells (2×2), summing the transverse energy of each cell. The size of the cluster is chosen to simplify connections in the trigger system but is sufficient to contain a large fraction (90%) of the total energy deposited by the particle. Furthermore, for simplification reasons, 2×2 clusters are only made of cells of same sizes located in the same area (Inner, Middle or Outer), and on the same side (only A-side or only C-side).

Calorimeter cells are read out and the detector data is processed first in ECAL and HCAL Front-End Boards as will be described in details below. One Front-End Board covers an area of 8×4 cells (8 along the x axis and 4 along the y axis). The borders of the areas covered by the Front-End Boards are shown for the ECAL and HCAL in Fig. 2.6. The first stage of the trigger processing is to compute the 2×2 cluster with highest E_{T} inside each board in the ECAL and the HCAL . From these clusters, several types of candidates are obtained together with global event quantities:

electron a ECAL cluster with one or two cells with hits in the PS 2×2 cluster located in front of the ECAL cluster, but rejecting clusters with 0, 3 or 4 hits in the PS. The SPD cluster in front of the ECAL cluster must have at least one hit, and the PS and SPD clusters must also have at least one hit in common. Since the particle multiplicity was higher than design due to higher pile-up during the 2010 and 2011 LHCb runs, the rejection of clusters with 3 or 4 hits in the PS was causing a large loss of efficiency for the electron trigger in the Inner part of the ECAL. Since beginning of 2011,

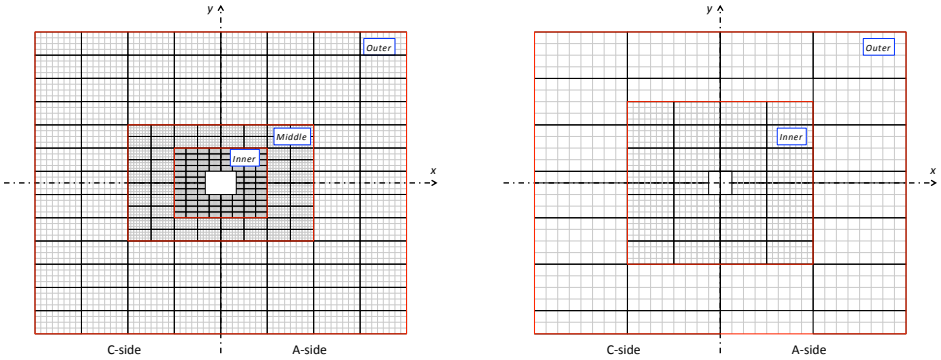

Figure 2.6 – *Borders of the areas covered by the Front-End Boards in ECAL (left) and HCAL (right).*

the electron definition has been modified for the Inner area to also validate as electron, clusters with 3 or 4 hits in the PS.

photon a ECAL cluster with one or two cells with hits in the PS cluster located in front. Clusters with 0, 3 or 4 hits are rejected. The SPD cluster in front of the PS cluster should have no hit in common with the PS one. The same modification of the algorithm done for electrons was applied for photons for the Inner area, i.e. accepting in this zone clusters with 3 or 4 hits in the PS.

hadron a HCAL cluster. If one of the ECAL clusters is in front of the HCAL cluster, the transverse energy of this ECAL cluster is added to the E_{T} of the HCAL cluster. Since the HCAL cells are larger than the ECAL cells, a HCAL cluster can be in front of more then one ECAL clusters (four at most). In this case, the selected hadron candidate is the one with highest E_{T} after adding the ECAL energy. In total, 50 candidates are computed, one per HCAL Front-End board.

local π^0 a large cluster in ECAL, where the cluster is formed by 32 cells (8×4, 8 cells along x and 4 cells along y) and corresponds to one Front-End board. This cluster must have at least one hit in the PS 2×2 cluster in front of the 2×2 ECAL cluster with highest E_{T} is this Front-End board. During the 2010 and 2011 LHCb runs, these trigger candidates were not used.

global π^0 formed associating two ECAL clusters located in neighbor Front-End boards. The E_{T} of the candidate is the sum of the E_{T} of the two clusters. During the 2010 and 2011 LHCb runs, these trigger candidates were not use.

Table 2.2 – *Thresholds and rates of L0CALO.*

Candidate	Condition	Rate (kHz)
hadron	$E_{\mathrm{T}} > 3.5\,\mathrm{GeV}$ and SPD Multiplicity < 600	400
electron	$E_{\mathrm{T}} > 2.5\,\mathrm{GeV}$ and SPD Multiplicity < 600	120
photon	$E_{\mathrm{T}} > 2.5\,\mathrm{GeV}$ and SPD Multiplicity < 600	60

Hadron Sum E_{T} the sum of the E_{T} of all 50 hadron candidates in the event. This trigger line was mainly used to identify empty bunch crossings to determine the luminosity.

SPD Multiplicity the total number of cells with hit in the SPD [54]. This trigger line was used as "Global Event Cut" in order to reject events with large multiplicity which would be very long to process in the HLT.

The E_{T} of the candidates is compared to a fixed threshold and events containing at least one candidate above threshold is accepted by the L0. In order to reject busy events which would saturate the HLT processing farms, a veto is also applied on events containing more than 600 hits in the SPD. Table 2.2 shows the thresholds applied during the 2011 LHCb run and the output rates observed with an instantaneous luminosity of $3.5 \times 10^{32}\,\mathrm{cm}^{-2}\mathrm{s}^{-1}$ and 1 296 pairs of proton bunches colliding at the LHCb interaction point which were the typical running conditions encountered at the end of 2011. The trigger configuration is defined by a Trigger Configuration Key (TCK), which is a number defining uniquely the thresholds and algorithms used in the full trigger chain, L0 and HLT.

2.2 Implementation

The computing of the L0CALO trigger candidates described above is realized in custom electronic boards integrated in the LHCb data acquisition (DAQ) system. The detector information is processed in successive steps in Front-End Boards, Trigger Validation Boards and then Selection Boards and the final result is obtained in the L0 Decision Unit (L0DU).

2.2.1 Data Acquisition Structure

The general structure of the LHCb DAQ system [55] is represented in Fig. 2.7. The detector signals are processed in Front-End Boards and the event information is stored in buffers. The ECAL, HCAL and MUON electronics also provide information for the L0 trigger system which decides if the event should be sent to the HLT farm for further processing or not. Upon reception of a L0 decision for a given event, the content of the Front-End buffer for this event is sent to read-out boards. These boards, called TELL1 (or ULK1 for the RICH detectors), format the content of the detector information and send event fragments through an ethernet network to a CPU farm. One node of the farm receives the fragments and builds complete events out of them. These events are then processed on the same CPU node by the HLT algorithms which decide if the event should be sent to storage for offline data analysis. The Front-End boards are located in the cavern, close to the detector and are exposed to radiations. The TELL1 boards are located in barracks in the cavern, protected behind a concrete shielding wall, approximately 50 m from the detector.

The coordination of the processing is ensured by the Timing and Fast Control (TFC) system. The various functions of this system are described in detail in Ref. [56]. The system schematically consists in one master board called ODIN sending clock, synchronization and control signals to the various boards. The signals relevant for the L0 are:

1. **Clock**: a common clock is sent to all electronics boards. The frequency of the clock is the frequency of the LHC, 40.08 MHz. During collisions, the clock is synchronized on the beam and its phase is adjusted such that each sub detector sample at its maximum the signal induced by particles coming from the interaction point.

2. **Bunch Crossing Id (BCID) Reset**: in order to align and process coherently the information from the different detectors, each event fragment is identified with a local counter (BCID). This counter is synchronized to the LHC bunch structure, which is composed of 3 564 bunch slots, thanks to the BCID Reset signal. Figure 2.8 shows the nominal LHC filling scheme. The substructures are due to the fact that the LHC is filled from the PS and SPS accerators whose own filling schemes are reflected in the final one. The bunch identified as BCID 0 is the first bunch after the long gap of 119 empty bunches marked as τ_5 in the figure.

3. **L0 accept**: this signal transmits the trigger decision to the Front-End electronics. When they receive this signal, the Front-End boards send the data

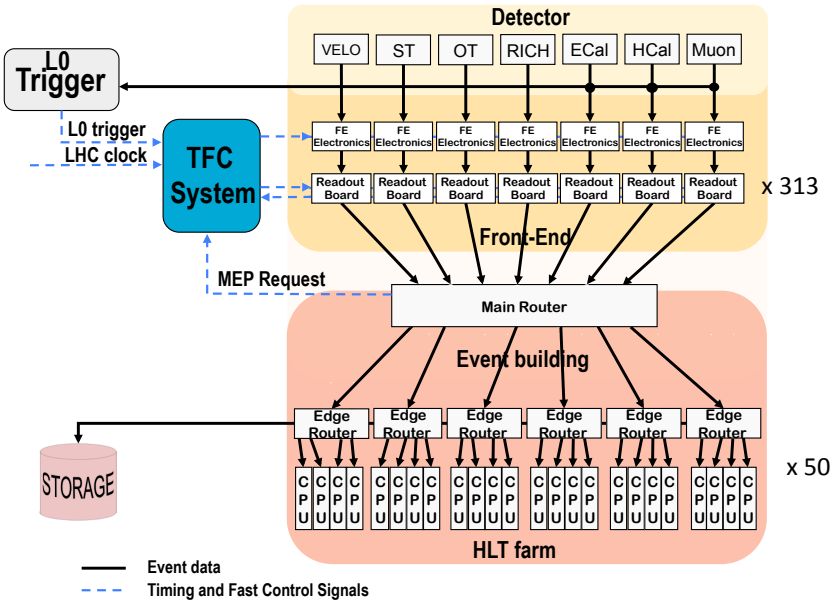

Figure 2.7 – *Schematics of the LHCb Data Acquisition System.*

corresponding to the event to the TELL1 boards for further processing. This signal is mainly generated by the L0 physics trigger decision computed from the MUON and Calorimeter data but it also includes technical triggers such as random or periodic triggers. In order to send to the HLT farm the correct event, the latency (i.e. the time between the collision and the arrival of the corresponding trigger signal at the Front-End board) of the physics trigger system is fixed and equal to $4\,\mu$s or 160 clock cycles. The system is designed to accept a maximum L0 accept rate of 1.1 MHz.

4. **L0 Event ID Reset**: this signal allows to reset local counters of numbers of received trigger decisions. These counters are used to identify event fragments that must be assembled together by the computer farm.

5. **Calibration Command**: this functionality is used in the L0CALO to perform tests or checks of the trigger processing in the electronics. This is a signal which can trigger the injection of known test patterns in the processing chain whose result can then be checked and compared to the ex-

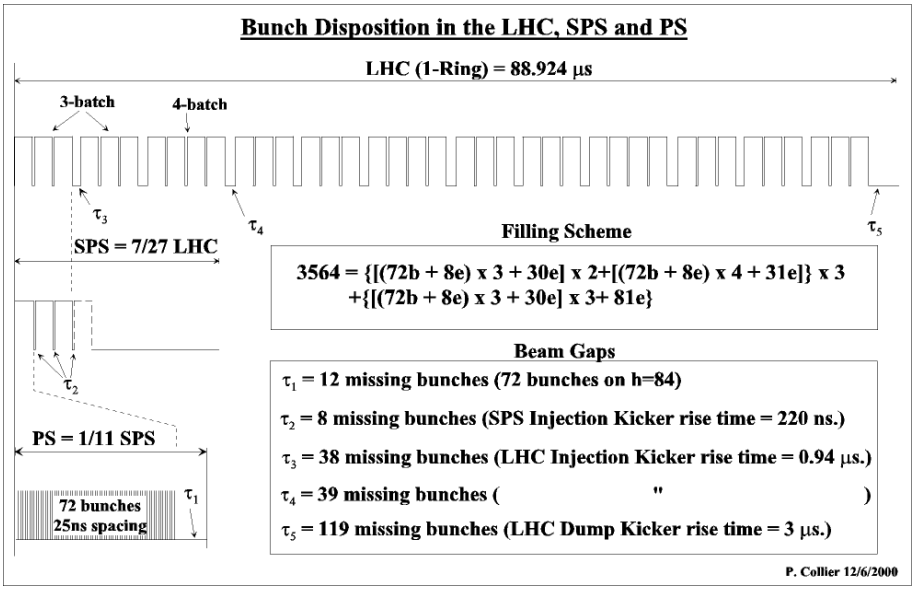

Figure 2.8 – *LHC nominal filling scheme.*

pected values. This command is composed of two signals: a calibration pulse which is decoded in the Front-End electronics and is used to inject the known pattern, and a L0 accept signal sent unconditionally 160 clock cycles after the calibration pulse in order to collect the result of the processing of the injected signal.

The TFC signals are distributed over a custom optical fiber network (TTC) developed at CERN for the LHC experiments [57]. The optical fibers are single mode fibers operated at a laser wavelength of 1 310 nm and equipped with connectors of type "ST". At the end of the fibers, a receiver (TTCrx) delivers the signals to the Front-End electronics [58] and is usually mounted on a mezzanine board (TTCrq) to ease its usage. The length of the TTC fibers between the ODIN board which is located in the barracks behind the shielding wall, and the Calorimeter Front-End electronics located close to the detector is equal to 100.5 m: 2.5 m inside the barrack, 56 m [59] between the barrack and a fixed point located behind the MUON in the cavern, as shown in Fig. 2.9 and 42 m between the fixed point and the Front-End electronics, going inside a cable chain. For reference, the details of the cabling is given in Appendix A.

A partitioning system allows to send clock and TFC commands only to a single sub detector or to a group of sub detectors without affecting the others. This is useful to test parts of the LHCb detector in parallel when there are no collisions delivered by the LHC for example. The calorimeter system is divided into

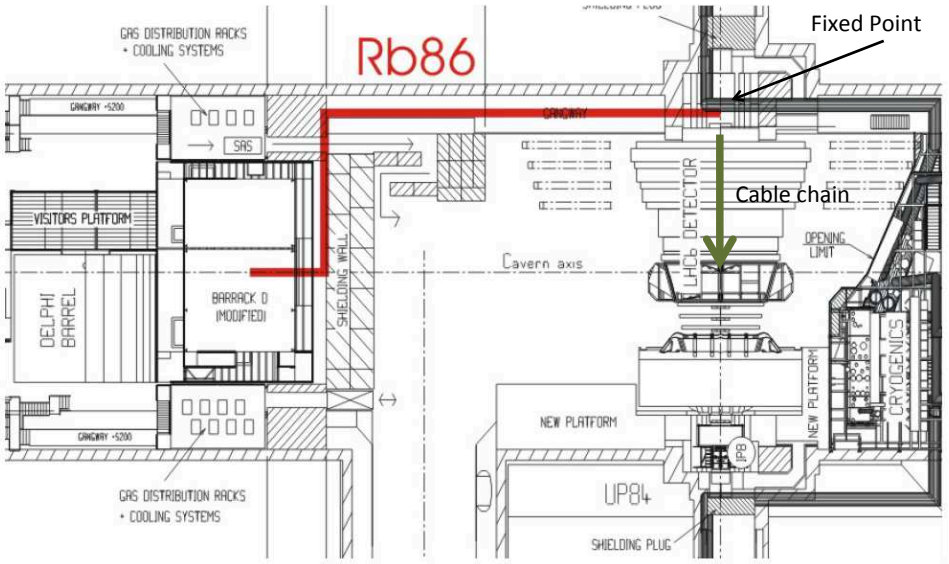

Figure 2.9 – *Path of the optical cables between the barracks and the Calorimeter Front-End electronics.*

three partitions: **ECAL**, with the ECAL Front-End electronics and the L0CALO electronics (Trigger Validation Boards and Selection Boards), **HCAL** and **PS**, containing the PS and SPD Front-End boards and the SPD control boards. The L0DU can also be affected to a separate partition.

2.2.2 L0 Calorimeter Electronics Chain

The processing of the calorimeter informations for the L0 is realized in several successive steps aiming at reducing the information to obtain in the end the candidates with the maximum E_T for each category. The computations are fully synchronous at 40 MHz and have a fixed latency. Figure 2.10 shows the different steps of the L0CALO and the architecture of the system.

The electronics boards involved in the L0CALO are (in sequential order):

1. **ECAL and HCAL Front-End Boards** (cavern) compute the 2×2 cluster with highest E_T in the 8×4 cell area covered by the board. This cluster is

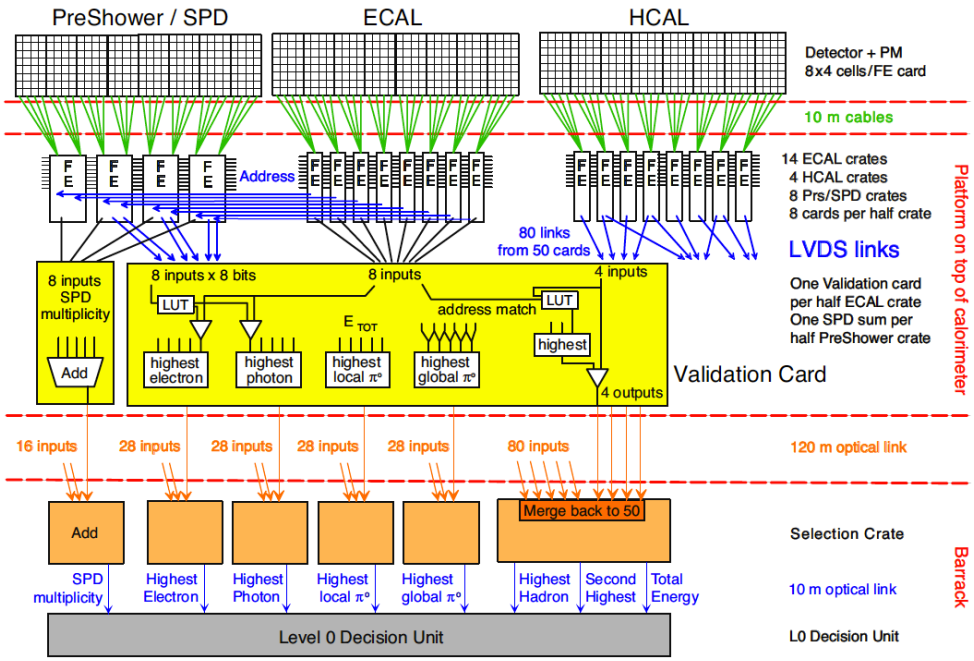

Figure 2.10 – *Architecture of the L0CALO system.*

sent to Trigger Validation Boards and to PS Front-End Boards for the ECAL case.

2. **PS Front-End Boards** (cavern) collect the hit pattern in the PS and SPD in front of the cluster received from the ECAL Front-End Boards, and send this pattern to Trigger Validation Boards. They also compute the SPD hit multiplicity over the area covered by the board (8×8 cells) and send it to the SPD Control Boards.

3. **Trigger Validation Boards** (cavern, called Validation Cards in Fig. 2.10) validate ECAL clusters using the pattern received from the PS Front-End Boards to form electron, photon and π^0 candidates. They also add ECAL cluster energy to HCAL clusters when the ECAL clusters are in front of the HCAL ones. They send their results to the Selection Boards.

4. **SPD Control Boards** (cavern) receive SPD multiplicities from the PS Front-End Boards and sum them. They then send the value to one Selection Board.

5. **Selection Boards** (barrack) compute the candidates with highest E_{T} among all calorimeter candidates. They also compute the total SPD multiplicity and the sum of the E_{T} of the hadron candidates. They send their result to the L0DU.

6. **L0DU** (barrack) compute the final trigger decision, comparing the E_{T} of the different candidates with a threshold. It sends the decision to the ODIN board.

Amongst the boards listed above, all Front-End Boards, the Selection Boards and the L0DU are connected to TELL1 boards and thus also send data that will be written on disk and available offline for analysis and monitoring. The comparison between the data sent by the Front-End Boards and the data sent by the other boards allows a powerful cross-check of the correct behavior of the trigger.

The boards in the cavern are installed on top of the detector, on a platform located above the calorimeters. They are installed in crates which can hold at maximum 16 Front-End Boards, 2 Trigger Validation Boards or SPD Control Boards and one CROC (Calorimeter Readout Card). The CROC [60] acts as an interface between the Front-End boards and the calorimeter TELL1 boards (and the DAQ network). It also dispatches signals from the TFC and the Experimental Control System (ECS) to all boards in the crate, via the backplane of the crate. The mapping between Front-End boards (with their identification number), crates and detector cells is represented in Fig. 2.11 for PS and SPD, in Fig. 2.12 for the ECAL and in Fig. 2.13 for the HCAL.

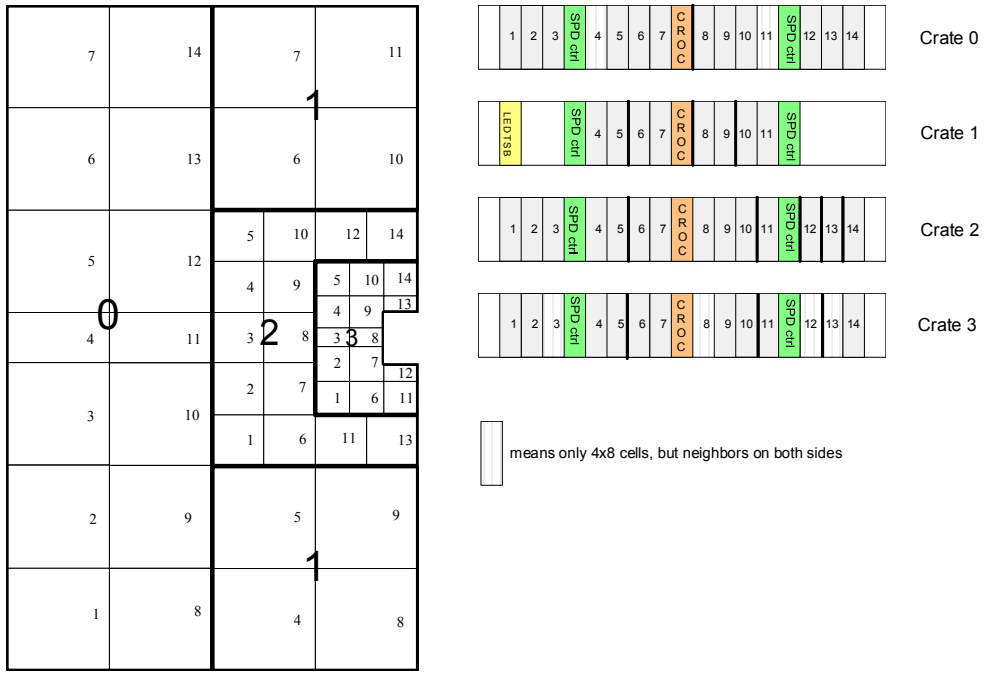

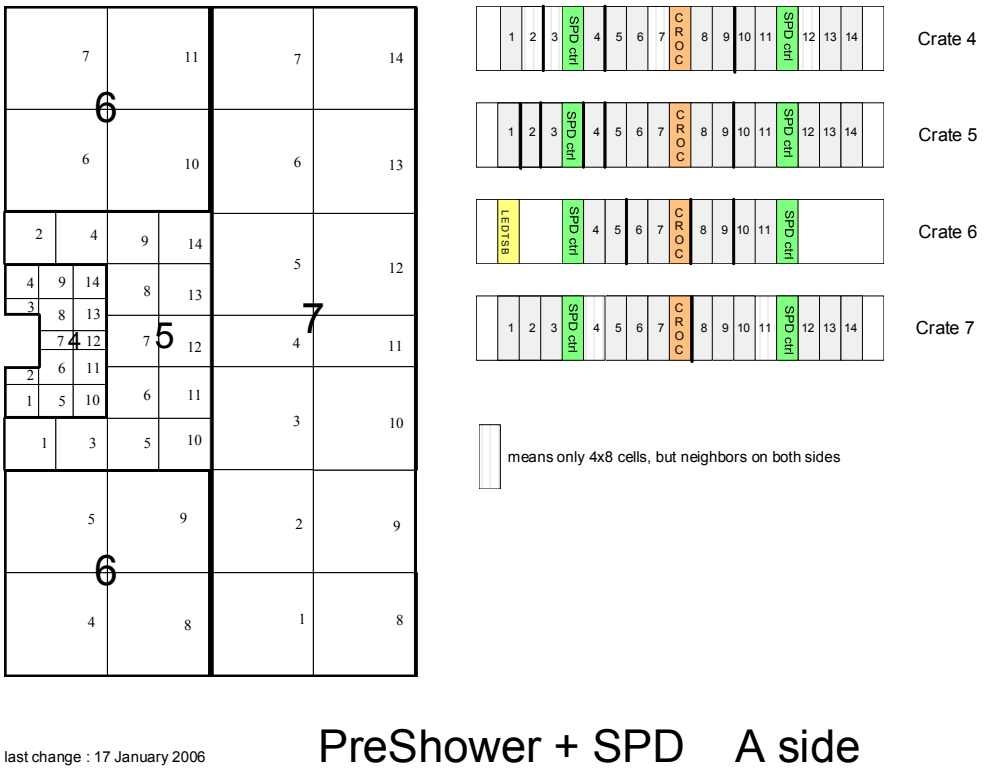

Figure 2.11 – *Preshower and SPD Front-End crates.*

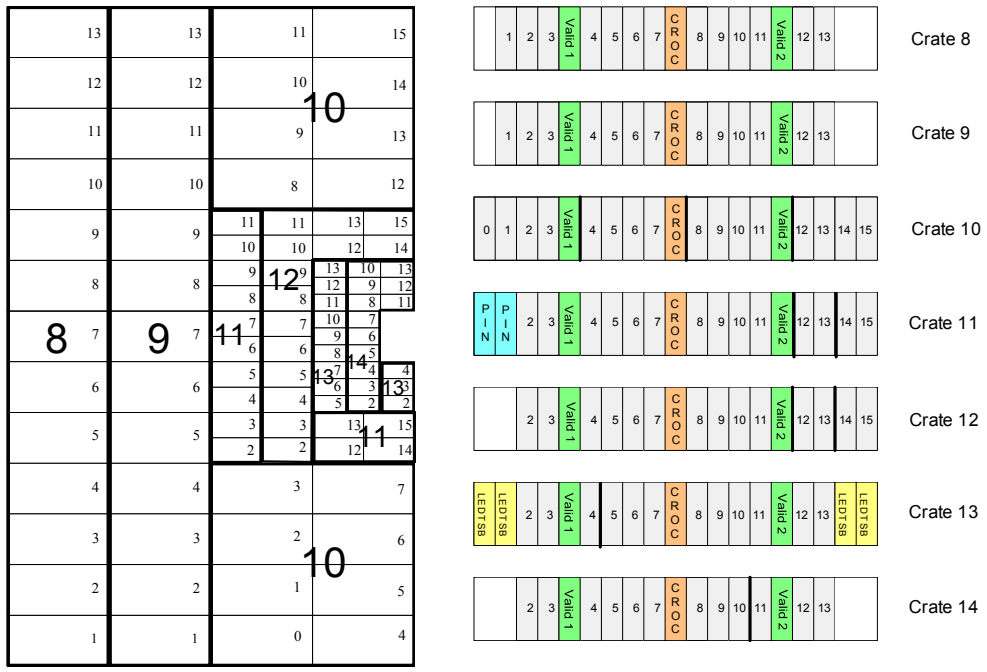

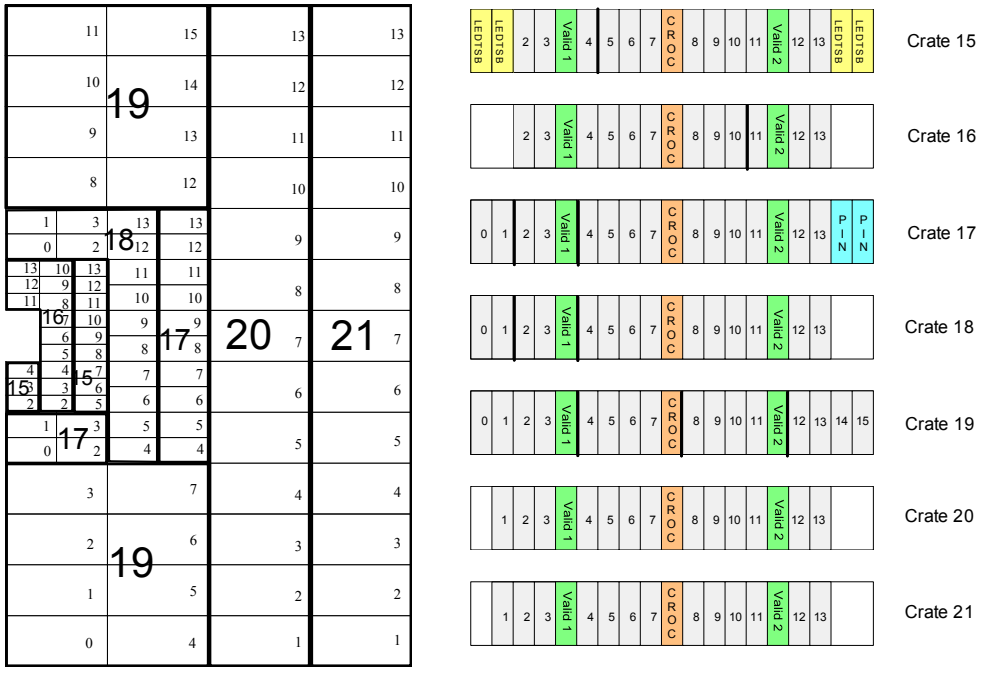

Figure 2.12 – *ECAL Front-End crates.*

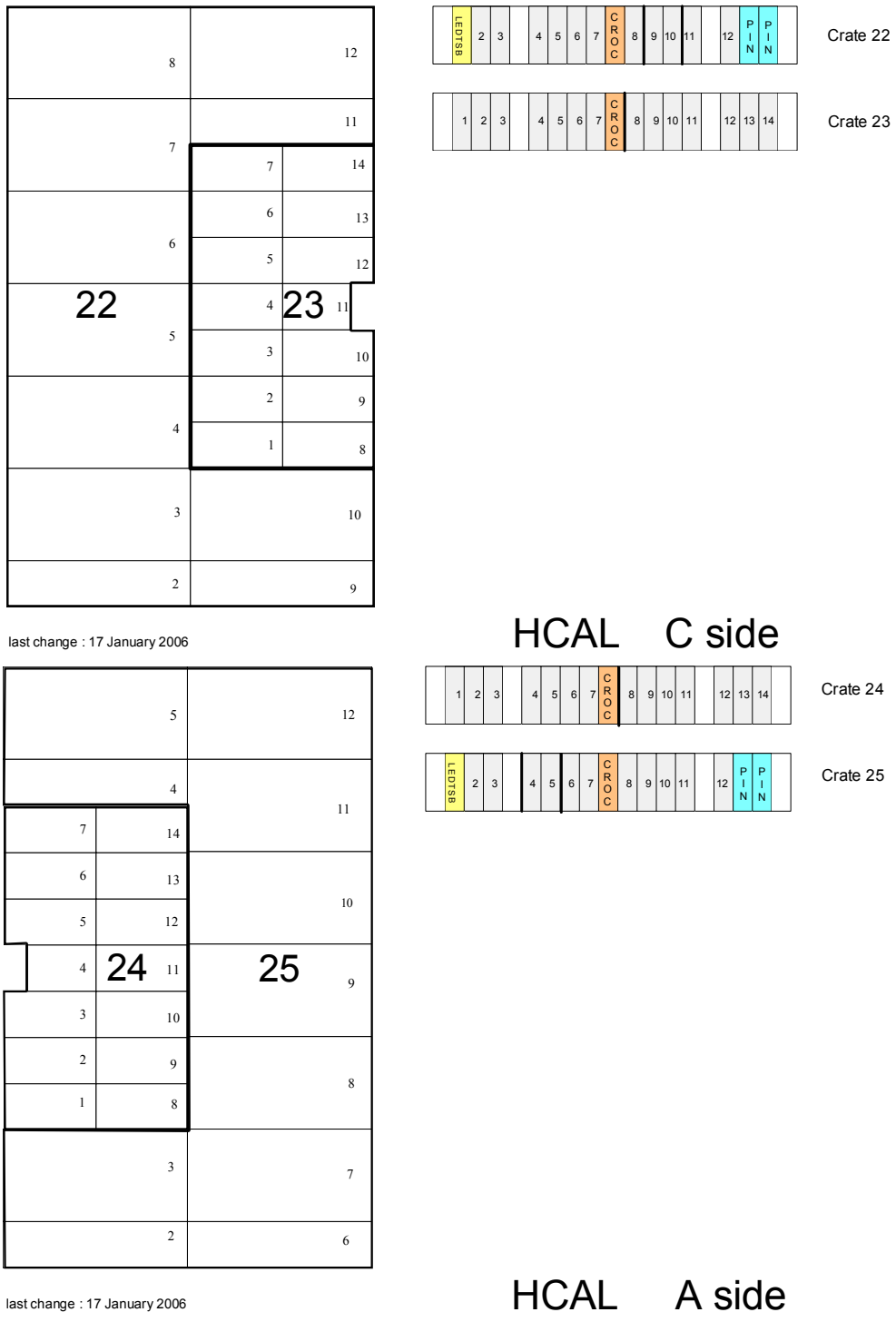

Figure 2.13 – *HCAL Front-End crates.*

The Front-End crates are mounted in vertical racks which can hold up to three crates. The SPD, PS and ECAL crates are installed in racks located on top of the ECAL detector, with SPD/PS crates being on top of the rack, as shown schematically on Fig. 2.15. HCAL crates are installed in racks on top of the HCAL detector as shown in Fig. 2.14.

The Selection Boards and the L0DU are installed in the barrack located behind the shielding wall, on the third floor (D3). The TELL1 boards used for the trigger and for the calorimeter are also in the same barrack. The system uses a large number of cables to exchange data between the different boards [61], this will also be described in the following.

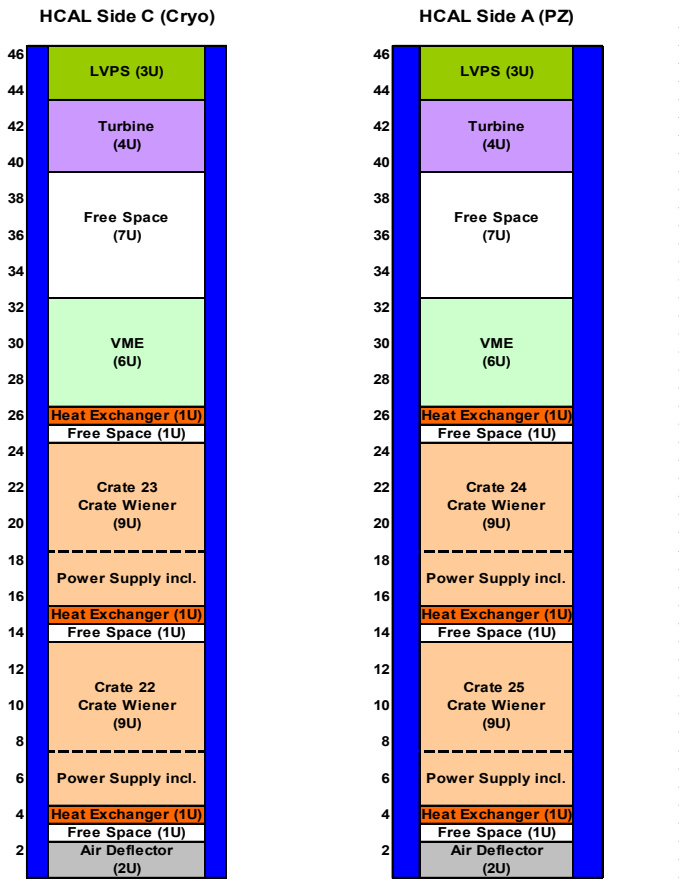

Figure 2.14 – *HCAL racks installed on the HCAL platform: C-side (left) and A-side (right).*

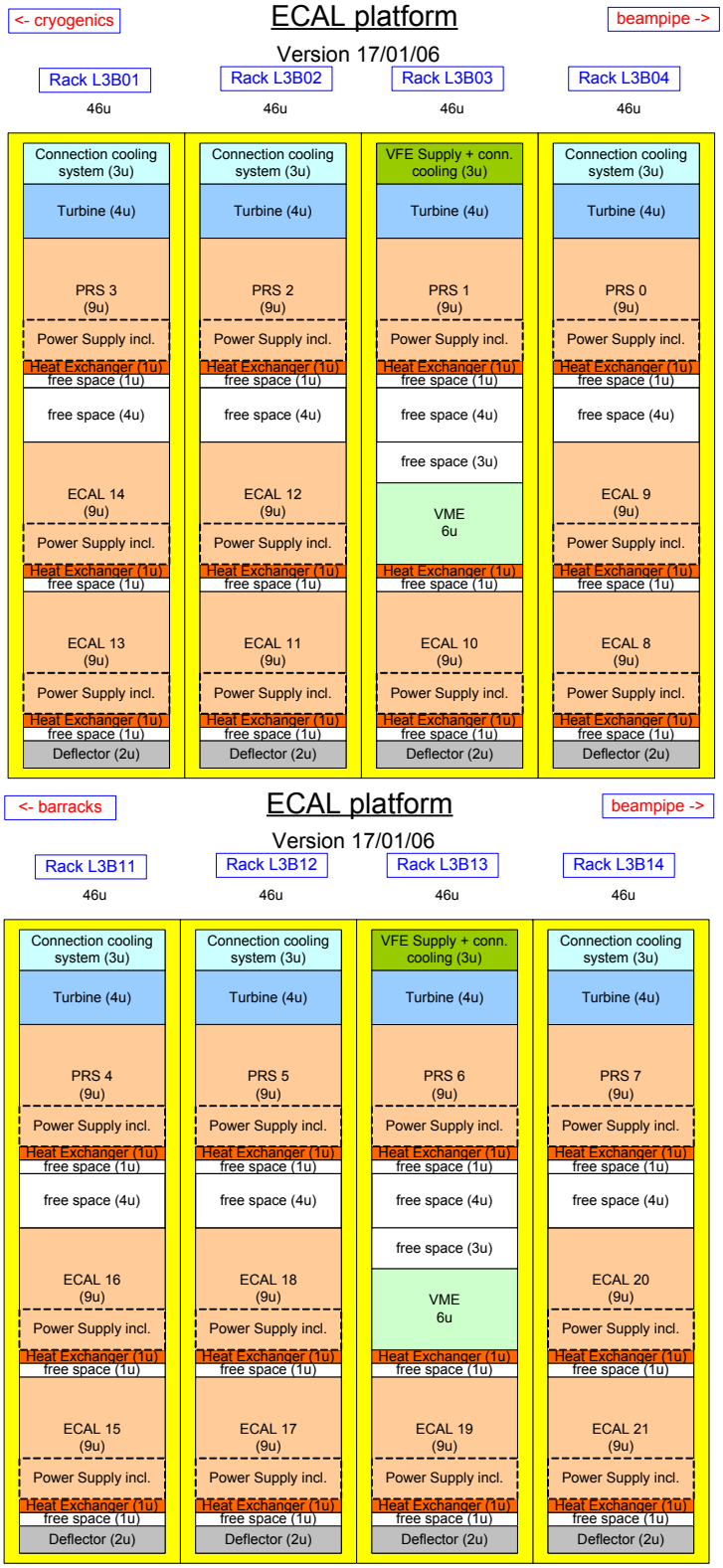

Figure 2.15 – *SPD, PS and ECAL racks installed on the ECAL platform: C-side (top) and A-side (bottom).*

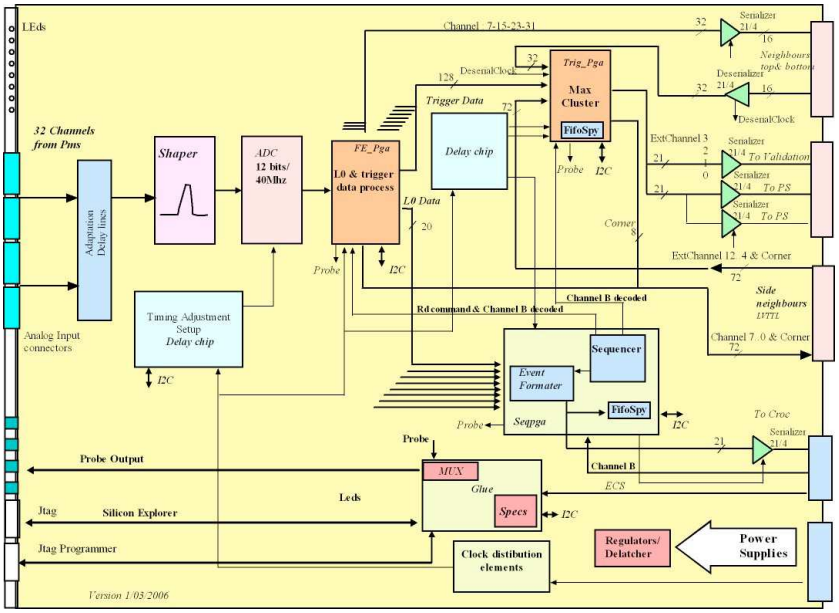

Figure 2.16 – *Diagram of the ECAL/HCAL Front-End Board.*

2.3 Calorimeter Trigger Boards

2.3.1 ECAL and HCAL Front-End Boards

The L0CALO trigger decision is computed from the E_{T} of 2×2 clusters in the ECAL and the HCAL. The first step in the processing chain consists in computing the maximum transverse energy deposited in a cluster in a ECAL or HCAL module and identifying the position of this deposit. This is realized in a Front-End Board which is strictly identical for the ECAL and the HCAL and which was designed at LAL, Orsay [62].

a) Boards description

The ECAL and HCAL Front-End boards perform several tasks, represented in Fig. 2.16, the trigger part of the board being a small part of it. The analog signals coming from the PMTs of the detectors are sampled, shaped and then digitized in a 12 bit Analog-to-Digital Converter (ADC) for every clock cycle at the LHCb 40 MHz frequency. As shown in Fig. 2.6, a Front-End board handles 32 input channels (32 cells). After shaping, the pulses induced in the ECAL and HCAL PMTs by the particles coming from the LHC collisions have widths

slightly smaller than the 25 ns period of the clock. In order to maximize the integrated signal within a clock cycle [63], the phase of each input channel (which can be different because of different cable lengths, of different times of flight of the particles with respect to the interaction point or of different high voltages applied on the PMTs) can be separately adjusted in 1 ns steps using custom delay chips developped at LAL.

The processing of the digital information out of the ADC is realized in several Field-Programmable Gate Array (FPGA) chips:

1. Front-End FPGA (*FE_PGA* in Fig. 2.16): eight in total, one FE_PGA deals with 4 channels. It handles the data at the output of the ADC and performs pedestal subtraction in order to decrease the detector noise for the energy measurement. This is done subtracting from the current measurement the signal seen in the previous bunch crossings. The FE_PGA implements the L0 buffer which holds the data until a L0 accept signal is received from the TFC system and the data is sent to the TELL1 boards. The FE_PGA computes also the E_{T} value of each cell that will be used by the L0 algorithms, as will be described later.

2. Sequencer FPGA (*SEQ_PGA* in Fig. 2.16). This component builds data blocks from the L0 buffers of the FE_PGA when a L0 accept signal is received, and sends these blocks through the crate backplane to the CROC that will then send all data from the crate via optical fibers to the calorimeter TELL1 boards located behind the shielding wall in the barrack. The SEQ_PGA is also responsible for dispatching inside the Front-End the TFC signals.

3. Glue FPGA (*Glue* in Fig. 2.16). This FPGA is the interface to the LHCb control system (ECS). It is based on the SPECS system [64], designed at LAL. Through this system, the full Front-End board can be controlled from the LHCb control network [65]. The main function of the Glue is to transform the signals received in SPECS protocol format [64] into the standard $\mathrm{I}^2\mathrm{C}$ format [66] that all the other components on the board can understand. Registers and memories can then be read or written to configure properly the board.

4. Trigger FPGA (*TRIG_PGA* in Fig. 2.16). This FPGA realizes the trigger computations and will be described in details in the next section.

b) Trigger algorithm

The first step in the trigger processing is done in the FE_PGA. In order to reduce the number of links, the 12 bit ADC energy value of each cell is transformed into a roughly calibrated 8 bit trigger ADC value of E_{T}. The 12 bit ADC energy has a dynamic range between 0 and approximately 10 GeV, but for the trigger ADC, a range between 0 and 5 GeV is enough. This way, one bit of trigger ADC is equal to 20 MeV. The reduced precision compared to the energy values used for offline analysis is still good enough for trigger purposes. The same dynamic range is used for the entire ECAL and HCAL detectors so that E_{T} from different parts of the detectors can be directly added or compared.

Since the calibration of the cell can be different, the conversion between the 12 bit ADC value after pedestal subtraction (**ADC**) and the 8 bit trigger ADC value (**L0ADC**) depends on a programmable *calibration constant*, **CALIB** and the relation between **ADC** and **L0ADC** is approximately

$$\mathbf{L0ADC} = \mathbf{ADC} \times \frac{\mathbf{CALIB}}{128} \times \frac{255}{4095} \times \frac{10}{5}, \tag{2.8}$$

i.e. if the detector is calibrated to give an ADC value of 4095 for a transverse energy of 10 GeV, the trigger value will be equal to 255 for $E_{\mathrm{T}} = 5\,\mathrm{GeV}$ and a calibration constant of 128. The exact computation is

$$\begin{aligned}
V_i &= \mathbf{ADC} \times 2^i, \;\; 0 \le i \le 7 \\
R_0 &= \mathbf{CALIB}[0] \times (V_0[11:2] \times 2^2) + \mathbf{CALIB}[1] \times (V_1[12:2] \times 2^2) \\
R_1 &= \mathbf{CALIB}[2] \times (V_2[13:4] \times 2^4) + \mathbf{CALIB}[3] \times (V_3[14:4] \times 2^4) \\
R_2 &= \mathbf{CALIB}[4] \times (V_4[15:6] \times 2^6) + \mathbf{CALIB}[5] \times (V_5[16:6] \times 2^6) \\
R_3 &= \mathbf{CALIB}[6] \times (V_6[17:8] \times 2^8) + \mathbf{CALIB}[7] \times (V_7[18:8] \times 2^8) \\
T &= (R_0 + R_1 + R_2 + R_3) \\
\mathbf{L0ADC} &= \begin{cases} T[17:10] & \text{if } T \le 255 \text{ and } T[9] = 0, \\ T[17:10] + 1 & \text{if } T \le 255 \text{ and } T[9] = 1, \\ 255 & \text{if } T > 255. \end{cases}
\end{aligned} \tag{2.9}$$

ADC can be negative because of the pedestal subtraction. In this case **L0ADC** is set to 0. **CALIB** is stored, per cell, in a 8 bit register and its value ranges from 0 to 255. It can optionally be multiplied by 4 when a special flag (per cell) is set in the FE_PGA configuration. The HCAL is calibrated such that the maximum of the 12 bit ADC dynamic range corresponds in fact to 15 GeV of transverse energy is all cells, thus the calibration constant is equal to 187 in the HCAL Front-End boards.

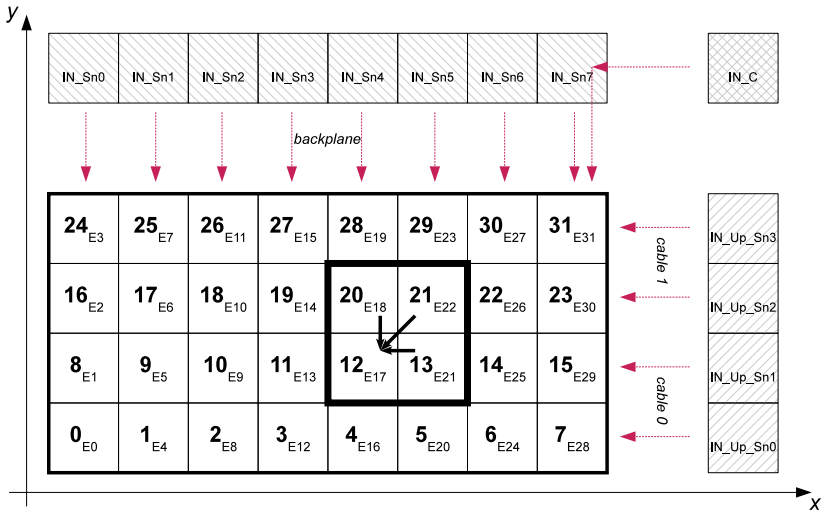

Figure 2.17 – *Input channels of the Trigger FPGA. The bold numbers are the cell numbers used for the clusters addresses and the other numbers are the input channel numbering used for the trigger processing.*

In the ECAL, the ADC dynamic range is not constant and increases from the Inner to the Outer area. The maximum of the range is given by

$$E_{\mathrm{T}}^{\mathrm{max}} = 10 + 7 \sin\theta \text{ in GeV}, \tag{2.10}$$

where θ is the polar angle of the cell. The calibration constants for the ECAL vary then between 126 (Inner) and 156 (Outer).

The 32 **L0ADC** values obtained are sent from the 8 FE_PGA to the Trigger FPGA. In order to minimize the number of links and FPGA pins used, the **L0ADC** are multiplexed at 80 MHz, i.e. the same physical line transmits alternatively one bit of one channel, and the same bit of another channel.

The remaining part of the trigger processing of the Front-End Board is realized in the Trigger FPGA. This FPGA is an ACTEL AX500 anti-fuse FPGA of the Axcelerator family [67]. This type of FPGA has been selected because of its immunity to radiation damage and because of its excellent performances. The drawback of such a technology is that the program (firmware) of the FPGA cannot be modified once it is loaded permanently into the chip. The AX500 FPGA contains up to 500 000 logical cells, 336 Input/Output pins (out of which 306 are used) and 73 000 bits of memory (RAM).

The Trigger FPGA computes the total E_{T} (`TotalEt`, on 8 bits) deposited in the module connected to the Front-End board and also locates and computes the

maximum 2×2 cluster of the module (`Address` on 5 bits and `MaxEt` on 8 bits). A 2×2 cluster is formed by four cells: (x,y), $(x+1,y)$, $(x,y+1)$ and $(x+1,y+1)$ as shown in Fig. 2.17 and its energy is the sum of the energy in each cell. The cluster is identified by an address equal to the cell number of the left corner of the cluster. 32 different sums (`S0` to `S31`) have to be computed, and for this the Trigger FPGA receives the transverse energy of 45 input channels (8 bit for each of them), represented in Fig. 2.17:

1. 32 channels of the Front-End board itself (named `E0` to `E31`, where the notation differs from the channel number). One column of cells is received, multiplexed at 80 MHz, from one single FE_PGA.

2. 8 top neighbors (`IN_Sn0` to `IN_Sn7`),

3. 4 right neighbors (`IN_Up_Sn0` to `IN_Up_Sn3`),

4. 1 corner neighbor (`IN_C`).

For example, the cluster of Fig. 2.17 has address **12**, its energy is noted as `S17` and is equal to `E17+E21+E18+E22`. Figure 2.18 shows the diagram of the computation of one sum, realized in two steps, each sum having as input a 8 bit value and as output a 8 bit value saturated at 255.

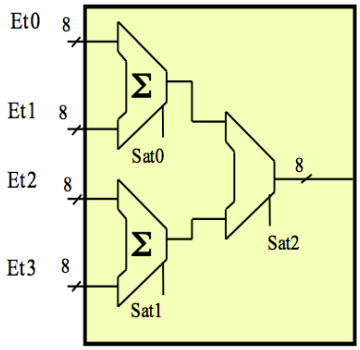

Figure 2.18 – *Diagram of the* 2×2 *sum computation in the Trigger FPGA.*

From the 32 sums, the maximum (`MaxEt`) is selected following the diagram shown in Fig. 2.19, in 5 steps and 3 clock cycles, using comparators with two inputs. The address of the maximum (`Address`) is also kept along. In case of equality, the address of the sum with the lowest index is kept. The total transverse energy of the module (`SumEt`) is obtained summing the E_T of 8 non-overlapping

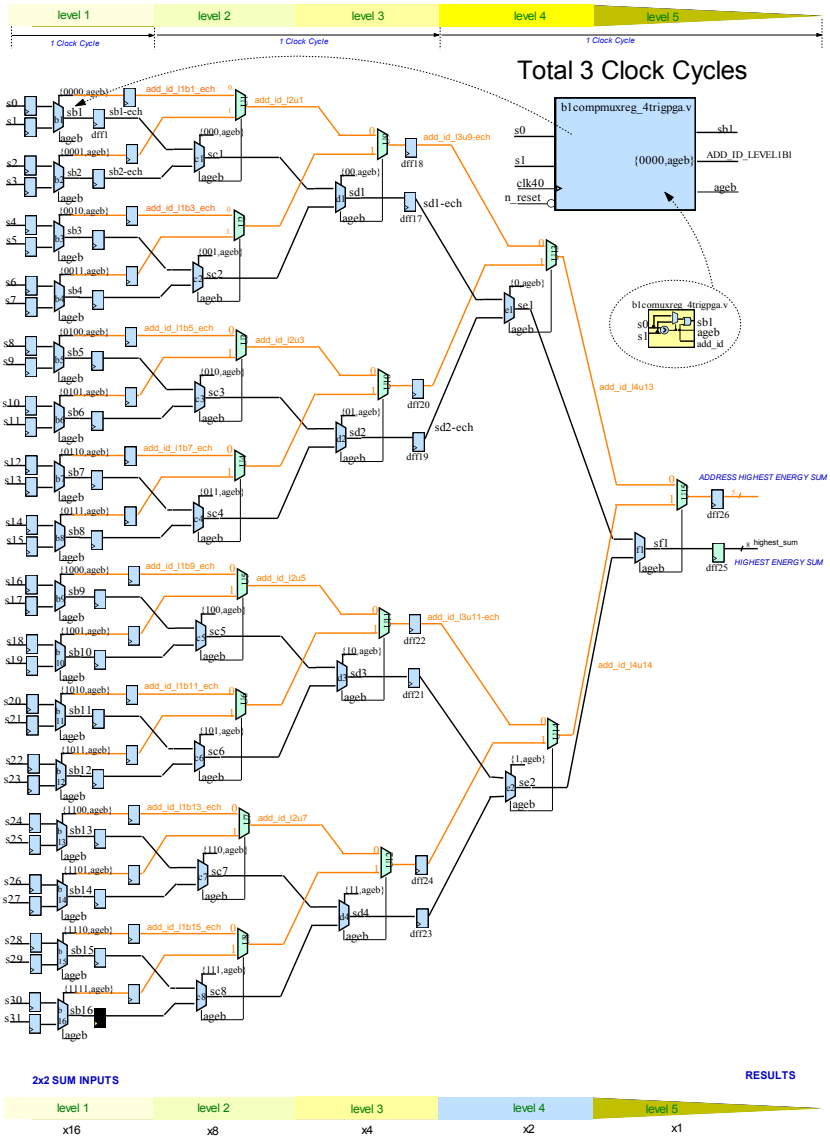

Figure 2.19 – *Diagram of the maximum search in the Trigger FPGA.*

clusters and excluding clusters containing neighbor cells which are part of a different module, namely

$$\texttt{SumEt} = \texttt{S0} + \texttt{S2} + \texttt{S8} + \texttt{S10} + \texttt{S16} + \texttt{S18} + \texttt{S24} + \texttt{S26}, \tag{2.11}$$

and is saturated at 255. This is also done in 3 clock cycles, in parallel to the maximum search.

Each of the input channels can be masked in the computation, for example to suppress a noisy channel. This is done via configuration registers (one bit per

channel). When a channel is masked, the transverse energy value is replaced by 0 at the input stage. A local BCID counter (`BCID`) is also implemented to allow to use easily the obtained results in the following steps of the processing. This counter is aligned to the LHC bunch structure using the TFC BCID reset signal, which is delayed by a programmable delay equal to 3 407 clock cycles before setting the `BCID` counter to zero. The TFC BCID reset signal has a fixed frequency, so this corresponds in fact to a negative delay since the triggering energy is deposited and analyzed in the Trigger FPGA roughly 4 μs before the associated L0 accept signal arrives back to the Front-End board.

c) Input channels

32 of the Trigger FPGA input channels (`E0` to `E31`) are data coming from the board itself, from the 8 FE_PGA. Each FE_PGA produce 4 channels (`E0` to `E3`, `E4` to `E7`, ..., `E28` to `E31`). In order to divide the number of links by 2, they are multiplexed at 80 MHz sending on the same link the same bit of two consecutive channels (`E0` and `E1` are multiplexed together like `E2` and `E3`). The demultiplexing is performed in the Trigger FPGA according to the diagram shown in Fig. 2.20 and takes one clock cycle.

The 13 other channels are neighbor cells whose transverse energy is computed in different boards and needs to be transported between the board producing the E_T values and the board hosting the Trigger FPGA using it. 8 of these channels are **top neighbors** (`IN_Sn0` to `IN_Sn7`) and are received by the Trigger FPGA from the Front-End board located in the same crate in the slot on the right, as can be seen from Figs. 2.12 and 2.13 (since the emitting board is located on the side of the receiving board, these channels are also referred to as "side neighbors" like for example in Fig. 2.16). These channels are transmitted through the backplane of the crate, which is a custom backplane designed at LAL [68]. They use LVTTL links (64 in total, 8 $\times$ 8 bits) that originate from the 8 FE_PGA of the emitting board and arrive to the Trigger FPGA of the receiving board.

4 of the neighbor channels are **right neighbors** (`IN_Up_Sn0` to `IN_Up_Sn3`) which are received from a Front-End board located either in the same crate but not in an adjacent slot, in a different crate in the same rack or even in a crate of a different rack (see Fig. 2.12 and Fig. 2.13). Since the usual configuration is that these channels are received from a different crate located in the same rack but placed higher in the rack, they are also called "top/bottom neighbors" like in Fig. 2.16. These channels are transmitted through two standard Ethernet Category 6 cables (with 4 twisted pairs of cables), equipped with RJ45 connectors and plugged on the back of the crate backplane, behind the Front-End board. The data is se-

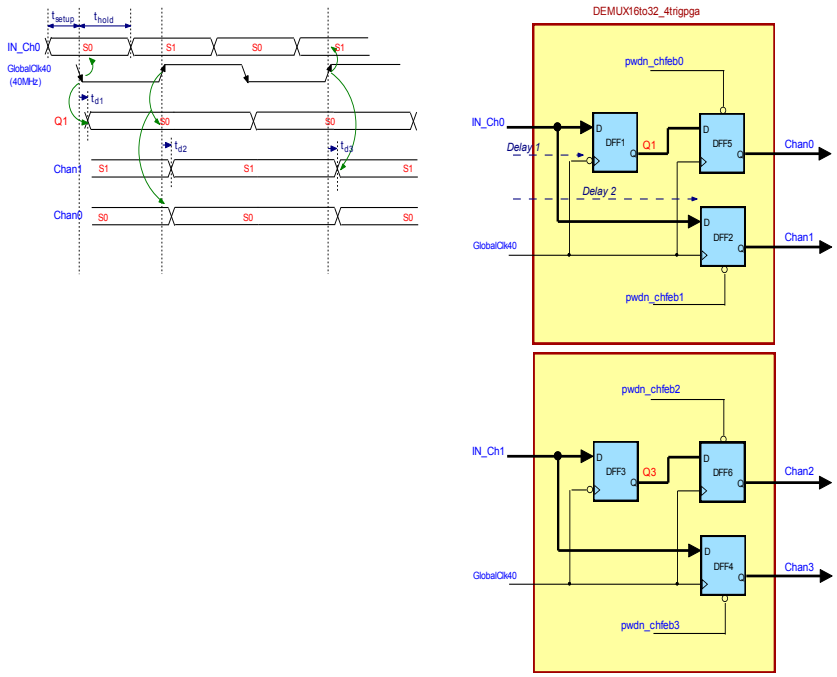

Figure 2.20 – *Diagram of the demultiplexing of two data links coming from one FE_PGA,* `IN_Ch0` *and* `IN_Ch1` *containing 4 channels,* `Chan0`*,* `Chan1`*,* `Chan2` *and* `Chan3`*.*

rialized before being sent from the first FE_PGA in the cable and deserialized before entering the Trigger FPGA. One cable (cable 0) is used for `IN_Up_Sn0` and `IN_Up_Sn1` and another cable (cable 1) for `IN_Up_Sn2` and `IN_Up_Sn3`. The DS90CR215 serializer and DS90CR216 deserializer [69] are used to encode and decode the data. The phase of the clock of the serializer can be adjusted thanks to a delay chip by steps of 1 ns, so that it is at the optimal value for the serialization of the data (the rising edge of the clock being in-between data transitions). They allow to transmit 21 bits of data at 40 MHz on three pairs of the cable in LVDS signals (7 bits per pair are then transmitted in 25 ns), the fourth pair being used for the associated clock signal. The serialization and deserialization of the signal introduce a delay of 86 ns. For the transmission of neighbor channels, only 16 bits per cable are transmitted. Cables of different lengths are used since the distance between the emitting and receiving boards vary according to the different configurations. Cables of 70 cm are used to connect boards located in the same crate (in the HCAL for example), 2 m long cables connect boards in different crates but in the same rack, and 4.6 m long cables connect crates of different racks (between crates 9 and 10, and between crates 19 and 20 in the ECAL).

The last neighbor channel is the **corner** (`IN_C`). It is in fact one right neighbor

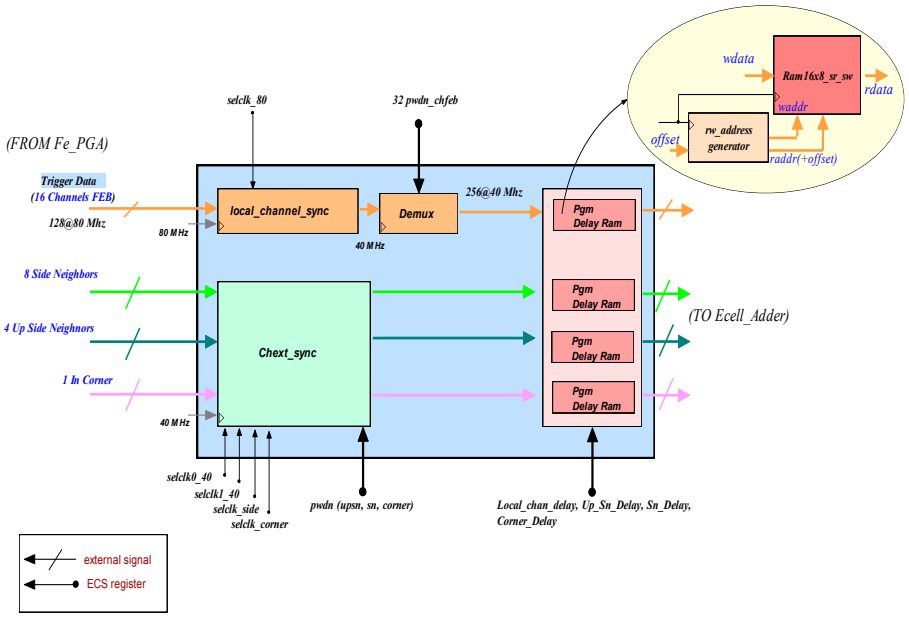

Figure 2.21 – *Diagram of the time alignment of the Trigger FPGA input channels.*

(`IN_Up_Sn0`) of the Trigger FPGA of the Front-End board located next to the right in the same crate. The corner's transverse energy is thus first sent as a right neighbor, from the FE_PGA of the corner Front-End board to the Trigger FPGA of the side board in the same crate. This Trigger FPGA re-emits it via the backplane using 8 LVTTL links.

All input channels must be time aligned before being used in the Trigger FPGA algorithms so that data of the same bunch crossing are processed together. Each category of input channels can be delayed up to 16 clock cycles, using FIFO memories where the *read* position is shifted by a programmable offset compared to the *write* position, as represented in Fig. 2.21. The top neighbor channels which arrive first are delayed by 5 clock cycles, the local channels which arrive later because of the demultiplexing are delayed by 4 clock cycles, the right neighbor channels are delayed by 1 clock cycle and the corner neighbor channel which arrives last is not delayed. It has to be noted that 16 out of the 264 Front-End boards produced use an older firmware version for which the latency step is 1 clock cycle faster (but could have been not stable, and the safety margin was increased in the final firmware, with version 16). For boards programmed with this firmware (version 15), all delays hve to be increased by 1 clock cycle to be aligned with all the other boards programmed with the new version (16).

d) Output link

The result of the computation in the Trigger FPGA is sent:

- For an ECAL board:

  1. To one PS Front-End board: the address of the maximum transverse energy cluster (`Address`) together with the local BCID (`BCID`) counter value are transmitted to the PS Front-End board covering the area in front of the ECAL Front-End Board. As can be seen in Fig. 2.11 and 2.12, the ECAL and PS Front-End boards which are connected are located in the same rack. The transmitted data is serialized with the same method as the one used for right neighbors described above (with the exception that the serializer is a FIN1215 chip [70], however with identical functionalities than the other one used for neighbors). The data is sent over Category 6 Ethernet cables of 2 m length when the ECAL crate is in the middle of the rack, or of 2.5 m length when the ECAL crate is at the bottom of the rack. These cables are plugged on the back of the crate backplane, behind the ECAL or the PS Front-End board. The data format used is represented in Fig. 2.22 (the `MaxEt` value is not used by the PS Front-End board).

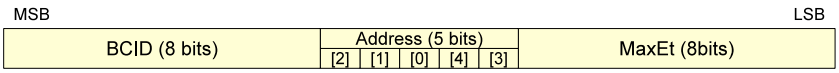

Figure 2.22 – *Format of the data sent from the ECAL Front-End Boards to the PS Front-End Boards and from the HCAL Front-End Boards to the Trigger Validation Boards.*

  2. To one Trigger Validation board: the address (`Address`), the maximum transverse energy (`MaxEt`) and the total energy (`SumEt`) is transmitted to the closest Trigger Validation Board, i.e. the Trigger Validation Board located in the same half crate as the Front-End Board (see Fig. 2.12). The data is sent via the backplane in LVDS serialized links, using the FIN1215 chip as serializer with the same method as the right neighbors. The data format is shown in Fig. 2.23.

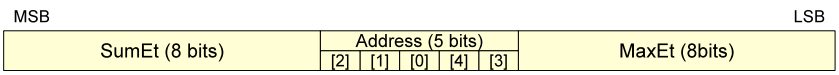

Figure 2.23 – *Format of the data sent from the ECAL Front-End Boards to the Trigger Validation Boards.*

- For an HCAL board:

    1. To one or two Trigger Validation boards: the address (`Address`), the maximum energy (`MaxEt`) and the local BCID counter (`BCID`) are sent to Trigger Validation Boards. The data is transmitted serialized with the same method as described above, using FIN1215 serializers, through Ethernet cables plugged on the back of the backplane. The problem here is that the length of the cables has to be larger because the HCAL Front-End boards and the Trigger Validation Boards are located on two different platforms that can be moved apart. The necessary cable length is 15.5 m and the crucial point is that the difference between the signal travel times in the different pairs of the same cable (skew) must be small to allow a correct deserialization of the information. With 7 bits being transmitted in 25 ns in each pair of the cable, the skew at the end of the 15.5 m length must be smaller than $\sim$2 ns. The selected cable is a special cable with 4 twisted pairs (SkewClear from AMPHENOL [71]) with a skew of 3.3 ns/100 m. The data format is represented in Fig. 2.22.

e) Timing

All input channels of the Trigger FPGA have a phase with respect to the clock which can vary between them, because of the different paths that they follow (different cable lengths, different routing paths on the boards, ...). All channels are captured and re-phased to the Trigger FPGA clock when they enter the FPGA in order to have a stable behaviour. The principle of the data capture is represented in Fig. 2.24. The data is first captured by a Data Flip-Flop (DFF) on either the rising or the falling edge of the Trigger FPGA clock, and a second DFF resynchronizes the data with the Trigger FPGA clock. The capture of the data is done within one clock cycle.

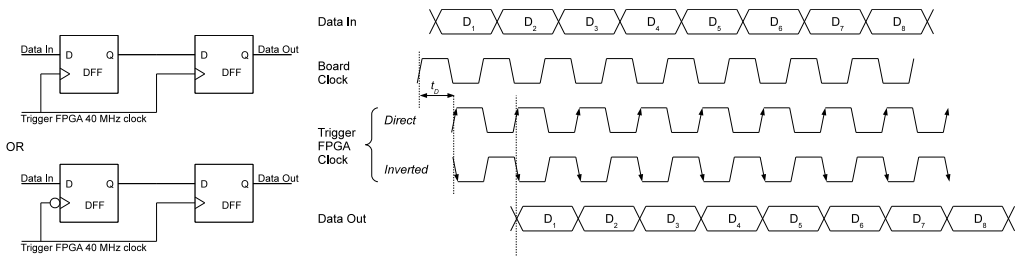

Figure 2.24 – *Logic (*left*) and timing (*right*) diagrams of the input data capture stage.*

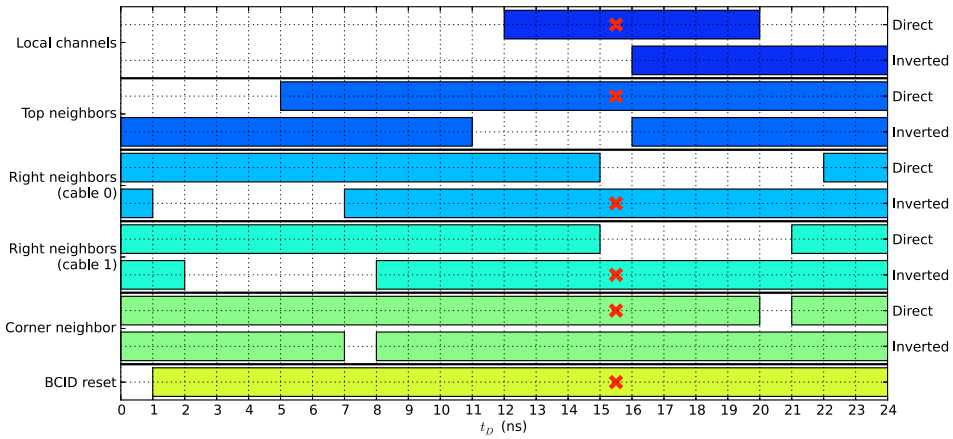

Figure 2.25 – *Allowed ranges for the delay of Trigger FPGA clock phase with respect to the board clock (t_D). The allowed ranges for each category of input is represented by a colored bar, for both clock polarities. The chosen working point is shown with a red cross.*

The phase clock of the Trigger FPGA can be adjusted by a delay t_D ($0 \leq t_D < 25\,\text{ns}$) so that the sampling edge is in a region where the data is stable, far from the transitions, as shown on the right of Fig. 2.24. This is done by steps of 1 ns using a delay chip. For one bit of data, there are usually one or two values of t_D where the data cannot be sampled correctly. For multiplexed links, the range of allowed value is reduced (and is at maximum 12 ns, half of the period).

In order to increase the range of allowed values, the edge of the clock used to sample the data can be chosen between the rising or the falling edge (Direct or Inverted clock in Fig. 2.24). The delay t_D is unique for all input channels of the Trigger FPGA; due to timing variations a single t_D value may not accommodate all non-multiplexed links. This is why the functionality to use the inverted clock is also implement for the other links, not only for the multiplexed ones. The choice of the sampling edge is done via configuration registers, per group of input channels: one choice for all the 32 local input channels, one choice for the top neighbors, two choices for the right neighbors (one per cable), and one choice for the corner neighbor.

Figure 2.25 shows the allowed ranges for the value of t_D for the different channels and for the BCID reset signal which is also sampled in the same way than the input channels (without the possibility to change the sampling edge of the clock). The working point used is $t_D = 15\,\text{ps}$, with inverted clocks for the right neighbors, and is indicated with a cross on the drawing.

f) Configuration and debugging

The Trigger FPGA contains several registers to configure its behaviour and to set the proper delays, to select the sampling edges of the clock, etc... The FPGA is configured from the LHCb ECS using the SPECS system through the Glue FPGA of the board, using a I^2C protocol. The Glue FPGA provides 12 I^2C local buses on the Front-End board. The Trigger FPGA is connected to the 12^{th} bus and is an I^2C slave for data transfers with address **0x53**. The mode of I^2C addressing of the FPGA is derived from the standard I^2C protocol but is modified to use also "subaddresses". Each configuration register of the FPGA has a unique subaddress which is sent as the first byte of data transferred after the usual I^2C slave address. The complete list of configuration registers is given in Appendix B.

All configuration registers are protected with a tripple voting technique. Since the content of the register can be altered because of radiation effects (Single Event Upsets), three copies of the register are stored in the FPGA. The value corresponding to the majority of the individual copies is used for the configuration, keeping the effect of radiation induced effects to a very low level [72].

To be able to develop, debug and check the processing of the data in the Front-End board, a "test RAM" system has been designed. In the FE_PGAs, patterns can be loaded in a memory (RAM). They consist in a sequence of 256 values that replace the data coming from the PMTs of the detector. When the Front-End board receives a "Calibration Command" from the TFC system, the values of the sequence of data stored in these RAM are injected every 25 ns and are processed as if they were normal data. In particular, they enter the Trigger FPGA which computes for each event of the sequence the address, the maximum energy and the total energy. In the Trigger FPGA, a "spy memory" is also implemented. It can store 256 consecutive results of the trigger processing. The recording of the results is triggered similarly by the TFC "Calibration Command". Comparing the results stored in the "spy memory" with the results expected from the known injected patterns allows to understand problems in the trigger path.

g) Latency

The total processing time of the trigger information in the Front-End board, between the time when the signal from the detector's PMTs arrives at the input of the shaping step and the time after the trigger result is serialized to be sent to a PS Front-End board or to a Trigger Validation Board is equal to 552 ns. The breakdown of the various contributions to the latency is given in Table 2.3.

Table 2.3 – *Processing time in the ECAL and HCAL Front-End Boards*

Step	Time (ns)
Shaping of the PMT's signal	88
Digitization	50
Calibration	62
Data capture at input of Trigger FPGA	25
Collecting neighbors	200
Computation of address, maximum E_T and total E_T	75
Various signal propagation	9
Serialization	43
Total	**552**

2.3.2 PS Front-End Boards

The PS Front-End Boards were designed at LPC (Clermont-Ferrand). They deal with the processing of the PS and SPD data which are sent through the CROC to the DAQ network. They also have a trigger part which will be described briefly here. For complete details about the PS Front-End Boards functionalities, the reader can refer to Ref. [73].

A PS Front-End Board usually handles 64 channels (8×8) and covers the area corresponding to two ECAL Front-End Boards, as shown in Fig. 2.26. Some PS Front-End Boards (see Fig. 2.11) only cover 32 channels (8×4, like board 4 in crate 7) and are called "half boards". The goals of the trigger part of the PS Front-End are to extract the PS and SPD hit patterns in the cells in front of the 2×2 ECAL clusters received from the ECAL Front-End boards (`Pattern`, on 8 bits: one bit per PS cell and one bit per SPD cell), and to compute the SPD hit multiplicity in the 64 or 32 channels covered by the board (`SPDMult`, on 7 bits). These calculations are realized in a dedicated FPGA. This FPGA is an Actel APA450 FPGA of the ProASIC Flash family FPGAs [74], which is a radiation tolerant FPGA but which uses internal flash memory to contain their firmware which can be reprogrammed. This FPGA has up to 450 000 logical cells, 344 Input/Output pins and 126 000 bits of RAM.

The PS Trigger FPGA receives two ECAL addresses (only one for half boards). As described above, the data are received serialized through cables according to

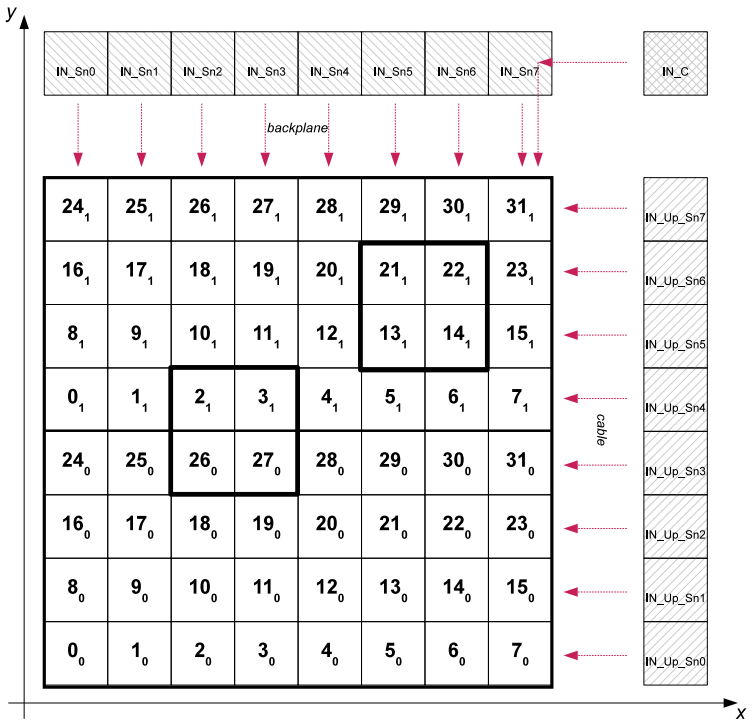

Figure 2.26 – *PS Front-End board trigger channels: one board covers the area of two ECAL Front-End boards, the numbers in each cell indicate the corresponding addresses in the ECAL, for Front-End board 0 and Front-End board 1.*

the format given in Fig. 2.22, and are deserialized before entering the PS Trigger FPGA. After deserialization, the data have to be sampled and rephased at the input of the PS Trigger FPGA. In order to do this, two delay chips are used to adjust the sampling clock with respect to the data out of the deserializer. However, due to worse performances of the FPGAs of type APA45 compared to the FPGA used in the ECAL and HCAL boards, the allowed range for a correct sampling is quite narrow and can be as small as 3 or 4 ns. The ECAL data is delayed by a programmable number of clock cycles in order to align them with the PS and SPD data.

For each of the two addresses received (for example in Fig. 2.26 address **26** for the Front-End board 0 and address **13** for the Front-End board 1), the PS Trigger FPGA computes the hit pattern corresponding to this address. This pattern is a 8 bit value containing the information about which cells of the clusters in front of the ECAL 2×2 cluster have trigger hits in the PS and SPD. The pattern is coded as shown in Fig. 2.27 for the address `Add` received from the ECAL. The individual bits Add_{SPD}, T_{SPD}, C_{SPD} and R_{SPD} are set to one when the corresponding cell

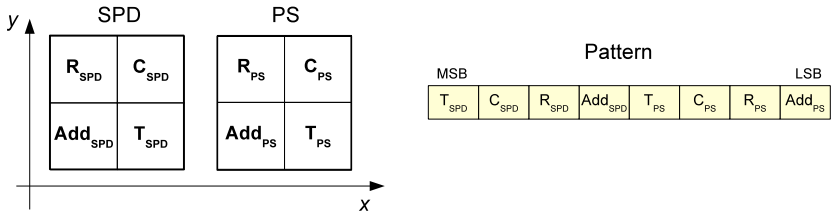

Figure 2.27 – *PS Trigger Pattern: definition of the individual bits of the pattern (*left*) and format of the* `Pattern` *byte result.*

receives an energy deposit above the threshold set for the SPD, and similarly for the PS. The mapping between these bits and their position in the cluster is also shown in Fig. 2.27.

The pattern evaluation requires to obtain the SPD and PS trigger bits of neighbor cells located in different Front-End board. As shown in Fig. 2.26, there are:

1. **8 top neighbors** (`IN_Sn0` to `IN_Sn7`), received from the board located on the right in the crate (see Fig. 2.11) via the backplane on LVTTL links (16 bits in total, 8 for SPD and 8 for PS),

2. **8 right neighbors** (`IN_Up_Sn0` to `IN_Up_Sn7`), received via serialized LVDS links (using the same method as the ECAL right neighbors) through one cable (using 16 bits out of the 21 available, 8 for SPD and 8 for PS). These neighbors are either received from the same crate or from a crate located in a different rack (between PRS Crate 0 and PRS Crate 1, and between PRS Crate 6 and PRS Crate 7). The cable length is equal to 70 cm for links between boards in the same crate and to 4.6 m for links between boards in different racks.

3. **1 corner neighbor** (`IN_C`), received first through a cable by the right side PS Front-End board and then re-emitted via the backplane to the PS Trigger FPGA (2 bits, 1 for SPD and 1 for PS).

The PS Trigger FPGA computes a local BCID counter (`PS_BCID`) used for synchronization. It also checks that the BCID values received from the two ECAL Front-End boards are equal, to avoid possible desynchronization between the two inputs. When they differ, the pattern is set to 0 for both candidates. Since this check is also applied for half boards which have only one input, an extra cable coming from a free slot in an ECAL crate has to be plugged in so that the BCID verification can also be performed.

The two patterns resulting from the trigger computation are sent via LVDS serialized links to Trigger Validation Boards using the DS90CR215 serializer [69]. The result corresponding to the address sent by a ECAL Front-End board is sent to the Trigger Validation Board to which the ECAL board sends also its own result. This data are transmitted via Ethernet Category 6 cables plugged on the back of the backplane, behind the PS board. The cable length is either 2 m or 2.5 m and is equal to the length of the cable between the ECAL and the PS Front-End boards. The format used is shown in Fig. 2.28 where the address is a copy of the address received from the ECAL:

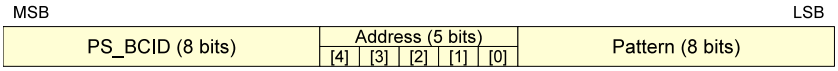

Figure 2.28 – *Format of the data sent from the PS Front-End Boards to the Trigger Validation Boards.*

The SPD multiplicity computed in the PS Front-End board is sent to the closest SPD Control Board, located in the same half-crate as the PS Front-End board (see Fig. 2.11). The data is sent via the backplane through serialized LVDS links, with the format given in Fig. 2.29:

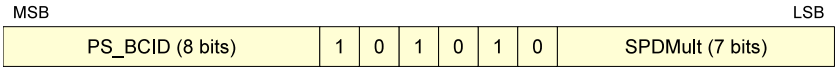

Figure 2.29 – *Format of the data sent from the PS Front-End Boards to the SPD Control Boards.*

The PS Trigger FPGA is configured from the LHCb ECS through the SPECS system, using the "Glue" FPGA as SPECS slave. The Trigger FPGA is connected to one of the I^2C busses delivered by the Glue. The PS Trigger FPGA also provides a "spy memory" functionality, and patterns can be injected from the Front-End FPGAs to replace the signals from the PMTs. This is also triggered by the TFC "Calibration command" and allows to verify the data transmissions and the results of the computations inside the FPGA.

The total computing time of the PS and SPD trigger information is equal to 568 ns, between the time when the PS detector signals arrive at the input of the Front-End board and the time after the serialization of the result to be sent to the Trigger Validation Boards. The breakdown of the different contributions to the latency is given in Table 2.4.

Table 2.4 – *Processing time in the PS Front-End Boards*

Step	Time (ns)
Digitization	150
Front-End Processing (in the FE_PGAs)	100
PS trigger bit generation (in the FE_PGAs)	125
Collecting neighbors	225
Wait for ECAL data	0
Compute pattern	25
Serialization	43
Total	**668**

2.3.3 Trigger Validation Boards

The Trigger Validation Boards (TVB) are in charge of combining the information received from the ECAL, HCAL and PS Front-End boards to obtain hadron, electron, photon, local π^0 and global π^0 trigger candidates. The board was designed at LAPP (Annecy) and is described in details in Ref. [75]. There are 28 TVB in total, one per half ECAL crate. As described in the previous sections, each TVB receives data from:

1. Up to 8 ECAL Front-End boards, which are the boards located in the same half-crate than the TVB (see Fig. 2.12). The data is received though the backplane of the crate according to the format given in Fig. 2.23.

2. Up to 8 PS Front-End boards. These are the boards which are connected to the ECAL Front-End boards mentioned just above. The data is received though cables plugged on the back of the backplane behind the TVB according to the format of Fig. 2.28.

3. Up to 4 HCAL Front-End boards. The data is received through cables plugged on the back of the backplane behind the TVB according to the format given in Fig. 2.22. The mapping between HCAL Front-End boards and TVB is represented in Fig. 2.30. On this figure, in each rectangle representing HCAL Front-End boards, the TVB to which the board are connected are given in the form "`TVB N.S (C)`", where `N` is the ECAL crate number of the TVB, `S` is the slot in which the TVB is plugged (*0* for the left side and

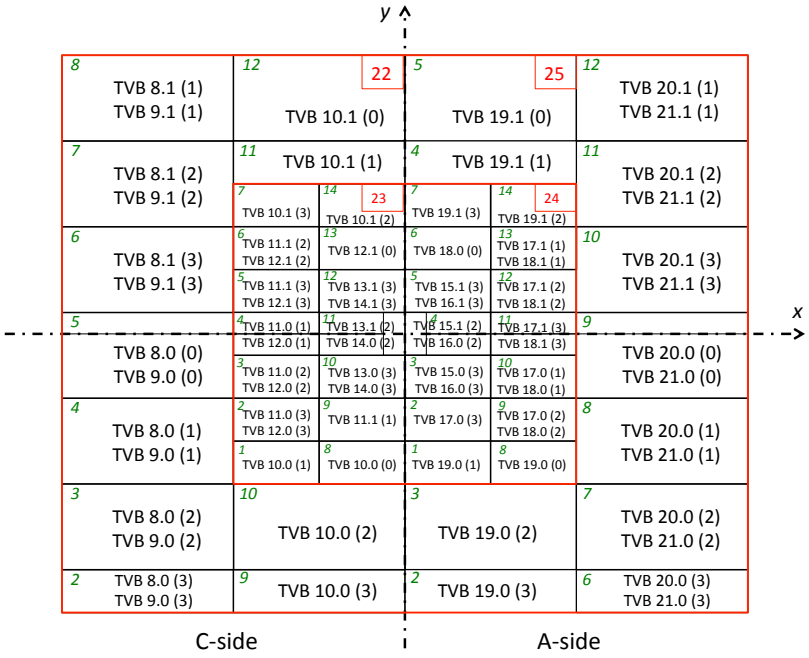

Figure 2.30 – *Mapping between HCAL Front-End boards and Trigger Valiration Boards.*

1 for the right side in the crate) and `C` is the connector number where the cable is plugged. There are 4 connectors placed vertically behind each TVB for cables coming from the HCAL boards. They are numbered from 0 to 3, 0 being the top one. Some HCAL boards send the same trigger result to two different TVB. The candidates are then called "duplicates".

The processing of the data is performed in two Actel APA750 FPGAs [74] of the ProASIC Flash family whose firmware can then be reprogrammed. The FPGAs contain each up to 750 000 logic cells, 562 Input/Output pins and 144 000 bits of RAM. One FPGA is dedicated to the computation of the "electromagnetic" candidates (electron, photon and π^0) and is called **EPPI** and the other takes care of the hadron candidates and is called **HCAL**.

After deserialization (with the DS90CR916 deserializer [69]), the input data enter the FPGAs. Each input link is delayed by a programmable number of clock cycles in order to align them properly. This step is facilitated because the HCAL and PS boards send their BCID counters which is then aligned with the local BCID counter of the TVB (`TVB_BCID`). At the input of the EPPI FPGA, the ECAL data are delayed by 17 clock cycles and the PS data are not delayed. At the input of the HCAL FPGA, the ECAL data are delayed by 5 clock cycles and the HCAL data by

2 clock cycles (the processing in the EPPI and HCAL FPGAs are independent and do not need to be synchronized). Because of the cable length (15.5 m), the HCAL signal is adapted at the end of the cable, before deserialization, to compensate for the loss in the cable.

As for the other boards, the correct sampling of the input data is ensured adjusting the phase of FPGA clock with a delay chip, by steps of 1 ns. One single delay can be applied per FPGA to read correctly its input data (up to 16 inputs for the EPPI FPGA: 8 ECAL and 8 PS; up to 12 inputs for the HCAL FPGA: 8 ECAL and 4 HCAL). However, in order to increase the flexibility, the sampling edge of the clock can be selected between the falling edge or the rising edge individually for each of the input, using a configuration register.

The **HCAL FPGA** computes one hadron candidate for every 2×2 cluster received from HCAL Front-End boards, thus 4 hadron candidates at maximum. The address of the hadron candidate (`Address`) is the address of the HCAL cluster. The E_{T} of the candidate (`Et`) is the sum (saturated at 255) of the HCAL cluster E_{T} and of the E_{T} of one of the 8 ECAL clusters (at maximum) received by the TVB, if one of these clusters is located in front of the HCAL cluster. If several of the ECAL clusters are in front of the HCAL one, the combination giving the highest E_{T} is selected. The test if one ECAL cluster is in front of the HCAL cluster is done using the addresses. Since the geometries of the detectors covered differ from TVB to TVB, this test cannot be universal and has to be adapted for each board. In order to do that, the firmware of the HCAL FPGA uses a large Look Up Table (LUT) loaded via ECS when the board is configured. The LUT is basically a matrix indicating for each pair of HCAL and ECAL addresses in the area covered by the TVB, if the two candidates are in front of each other or not.

Each hadron candidate is then sent to the Selection Boards. 32 bits of data are sent (per candidate), in two consecutive words of 16 bits, with the format shown in Fig. 2.31, where `Type` is equal to 4 for the hadron candidate received on the connector 3, 5 for connector 2, 6 for connector 1 and 7 for connector 0, and where Number is the TVB number, equal to $2 \times (\mathrm{Crate} - 8) + \mathrm{S}$ for the C-side and $2 \times (\mathrm{Crate} - 15) + \mathrm{S}$ for the A-side (S being the slot number as defined above).

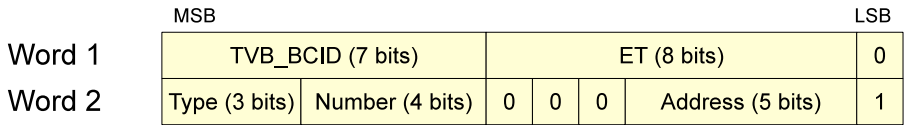

Figure 2.31 – *Format of the hadron data sent from the Trigger Validation Boards to the Selection Boards.*

The **EPPI** FPGA computes one electron, one photon, one local π^0 and one global π^0 candidate for the entire TVB:

Electron Each 2×2 cluster coming from the ECAL boards is "validated" with the corresponding pattern received from the PS Front-End boards. If the pattern corresponds to the definition of an electron (see Sec. 2.1.2), the candidate is kept, if not it is rejected. For flexibility, the definition of an electron is stored in a LUT that is loaded at configuration by ECS. This LUT lists the patterns which have to be considered as electron. The final candidate selected by the TVB is the one with highest E_T among the at most 8 candidates. The transverse energy and the address are equal to the E_T and address of the ECAL candidate.

Photon The processing is identical to the electron case, only the definition of the photon is different in the validation LUT.

Local π^0 The processing is identical to the electron case, but the definition of the local π^0 is different in the validation LUT. The address of the candidate is also equal to the address of the ECAL cluster but the E_T is equal to the total energy of the Front-End board (`SumEt`) instead of the cluster E_T.

Global π^0 These candidates are formed adding two ECAL clusters located in two consecutive boards. Two boards are consecutive if they share an horizontal border (for example boards 1 and 2 in crate 8 in Fig. 2.12). Boards located in different half crates are not combined in a global π^0 candidate (like boards 7 and 8 of crate 8) because they belong to different TVB. The pairing of the ECAL Front-End boards is also coded in a LUT since this differs from TVB to TVB. The E_T of the candidate is the sum saturated at 255 of the E_T of the two ECAL clusters except when these two clusters have at least one cell in common. In this case, the global π^0 E_T is the E_T of the candidate located in the bottom board. The address of the global π^0 candidate is the address of the cluster located in the bottom board and only the candidate with highest E_T is selected per TVB.

The results are sent to the Selection Boards, using 32 bit words for each of the candidates, with the format shown in Fig. 2.32, where `Type` is equal to 0 for the electron, 1 for the photon, 2 for the local π^0 and 3 for the global π^0, and `Input` is the ECAL Front-End board number from which the candidate is selected by the TVB. This number varies from 0 (the most left board in the half crate) to 7 (the most right board in the half crate).

All results of the TVB are sent via optical fibers to the Selection Boards which are located in the barrack behind the shielding wall. The transmission of the

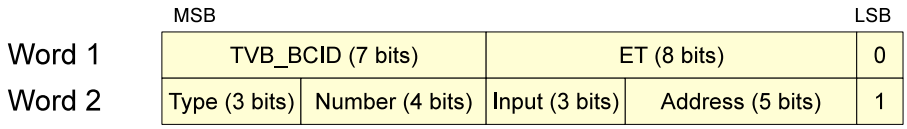

Figure 2.32 – *Format of the electromagnetic candidate data sent from the Trigger Validation Boards to the Selection Boards.*

data is performed by a 8 channel optical mezzanine, developed in Bologna. The 32 bit information of each candidate is serialized at a frequency of 1.6 GHz by a custom chip developed at CERN for the LHC experiments, called GOL [76]. On the optical mezzanine, one GOL per candidate is installed and the phase of the clock of all GOL chips can be adjusted thanks to one delay chip to sample correctly the data coming from the FPGAs of the TVB. The serialized data is sent in multimode optical fibers, of core diameter of 50 μm, using the Agilent HFBR-772BH optical transmitter [77] which contains 12 Vertical Cavity Surface Emitting Lasers (VCSEL) operating at a light wavelength of 850 nm. The fibers used are grouped in ribbons of 12 fibers (only 8 fibres are used in the ribbon) and the ribbons are equipped with standard MPO (female) connectors. The total length of the fibers between the TVB and the Selection Boards is equal to 96.5 m for the A-side and 101.5 m for the C-side: 37 m or 42 m between the TVB and the fixed point behind the calorimeter, 56 m between the fixed point and a patch panel in the barrack and 3.5 m between the patch panel and the Selection Boards.

The FPGAs of the TVB are configured from the ECS using the SPECS system with a "Glue" FPGA as SPECS slave. The FPGAs are connected to the I^2C busses provided by the Glue. The TVB contain "spy memories" that allow to inspect the values of the input data before the processing in the FGPA and also the values after processing, before they are sent to the Selection Boards. The recording in the "spy memories" is triggered by the TFC "Calibration Command", i.e. by the same command that triggers the injection of predefined patterns in the Front-End boards. Since the "Calibration Command" is sent synchronously to all boards in the system, this provides a powerful way of checking the connections and the processing of the entire chain, injecting data in place of the PMTs signals in the Front-End boards, and reading the result of the processing at the output of the TVB.

The processing time in the Trigger Validation Board is equal to 518 ns for the EPPI FPGA and 368 ns for the HCAL FPGA. It is computed between the time when the data arrive at the input of the board and the time the data are sent to the Selection Board, after serialization. The detail of the latency is given in Table 2.5.

Table 2.5 – *Processing time in the Trigger Validation Boards*

Step	Time (ns)
Deserialization of all inputs	43
Input data sampling and rephasing	50
Wait for PS data (only for EPPI)	150
Compute candidates	225
Optical link serialization	50
Total	**518 (EPPI), 368 (HCAL)**

2.3.4 SPD Control Boards

The SPD Control Boards [78] were designed in Barcelona. They are located in the PS crates and their function for the trigger is to compute the SPD multiplicity for the half crate where they are located. One SPD Control Board receives SPD multiplicity values from up to 7 PS Front-End board according to the format described in Fig. 2.29 through LVDS serialized links via the backplane. After deserialization with the DS90CR216 deserializer, proper signal capture and time alignment, the board adds all multiplicities to obtain the total SPD multiplicity for the half-crate (`SPDMultiplicity`, on 10 bits) and sends it together with its local BCID counter (`SPD_BCID`) to one Selection Board using the format of Fig. 2.33 where `Crate` is the crate number (see Fig. 2.11) and `S` the slot where the SPD Control Board is plugged in the crate (*0* for the left slot, *1* for the right slot).

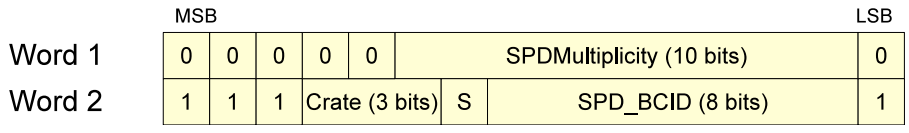

Figure 2.33 – *Format of the SPD multiplicity data sent from the SPD Control Boards to the Selection Boards.*

The processing is realized in a APA300 FPGA of the Actel ProAsic Plus family containing up to 300 000 logical cells, 290 Input/Output pins and 72 000 bits of memory. The data is sent serialized with the GOL chip as for the TVB but using a single channel optical mezzanine. The mezzanine hosts a VCSEL of type ULM850-05-TN made by Ulm Photonics [79], that emits light at a wavelength of

850 nm. The fiber plugged in the SPD control board is a multimode single fiber equipped with a standard SMA connector. The single fibers that are connected to the SPD Control Boards are grouped into a 12-fiber ribbon in a CERN made special box on top of the platform. The total length of the fiber between the SPD Control Board and the Selection Board is equal to 102.5 m for the A-side and 107.5 m for the C-side: 7 m between the SPD Control Boards and the box on the platform, 37 m or 42 m between the box and the fixed point behind the calorimeter, 56 m between the fixed point and the patch panel in the barrack, and 2.5 m between the patch panel and the Selection Board.

The FPGA of the board is controlled via the SPECS system (the board hosts a SPECS Mezzanine as SPECS Slave) using the parallel bus provided by the SPECS Mezzanine. The "spy memory" functionality controlled by the TFC "Calibration Command" is also available for test and debugging purposes.

The total latency in the SPD Control Board is of 143 ns between the time the data arrive at the input of the board and the time the data are sent to the Selection Board. Details are given in Table 2.6.

Table 2.6 – *Processing time in the SPD Control Boards*

Step	Time (ns)
Deserialization of all inputs	43
Multiplicity computation	50
Optical link serialization	50
Total	**143**

2.3.5 Selection Boards

The last boards in the L0CALO processing chain are the Selection Boards [80], which were developed at Bologna. They compute the final candidates and also provide the interface to the DAQ network of the L0CALO. The complete description of the board can be found in Ref. [81].

a) Board description

There are 8 Selection Boards: one per electromagnetic candidate (electron, photon, local π^0 and global π^0), three for the hadron candidate and one for the SPD multiplicity computation. Each board has up to 28 inputs (this is why 3 boards are needed for the hadron candidate, since there are 80 candidates coming from the TVB in total, including the "duplicates") and up to 3 outputs to the L0DU and to TELL1 boards.

The data processing in the Selection Board is realized with 7 FPGAs. The FPGAs used are XILINX Virtex II Pro XC2VP40 FPGAs [82] which contain up to 44 000 logical cells, 804 Input/Output pins and 3 456 000 bits of memory:

- 5 "Input FPGAs" are in charge of receiving and aligning the data received from the TVB or the SPD Control Boards,
- 1 "Process FPGA" performs the computation of the results,
- 1 "Control FPGA" handles the control signals (clock, reset, ...) of all the other components of the board.

Each Selection Board is connected to the LHCb ECS network via a Credit Card PC (CCPC) [83] which is a custom LHCb system designed at CERN that uses an ethernet network as communication medium and an embarked linux system on a small card as interface for the configuration of the hardware. The FPGAs are configured though the local parallel bus provided by the CCPC and the configuration registers available on the board are detailed in Appendix C. All boards are also connected to the TFC system via a TTCrq mezzanine. The length of the TTC fibers between the ODIN board and the Selection Boards is equal to 13 m.

The Selection Boards are independent of each other except the three boards for the hadron candidate. They have to exchange data between them to identify the highest candidate over the entire detector and also to compute the sum of the transverse energy of all candidates. The data exchange between these three boards is done via a small custom backplane on which these three boards are plugged. For this reason, the three boards have to be located next to each other. One board realizes the final computation and is called "Master". The two other boards are called "Slave", they compute partial results corresponding to their inputs and send them to the "Master" board.

b) Input data

The data coming from the TVB and the SPD Control Boards are received via optical fibers through an Agilent HFBH-782 optical receiver [77] using PIN photodiodes and handling 12 channel at a time. The fibers plugged in the Selection Boards are grouped in 12-fiber ribbons equipped with MPO (female) connectors.

The fibers arriving from the TVB contain 8 candidates, one of each type. The data need then to be dispatched before arriving to the Selection Board. This is done in a patch panel which contains "MPO-SC" cassettes which split the 12-fiber ribbons into 12 individual connectors. The schematics of the cassettes is shown in Fig. 2.34 where the assignment of each output connector is represented. For hadron candidates, the number between parentheses is the HCAL connector number as explained in Sec. 2.3.3. Another fiber with on one end 12 individual fibers equipped with SC connectors and on the other end a 12-fiber ribbon with a MPO connector, groups for example 12 electron candidates together and connects the cassettes of the patch panel to the Selection Boards.

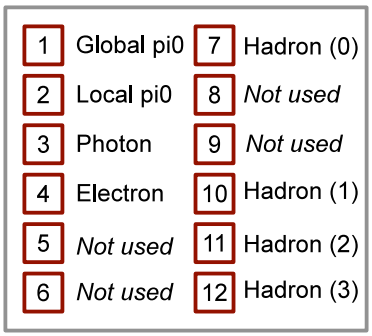

Figure 2.34 – *Schematics of the MPO to 12 SC cassettes in the Selection Boards patch pannel.*

The first step to read the received data is to deserialize them. As described above, the data is serialized by the GOL: two 16 bit words are sent in a serial stream over the link with an output stream frequency of 1.6 GHz. The deserialization is done with a TLK2501 deserializer from Texas Instrument [84]. In order to deserialize properly the data, the receiver needs to be synchronized with the emitted data structure so that it knows the position of the data 16 bit boundaries in the serialized stream. This is done thanks to a specific data pattern sent by the GOL, called "IDLE", that the deserializer recognizes and uses to synchronize itself.

Since the emitter is located close to the LHC beam, the synchronization between the emitter and the receiver may be lost because of Single Event Upsets (SEU) induced by radiations. This is why the synchronization procedure is in fact

repeated periodically, just before the beginning of each LHC cycle: the GOL of the TVB and of the SPD Control Boards are configured to send "IDLE" patterns during the N clock cycles preceding BCID 0, where N can be programmed by ECS. According to Ref. [85], N is chosen to be equal to 3. During the three synchronization cycles, the trigger system is blind because the data from the detector are replaced by "IDLEs". However, the position of these cycles is chosen to lie at the end of the LHC cycle, in a large gap without beam and when no collision occur.

One major problem in desynchronizing optical links is that the latency of the data reception (the time between between the first bit of serialized data arrives and the time the data is decoded at the output) is fixed only when the link is established, i.e. when the emitter is powered on. The latency can vary between 47 ns and 67 ns, i.e. between 2 and 3 clock cycles, depending on environmental conditions like the temperature which can then change during the LHCb operation. Since a fixed and constant latency is needed for the trigger, a special method has been developed to ensure a well defined latency for reading the input data of the Selection Boards, illustrated in Fig. 2.35, and realized in the Input FPGAs.

The principle of the method is to store the data of each input channel in one First In-First Out (FIFO) memory before using it and to adjust the position of the write and read addresses in this FIFO to obtain a fixed latency and to align all data at the output of the FIFO. The read address must be based on a stable signal with respect to the receiver: the BCID reset from the TFC is used. The write address has to be based on a stable signal with respect to the emitter (TVB or SPD Control Board): the chosen signal is the "Data Valid" signal which is set by the optical receiver when it receives the first data after the 3 "IDLE" cycles. According to the procedure described before, this signal is set when the data corresponding to the BCID 0 arrive in the Selection Board. Note that the "Data Valid" signal is not fixed with respect to the receiving side since it is decoded after the optical link synchronization in the TLK2501 deserializer and is thus not obtained with a fixed latency as explained above.

The time difference between these two signals (BCID reset and Data Valid) is the delay that have to be applied to individual input channels so that they are aligned at the output of the FIFO and so that the latency is constant. This difference is computed and applied each time the TVB, SPD Control Boards and Selection Boards are configured (in practice, each time a run is started, to be sure that all inputs are active before begin synchronized). In order to minimize the latency, the BCID reset signal can in fact be adjusted with a delay so that it arrives only few clock cycles after the "Data Valid" signal, a small margin is left so that it is guaranteed that it always arrives later and not earlier.

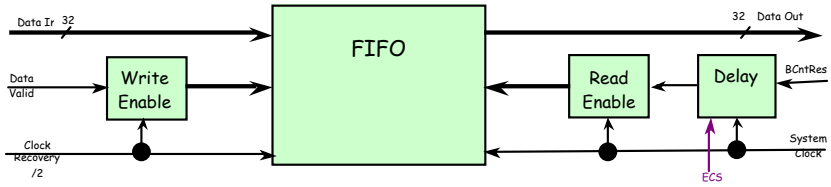

Figure 2.35 – *Block diagram of the input data alignment of the Selection Boards.*

c) Algorithm

The processing of the input data to obtain the trigger results, namely the highest or the sum of the input candidates is realized in the "Process FPGA". The block diagram of the algorithm implemented in this FPGA is represented in Fig. 2.37.

The first step, called "Mask & Ghost" in the diagram is the possibility to mask completely one channel in the computation, using configuration registers that can be written via the ECS. The other function applies only to the hadron boards and is needed to suppress "duplicate" or "ghost" candidates for the hadron processing. Two input candidates are called "duplicates" when they originate from the same HCAL Front-End board but through different TVB. These candidates have the same address but may have different E_{T} since the HCAL candidate was combined with different ECAL clusters in the TVB. As can be seen in Fig. 2.30, out of the 80 input hadron candidates, 60 are duplicates, so in total there are only 50 independent candidates. When two inputs are flagged as "ghost", then only the candidate with highest E_{T} is considered for the rest of the processing, so as not to count it twice for the computation of the hadron sum E_{T}, which is the sum of the E_{T} of the 50 independent hadron candidates. The assignment of "ghosts" is done via configuration registers loaded with the ECS.

The second step is to translate the local 5 bit address received from the TVB (i.e. the address of the bottom left corner of the 2×2 cluster) into a global 14 bit address that can be understood by the offline analysis software. The convention defined for calorimeter addresses is given in Ref. [86] and illustrated in Fig. 2.36, where `Area` is the calorimeter area: for the ECAL, 0 is the Inner Area, 1 the Middle Area and 2 the Outer Area, for the HCAL, 0 is the Inner Area and 1 is the Outer Area. `Row` is the row of the cell and `Column` the column of the cell.

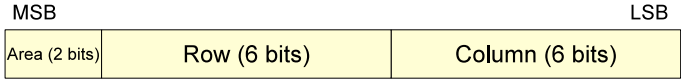

Figure 2.36 – *Format of the global 14 bit calorimeter address.*

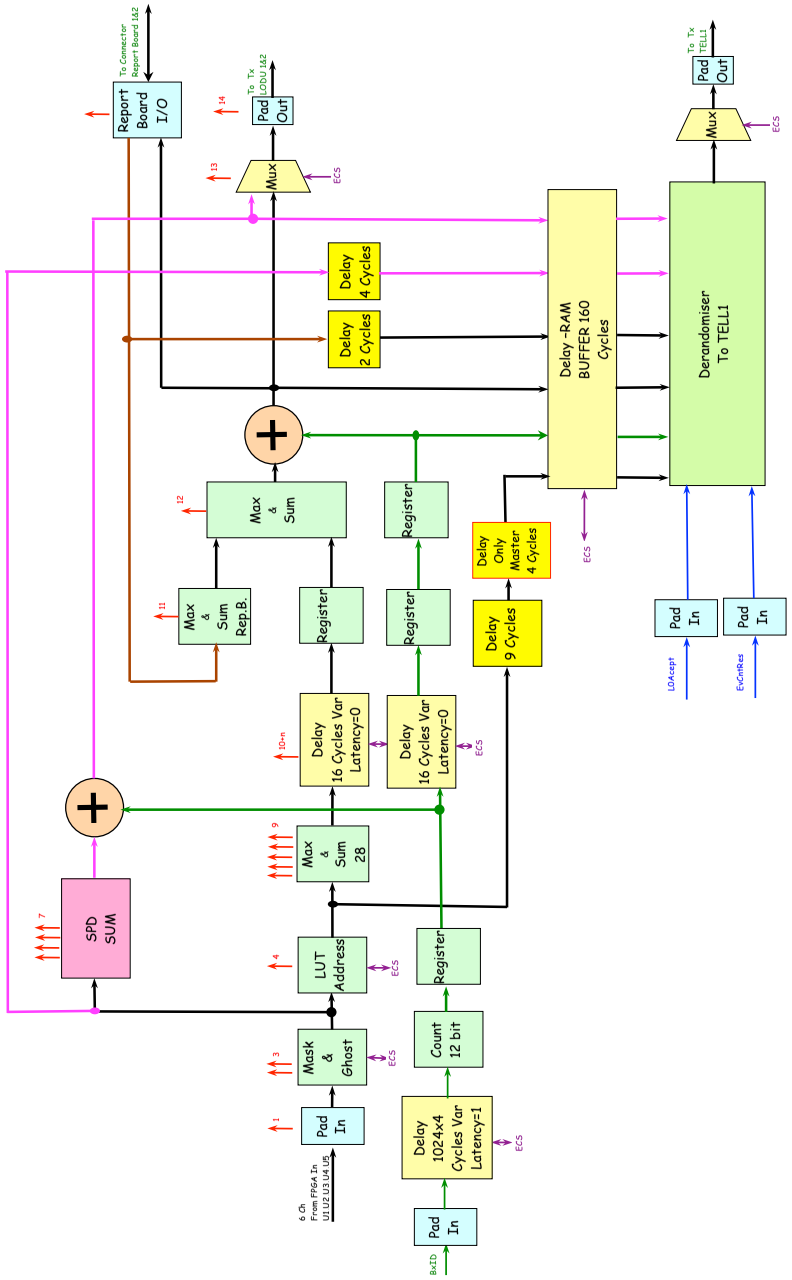

Figure 2.37 – *Block diagram of the data processing in the Selection Boards.*

Rows and columns are numbered such that `Column` increases with x and `Row` increases with y and such that the middle of the ECAL is between rows and columns 31 and 32, and that the middle of the HCAL is between rows and columns 15 and 16. This means that the cell at the bottom left of:

- Inner Area of ECAL has column 0 and row 8,
- Middle Area of ECAL has column 0 and row 12,
- Outer Area of ECAL has column 0 and row 6,
- Inner Area of HCAL has column 0 and row 2,
- Outer Area of HCAL has column 0 and row 3.

The correspondence between local addresses and global addresses is registered in LUTs which are loaded in a Permanent Read Only Memory (PROM) located on each board. The content of the PROM is transferred to the process FPGA each time the board is configured. Since this step is not needed for the computation of the SPD multiplicity, is is skipped in the Process FGPA of the SPD multiplicity Selection Board.

The last step of the computation is to find the maximum E_{T} candidate amongst all inputs. For the SPD multiplicity and the hadron boards, the sum of the multiplicity or E_{T} of the non duplicate inputs is also calculated. For the hadron boards, this is done in two steps. First the three boards obtain the maximum and the sum of their inputs. Then the two slave boards send their results to the master board which compares them with its own maximum and adds them to its own sum. The results of the master board are properly delayed so that they are time aligned with the results received from the slave boards.

The boards compute a local BCID counter (`SB_BCID`) to ease the alignment of the results for the final trigger decision, in particular to align them with the results from the Muon trigger. A status bit (`Status`) is also provided and sent together with the results in order to indicate possible problems. The status is equal to 0 except when at least one of these conditions occurs:

1. At least one input optical link is in error. This is checked reading the "faulty" flag set by the optical receiver when the connection is lost with the emitter.
2. At least one input link is desynchronized with respect to the other. This is checked comparing the `TVB_BCID` (or `SPD_BCID`) values received with the candidates between all input links, after time alignment and ignoring masked channels.

Finally, the boards implement a circular buffer (derandomizer) to hold the data until a "L0 Accept" signal is received and the data are sent to TELL1 boards. In order to send to the TELL1 the correct event (i.e. the one associated with the trigger), the depth of the derandomizer can be adjusted via configuration registers. It is equal to 47 clock cycles for the electromagnetic Selection Boards, 52 clock cycles for the master hadron board, 56 clock cycles for the two slave hadron boards and 62 clock cycles for the SPD board. The derandomizer has been implemented to be able to cope with a 1.1 MHz rate of "L0 Accept".

d) Output connections

The results are sent to the L0 Decision Unit (L0DU) where the trigger decision is taken. Six of the eight boards are connected to the L0DU:

- the four electromagnetic boards which send the final candidate's address and E_{T},
- the master hadron board which is connected via two links to the L0DU, one sends the hadron candidate's address and E_{T} and the other sends the total hadron sum E_{T},
- the SPD multiplicity board which sends the total SPD multiplicity.

The results consist of 32 bits (two 16 bit words) sent over optical fibers by a single channel mezzanine of the same type as the one used on the SPD Control Board and described in Sec. 2.3.4. The data format is represented in Fig. 2.38 for the electromagnetic and hadron candidates, in Fig. 2.39 for the total hadron sum E_{T} and in Fig. 2.40 for the SPD multiplicity.

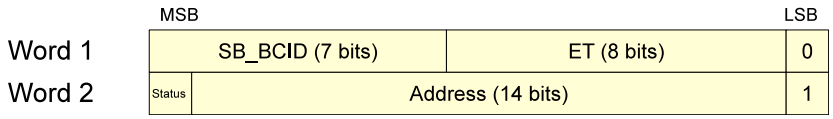

Figure 2.38 – *Format of the electromagnetic and hadron candidate data sent from the Selection Board to the L0DU.*

The optical fibers used between the Selection Boards and the L0DU are multimode fibers equipped with SMA connectors at the end it is plugged to the Selection Board and with SC connectors at the other end. The length of the fiber is equal to 11 m up to a patch panel located in the L0DU rack. There is an extra length of 2 m to reach the L0DU from the patch panel.

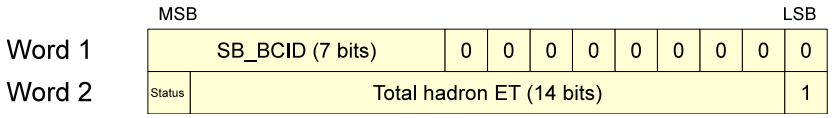

Figure 2.39 – *Format of the total hadron E_T data sent from the Selection Board to the L0DU.*

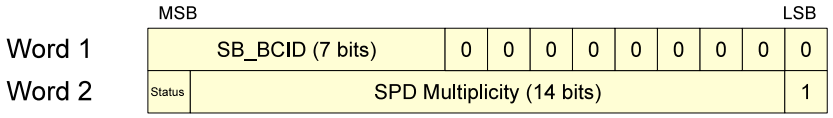

Figure 2.40 – *Format of the SPD multiplicity data sent from the Selection Board to the L0DU.*

All Selection Boards are connected to two TELL1 boards, which are the interfaces of the L0CALO system to the DAQ network and thanks to which offline access to trigger data is possible. The principle of the DAQ part of the Selection Board is to send to the TELL1 board, when a "L0 Accept" signal is received from the TFC, all the inputs and the results of the Selection Board corresponding the triggering event . The main goal is to be able to verify offline the trigger behavior since the information used in the Selection Boards will be retained. The trigger data is also used by the HLT algorithms to have fast access to ECAL or HCAL clusters.

The data is transmitted from the Selection Board through optical fibers using single channel optical mezzanines as described above. The fibers are multimode fibers with 12 individual fibers on one side equipped with SMA connectors and plugged in the Selection Boards. The other side is a 12-fiber ribbon where all individual fibers have been grouped, equipped with a MPO (female) connector and plugged in the TELL1 board.

Two TELL1 boards are used for the L0CALO [87]:

1. One board (TCATELL01) receiving data from the three hadron Selection Boards. The master board is connected to the input 1 of the TELL1, the first slave to the input 2 and the second slave to the input 3.

2. One board (TCATELL02) receiving data from the four electromagnetic and from the SPD Selection Boards. The photon board is connected to the input channel 1 of the TELL1, the electron to the input 2, the local π^0 to the input 3, the global π^0 to the input 4 and the SPD multiplicity to the input 5.

Following the requirements of the TELL1 implementation [88], the data are sent in a buffer of fixed length: 35 words of 32 bits each. The buffer is composed of three header words and 32 data words. The format of the header word is represented in Fig. 2.41, where `L0 Event ID` is a counter incremented at each "L0 Accept" and reset when the "L0 Event ID Reset" command is received from the TFC, allowing the event building stage to assemble fragments from the same event. `Source ID` is a field identifying the Selection Board and is equal to 0 for the photon board, 1 for the electron board, 2 for the local π^0 board, 3 for the global π^0 board, 4 for the first hadron slave board, 5 for the master hadron board, 6 for the second hadron slave board and 7 for the SPD multiplicity board.

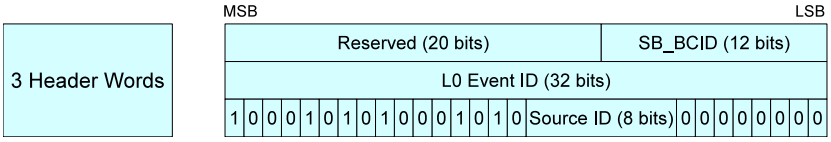

Figure 2.41 – *Format of the header words sent from the Selection Boards to the TELL1.*

The format of the data word is shown in Fig. 2.42 where `IO` is one bit which set to 0 to indicate that the data corresponds to an input of the Selection Board and to 1 when it corresponds to the result of the Selection Board. `Slave` is a two bit value equal to 0 for all Selection Boards except for the first slave hadron board where it is equal to 1 and for the second slave hadron board where it is equal to 2. `Mask` is a bit which is set to 0 except when the input value is masked in the Selection Board by configuration. In this case, it is equal to 1. `Type` indicates the type of the candidate and is equal to 0 for electron, 1 for photon, 2 for hadron, 3 for local π^0, 4 for global π^0, 5 for the total hadron E_T and 6 for the SPD multiplicity.

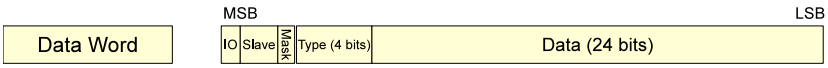

Figure 2.42 – *Format of the data words sent from the Selection Boards to the TELL1.*

The `Data` field format depends on the type of candidate sent. For electromagnetic and hadron candidates, the format is shown in Fig. 2.43. `Det` is a 2 bit value which is needed to complement the address received from the Selection Board and described in Fig. 2.36 and to transform it into the offline Cell ID used by the reconstruction and analysis software and described in Ref. [86]. It is equal to 2 for the electromagnetic candidates (corresponding to the ECAL detector) and 3 for the hadron candidates (corresponding to the HCAL detector). The format for the total hadron E_T and for the SPD multiplicity are shown in Fig. 2.44 and 2.45 respectively.

Figure 2.43 – *Format of the data field for electromagnetic and hadron candidates.*

Figure 2.44 – *Format of the data field for the total hadron* E_{T}.

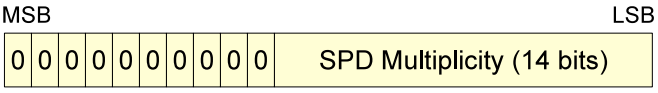

Figure 2.45 – *Format of the data field for the SPD multiplicity.*

The buffer sent to the TELL1 is completed with words filled with 0 to obtain a fixed length of 35 words. As an example, the full buffer sent from the hadron master Selection Board to its TELL1 is given in Fig. 2.46.

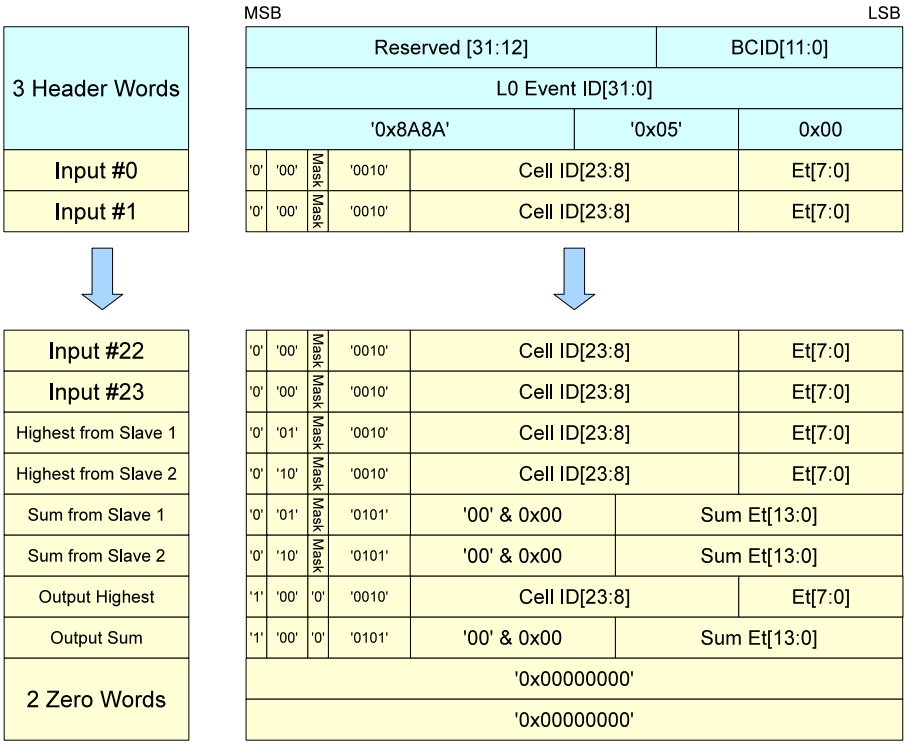

Figure 2.46 – *Buffer sent from the hadron master Selection Board to the TELL1.*

e) Processing in the L0CALO TELL1 and offline decoding

The processing of the L0CALO data in the TELL1 is a simple suppression of all data with an E_T or a multiplicity smaller than a configurable threshold [87, 89]. The data sent to the DAQ network and eventually written to storage for analysis are a copy of the data received by the TELL1 but where candidates with E_T or multiplicity below threshold are removed. By default (and this is the case for the current LHCb configuration), the threshold is set to 0 and only a zero-suppression is applied, but a threshold different than 0 can be set in each TELL1 using a 8 bit configuration register.

The format of the data sent by the TELL1 boards (raw data bank) conforms to the LHCb raw bank format defined in Ref. [90]. The raw bank is a variable length buffer of 32 bit words consisting of a 2 word header and a bank body. The format of the bank header is shown in Fig. 2.47. The header contains the

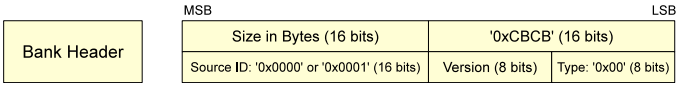

Figure 2.47 – *Raw data bank header sent by the L0CALO TELL1 boards.*

size of the total raw bank, a source identifier (`Source ID`) which is equal to 0 for the TELL1 connected to the hadron Selection Boards (TCATELL01) and to 1 for the other TELL1 (TCATELL02). It contains also a version number and a `Type` identifier (equal to 0 for L0CALO) allowing the software to dispatch the raw banks to the correct decoder in order to reconstruct the event. The raw bank body contains all data words received from the Selection Boards by the TELL1 which are not suppressed by the algorithm described above and excluding also header words represented in Fig. 2.41. The typical average bank sizes obtained for nominal 2011 LHCb beam conditions were equal to 320 bytes per event for the TELL1 connected to the hadron Selection Boards and 390 bytes per event for the electromagnetic and SPD multiplicity TELL1.

For debugging purposes, the TELL1 can also send in addition non-zero suppressed banks, which are an exact copy of the data received from the Selection Boards, without suppression and including the header words. This feature is deactivated during normal data taking since it increases notably the data size of the recorded events. The TELL1 can report errors during the processing through an error bank [91]. The format of the error bank is given in Fig. 2.48 and allows to report about input optical links in error (`TLK link loss`, `Optical link disable` or `Optical link no clock detect`), about BCID or L0 Event ID values not synchronized between input links (`EvID Mismatch`

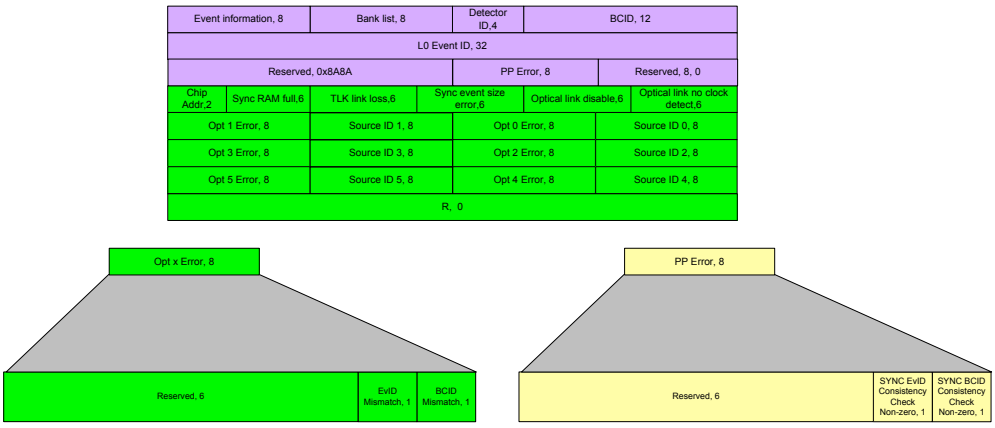

Figure 2.48 – *Raw data bank header sent by the L0CALO TELL1 boards.*

or `BCID Mismatch`) or internally (`SYNC EvID Consistency Check` or `SYNC BCID Consistency Check`), and about errors during the TELL1 processing (`Sync RAM full` or `Sync event size error`). Error banks are deactivated during normal LHCb running since errors in the calorimeter trigger can be detected with other methods as will be described in the next section.

The raw data banks are decoded by the LHCb reconstruction software into C++ event model class objects that hold the necessary information about the candidates. These objects are saved, after the reconstruction is done, in the files that will be used for the analysis, giving access at the analysis level to all the information received by the L0CALO TELL1.

The event model class representing L0CALO candidates is called `L0Calo-Candidate` and contains the following data members:

type() an integer identifying the type of the candidate, and equal to 0 for electron, 1 for photon, 2 for hadron, 3 for local π^0, 4 for global π^0, 5 for the hadron total E_{T}, 6 for the SPD multiplicity.

id() is the cell identifier of the address of the candidate, i.e. the identifier of the bottom left cell of the 2×2 cluster. The convention used for the cell

identifier follows the one defined in Ref. [86] and explained above.

etCode() is the E_T of the candidate, in trigger ADC counts, i.e. the 8 bit integer value used in the trigger processing in the electronics.

et() is the E_T of the candidate, in MeV. For the current configuration of the calorimeter, 1 trigger ADC count equals to 20 MeV.

position() is the position in the (x,y) plane of the center of the 2×2 cluster, i.e. the intersection of the cluster diagonals.

posTol() is a tolerance estimate of the cluster position and is equal to half of the cell sizes of the cluster.

A read-out status object is also filled when decoding the raw event and stored with the data. It indicates possible errors encountered during the decoding. The values of this object are equal to the following predefined constants:

Corrupted (1) when the same output candidate appears several times (for example when there are two maximum E_T electron candidates), when the address of the candidate is not a valid address in the calorimeters, or when the header of the bank is malformed,

Incomplete (2) when at least one input channel of the Selection Board is masked,

Missing (4) when one complete raw bank from one of the TELL1 board is missing in the event,

NonUnique (16) when two raw banks from the same TELL1 are present in the same event,

ErrorBank (256) when an error bank has been issued (currently deactivated),

f) Latency

The processing time in the Selection Board is equal to 475 ns for the electromagnetic Selection Boards, 525 ns for the hadron boards and 200 ns for the SPD multiplicity board, between the time the data arrives at the input of the optical receiver and the time the result is serialized before being sent to the L0DU. The detail of the processing is given in Table 2.7.

Table 2.7 – *Processing time in the Selection Boards*

Step	Time (ns)
Electron, photon, local and global π^0	
Deserialization of optical link inputs	50
Input data time alignment	50
Selection of highest candidate	325
Optical link serialization	50
Total	**475**
Hadron	
Deserialization of optical link inputs	50
Input data time alignment	50
Selection of highest candidate	325
Wait for slave boards	25
Selection of highest candidate between slaves and master boards	25
Optical link serialization	50
Total	**525**
SPD Multiplicity	
Deserialization of optical link inputs	50
Input data time alignment	50
Computation of multiplicity	50
Optical link serialization	50
Total	**200**

g) Error checks

The correct behavior of the full L0CALO chain is checked constantly while taking data. Several methods are used to verify that the data are correctly calibrated, aligned and that the trigger result is the one expected. One of the verification is implemented directly in the electronics, in the Selection Boards, and is performed for every clock cycle. It consists in comparing between all inputs, the BCID values received from the Trigger Validation Boards. This check is done in the Input FPGAs of the Selection Board and for each clock cycle, if there is a

difference between one link and the others, an error counter is incremented. The error counter is read by ECS and reset regularly (automatically when the counter is read), which allows to distinguish transient errors due to Single Event Upset in the emitter from permanent errors that will affect the result of the trigger. When the last case occurs, an alarm is transmitted to the LHCb shift crew so that it can be corrected.

The case where all links are desynchronized by the same delay cannot be detected by this method. Another verification has been implemented in the Selection Boards. It consists in using "spy memories" which store the values of the input data received from the TVB, including their BCID, after time alignment in the Input FPGAs. These memories are read regularly via ECS and the BCID values stored in them compared to a reference BCID. The writing in the RAM is triggered by the BCID reset TFC command so that it always happen at the same time inside the LHC cycle. Thus when the input channels are properly time-aligned, their BCID must be equal to the reference BCID. When a difference is detected, it is also reported to the LHCb shift crew.

The last category of checks are realized using the calorimeter and trigger data sent to the DAQ. A small part of the computer farm is dedicated to monitoring tasks which analyze online a small fraction of the data recorded by the experiment. The results of these analyses, usually collections of histograms showing basic quantities representative of the good behavior of the detector, are displayed in a custom application, called "presenter" [92] which is used by the shift crew to control the quality of the recorded data.

In order to check that the calibration constants described in Sec. 2.3.1 are correctly loaded in the Front-End electronics, the trigger ADC values sent to the DAQ by the Front-End boards are compared to the values expected from Eq. (2.9) using the ADC value (also sent to the DAQ) and the calibration constants stored in the LHCb condition database.

The other verification conducted using the same method is to compare the trigger results from the Selection Boards (either the input values from the TVB or the result of the computation by the Selection Board since both are available in the trigger data) with the trigger results obtained from a simulation program using as input the data sent by the Front-End boards. This simulation program reproduces exactly the computations realized in the electronics boards of the L0CALO. Thus, starting from the same ADC values, the program should give the same results than the ones recorded by the Selection Board.

A typical histogram page showing the result of the comparison and available to the shift crew is represented in Fig. 2.49. The top right plot shows the position of

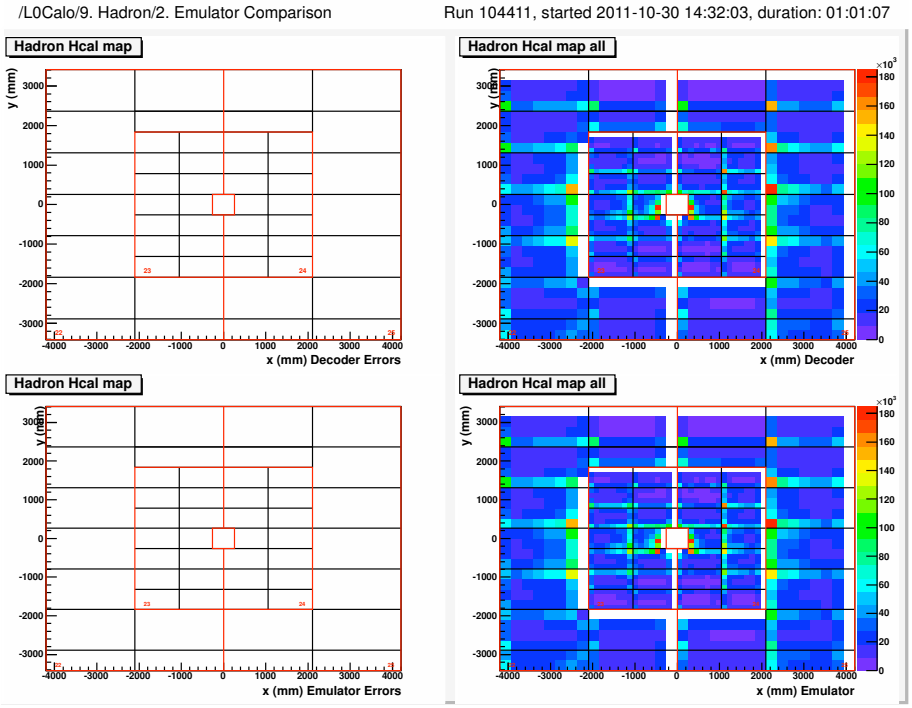

Figure 2.49 – *Monitoring histograms of the hadron trigger displayed online to the LHCb shift crew by the LHCb histogram presenter application.*

all hadron candidates computed in the trigger (the inputs of the Selection Boards, i.e. the outputs of the TVB) and the bottom right plot is the same plot but obtained with hadron candidates computed with the simulation software starting from the Front-End board data. The differences between the two plots is shown on the two 2-D histograms of the left part of the figure. When a hadron candidate from the trigger data is missing in the list of simulated candidates or is present with a different E_{T}, its position appears in the top left histogram, and similarly for the bottom left histogram taking as reference the simulated hadron candidates. Non empty histograms on the left part would indicate and locate a problem in the trigger computation.

Similar histogram pages exist for all types of candidates, for the total hadron E_{T} and the SPD multiplicity. They are updated and refreshed regularly, and they are also looked at by the LHCb shift crew to ensure the experiment is running properly. They provide an extremely powerful method to detect quickly problems in the calorimeter trigger.

2.4 Summary

2.4.1 Total latency

The total latency of the L0CALO trigger is defined as the time between the collision occurs at the LHCb interaction point and the time the corresponding "L0 Accept" signal from the TFC is received on the Front-End board electronics to collect the data of the triggering event in the various detectors. This time includes delay of propagation of particles in the detector, delay of propagation of the corresponding analog and digital signals in the various cables and the time for the processing of the data.

The latency is equal to 4000 ns for the electromagnetic candidates, 3997 ns for the hadron candidates and 3439 ns for the SPD multiplicity. The details of the computation are given in Table 2.8. The total latency must be equal to $4\,\mu$s by design and the necessary delay is added inside the ODIN board to adjust it to this value.

2.4.2 Conclusions

The implementation of the calorimeter trigger in the LHCb read-out architecture was described. The hadron trigger is one of the main contributor to the Level-0 LHCb trigger and is crucial to study hadronic decays of B which cover an important part of the LHCb physics program. For example, the measurement of the γ angle of the Unitarity Triangle can be performed from studies of $B \to DK$ decays [93] which rely on the hadron trigger to detect them. Photon and electron triggers are also very important for the study of radiative decays like $B^0 \to K^{*0}\gamma$ or $B_s^0 \to \phi\gamma$ and for the study of the $B^0 \to K^{*0}e^+e^-$ decays.

The operation of the L0 Calorimeter trigger was succesful for the recording of the first data at LHCb. Precise studies of the L0 Calorimeter performances (efficiencies and biases) are ongoing in order to improve it in the future.

Table 2.8 – *Total latency of the calorimeter trigger*

Step	Time (ns)
Electron, photon, local and global π^0	
Particle time of flight from interaction point	44
ECAL PMT response	30
Signal propagation to Front-End board	65
Processing in ECAL Front-End board	552
Processing in TVB	518
Signal propagation to Selection Board	505
Processing in Selection Board	475
Signal propagation to L0DU	71
Processing in L0DU	485
Signal propagation to ODIN board	15
Processing in ODIN board	735
Signal propagation to Front-End boards	505
Total	**4000**
Hadron	
Particle time of flight from interaction point	47
HCAL PMT response	30
Signal propagation to Front-End board	81
Processing in HCAL Front-End board	552
Signal propagation to TVB	78
Processing in TVB	368
Signal propagation to Selection Board	505
Processing in Selection Board	525
Signal propagation to L0DU	71
Processing in L0DU	485
Signal propagation to ODIN board	15
Processing in ODIN board	735
Signal propagation to Front-End boards	505
Total	**3997**
SPD Multiplicity	
Particle time of flight from interaction point	43
Shifting fibers	6
Propagation of signal to PMT	18
SPD PMT response	5
Very Front-End processing	50
Signal propagation to Front-End board	130
Processing in PS Front-End board	493
Processing in SPD Control Board	143
Signal propagation to Selection Board	540
Processing in Selection Board	200
Signal propagation to L0DU	71
Processing in L0DU	485
Signal propagation to ODIN board	15
Processing in ODIN board	735
Signal propagation to Front-End boards	505
Total	**3439**

CHAPTER 3

Measurement of J/ψ production at LHCb

This chapter presents an analysis of J/ψ production in proton-proton (pp) collisions at a centre-of-mass energy of $\sqrt{s} = 7\,\text{TeV}$ with the LHCb detector. This analysis was performed by several people forming the "quarkonium analysis working group" that I was coordinating at that time [94] and the preparation of the analysis with simulated data was the subject of the thesis of Wenbin QIAN [95]. The measurement was published in Ref. [10].

The production of J/ψ mesons was studied by several experiments in the past, however the underlying production mechanism is not yet completely understood [96]. In the Colour Singlet Model (CSM), J/ψ production occurs through the Leading Order process $gg \to J/\psi g$, which can be computed using perturbative QCD combined with a non-relativistic model for the heavy quarkonium [97, 98]. However, experiments at the Tevatron have shown that the CSM under-predicts J/ψ production by two orders of magnitude [99, 100]. This is especially true at high p_{T}, where the observed p_{T} dependence ($\propto p_{\text{T}}^{-4}$) differs from the p_{T} dependence expected from the CSM ($\propto p_{\text{T}}^{-8}$).

Several processes can contribute to the J/ψ production in addition to the one considered in the CSM, such as quark and gluon fragmentation [101, 102]. These can better explain the p_{T} shape at high p_{T}, but still fail to saturate the production rates. In the so-called Colour Octet Mechanism (COM) [103–105], the $c\bar{c}$ pair is produced in a coloured state, and hadronizes at long distance into a J/ψ. This process can explain the shape and the magnitude of the measured J/ψ cross-section. However it depends on free parameters (long distance non-perturbative matrix elements) that have large theoretical uncertainties. Parameters extracted from the CDF measurements allow the COM to reproduce correctly their data, but disagree with measurements at ep experiments [106, 107]. A precise prediction of the COM is that the J/ψ is predominantly produced with transverse polarisation at high p_{T}.

However, this is in disagreement with the CDF polarisation measurement [108], which casts doubt on the conclusion that the Colour Octet terms dominate J/ψ production.

Recent theoretical studies have considered the addition of the $gg \to J/\psi c\bar{c}$ process to the CSM [109, 110], or higher order corrections: $gg \to J/\psi gg$ [111] and $gg \to J/\psi ggg$ [112]. With these additions, the discrepancy between theoretical predictions and experimental measurements significantly decreases. However the agreement is still not perfect, leaving open the question of the complete description of J/ψ production. New measurements at the LHC will help to understand further the production properties of J/ψ and the measurements performed in the forward region by the ALICE [113] and LHCb [10] experiments will be complementary to the measurements in the central region by the ATLAS [114] and CMS [115] detectors.

In the comparison between experimental observables and theoretical calculations, three major sources of J/ψ meson production in pp collisions need to be considered:

- direct J/ψ production;
- feed-down J/ψ from the decay of other heavier prompt charmonium states like χ_{c1} or χ_{c2};
- J/ψ from b-hadron decay chains, possibly also from the decay of heavier charmonium intermediate decays.

The first two sources will be called "prompt J/ψ" in the following. The third source will be abbreviated as "J/ψ from b".

This chapter presents the measurement of the differential production cross-section of prompt J/ψ as a function of the J/ψ transverse momentum $p_{\rm T}$ in the range $p_{\rm T} \in [0;14]\,{\rm GeV}/c$ and rapidity y in the range $y \in [2;4.5]$. The fraction of J/ψ from b, $F_{\rm b}$, is also measured with the same $p_{\rm T}$ and y binning.

This will lead to a measurement of the cross-section in the LHCb acceptance $\sigma(\text{prompt } J/\psi,\, p_{\rm T} < 14\ {\rm GeV}/c,\, 2 < y < 4.5)$ and $\sigma(J/\psi \text{ from } b,\, p_{\rm T} < 14\ {\rm GeV}/c,\, 2 < y < 4.5)$. The J/ψ from b cross-section together with the branching fraction $\mathscr{B}(b \to J/\psi X)$ is used to extrapolate to the full angular acceptance with the PYTHIA 6.4 program [12], and to measure the total $b\bar{b}$ cross-section at $\sqrt{s} = 7\,{\rm TeV}$. The analysis fiducial region is chosen to ensure that a sufficiently large number of J/ψ is reconstructed in each bin to be able to separate the prompt J/ψ and J/ψ from b contributions.

3.1 The LHCb detector and dataset

The study reported here uses 5.2 pb^{-1} of pp collision data taken at the Large Hadron Collider (LHC) at a centre-of-mass energy of 7 TeV in September 2010. The data were collected using different trigger configuration keys (TCKs; a TCK uniquely defines the sequence of algorithms, thresholds and cuts used by the trigger):

- 0.66 pb^{-1} with TCK **0x001D0030**;
- 2.98 pb^{-1} with TCK **0x001F0029**;
- 1.56 pb^{-1} with TCK **0x001E0030**.

TCKs 0x001D0030 and 0x001E0030 are identical for what concerns the muon trigger, as only the hadron threshold at the Level0 differs between the two. For TCK 0x001F0029, one of the muon trigger lines was prescaled by a factor of five, while every other condition was identical to the two other TCKs. As a result, the trigger efficiency must be computed for TCKs 0x001F0029 (prescaled) and 0x001D0030. For the data included in this analysis all detector components were fully operational and in a stable condition and the polarity of the magnetic field was negative, i.e., the main component of the dipole field was pointing upwards ($B_y > 0$).

3.1.1 Monte Carlo simulation

The details of the LHCb generation software are given in Chapter 1. With these settings, the differential cross-sections at generator level for prompt J/ψ and J/ψ from b with rapidity $y \in [2,4.5]$ are shown in Fig. 3.1. The prompt J/ψ production cross-section in the acceptance is $21.4\,\mu$b and the cross-section for J/ψ from b is $2.5\,\mu$b.

The simulated samples used for efficiency computations for this analysis were generated with a mean number of interactions per bunch crossing equal to $\nu = 2.5$ to reflect the conditions encoutered during the 2010 LHCb run.

3.1.2 The trigger

The LHCb trigger system is described in Chapter 2. This analysis is based on two L0 lines: the **single muon**, which requires one muon candidate with a p_{T} larger

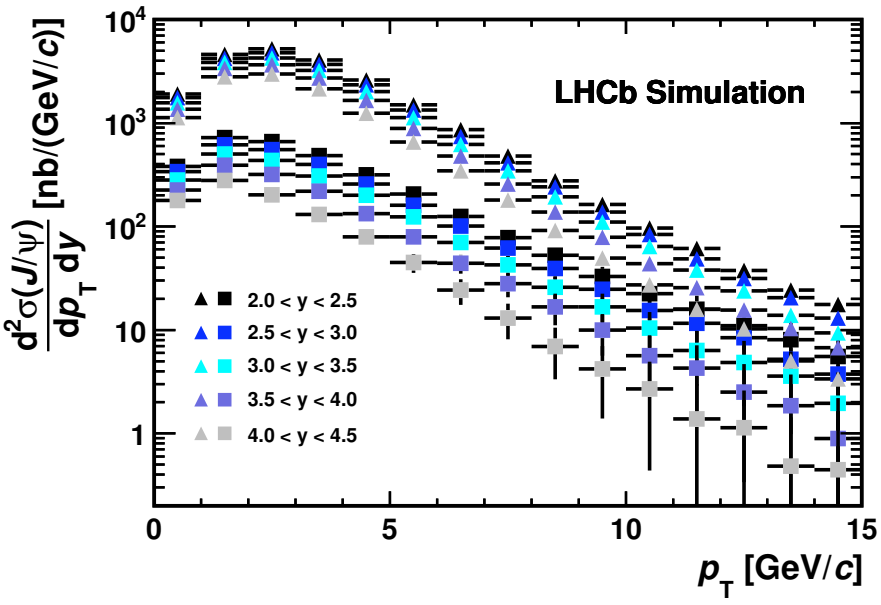

Figure 3.1 – *The (p_T,y) double-differential cross-section for* prompt J/ψ *(triangles) and* J/ψ from *b (squares), as generated in the Monte Carlo.*

than 1.4 GeV/c, and the **di-muon**, which requires two muons with p_T larger than 0.56 GeV/c and 0.48 GeV/c, respectively. They provide the input candidates for the HLT1 lines: the first one (*Hlt1SingleMuonNoIP*) confirms the muon candidate found by the L0 single muon, and applies a harder cut on the muon p_T at 1.8 GeV/c; the second line (*Hlt1DiMuonNoIPL0Di*) confirms the di-muon candidates found by the L0 di-muon line and requires their combined mass to be greater than 2.5 GeV/c^2. It should be noted that only trigger lines with no impact parameter information (*NoIP*) are used in this analysis. At the HLT2 level, events are selected having two muon candidates with an invariant mass greater than 2.9 GeV/c^2. The trigger lines used in the analysis are summarised in Table 3.1. Line *Hlt1SingleMuonNoIP* was prescaled by a factor five in the data taken with TCK 0x001F0029.

To avoid that a few events with a high occupancy in the Vertex Locator (VELO), Outer Tracker (OT), and Inner tracker (IT) dominate the HLT CPU time, a set of global event cuts (GEC) is applied, typically on the detectors' hit multiplicities. These requirements are set for each subdetector that is used by the pattern recognition algorithms, as illustrated in Table 3.2. A cut on the SPD (Scintillating Pad Detector) hit multiplicity at L0 also limits the rate at which the detector is read out. Generally, the cut values are chosen to loose a minimal amount of luminosity while effectively rejecting busy events. The only global event cut that rejects a

Table 3.1 – *Summary of the trigger lines used for this analysis.*

Trigger line	Main cuts
L0SingleMuon	$p_{\mathrm{T}} > 1.4\,\mathrm{GeV}/c$
L0DiMuon	$p_{\mathrm{T},1} > 0.56\,\mathrm{GeV}/c$, $p_{\mathrm{T},2} > 0.48\,\mathrm{GeV}/c$
Hlt1SingleMuonNoIP	*L0SingleMuon* and $p_{\mathrm{T}} > 1.8\,\mathrm{GeV}/c$
Hlt1DiMuonNoIPL0Di	*L0DiMuon* and $M_{\mu\mu} > 2.5\,\mathrm{GeV}/c^2$
Hlt2UnbiasedDiMuon	$M_{\mu\mu} > 2.9\,\mathrm{GeV}/c^2$

significant fraction of the luminosity is the requirement on the number of VELO clusters. This cut was introduced to cope with the high pile-up running conditions encountered during the 2010 running period of the LHC while only one fifth of the Event Filter Farm was installed. A discussion of the trigger configuration and performance for the 2010 run can be found in [116].

3.1.3 Muon identification and tracking

The muon identification algorithm [117] is based on the following: given a reconstructed track in the LHCb tracking system, hits in the muon stations are searched around the track extrapolation in some Field of Interest (FOI). A boolean decision (IsMuon) is applied to tracks that satisfy the requirement to have at least one hit in the FOI in a number of stations that depends on the momentum of the track. The stations required by the IsMuon decision are shown in Table 3.3 as a function of

Table 3.2 – *Summary of global event cuts (GEC).*

Trigger level	GEC	Value
L0	# SPD hits	< 900
HLT1	# Velo clusters	< 3000
HLT1	# IT clusters	< 3000
HLT1	# OT clusters	< 10000
HLT2	# Velo tracks	< 350

Table 3.3 – *Muon stations required to trigger the IsMuon decision as a function of momentum range.*

Momentum range	Muon stations
$3\,\text{GeV}/c < p < 6\,\text{GeV}/c$	M2+M3
$6\,\text{GeV}/c < p < 10\,\text{GeV}/c$	M2+M3+(M4 or M5)
$p > 10\,\text{GeV}/c$	M2+M3+M4+M5

the track momentum.

3.2 J/ψ selection

J/ψ candidates are formed from pairs of opposite sign tracks reconstructed in the full tracking system (long tracks). Both tracks must have a transverse momentum p_{T} above $700\,\text{MeV}/c$, be identified as muons and have a good quality of the track fit ($\chi^2/\text{ndof} < 4$). The two muons are required to originate from a common vertex, and only candidates with a χ^2 probability of the vertex fit larger than 0.5% are kept. The event is required to have at least one reconstructed primary vertex since the information about the primary vertex position will be used to distinguish between prompt J/ψ and J/ψ from b. Primary vertices are reconstructed with an iterative method and formed with at least 5 tracks reconstructed in the VELO.

To suppress clones, i.e. cases where the reconstruction has created duplicate tracks from one particle, when an event has more than one J/ψ candidate, for each pair $J/\psi_1 \to \mu_1^+\mu_1^-$ and $J/\psi_2 \to \mu_2^+\mu_2^-$, one of the J/ψ candidates is randomly rejected if $\cos\theta(\mu_1^+,\mu_2^+) > 0.9999$ and $\cos\theta(\mu_1^-,\mu_2^-) > 0.9999$. In all other cases, all J/ψ candidates are retained.

The final selection criteria are listed in Table 3.4. Figure 3.2 shows the mass distribution of all reconstructed J/ψ candidates having a transverse momentum $p_{\text{T}} \in [0;14]\,\text{GeV}/c$ and a rapidity $y \in [2;4.5]$, where $y = \frac{1}{2}\ln\frac{E+p_z}{E-p_z}$ and E and p_z are the J/ψ energy and momentum in the z direction, respectively; the z axis is defined along the beam axis in the LHCb frame, and is oriented from the VELO to the Muon detector.

Table 3.4 – *$J/\psi \to \mu^+\mu^-$ selection criteria*

Quantity	Requirement
μ: track	Long track with MUON hits (IsMuon)
μ: p_{T}	$> 700\,\mathrm{MeV}/c$
μ: track quality χ^2/ndof	< 4
J/ψ: Mass Window	$\pm 150\,\mathrm{MeV}/c^2$
J/ψ: Vertex $p(\chi^2)$	$> 0.5\%$
J/ψ: L0 Trigger On Signal	*L0SingleMuon* or *L0DiMuon*
J/ψ: HLT1 Trigger On Signal	*Hlt1SingleMuonNoIP* or *Hlt1DiMuonNoIPL0Di*
Event: Number of primary vertices	> 0

3.2.1 Distinction between prompt J/ψ and J/ψ from b

J/ψ from b tend to be produced away from the primary vertex and are separated from prompt J/ψ, which are produced at the primary vertex, by exploiting the J/ψ pseudo-propertime defined as:

$$t_z = \frac{(z_{J/\psi} - z_{\mathrm{PV}}) \times M_{J/\psi}}{p_z}\,, \tag{3.1}$$

where $z_{J/\psi}$ and z_{PV} are the positions along the z-axis of the J/ψ decay vertex and of the primary vertex from which it originates. This variable was found to give a good approximation of the b-hadron decay proper time [95]: given that b-hadrons are not fully reconstructed, the J/ψ momentum is used instead of the exact b-hadron momentum. For events with several primary vertices, the one which is closest to the J/ψ vertex in the z direction is selected; p_z is the measured J/ψ momentum in the z direction and $M_{J/\psi}$ the nominal J/ψ mass. The primary vertex used in the analysis, is not refitted removing the two tracks from the reconstructed J/ψ. The bias induced by this procedure was found to be negligible.

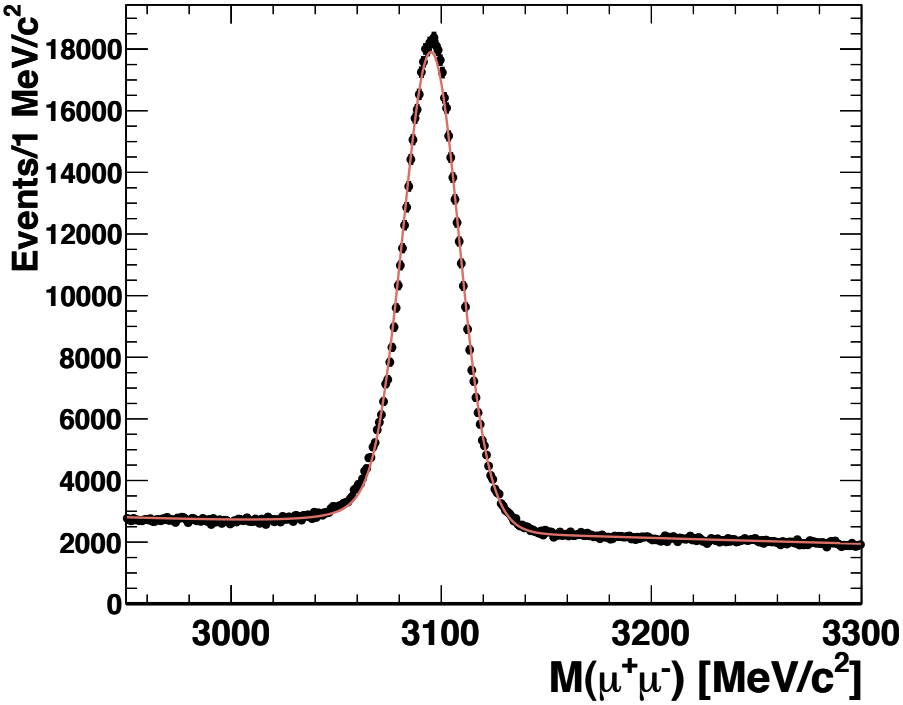

Figure 3.2 – *Invariant mass distribution for J/ψ candidates with $p_T \in [0;14]$ GeV/c and $y \in [2;4.5]$. The total number of signal events (calculated using the procedure described in Section 3.3.1) is* $564\,603 \pm 924$.

3.3 Cross-section determination

The differential cross-section σ for prompt J/ψ production in a given (p_T,y) bin is defined as:

$$\frac{d^2\sigma}{dy\,dp_T} = \frac{N(J/\psi \to \mu^+\mu^-)}{\mathscr{L} \times \varepsilon_{tot} \times \mathscr{B}(J/\psi \to \mu^+\mu^-) \times \Delta y \times \Delta p_T}, \tag{3.2}$$

where $N(J/\psi \to \mu^+\mu^-)$ is the number of observed prompt $J/\psi \to \mu^+\mu^-$ in bin (p_T,y), ε_{tot} is the J/ψ detection efficiency including acceptance effects in bin (p_T,y), $\mathscr{L}$ the integrated luminosity, $\mathscr{B}(J/\psi \to \mu^+\mu^-)$ the branching fraction of the $J/\psi \to \mu^+\mu^-$ decay ($(5.94 \pm 0.06) \times 10^{-2}$ [19]) and $\Delta y = 0.5$ and $\Delta p_T = 1$ GeV/c are the rapidity and p_T bin sizes, respectively.

The number of signal J/ψ candidates in the data sample, without separating prompt J/ψ and J/ψ from b, is estimated from fits to the invariant mass distribution. The fits are performed independently in 14 p_T bins between 0 and 14 GeV/c,

and 5 rapidity bins in the range $y \in [2;4.5]$. The fraction of J/ψ from b is extracted from a fit to the t_z distribution in each bin. From the knowledge of the efficiencies and of the total integrated luminosity, the differential cross-section $\frac{d^2\sigma}{dy dp_T}$ is then derived.

3.3.1 Fit to the number of J/ψ

The total number of J/ψ is determined from an extended unbinned maximum likelihood fit to the mass of the reconstructed J/ψ candidates in the interval $M_{\mu\mu} \in [2.95;3.30]\,\text{GeV}/c^2$. The mass distribution is described by a Crystal Ball function for the signal and an exponential function ($f_{\text{Bk}}(M_{J/\psi}) = a_0 e^{-p_0 M_{J/\psi}}$) for the combinatorial background. The Crystal Ball function is defined as [118, 119]

$$f_{\text{CB}}(x;M,\sigma,a,n) = \begin{cases} \dfrac{\left(\frac{n}{|a|}\right)^n e^{-\frac{1}{2}a^2}}{\left(\frac{n}{|a|} - |a| - \frac{x-M}{\sigma}\right)^n} & \dfrac{x-M}{\sigma} < -|a| \\ \exp\left(-\dfrac{1}{2}\left(\dfrac{x-M}{\sigma}\right)^2\right) & \dfrac{x-M}{\sigma} > -|a|. \end{cases} \tag{3.3}$$

The shape of the Crystal Ball function allows to describe the tail that can be seen on the left of the J/ψ mass peak and that is due to energy lost because of radiated photons. The parameters a and n of the function describe this radiative tail.

Due to large correlations between these parameters, their values are fixed using the simulation as follows. The true di-muon mass obtained from an inclusive J/ψ Monte Carlo sample is smeared with a Gaussian with a σ between $7\,\text{MeV}/c^2$ and $30\,\text{MeV}/c^2$. The resulting mass distributions are then fitted with the Crystal Ball function, fixing the σ parameter of the function to the value used when smearing the initial distribution, but leaving all other parameters free. Figure 3.3 shows the variation of a and n as a function of the mass resolution σ. From these curves, a and n are parametrised as a function of σ,

$$a = 2.22 + 0.004\sigma - 0.001\sigma^2, \tag{3.4}$$

$$n = 1.04 - 0.041\sigma + 0.002\sigma^2. \tag{3.5}$$

This parametrisation is then used to perform the mass fits on data.

The mass fit function

$$\begin{aligned} F_{\text{mass}}(M_{J/\psi};M,\sigma,f_{J/\psi},p_0,a_0) = f_{J/\psi} f_{\text{CB}}(M_{J/\psi};M,\sigma) + \\ (1-f_{J/\psi}) f_{\text{Bk}}(M_{J/\psi};p_0,a_0) \end{aligned} \tag{3.6}$$

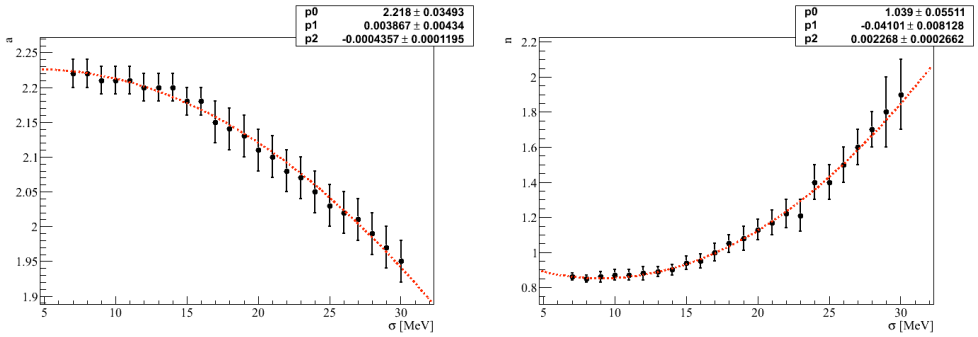

Figure 3.3 – *Variation of the parameters a (left) and n (right) of the Crystal Ball function of Eq. 3.3 as a function of the resolution σ used to smear the Monte Carlo generated J/ψ invariant mass distribution.*

has in total five free parameters:

- M, the mean value, and σ of the Crystal Ball function describing the J/ψ signal;
- p_0, the slope, and a_0, the value at the origin of the exponential describing the background;
- $f_{J/\psi}$, the signal fraction.

The fit to the invariant mass distribution is performed independently for each of the 14×5 bins in p_{T} and y. The mass distribution together with the fit results for bin ($3 < p_{\mathrm{T}} < 4\,\mathrm{GeV}/c$, $2.5 < y < 3.0$) is shown in Fig. 3.7 (*left*). Figure 3.4 shows the variation of the Crystal Ball parameters describing the signal J/ψ as a function of p_{T} and y. The deviation from the nominal J/ψ mass is due to the not yet optimal calibration of the magnetic field and alignment of the spectrometer. The fit to the mass distribution shown in Figure 3.2 is obtained by summing the individual mass fits for the 14×5 bins. The selection yields a signal candidate sample of $564\,603 \pm 924$ J/ψ mesons, where the error is statistical.

3.3.2 Determination of the fraction of J/ψ from b

The fraction of J/ψ from b, F_{b}, is determined from a simultaneous fit to the pseudo-propertime t_z and the $\mu^+\mu^-$ invariant mass. The signal propertime distribution is described by a delta function at $t_z = 0$ for the prompt J/ψ, an exponential

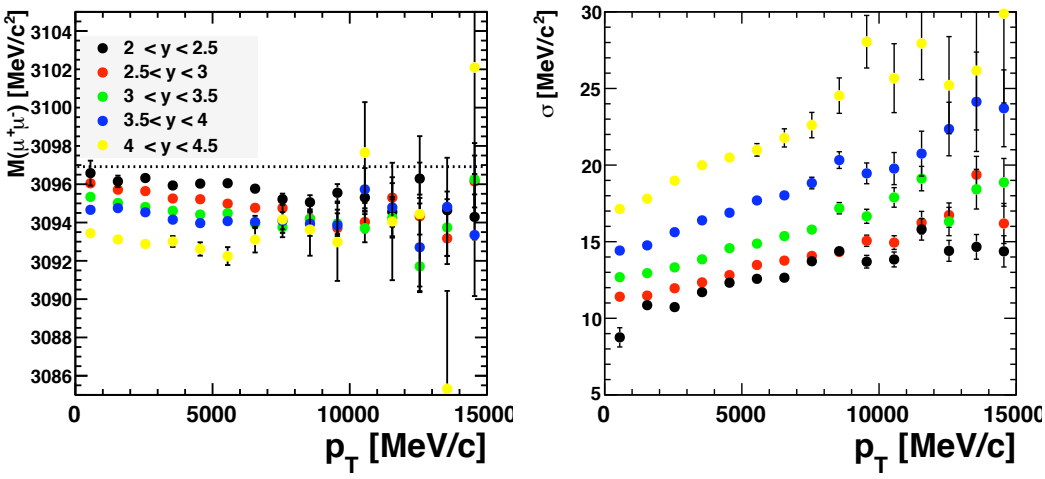

Figure 3.4 – *Mean values M (left) and σ (right) of the Crystall Ball function of Eq. 3.3 describing the J/ψ mass distribution as a function of p_{T} in bins of y.*

decay function for the J/ψ from b component and a long tail arising from the association of the J/ψ vertex to a wrong primary vertex. There are two reasons for the wrong association:

1. the primary vertex from which the J/ψ originates is not found; this is because not enough tracks originating from the vertex are reconstructed and the J/ψ is wrongly associated with another primary vertex;

2. the wrong primary vertex is chosen among several reconstructed primary vertices close to each other.

In the second case, the positions of the reconstructed and unreconstructed primary vertices are correlated. This category of events is distributed around $t_z = 0$ for the prompt component, with a width larger than the t_z distribution for correctly reconstructed primary vertices. The contribution of these events to the t_z distribution is included in the resolution function.

The long tail is predominantly composed of events in the first category and since the tail distribution affects the measurement of the J/ψ from b component, a method has been developed to extract it from data [95]. The method consists in associating a J/ψ from a given event to the primary vertex of the next event in the J/ψ sample. The position of the primary vertex of the next event simulates the position of an uncorrelated primary vertex to which the J/ψ is associated. The

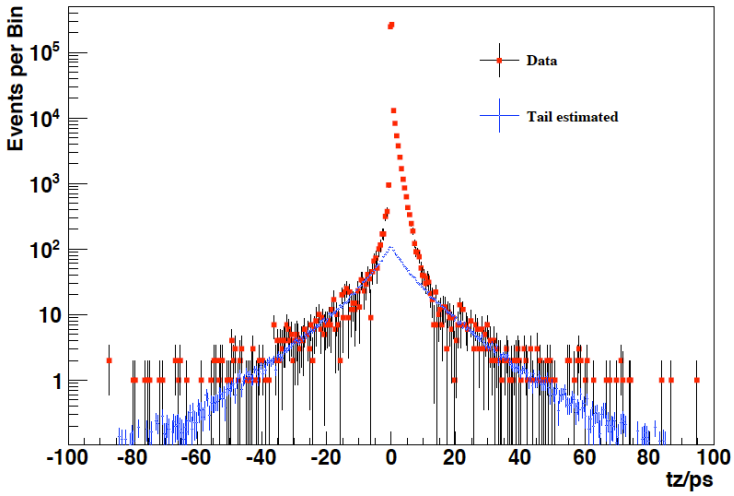

Figure 3.5 – *Signal t_z distribution (red), obtained by subtracting the t_z distribution measured from the J/ψ sidebands defined as $M_{\mu\mu} \in [2.95;3.00] \cup [3.25;3.30]\,\mathrm{GeV}/c^2$ and tail t_z distribution (blue) obtained from the "next event" mehod.*

shape of the tail contribution to the signal t_z distribution is then obtained from the distribution of:

$$t_z^{\mathrm{next}} = \frac{\left(z_{J/\psi} - z_{\mathrm{PV}}^{\mathrm{next}}\right) \times M_{J/\psi}}{p_z}, \tag{3.7}$$

where z_{PV}^{next} is the coordinate of the primary vertex of the next event along the z-axis.

Figure 3.5 shows the signal t_z distribution for the full sample after sideband subtraction together with the tail distribution obtained with the method described above. The agreement between the shape of the signal tail and the shape obtained with this method is good. The method also allows us to measure the fraction of events for which the primary vertex of the J/ψ is correctly reconstructed (99.4%). The primary vertex reconstruction efficiency is assumed to be equal for prompt J/ψ and J/ψ from b. Given the very high primary vertex reconstruction efficiency, the uncertainty related to this assumption is neglected.

The function describing the t_z distribution for the signal is therefore

$$f_{\mathrm{signal}}(t_z; f_{\mathrm{p}}, f_{\mathrm{b}}, \tau_{\mathrm{b}}) = f_{\mathrm{p}}\delta(t_z) + f_{\mathrm{b}}\frac{e^{-t_z/\tau_{\mathrm{b}}}}{\tau_{\mathrm{b}}} + (1 - f_{\mathrm{b}} - f_{\mathrm{p}})h_{\mathrm{tail}}(t_z)\,, \tag{3.8}$$

where f_{p} is the fraction of prompt J/ψ candidates for which the primary vertex is correctly reconstructed, f_{b} the fraction of J/ψ from b for which the primary vertex is correctly reconstructed, and τ_{b} the b-hadron pseudo-lifetime; $h_{\mathrm{tail}}(t_z)$ is the

probability density function (histogram) obtained from the "next event" method. It is assumed that the fraction of J/ψ from b in the tail events is equal to the fraction measured with the events for which the primary vertex is correctly reconstructed. The choice of the fit function has been validated by a Monte Carlo simulation in which the fit to the true t_z distribution of J/ψ from b with an exponential gives a slope of $\tau_b^{MC} = 1.41 \pm 0.03$ ps [95]. The overall fraction of J/ψ from b is defined as

$$F_b = \frac{f_b}{f_p + f_b} \tag{3.9}$$

The signal function, minus the tail function h_{tail}, is convolved with a resolution function, which is the sum of two Gaussian functions

$$f_{resolution}(t_z;\mu,S_1,S_2,\beta) = \frac{\beta}{\sqrt{2\pi}S_1\sigma} e^{-\frac{(t_z-\mu)^2}{2S_1^2\sigma^2}} + \frac{1-\beta}{\sqrt{2\pi}S_2\sigma} e^{-\frac{(t_z-\mu)^2}{2S_2^2\sigma^2}}, \tag{3.10}$$

where σ is the event-by-event t_z error, S_1 and S_2 two scale factors applied to the event-by-event error, μ the bias of the t_z measurement and β the fraction of the Gaussian with the smallest scale factor. For bins with low statistics, only one Gaussian is used for the resolution function.

The background contribution to the t_z distribution is parametrised with an empirical function, which is the sum of a delta function and five exponentials (three for positive t_z and two for negative t_z, the negative and positive exponentials with the largest lifetimes have their lifetimes fixed to the same value τ_4), convolved with the sum of two Gaussian functions

$$f_{background}(t_z) = \left[(1-f_1-f_2-f_3-f_4)\delta(t_z) + \theta(t_z)\left(f_1\frac{e^{-t_z/\tau_1}}{\tau_1} + f_2\frac{e^{-t_z/\tau_2}}{\tau_2}\right) + \theta(-t_z)\left(f_3\frac{e^{t_z/\tau_3}}{\tau_3}\right) + f_4\frac{e^{-|t_z|/\tau_4}}{2\tau_4}\right] \otimes \left(\frac{\beta'}{\sqrt{2\pi}\sigma_1} e^{-\frac{t_z^2}{2\sigma_1^2}} + \frac{1-\beta'}{\sqrt{2\pi}\sigma_2} e^{-\frac{t_z^2}{2\sigma_2^2}}\right), \tag{3.11}$$

where $\theta(t_z)$ is the step function.

The choice of the background function is motivated by the shape of the t_z distribution seen in the J/ψ mass sidebands and is similar to the function used by CDF for the J/ψ cross-section measurement [42]. The positive tail of the background t_z distribution mostly consists of random combinations of muons from semi-leptonic b and c decays. Misreconstructed tracks from decays in flight of kaons and pions contribute both to the positive and the negative background t_z tails. For bins with low statistics, the number of exponentials is reduced.

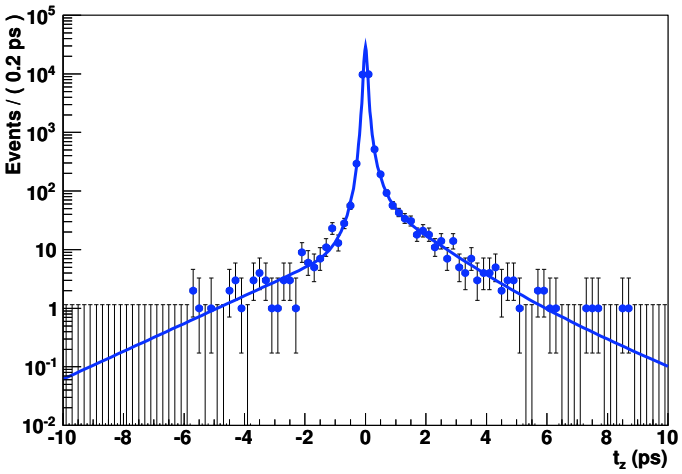

Figure 3.6 – *t_z background function for bin ($3 < p_T < 4$ GeV/c, $2.5 < y < 3$).*

The parameters of the background function are obtained from a fit to the t_z distribution of the J/ψ mass sidebands defined as

$$M_{\mu\mu} \in [2.95;3.00] \cup [3.25;3.30]\,\text{GeV}/c^2. \tag{3.12}$$

Upper and lower sidebands do not show exactly the same t_z distributions because of the different p_z spectra in the different regions. Taking equal intervals of upper and lower sidebands, this effect becomes negligible.

The parameters of the background function are fixed for the final fit. The errors on the background function parameters are propagated to the errors on the parameters of the final fit with toy Monte Carlo techniques. Figure 3.6 shows the background function used for the bin $3 < p_T < 4$ GeV/c and $2.5 < y < 3$.

The total function used for the t_z fit is therefore

$$\begin{aligned} F_{\text{pseudo-propertime}}(t_z; f_p, f_b, f_{J/\psi}, \mu, S_1, S_2, \beta, \tau_b) = \\ f_{J/\psi}\Bigg[\left(f_p\delta(t_z) + f_b\frac{e^{-t_z/\tau_b}}{\tau_b}\right) \otimes f_{\text{resolution}}(t_z;\mu,S_1,S_2,\beta) + \\ (1-f_b-f_p)f_{\text{tail}}(t_z)\Bigg] + (1-f_{J/\psi})f_{\text{background}}(t_z)\,. \end{aligned} \tag{3.13}$$

The function used for the description of the invariant mass distribution is given in Section 3.3.1. The total fit function is the sum of the products of the mass and t_z fit functions defined in Eqs. (3.6) and (3.13) for the signal and background.

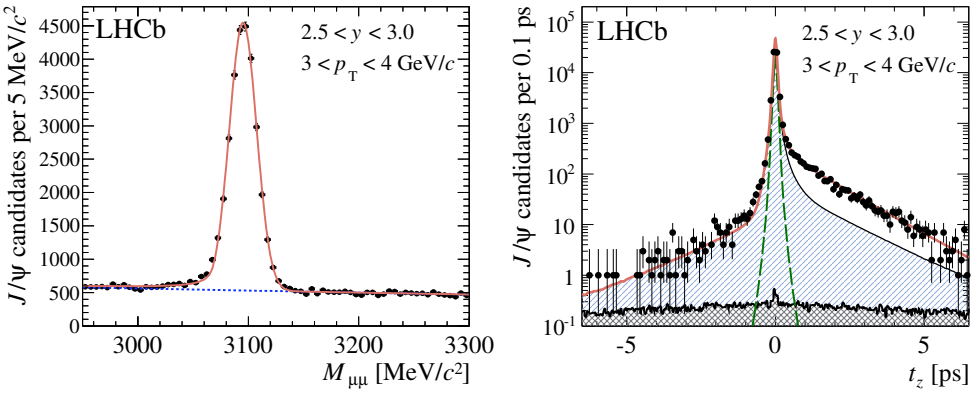

Figure 3.7 – *Dimuon mass distribution (*left*) and t_z distribution (*right*), with fit results superimposed, for one bin ($3 < p_{\rm T} < 4\,{\rm GeV}/c$, $2.5 < y < 3.0$). On the mass distribution, the* solid red line *is the total fit function, where the signal is described by a Crystal Ball function, and the* dashed blue line *represents the exponential background function. On the t_z distribution, the* solid red line *is the total fit function described in the text, the* green dashed line *is the* prompt J/ψ *contribution, the* single-hatched area *is the background component and the* cross-hatched area *is the tail contribution.*

The part of the fit function related to the description of the t_z observable has in total seven free parameters:

- $f_{\rm p}$ and $f_{\rm b}$, the fractions of prompt J/ψ and J/ψ from b events, respectively;
- μ, S_1, S_2 and β, the common mean, the error scale factors and the fraction of the two Gaussians for the resolution;
- $\tau_{\rm b}$, the b pseudo-lifetime.

Figure 3.7 (*right*) represents the t_z distribution for bin ($3 < p_{\rm T} < 4\,{\rm GeV}/c$, $2.5 < y < 3$) with the fit result superimposed. To access the quality of the fit, a χ^2 is calculated for the fit function using a binned event distribution. The resulting fit probability for the histogram of Fig. 3.7 (*right*) is equal to 87% and similar good fits are seen for the other bins.

Figures 3.8 show the values of the t_z fit function main parameters (μ, mean error scale factor S and $\tau_{\rm b}$) as a function of the $(p_{\rm T}, y)$ bin. The variations of the parameters between $p_{\rm T}$ and rapidity bins are found to be small and to lie within a reasonable range. The variation of the values of τ_b as a function of $p_{\rm T}$ is explained by the fact that this quantity is only an approximation of the b lifetime, and the deviation between the true b lifetime and τ_b is more pronounced at large $p_{\rm T}$.

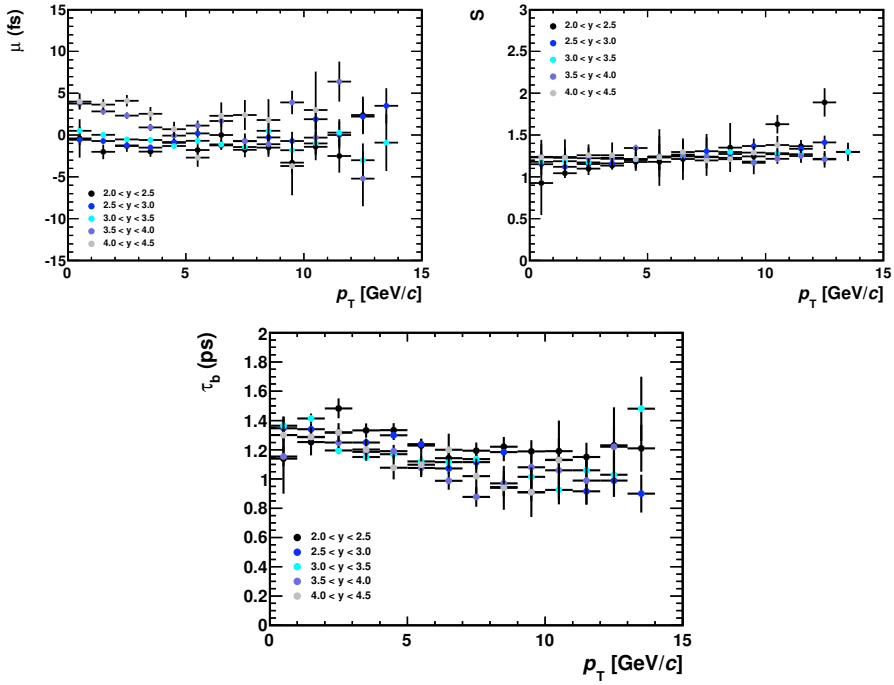

Figure 3.8 – *Parameters of the t_z fit function of Eq. (3.13) as a function of the (p_T, y) bin: μ (top left), mean error scale factor S (top right) and τ_b (bottom).*

3.3.3 Luminosity

The luminosity was measured at specific periods during the data taking using both Van der Meer scans and the 'beam-profile' method [120]. Two Van der Meer scans were performed in a single fill. Analysis of these scans yielded consistent results for the absolute luminosity scale with a precision of around 10%, dominated by uncertainty in the knowledge of the beam currents. In the second approach, six separate periods of stable running were chosen, and the beam-profiles measured using beam-gas and beam-beam interactions. Using these results, correcting for crossing angle effects, and knowing the beam currents, it was possible to determine the luminosity in each period following the analysis procedure described in Ref. [52]. Consistent results were found for the absolute luminosity scale in each period, with a precision of 10%, also dominated by the beam current uncertainty. These results are in good agreement with those of the Van der Meer analysis. Note that the error on the luminosity was later reduced to 3.5% instead of the preliminary 10% uncertainty used for this measurement.

The knowledge of the absolute luminosity scale was used to calibrate the number of tracks in the VELO, which during data taking was sampled randomly at a

rate of 1 kHz, and is known to be a stable quantity throughout the data-taking period. The integrated luminosity of the runs considered in this analysis was determined to be 5.2 ± 0.5 pb^{-1}.

3.3.4 Efficiency calculation

A sample of fully simulated inclusive J/ψ is used to estimate the total efficiency ε_{tot} in each bin of p_{T} and rapidity. The total efficiency includes the geometrical acceptance ε_{acc}, the detection, reconstruction and selection efficiency combined in an efficiency term ε_{rec} and the trigger efficiency ε_{tri}

$$\varepsilon_{\text{tot}} = \varepsilon_{\text{acc}} \times \varepsilon_{\text{rec}} \times \varepsilon_{\text{tri}}. \tag{3.14}$$

The first efficiency term is the generator-level acceptance defined as

$$\varepsilon_{\text{acc}} = \frac{J/\psi \text{ in bin } (p_{\text{T}},y) \text{ with both } \mu \text{ in LHCb}}{J/\psi \text{ generated in bin } (p_{\text{T}},y)}. \tag{3.15}$$

It is estimated with a Monte Carlo sample generated with the J/ψ momentum direction in the forward region ($z > 0$). In Eq. 3.15, both μ in LHCb means that the polar angle of the momentum direction of each μ is required to be in $[10,400]$ mrad before the magnet. This is a little larger than the actual LHCb detector acceptance ($[15,300]$ mrad) to avoid the loss of events due to the magnetic field, for example. It has been checked with a Monte Carlo simulation that the acceptance for prompt J/ψ and J/ψ from b are the same within statistical errors, as illustrated in Fig. 3.9.

The second term of the efficiency ε_{rec} combines the J/ψ detection, reconstruction and selection efficiency. It is defined as

$$\varepsilon_{\text{rec}} = \frac{J/\psi \text{ detected, reconstructed and selected in bin } (p_{\text{T}},y)}{J/\psi \text{ in bin } (p_{\text{T}},y) \text{ with both } \mu \text{ in LHCb}} \tag{3.16}$$

The reconstruction efficiencies for prompt J/ψ and J/ψ from b are equal within statistical errors in each (p_{T},y) bin, as illustrated in Fig. 3.10. The reconstruction efficiency computed from the Monte Carlo simulation also includes the efficiency to match a reconstructed J/ψ to a true generated $J/\psi \to \mu\mu$. This term should not be included when correcting the data for the reconstruction efficiency. However, given that the matching efficiency is measured to be 99.9%, this effect is neglected.

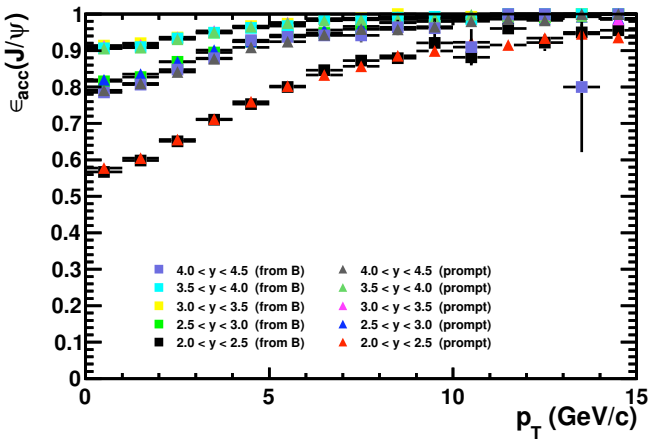

Figure 3.9 – *Monte Carlo-based acceptance* ε_{acc} *for* prompt J/ψ *and* J/ψ from b *as a function of* p_{T} *in bins of* y.

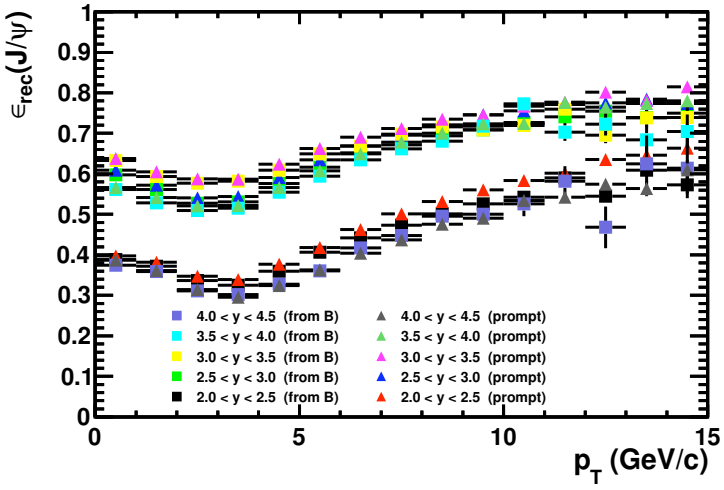

Figure 3.10 – *Monte Carlo-based reconstruction efficiency* ε_{rec} *for* prompt J/ψ *and* J/ψ from b *as a function of* p_{T} *in bins of* y.

One can observe that the reconstruction efficiencies decrease in the rapidity bins close to the edges of the fiducial region. The drop of efficiency seen at $p_{\text{T}}(J/\psi)$ close to $3.5\,\text{GeV}/c^2$ is a kinematic effect caused by the p_{T} cut on the two muons.

The third term is the L0xHLT1xHLT2 trigger efficiency ε_{tri}. It is defined as

$$\varepsilon_{\text{tri}} = \frac{J/\psi \text{ selected and TOS of L0xHLT1xHLT2 in bin } (p_{\text{T}},y)}{J/\psi \text{ selected in bin } (p_{\text{T}},y)}. \tag{3.17}$$

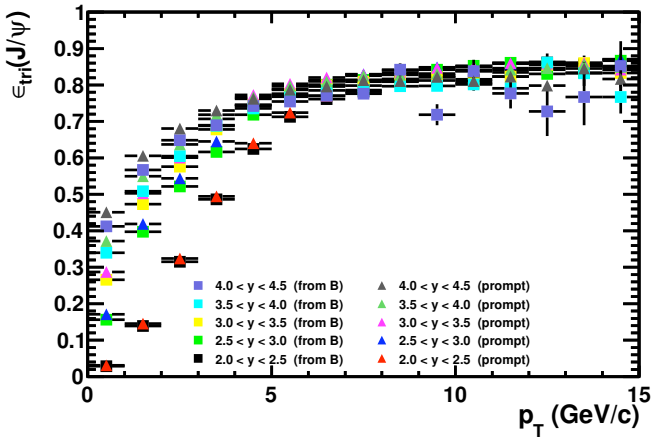

Figure 3.11 – *Monte Carlo-based trigger efficiency* ε_{tri} *for TCK 0x001D0030 for* prompt J/ψ *and* J/ψ from b *as a function of* p_{T} *in bins of y. Identical efficiencies are obtained for TCK 0x001E0030.*

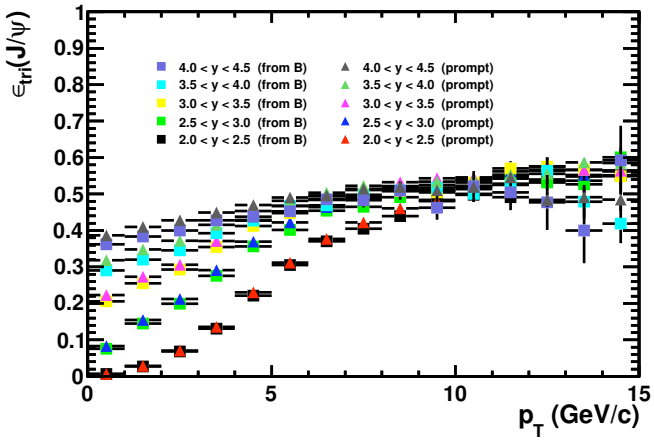

Figure 3.12 – *Monte Carlo-based trigger efficiency* ε_{tri} *for TCK 0x001F0029 for* prompt J/ψ *and* J/ψ from b *as a function of* p_{T} *in bins of y.*

The L0xHLT1xHLT2 trigger efficiency is equal for prompt J/ψ and J/ψ from b, as illustrated in Figs. 3.11 and 3.12 for the different trigger conditions, because of the TOS requirement on the J/ψ daughters (TOS or Trigger On Signal: one of the muons or both muons from the J/ψ candidate are associated with a L0 muon online candidate, which has sufficiently large transverse momentum to pass the trigger) and because the trigger does not make use of impact parameter information. The efficiency for TCK 0x001F0029 saturates at 50% because of the prescaling of the single muon line, which is the most efficient one.

Finally, the total efficiency (ε_{tot}) for the two TCKs is displayed in Figs. 3.13 and 3.14, averaged over prompt J/ψ and J/ψ from b, since all efficiencies are very similar for the two categories.

The total efficiency used to calculate the cross-sections is computed as

$$\varepsilon_{\text{tot}} = \frac{\mathscr{L}_1}{\mathscr{L}}\varepsilon_{\text{tot},1} + \frac{\mathscr{L}_2}{\mathscr{L}}\varepsilon_{\text{tot},2}\,, \tag{3.18}$$

where $\mathscr{L}_{1,2}$ and $\varepsilon_{\text{tot},1,2}$ are the integrated luminosities and total efficiencies for the two samples taken with TCKs 0x001D0030 plus 0x001E0030, and 0x001F0029, respectively.

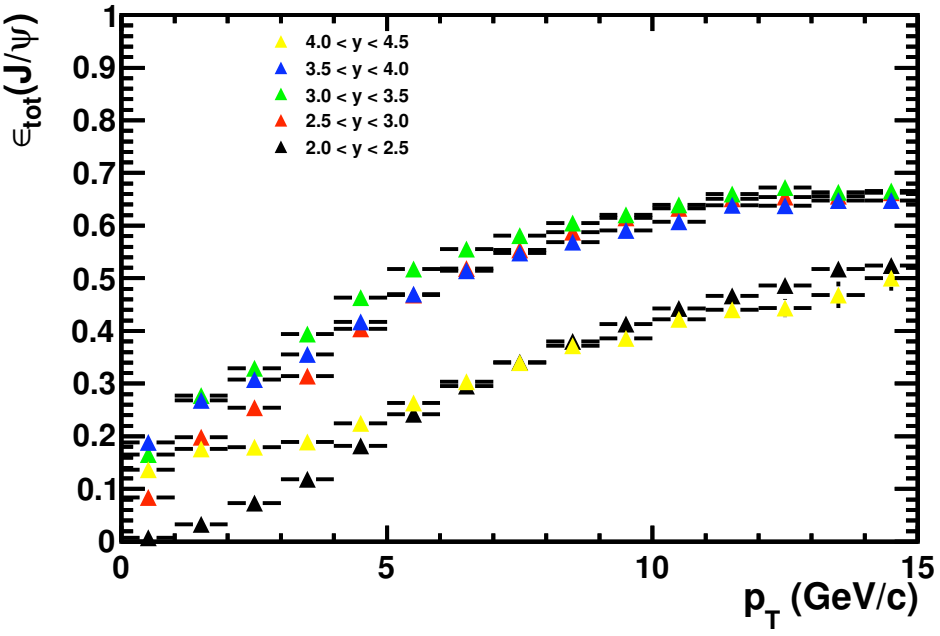

Figure 3.13 – *Monte Carlo-based total efficiency ε_{tot} for TCK 0x001D0030 as a function of p_{T} in bins of y. Identical efficiencies are obtained for TCK 0x001E0030.*

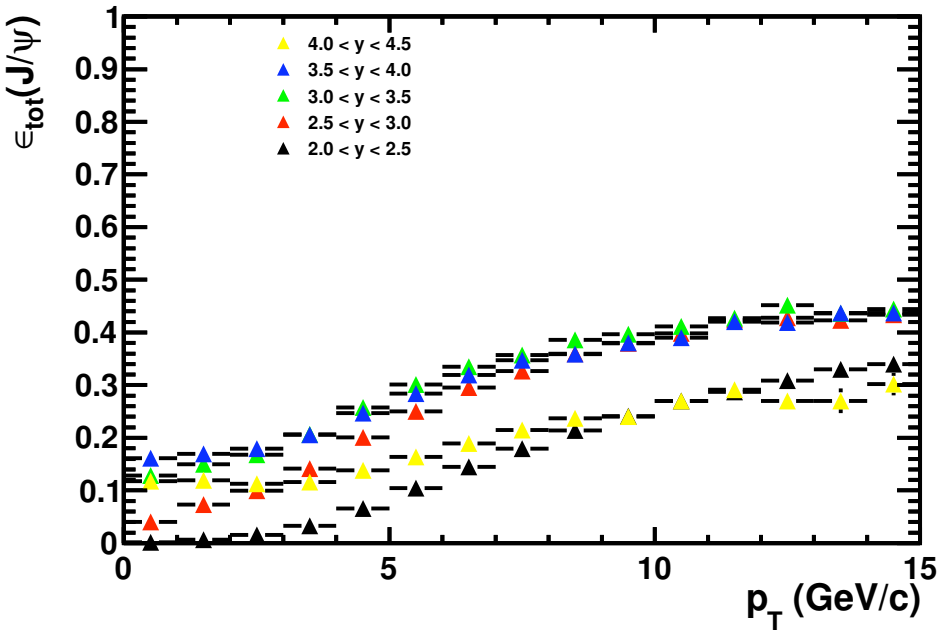

Figure 3.14 – *Monte Carlo-based total efficiency* ε_{tot} *for TCK 0x001F0029 as a function of* p_{T} *in bins of y.*

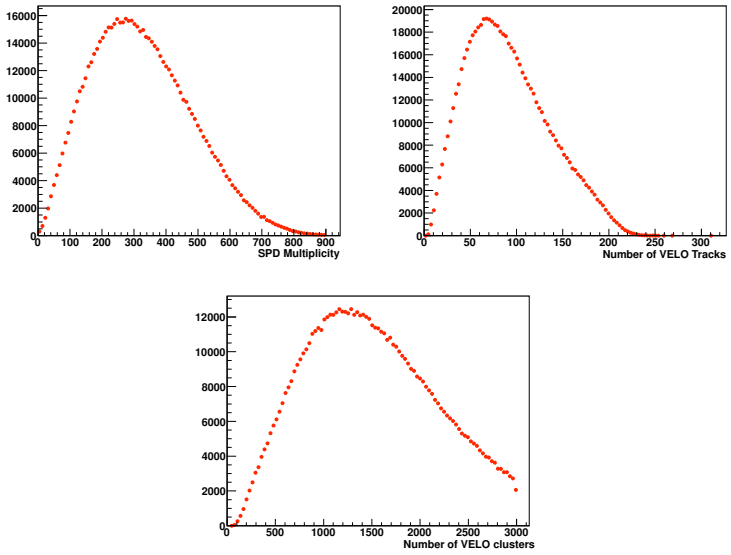

Figure 3.15 – *Distributions of quantities on which Global Event Cuts are applied for events containing a J/ψ candidate.*

3.3.5 Global event cuts

The GEC given in Table 3.2 were applied during data taking to remove high multiplicity events. Their effect on events containing a J/ψ candidate was evaluated by using an independent (prescaled) trigger, the so-called "MicroBias" trigger, which accepts events having at least one track reconstructed in either the VELO or the tracking stations, and is not subject to GEC (but is rate limited). The only GEC that is discussed here in detail is the requirement on the number of VELO clusters. The other GEC were also studied, but their effect was found to be negligible, as illustrated in Fig. 3.15 (*left* and *centre*) for the SPD multiplicity and number of VELO tracks, respectively. By comparing the number of MicroBias-triggered signal J/ψ candidates before and after applying the requirement on the number of VELO clusters, it was found that the cut has an efficiency of $(93 \pm 2)\%$. In the Monte Carlo simulation, the efficiency of the cut on the number of VELO clusters is measured to be $(96.8 \pm 0.1)\%$. Therefore, the Monte Carlo-based trigger efficiencies ε_{tri} are multiplied by the ratio of the efficiencies measured in data and Monte Carlo simulations, 96.1%, since the GEC is applied on Monte Carlo together with the trigger.

Figure 3.15 displays the distribution of the quantities on which the GEC are applied for the signal J/ψ selected by this analysis. These plots show that indeed only the cut on the number of VELO clusters has an effect.

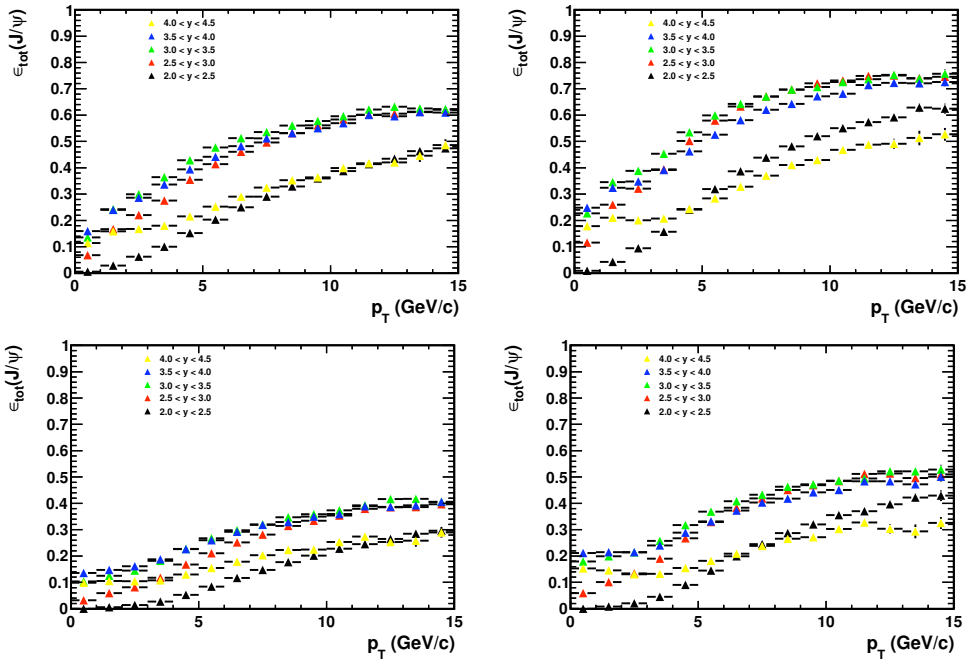

Figure 3.16 – *J/ψ total efficiencies for transversely (left plots) and longitudinally polarised J/ψ (right plots), as a function of p_T in bins of y. The top row of figures are the efficiencies obtained for TCK 0x001D0030 (identical efficiencies are obtained for TCK 0x001E0030), the bottom row of figures are obtained for TCK 0x001F0029.*

3.3.6 Effect of the J/ψ polarisation on the efficiency

The efficiency is evaluated from a Monte Carlo simulation in which the J/ψ is produced unpolarised. However, studies show that both longitudinal and transverse J/ψ polarisation may lead to very different efficiencies. In this analysis, the efficiency variation is only studied in the helicity frame.

The angular distribution of a polarised J/ψ is

$$\frac{\mathrm{d}^2N}{\mathrm{d}\cos\theta\mathrm{d}\phi} \propto 1+\lambda_\theta\cos^2\theta+\lambda_{\theta\phi}\sin 2\theta\cos\phi+\lambda_\phi\sin^2\theta\cos 2\phi\,, \qquad (3.19)$$

where θ is defined as the angle between the direction of the μ^+ momentum in the J/ψ centre-of-mass frame and the direction of the J/ψ momentum in the centre-of-mass frame of the colliding protons, and ϕ is the azimuthal angle measured with respect to the production plane formed by the momenta of the colliding hadrons in the J/ψ rest frame. When $\lambda_\phi = 0$ and $\lambda_{\theta\phi} = 0$, the values $\lambda_\theta = +1, -1, 0$ correspond to fully transverse, fully longitudinal, and no polarisation, respectively.

Figure 3.16 shows the total efficiency for the two extreme polarisation scenarios and can be compared to Figs. 3.13 and 3.14. The plots indicate that the polarisation significantly affects the acceptance and reconstruction efficiencies and that the effect depends on p_T and y. Therefore, the measurement of the prompt J/ψ cross-section will be given separately for the three polarisations.

Monte Carlo simulations show that the polarisation that the J/ψ acquires in the b decay is largely diluted when using as helicity quantisation axis the J/ψ momentum in the laboratory frame instead of the J/ψ momentum in the b rest frame. Therefore, no systematic uncertainty is assigned to the J/ψ from b cross-section measurement from the unknown J/ψ polarisation.

The measurement of the J/ψ polarisation is in itself an interesting measurement and will allow to distinguish between the theoretical models. The measurement is rather complicated and as pointed out in Ref. [121], has to be measured in different reference frames in order to simplify its interpretation [122]. A measurement of the J/ψ polarisation has been performed by the ALICE collaboration [123] and others from the other LHC collaborations will be public soon.

3.4 Systematic uncertainties

The different contributions to the systematic uncertainties are discussed in the following.

3.4.1 Trigger efficiency

As described in Section 3.3.4, the trigger efficiency is determined from the full Monte Carlo simulation. The systematic uncertainty associated with the trigger efficiency is evaluated by comparing data with simulation. Trigger efficiency in data uses a trigger unbiased event sample [124], i.e., a sample in which the event would still be triggered if the J/ψ candidate were removed (Trigger Independent of Signal, TIS). We use events that are TIS with respect to at least one of the trigger lines, which reduces the total sample of selected J/ψ candidates by a factor of approximately 10. The trigger efficiency is determined in each (p_T, y) bin using the formula

$$\varepsilon_{\text{tri}}(p_T, y) = \frac{J/\psi \text{ Reconstructed TIS\&TOS } (p_T, y)}{J/\psi \text{ Reconstructed TIS } (p_T, y)}. \tag{3.20}$$

The number of signal TIS and TIS&TOS events are evaluated in each bin using a fit to the invariant mass, as described in Sec. 3.3.1. The results are shown in

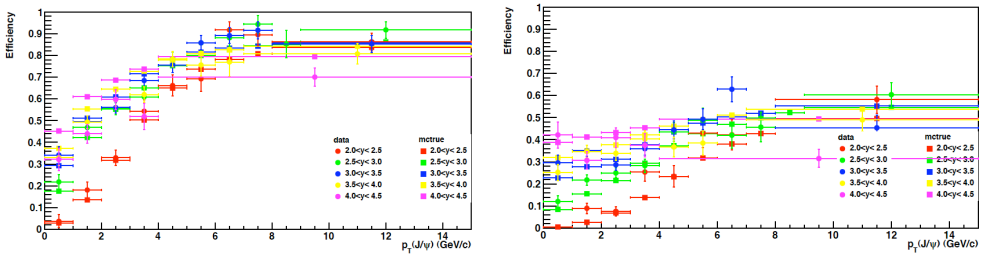

Figure 3.17 – *Trigger efficiency in Monte Carlo and its evaluation on data, for TCK 0x001D0030 (left) and TCK 0x001F0029 (right)*

Fig. 3.17. The systematic uncertainties displayed in Table 3.5 are computed from the difference between the trigger efficiency as measured in data and in the simulation.

Table 3.5 – *Systematic errors due to the trigger in bins of the J/ψ transverse momentum and rapidity, in %*

$p_T\,(\mathrm{GeV}/c)$	$0-1$	$1-2$	$2-3$	$3-4$	$4-5$	$5-6$	$6-7$	$7-8$	$8-14$
TCK0x001D0030									
$2<y<2.5$	3.0	3.7	3.5	5.1	4.9	3.9	5.1	4.1	4.1
$2.5<y<3$	3.4	2.6	2.6	3.1	3.1	3.8	4.0	6.3	3.8
$3<y<3.5$	3.8	2.5	2.6	2.9	3.4	3.7	3.9	4.0	4.0
$3.5<y<4$	3.6	2.9	3.1	3.5	3.5	6.6	4.7	4.7	4.7
$4<y<4.5$	5.2	4.3	4.7	6.0	4.2	4.2	4.2	4.2	4.2
TCK0x001F0029									
$2<y<2.5$	2.5	2.3	2.2	4.2	4.9	6.5	6.8	5.3	5.3
$2.5<y<3$	2.5	2.3	2.3	3.1	4.1	5.5	5.9	6.8	4.7
$3<y<3.5$	3.5	2.6	2.3	2.9	4.0	4.7	5.7	4.8	4.8
$3.5<y<4$	3.7	2.6	3.1	3.9	4.5	5.5	4.4	4.4	4.4
$4<y<4.5$	5.9	3.8	4.5	5.3	4.1	4.1	4.1	4.1	4.1

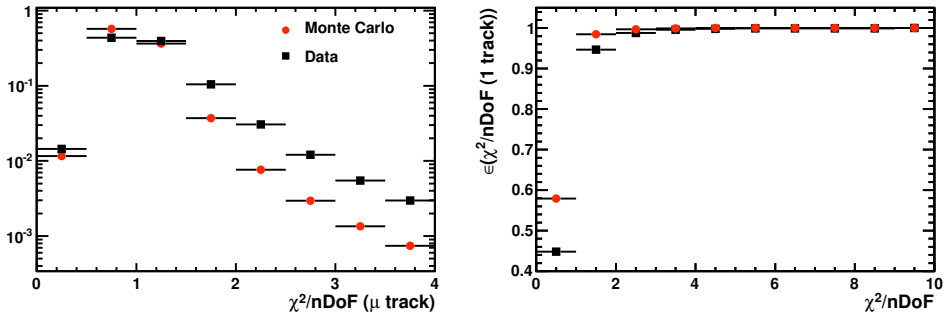

Figure 3.18 – Left*: χ^2/ndof of the track fit distribution for muons from J/ψ; the black squares show muons from signal J/ψ after background subtraction with sPlot techniques and the red dots the signal Monte Carlo. The cut value is at 4.* Right*: Efficiency of the track χ^2/ndof cut on data (*black squares*) and Monte Carlo simulation (*red dots*).*

3.4.2 Global Event Cuts

The statistical error on the GEC efficiency extracted from data (2%), as described in 3.3.5, is taken as systematic uncertainty associated with the GEC. This measures essentially the effect of GEC on prompt J/ψ production. However, the efficiency of the GEC may differ between prompt J/ψ and J/ψ from b. In the Monte Carlo simulation, a difference of 2% is measured, which is used as systematic uncertainty, applied to the J/ψ from b cross-section measurement.

3.4.3 Track χ^2

Given that the selection uses a cut on the χ^2 of the track fit (χ^2/ndof < 4), a difference in this variable between data and Monte Carlo simulation will contribute to the systematic uncertainty. Figure 3.18 (*left*) shows the distribution for this quantity in muons from J/ψ on data and Monte Carlo simulation. The background subtraction in data is obtained using sPlot techniques [125]. Figure 3.18 (*right*) shows the efficiency of the χ^2/ndof cut, when applied to one of the J/ψ muons. An uncertainty of 0.5% is assigned per track, which is the relative difference between the efficiency of the cut in the simulation and data.

3.4.4 Vertexing

A comparison between the J/ψ vertex χ^2 distributions for data (after background subtraction with sPlot techniques) and Monte Carlo simulation is shown in Fig. 3.19

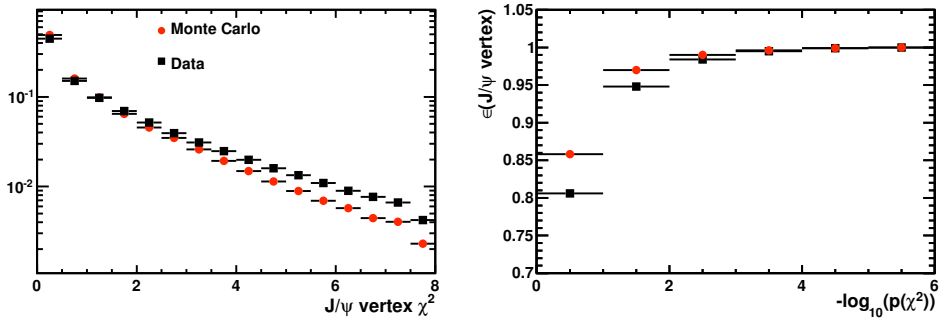

Figure 3.19 – *Left: J/ψ vertex χ^2 distribution for signal J/ψ after background subtraction with sPlot techniques (black squares) and Monte Carlo simulation (red dots). Right: Efficiency of the vertex $p(\chi^2)$ cut in data (black squares) and Monte Carlo simulation (red dots). The cut value is at $p(\chi^2) > 0.5\%$ ($-\log(p(\chi^2)) = 2.3$).*

(*left*). The analysis requires that $p(\chi^2) > 0.5\%$. The efficiency of this cut on the signal J/ψ sample is shown in Fig. 3.19 (*right*). With the analysis cut value, the efficiency difference between data and Monte Carlo is 1.6%. The Monte Carlo efficiencies are multiplied by 98.4% and a systematic uncertainty of 0.8% (half of the correction) is assigned.

3.4.5 Mass fits

The influence of the choice of the function used to describe the shape of the signal distribution is estimated by fitting the J/ψ invariant mass distribution with the sum of two Crystal Ball functions. The fitted number of signal J/ψ candidates found with this method is $558\,338 \pm 1422$. The relative difference with the number of signal events obtained by summing the results of the 14×5 analysis bins ($564\,603 \pm 924$) is taken as systematic uncertainty, i.e., 1%.

3.4.6 Unknown J/ψ spectrum

The unknown J/ψ p_{T} and y spectra affect the efficiency values used to extract the cross-section, because an average value of the efficiency is computed in each bin. To take into account possible efficiency variations inside the bins, each bin is divided into four sub-bins, dividing the p_{T} range in two bins of $500\,\mathrm{MeV}/c$ width and the y range in two bins of 0.25 width. The relative deviation between the bin efficiency and the average of the efficiencies in the sub-bins is then taken

Table 3.6 – *Systematic errors due to unknown J/ψ spectrum in bins of the J/ψ transverse momentum and rapidity, in %.*

p_T (GeV/c)	0 – 1	1 – 2	2 – 3	3 – 4	4 – 5	5 – 6	6 – 7	7 – 8
$2 < y < 2.5$	11.0	0.2	2.6	1.9	3.1	2.4	2.1	2.5
$2.5 < y < 3$	15.1	0.1	0.6	1.0	1.1	1.0	0.5	0.2
$3 < y < 3.5$	5.3	0.2	0.1	0.7	0.6	0.3	0.1	0.1
$3.5 < y < 4$	2.3	0.5	0.0	0.5	0.2	0.2	0.4	0.1
$4 < y < 4.5$	4.0	1.2	1.3	1.3	2.2	1.8	2.5	2.7
p_T (GeV/c)	8 – 9	9 – 10	10 – 11	11 – 12	12 – 13	13 – 14		
$2 < y < 2.5$	1.9	1.3	1.5	1.6	1.0	0.1		
$2.5 < y < 3$	0.2	0.3	0.0	0.2	0.4	0.0		
$3 < y < 3.5$	0.1	0.5	0.2	0.3	0.2	2.0		
$3.5 < y < 4$	0.0	0.0	0.2	0.7	0.5	2.5		
$4 < y < 4.5$	3.4	3.2	4.4	4.2	6.1	3.5		

as systematic uncertainty. The results are listed in Tab. 3.6. This error is bin dependent, and is uncorrelated between bins.

3.4.7 t_z fits

Uncertainties related to the t_z fit procedure are taken into account by studying the effect of the different components on the fitted number of J/ψ from b in a high statistics bin ($3 < p_T < 4, 2.5 < y < 3$):

- The central value of the prompt J/ψ component, μ, is found to be different from zero. This shift could be due to an improper description of the background for events close to $t_z = 0$. The impact of such a shift is studied by fixing μ at two extreme values, $\mu = -3$ fs and $\mu = 3$ fs and repeating the t_z fit. The relative variation of the number of J/ψ from b, 3.6%, is used as a systematic uncertainty.

- The "next event method" described in 3.3.2 is used to determine the shape of the tail component. This method, however, assumes that the primary vertex reconstruction efficiency does not depend on the z position of the primary vertex. The same method can also be used to determine the primary vertex reconstruction efficiency as a function of z. This is displayed in Fig. 3.20

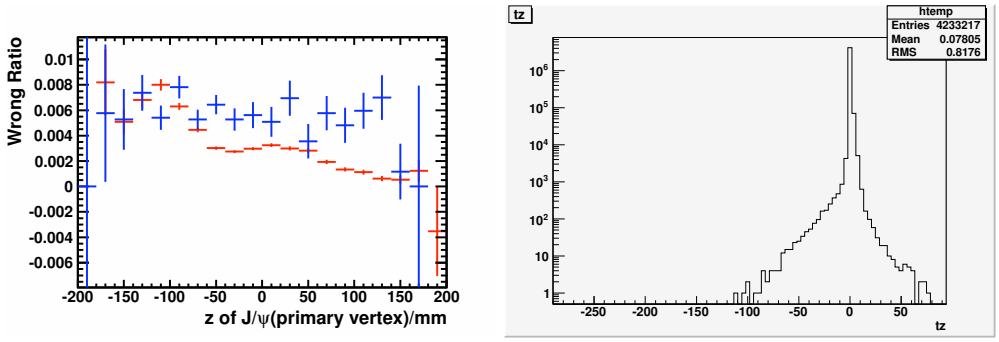

Figure 3.20 – Left*: J/ψ Primary vertex reconstruction inefficiency $(1-\varepsilon_{\rm PV})$ as a function of z position of the primary vertex estimated on data with the "next event method"* (blue)*, and for the Monte Carlo simulation* (red)*.* Right*: t_z distribution obtained in inclusive J/ψ Monte Carlo simulation.*

(*left*): the blue histogram shows (1-$\varepsilon_{\rm PV}$) as a function of $z_{\rm PV}$ in data, where $\varepsilon_{\rm PV}$ is the primary vertex reconstruction efficiency and $z_{\rm PV}$ the z position of the primary vertex. The red histogram represents the same quantity in the Monte Carlo simulation. In the simulation, there is a small dependence of the primary vertex efficiency on z. This dependence affects the shape of the tail, which would then be asymmetric, as shown for the simulation in Fig. 3.20 (*right*). In order to estimate the effect of an asymmetric tail, the shape observed in the Monte Carlo simulation is used to perform the t_z fit. A negligible variation of the number of fitted J/ψ from b is observed, and thus this effect is ignored in the final result.

3.4.8 Muon identification

To cross-check and assign a systematic uncertainty to the Monte Carlo determination of the muon identification efficiency, the single track muon identification efficiency is measured on data using a tag and probe method, as described in Ref. [126]. This method consists in reconstructing J/ψ candidates in which only one muon is identified by the muon system ("tag"), and the other one ("probe") is identified selecting a track depositing the energy of Minimum Ionizing Particles in the calorimeters. The probe muon is also required to be independent of the muon trigger lines, to avoid biases on the result. The absolute muon identification efficiency is then evaluated on the probe muon, as a function of the muon momentum. The results shown in Fig. 3.21 indicate that the measured muon identification efficiency is higher in data than in the Monte Carlo simulation.

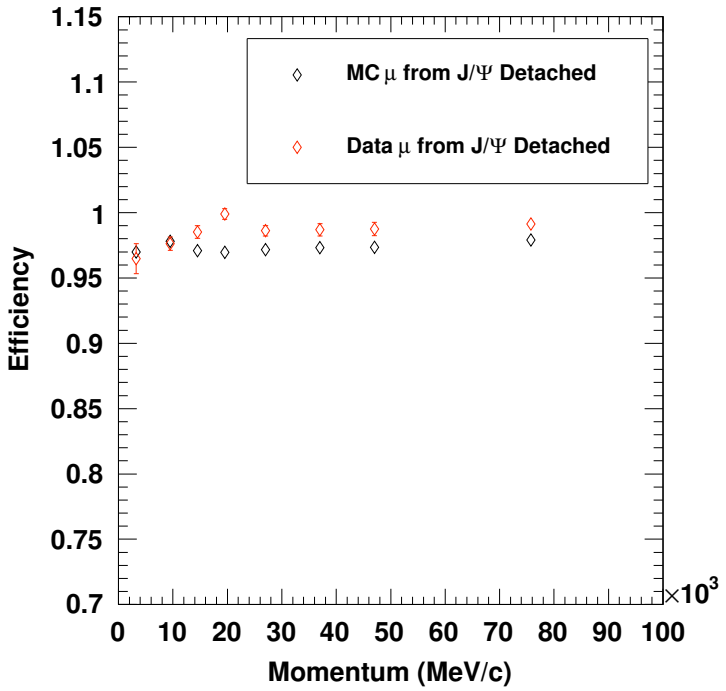

Figure 3.21 – *Muon identification efficiency as a function of the muon momentum for data and Monte Carlo simulation.*

The ratio of the muon identification efficiency measured in data to that obtained in the Monte Carlo simulation is convolved with the momentum distribution of muons from J/ψ to compute a correction factor. This factor is found to be 102.4% and is used to multiply the total Monte Carlo efficiencies which enter in the cross-section computations. Different terms contribute to the error on this factor:

- the statistical error due to the finite size of the tag and probe J/ψ sample, 0.4%,
- the residual dependence of the correction on the μ p_{T}, 0.1%,
- possible biases due to the background estimation, 0.9%,
- possible biases due to different efficiencies of the HCAL selection criteria used to select the "probe" muon, 0.4%,
- possible biases due to the trigger, 0.2%.

The combination of the components detailed above, 1.1%, is the systematic uncertainty assigned to the muon identification.

3.4.9 Other systematic uncertainties

Other systematic uncertainties are discussed below.

1. Tracking studies have shown that the Monte Carlo simulation reproduces the track-finding efficiency for long tracks within 4%. A systematic uncertainty of 4% per μ track is therefore assigned, resulting in a total systematic uncertainty of 8% due to the knowledge of the track reconstruction efficiency.

2. Due to the finite p_{T} and y resolutions, J/ψ candidates can be assigned to a wrong p_{T} bin (inter-bin cross- feed in Table 3.7). From Monte Carlo simulations, the average p_{T} resolution is computed to be $12.7 \pm 0.2\,\mathrm{MeV}/c$ and the y resolution $(1.4 \pm 0.1) \times 10^{-3}$. The effect of the y resolution is negligible compared to the width of the bins (0.5 in rapidity). The effect of the p_{T} resolution is estimated by recomputing the efficiency tables after smearing the p_{T} values with a Gaussian of $\sigma = 20\,\mathrm{MeV}/c$ (larger than the Monte Carlo value in order to take into account a possible worse p_{T} resolution in data). The maximum deviation observed is 0.5%, which is the value used as systematic uncertainty for the differential cross-section measurement. The effect on the total cross-section is much smaller and is ignored.

3. A fraction of J/ψ events have a lower mass because of the radiative tail. Based on Monte Carlo studies, we estimate 2% of the signal J/ψ to be outside the analysis mass window ($M_{\mu\mu} < 2.7\,\mathrm{GeV}/c^2$) and are not counted as signal. The fitted signal yields are therefore corrected by 2% (multiplied by 1.02), and an error of 1% is assigned to the cross-section measurements.

4. The extrapolations based on PYTHIA use the average branching fraction of inclusive b-hadron decays to J/ψ measured at LEP, i.e. $\mathscr{B}(b \to J/\psi X) = (1.16 \pm 0.10)\%$ [47–49]. The underlying assumption is that the b hadronisation fractions at pp collisions at $\sqrt{s} = 7\,\mathrm{TeV}$ are identical to those seen by the LEP experiments. However, recent CDF results [127] show that the b-baryon hadronisation fraction could be larger at different energies.

   To estimate the systematic uncertainty due to potential different b hadronisation fractions for pp collisions at $\sqrt{s} = 7\,\mathrm{TeV}$, the b-hadron to J/ψ branching fraction is computed by taking as central values of the fragmentation fractions those measured at the Tevatron, as calculated by the HFAG

Table 3.7 – *Summary of systematic uncertainties.*

Source	Systematic uncertainty (%)
Correlated between bins	
Inter-bin cross-feed	0.5
Mass fits	1.0
Radiative tail	1.0
Muon identification	1.1
Tracking efficiency	8.0
Track χ^2	1.0
Vertexing	0.8
GEC	2.0
$\mathscr{B}(J/\psi \to \mu^+\mu^-)$	1.0
Luminosity	10.0
Uncorrelated between bins	
Bin size	0.1 to 15.0
Trigger	1.7 to 4.5
Applied only to J/ψ from b cross-sections, correlated between bins	
GEC efficiency on B events	2.0
t_z fits	3.6
Applied only to the extrapolation of the $b\bar{b}$ cross-section	
b hadronisation fractions	2.0
$\mathscr{B}(b \to J/\psi X)$	9.0

group i.e. $f_{B_u} = f_{B_d} = 33.3\,\%$, $f_{B_s} = 12.1\,\%$ and $f_{\Lambda_b} = 21.4\,\%$ [38]. The relative difference between the estimate of the effective branching fraction $\mathscr{B}(b \to J/\psi X)$ based on the fragmentation functions measured at LEP and at the Tevatron, 2%, is taken as systematic uncertainty, which only affects the extrapolations of the $b\bar{b}$ cross-section.

Note that recently LHCb measured the b hadron fractions at the LHC energy [128] but this result shows that the approach described above is in fact conservative.

3.5 Results

The measured differential cross-sections for prompt J/ψ and J/ψ from b are shown in Figs. 3.22 and 3.23, respectively. Tables 3.8 and 3.9 give the measured double-differential cross-sections for prompt J/ψ and J/ψ from b in the various $(p_{\rm T}, y)$ bins, after all corrections and assuming no polarisation.

J/ψ produced in pp collisions in events with very few other tracks have been observed (so-called "exclusive" J/ψ production) [129]. Because in this analysis a reconstructed primary vertex is required, these exclusive J/ψ events only contribute to the tail of the t_z distribution and are counted for the crosss-section determination. The effect is estimated to be small (<0.1%) and is not subtracted from the measurement of the prompt J/ψ cross-section.

The results for transversely and longitudinally polarised J/ψ are given in Tables 3.10 and 3.11. Figures 3.24 shows the differential cross-sections for two ex-

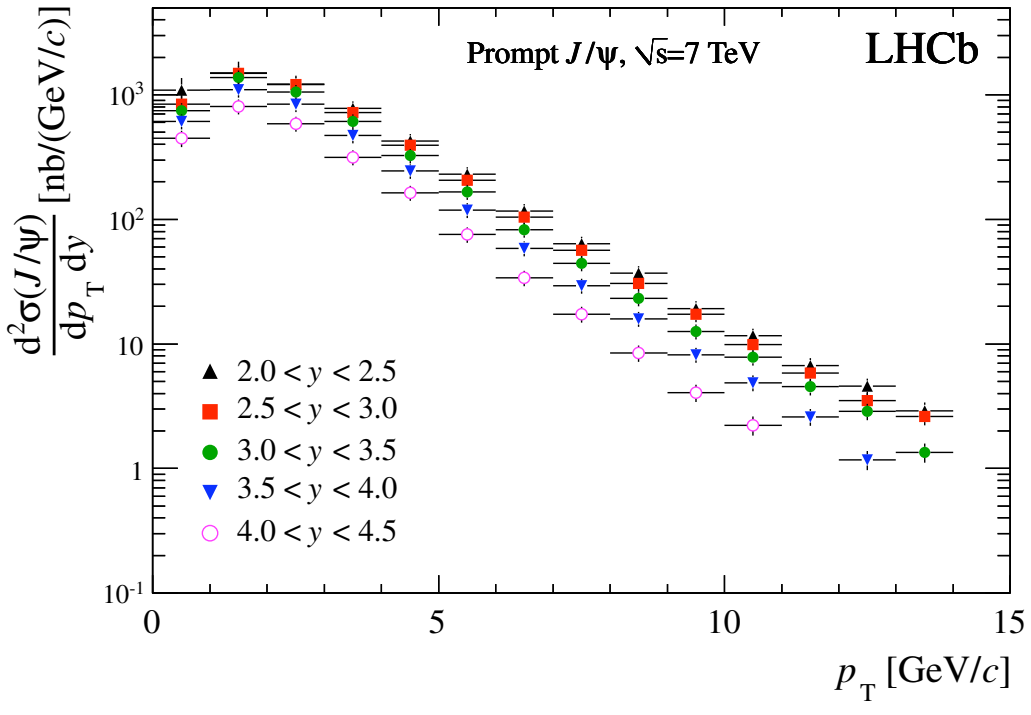

Figure 3.22 – *Differential cross-section for prompt J/ψ in data as a function of $p_{\rm T}$ in bins of y , assuming that* prompt J/ψ *are produced unpolarised. The errors are the quadratic sum of the statistical and partially-correlated systematic uncertainties.*

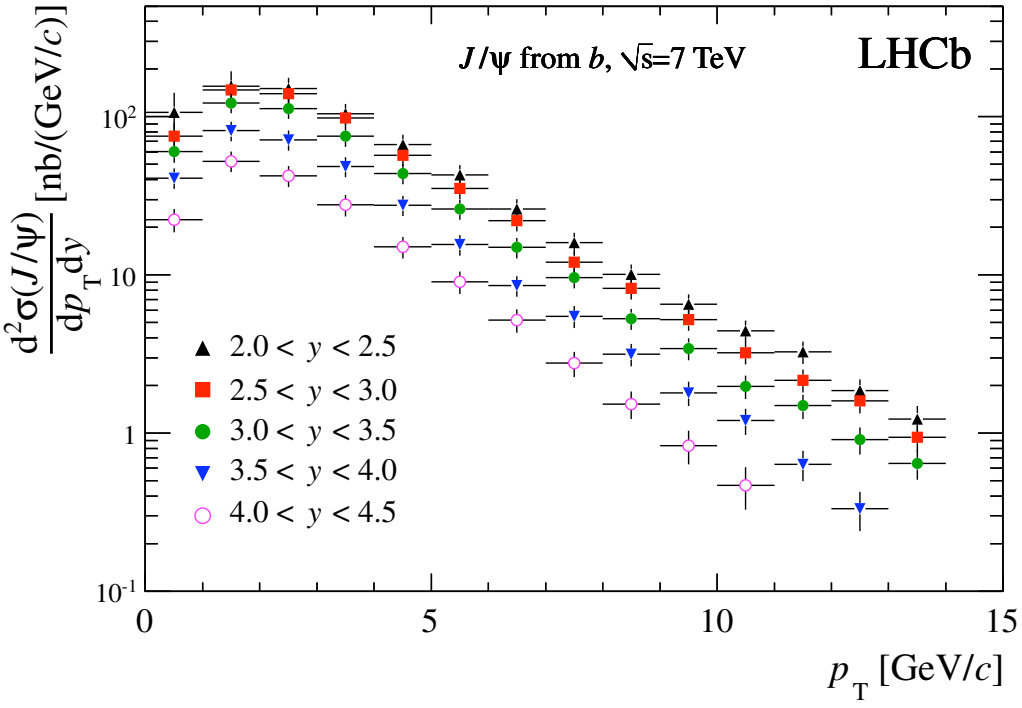

Figure 3.23 – *Differential cross-section for J/ψ from b in data as a function of p_T for the various y bins. The errors are the quadratic sum of the statistical and partially-correlated systematic uncertainties.*

treme polarisation scenarios, fully longitudinal (*right*) and fully transverse (*left*) in the helicity frame.

The integrated cross-section for prompt J/ψ production in the defined acceptance, summing over all bins of the analysis, is:

$$\sigma\left(\text{prompt } J/\psi, p_T < 14\ \text{GeV}/c, 2 < y < 4.5\right) = 10.52 \pm 0.04 \pm 1.40^{+1.64}_{-2.20}\,\mu\text{b}, \tag{3.21}$$

where the first uncertainty is statistical and the second one systematic. As the result is quoted assuming unpolarised J/ψ, the last error indicates the uncertainty related to this assumption.

The integrated cross-section for the production of J/ψ from b in the same acceptance is:

$$\sigma\left(J/\psi \text{ from } b, p_T < 14\ \text{GeV}/c, 2 < y < 4.5\right) = 1.14 \pm 0.01 \pm 0.16\,\mu\text{b}, \tag{3.22}$$

where the first uncertainty is statistical and the second one systematic.

Table 3.8 – $\frac{d^2\sigma}{dp_T dy}$ *in nb/(*GeV/c*) for prompt* J/ψ *in bins of the* J/ψ *transverse momentum and rapidity, assuming no polarisation. The first error is statistical, the second is the component of the systematic uncertainty that is uncorrelated between bins and the third is the correlated component.*

p_T (GeV/c)	$2.0 < y < 2.5$	$2.5 < y < 3.0$	$3.0 < y < 3.5$
0– 1	1091± 70±226±144	844± 13±133±111	749± 7± 46± 99
1– 2	1495± 38±282±197	1490± 12± 39±197	1376± 8± 26±182
2– 3	1225± 20±109±162	1214± 9± 24±160	1053± 7± 19±139
3– 4	777± 11± 44±103	719± 6± 18± 95	611± 5± 14± 81
4– 5	424± 6± 22± 56	392± 3± 12± 52	325± 3± 9± 43
5– 6	230± 4± 12± 30	206± 2± 8± 27	167± 2± 5± 22
6– 7	116± 2± 6± 15	104± 1± 4± 14	82± 1± 3± 11
7– 8	64± 1± 3± 8	57± 1± 3± 7	44± 1± 1± 6
8– 9	37± 1± 1± 5	31± 1± 1± 4	23± 1± 1± 3
9–10	19.3±0.7± 0.5± 2.6	17.4±0.5± 0.2± 2.3	12.6±0.4±0.1± 1.7
10–11	11.6±0.5± 0.3± 1.5	9.8±0.4± 0.1± 1.3	7.8±0.3±0.1± 1.0
11–12	6.7±0.4± 0.2± 0.9	5.9±0.3± 0.1± 0.8	4.5±0.3±0.1± 0.6
12–13	4.6±0.3± 0.2± 0.6	3.5±0.2± 0.1± 0.5	2.9±0.2±0.1± 0.4
13–14	2.9±0.3± 0.1± 0.4	2.6±0.2± 0.1± 0.3	1.3±0.2±0.1± 0.2
	$3.5 < y < 4.0$	$4.0 < y < 4.5$	
0– 1	614± 6± 23± 81	447± 5± 28± 59	
1– 2	1101± 7± 23±145	807± 7± 28±107	
2– 3	839± 6± 19±111	588± 6± 22± 78	
3– 4	471± 4± 13± 62	315± 4± 14± 42	
4– 5	244± 3± 7± 32	163± 3± 6± 22	
5– 6	119± 2± 5± 16	76± 2± 3± 10	
6– 7	59± 1± 2± 8	34±1.1± 1.4± 4.5	
7– 8	29± 1± 1± 4	17±0.7± 0.8± 2.3	
8– 9	15.9±0.5± 0.1± 2.1	8.5±0.5± 0.4± 1.1	
9–10	8.2±0.4± 0.1± 1.1	4.1±0.3± 0.2± 0.5	
10–11	4.9±0.3± 0.1± 0.6	2.2±0.2± 0.1± 0.3	
11–12	2.6±0.2± 0.1± 0.3		
12–13	1.2±0.1± 0.1± 0.2		

Table 3.9 – $\frac{d^2\sigma}{dp_T dy}$ *in nb/(*GeV/c*) for* J/ψ from b *in bins of the* J/ψ *transverse momentum and rapidity. The first error is statistical, the second is the component of the systematic uncertainty that is uncorrelated between bins and the third is the correlated component.*

p_T (GeV/c)	$2.0 < y < 2.5$	$2.5 < y < 3.0$	$3.0 < y < 3.5$
0– 1	107± 23± 22± 15	75± 4± 12± 10	60± 2± 4± 8
1– 2	156± 11± 30± 22	147± 4± 4± 20	123± 3± 2± 17
2– 3	151± 6± 14± 21	140± 3± 3± 19	113± 2± 2± 16
3– 4	105± 4± 6± 15	98± 2± 2± 14	75± 2± 2± 10
4– 5	67± 2± 3± 9	57± 1± 2± 8	44± 1± 1± 6
5– 6	43± 2± 2± 6	35± 1± 1± 5	26± 1± 1± 4
6– 7	26± 1± 1± 4	22± 1± 1± 3	14.9±0.6±0.5±2.1
7– 8	16.1±0.7±0.8±2.2	12.1±0.5±0.6±1.7	9.4±0.4±0.3±1.3
8– 9	10.1±0.6±0.3±1.4	8.2±0.4±0.8±1.1	5.3±0.3±0.1±0.7
9–10	6.5±0.4±0.2±0.9	5.2±0.3±0.1±0.7	3.4±0.2±0.1±0.5
10–11	4.4±0.3±0.1±0.6	3.2±0.2±0.1±0.4	2.0±0.2±0.1±0.3
11–12	3.3±0.3±0.1±0.4	2.2±0.2±0.1±0.3	1.5±0.2±0.1±0.2
12–13	1.9±0.2±0.1±0.3	1.6±0.2±0.1±0.2	0.9±0.1±0.1±0.1
13–14	1.2±0.2±0.1±0.2	0.9±0.1±0.1±0.1	0.6±0.1±0.1±0.1
	$3.5 < y < 4.0$	$4.0 < y < 4.5$	
0– 1	41± 2± 2± 6	22± 2± 1± 3	
1– 2	82± 2± 2± 11	52± 2± 2± 7	
2– 3	71± 2± 2± 10	42± 2± 2± 6	
3– 4	48± 1± 1± 7	28± 1± 1± 4	
4– 5	28± 1± 1± 4	15.0±1.0±0.6±2.1	
5– 6	15.6±0.7±0.7±2.2	9.0±0.7±0.3±1.3	
6– 7	8.6±0.4±0.3±1.2	5.2±0.5±0.2±0.7	
7– 8	5.5±0.3±0.2±0.8	2.8±0.3±0.1±0.4	
8– 9	3.2±0.3±0.1±0.4	1.5±0.2±0.1±0.2	
9–10	1.8±0.2±0.1±0.2	0.8±0.2±0.1±0.1	
10–11	1.2±0.2±0.1±0.2	0.5±0.1±0.1±0.1	
11–12	0.6±0.1±0.1±0.1		
12–13	0.3±0.1±0.1±0.1		

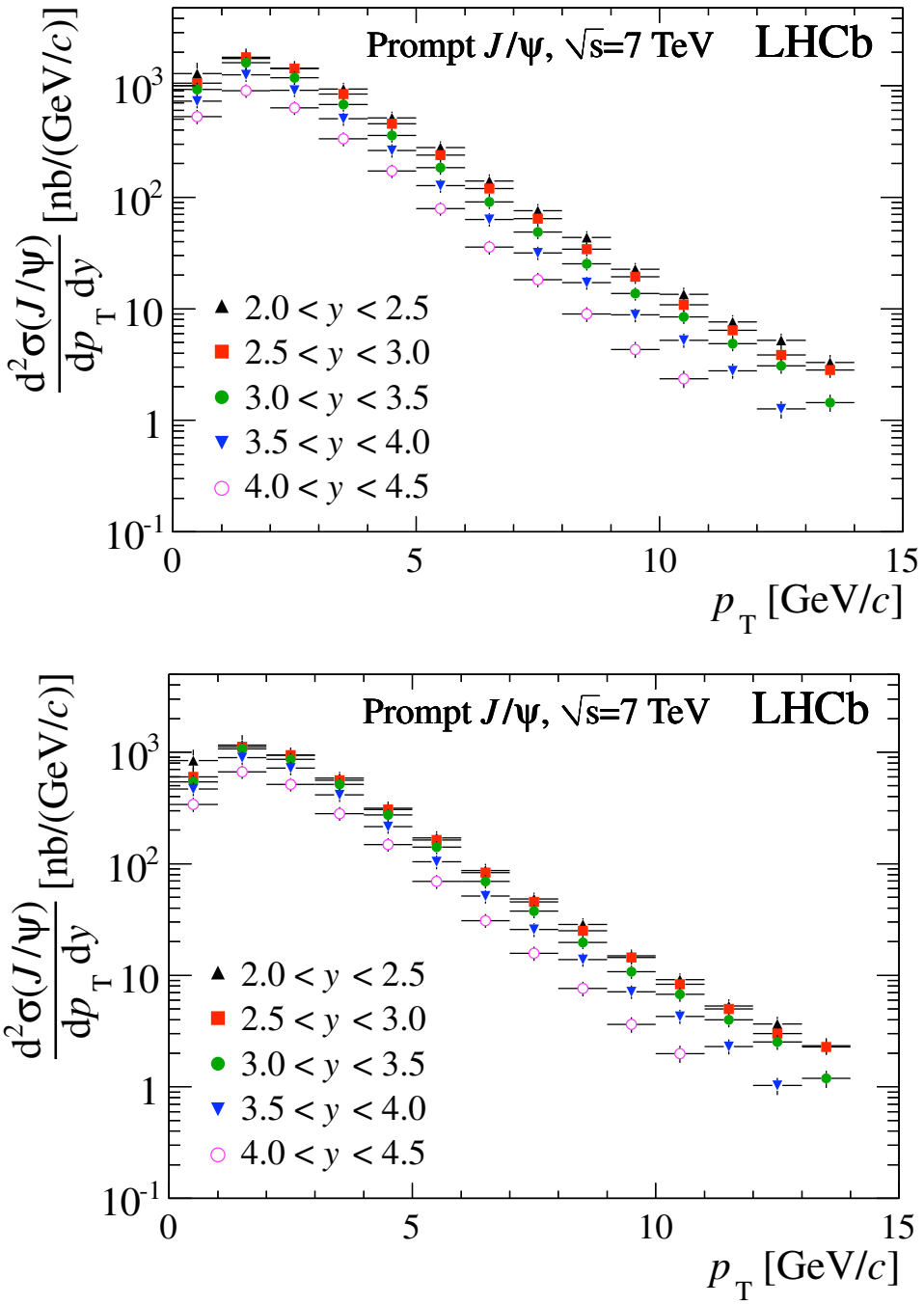

Figure 3.24 – *Differential cross-section for* prompt J/ψ *in data as a function of* $p_{\rm T}$ *in bins of y, assuming fully transverse* (top) *or fully longitudinal* (bottom) J/ψ*. The errors are the quadratic sum of the statistical and partially-correlated systematic uncertainties.*

Table 3.10 – $\frac{d^2\sigma}{dp_T dy}$ *in nb/(*GeV/c*) for prompt* J/ψ *in bins of the* J/ψ *transverse momentum and rapidity, assuming fully transversely polarised* J/ψ*. The first error is statistical, the second is the component of the systematic uncertainty that is uncorrelated between bins and the third is the correlated component.*

p_T (GeV/c)	$2.0 < y < 2.5$	$2.5 < y < 3.0$	$3.0 < y < 3.5$
0– 1	1282 ± 83 ± 266 ± 169	1058 ± 16 ± 166 ± 140	924 ± 9 ± 56 ± 122
1– 2	1751 ± 44 ± 331 ± 231	1791 ± 15 ± 47 ± 236	1603 ± 10 ± 31 ± 212
2– 3	1438 ± 24 ± 129 ± 190	1423 ± 11 ± 28 ± 188	1182 ± 7 ± 21 ± 156
3– 4	932 ± 13 ± 53 ± 123	839 ± 7 ± 21 ± 111	675 ± 5 ± 15 ± 89
4– 5	513 ± 7 ± 27 ± 68	455 ± 4 ± 14 ± 60	358 ± 3 ± 10 ± 47
5– 6	278 ± 4 ± 15 ± 37	238 ± 3 ± 9 ± 32	184 ± 2 ± 6 ± 24
6– 7	140 ± 3 ± 7 ± 19	120 ± 2 ± 5 ± 16	91 ± 1 ± 3 ± 12
7– 8	76 ± 2 ± 4 ± 10	64 ± 1 ± 3 ± 8	49 ± 1 ± 2 ± 6
8– 9	44 ± 1 ± 1 ± 6	34 ± 1 ± 1 ± 5	25 ± 1 ± 1 ± 3
9–10	23 ± 1 ± 1 ± 3	19.3 ± 0.6 ± 0.2 ± 2.6	13.7 ± 0.5 ± 0.1 ± 1.8
10–11	13.5 ± 0.6 ± 0.4 ± 1.8	10.9 ± 0.4 ± 0.1 ± 1.4	8.5 ± 0.4 ± 0.1 ± 1.1
11–12	7.7 ± 0.4 ± 0.3 ± 1.0	6.4 ± 0.3 ± 0.1 ± 0.8	4.9 ± 0.3 ± 0.1 ± 0.6
12–13	5.2 ± 0.3 ± 0.2 ± 0.7	3.8 ± 0.3 ± 0.1 ± 0.5	3.1 ± 0.2 ± 0.1 ± 0.4
13–14	3.3 ± 0.3 ± 0.1 ± 0.4	2.8 ± 0.2 ± 0.1 ± 0.4	1.4 ± 0.2 ± 0.1 ± 0.2
	$3.5 < y < 4.0$	$4.0 < y < 4.5$	
0– 1	728 ± 7 ± 27 ± 96	530 ± 6 ± 33 ± 70	
1– 2	1246 ± 8 ± 26 ± 164	902 ± 7 ± 31 ± 119	
2– 3	913 ± 6 ± 21 ± 120	631 ± 6 ± 24 ± 83	
3– 4	505 ± 4 ± 14 ± 67	334 ± 4 ± 15 ± 44	
4– 5	262 ± 3 ± 8 ± 35	172 ± 3 ± 7 ± 23	
5– 6	128 ± 2 ± 5 ± 17	79 ± 2 ± 3 ± 11	
6– 7	63 ± 1 ± 2 ± 8	36 ± 1 ± 2 ± 5	
7– 8	32 ± 1 ± 1 ± 4	18.3 ± 0.7 ± 0.8 ± 2.4	
8– 9	17.1 ± 0.6 ± 0.2 ± 2.3	8.9 ± 0.5 ± 0.4 ± 1.2	
9–10	8.8 ± 0.4 ± 0.1 ± 1.2	4.3 ± 0.3 ± 0.2 ± 0.5	
10–11	5.2 ± 0.3 ± 0.1 ± 0.7	2.4 ± 0.2 ± 0.1 ± 0.3	
11–12	2.8 ± 0.2 ± 0.1 ± 0.4		
12–13	1.3 ± 0.1 ± 0.1 ± 0.2		

Table 3.11 – $\frac{d^2\sigma}{dp_T dy}$ *in nb/(*GeV/c*) for prompt* J/ψ *in bins of the* J/ψ *transverse momentum and rapidity, assuming fully longitudinally polarised* J/ψ*. The first error is statistical, the second is the component of the systematic uncertainty that is uncorrelated between bins and the third is the correlated component.*

p_T (GeV/c)	$2.0 < y < 2.5$	$2.5 < y < 3.0$	$3.0 < y < 3.5$
0– 1	839± 54±174±111	601± 9± 94± 79	543± 5± 33± 72
1– 2	1157± 29±219±153	1114± 9± 29±147	1073± 7± 21±142
2– 3	945± 16± 84±125	938± 7± 19±124	865± 5± 16±114
3– 4	583± 8± 33± 77	559± 4± 14± 74	514± 4± 11± 68
4– 5	315± 4± 16± 42	307± 3± 9± 41	274± 2± 8± 36
5– 6	171± 3± 9± 23	163± 2± 6± 22	140± 2± 4± 19
6– 7	87± 2± 5± 12	83± 1± 3± 11	70± 1± 3± 9
7– 8	48± 1± 2± 6	46± 1± 2± 6	38± 1± 1± 5
8– 9	29± 1± 1± 4	25± 1± 1± 3	19.8±0.5±0.1± 2.6
9–10	14.9±0.5± 0.4± 2.0	14.5±0.4±0.2± 1.9	10.8±0.4±0.1± 1.4
10–11	9.1±0.4± 0.3± 1.2	8.3±0.3±0.1± 1.1	6.7±0.3±0.1± 0.9
11–12	5.3±0.3± 0.2± 0.7	5.0±0.3±0.1± 0.7	4.0±0.2±0.1± 0.5
12–13	3.7±0.2± 0.1± 0.5	3.0±0.2±0.1± 0.4	2.5±0.2±0.1± 0.4
13–14	2.3±0.2± 0.1± 0.3	2.3±0.2±0.1± 0.3	1.2±0.1±0.1± 0.2
	$3.5 < y < 4.0$	$4.0 < y < 4.5$	
0– 1	468± 4± 21± 62	341± 4± 21± 45	
1– 2	892± 5± 18±118	667± 6± 23± 88	
2– 3	721± 5± 16± 95	517± 5± 20± 68	
3– 4	415± 3± 12± 55	282± 4± 13± 37	
4– 5	215± 2± 7± 28	148± 2± 6± 20	
5– 6	104± 1± 4± 14	69± 2± 3± 9	
6– 7	51± 1± 2± 7	31± 1± 1± 4	
7– 8	26± 1± 1± 3	15.8±0.6±0.7± 2.1	
8– 9	13.9±0.5± 0.1± 1.8	7.6±0.4±0.3± 1.0	
9–10	7.1±0.3± 0.1± 0.9	3.6±0.3±0.2± 0.5	
10–11	4.3±0.2± 0.1± 0.6	2.0±0.2±0.1± 0.3	
11–12	2.3±0.2± 0.1± 0.3		
12–13	1.0±0.1± 0.1± 0.1		

3.5.1 Measured mean p_{T}

The mean and RMS of the p_{T} spectrum in each rapidity bin j are estimated, for the unpolarised J/ψ scenario, as:

$$\langle p_{\mathrm{T}} \rangle_j = \frac{\int_0^{p_{\mathrm{T}}^{\max}} p_{\mathrm{T}} f_j(p_{\mathrm{T}}) \mathrm{d}p_{\mathrm{T}}}{\int_0^{p_{\mathrm{T}}^{\max}} f_j(p_{\mathrm{T}}) \mathrm{d}p_{\mathrm{T}}} \quad \text{and} \quad \mathrm{RMS}_j = \sqrt{\frac{\int_0^{p_{\mathrm{T}}^{\max}} p_{\mathrm{T}}^2 f_j(p_{\mathrm{T}}) \mathrm{d}p_{\mathrm{T}}}{\int_0^{p_{\mathrm{T}}^{\max}} f_j(p_{\mathrm{T}}) \mathrm{d}p_{\mathrm{T}}} - \langle p_{\mathrm{T}} \rangle_j^2}, \tag{3.23}$$

where the function f_j is chosen as a cubic B-spline with a knot at the centre of each p_{T} bin i such that $\int_{\text{bin } i} f_j(p_{\mathrm{T}}) \mathrm{d}p_{\mathrm{T}}$ is exactly equal to the central value of the cross-section measurement in the (p_{T}, y) bin ij. It is assumed that $f_j(0) = 0$ and that f_j has an exponential behaviour in the last p_{T} bin. The uncertainties on the cross-section measurements are propagated on the mean p_{T} and RMS values, taking all correlations into account. The results are displayed in Table 3.12. The J/ψ mesons from b-hadron decays have a mean p_{T} and RMS which are approximately 20% larger than those of prompt J/ψ mesons. For each J/ψ source, the mean p_{T} and RMS are observed to decrease with increasing rapidity. The mean p_{T} as a function of the rapidity y is displayed in Fig. 3.25.

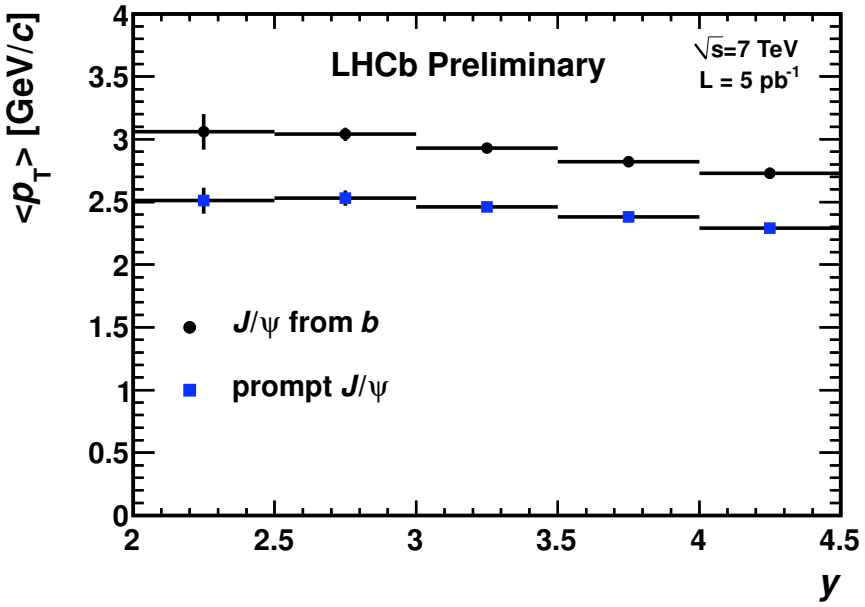

Figure 3.25 – *Mean p_{T} as a function of the J/ψ rapidity, y, for* prompt J/ψ *and* J/ψ from b, *for unpolarised* prompt J/ψ.

Table 3.12 – *Mean p_T and RMS for* prompt J/ψ *and* J/ψ from b*, for the unpolarised* prompt J/ψ *scenario. The first uncertainty is statistical and the second error is systematic.*

p_T range (GeV/c)	y bin	Mean p_T (GeV/c) of prompt J/ψ	RMS p_T (GeV/c) of prompt J/ψ
0 – 14	2.0 – 2.5	$2.51 \pm 0.03 \pm 0.10$	$1.80 \pm 0.01 \pm 0.04$
0 – 14	2.5 – 3.0	$2.53 \pm 0.01 \pm 0.06$	$1.74 \pm 0.01 \pm 0.01$
0 – 14	3.0 – 3.5	$2.46 \pm 0.01 \pm 0.02$	$1.68 \pm 0.01 \pm 0.01$
0 – 13	3.5 – 4.0	$2.38 \pm 0.01 \pm 0.02$	$1.61 \pm 0.01 \pm 0.01$
0 – 11	4.0 – 4.5	$2.29 \pm 0.01 \pm 0.02$	$1.50 \pm 0.01 \pm 0.01$
p_T range (GeV/c)	y bin	Mean p_T (GeV/c) of J/ψ from b	RMS p_T (GeV/c) of J/ψ from b
0 – 14	2.0 – 2.5	$3.06 \pm 0.09 \pm 0.11$	$2.22 \pm 0.02 \pm 0.04$
0 – 14	2.5 – 3.0	$3.04 \pm 0.02 \pm 0.05$	$2.12 \pm 0.01 \pm 0.01$
0 – 14	3.0 – 3.5	$2.93 \pm 0.02 \pm 0.02$	$2.03 \pm 0.01 \pm 0.01$
0 – 13	3.5 – 4.0	$2.82 \pm 0.02 \pm 0.02$	$1.92 \pm 0.02 \pm 0.01$
0 – 11	4.0 – 4.5	$2.73 \pm 0.03 \pm 0.03$	$1.77 \pm 0.03 \pm 0.01$

3.5.2 Fraction of J/ψ from b

Table 3.13 gives the values of the fraction of J/ψ from b, F_b, in the different bins, together with the statistic and systematic uncertainties (first and second term, respectively). F_b is quoted assuming that the prompt J/ψ are produced unpolarised. The third uncertainty in Tab. 3.13 gives the deviation from the central value when the prompt J/ψ are fully transversely or fully longitudinally polarised in the helicity frame. F_b is represented in Fig. 3.26, as a function of p_T, in bins of rapidity, assuming that prompt J/ψ are unpolarised. In this figure, only the statistical and systematic uncertainties are displayed, added quadratically, but not the uncertainties associated to the prompt J/ψ polarisation.

The b fraction increases as a function of p_T. For a constant p_T, the b fraction decreases with increasing rapidity, indicating that b-mesons are produced less forward than prompt J/ψ.

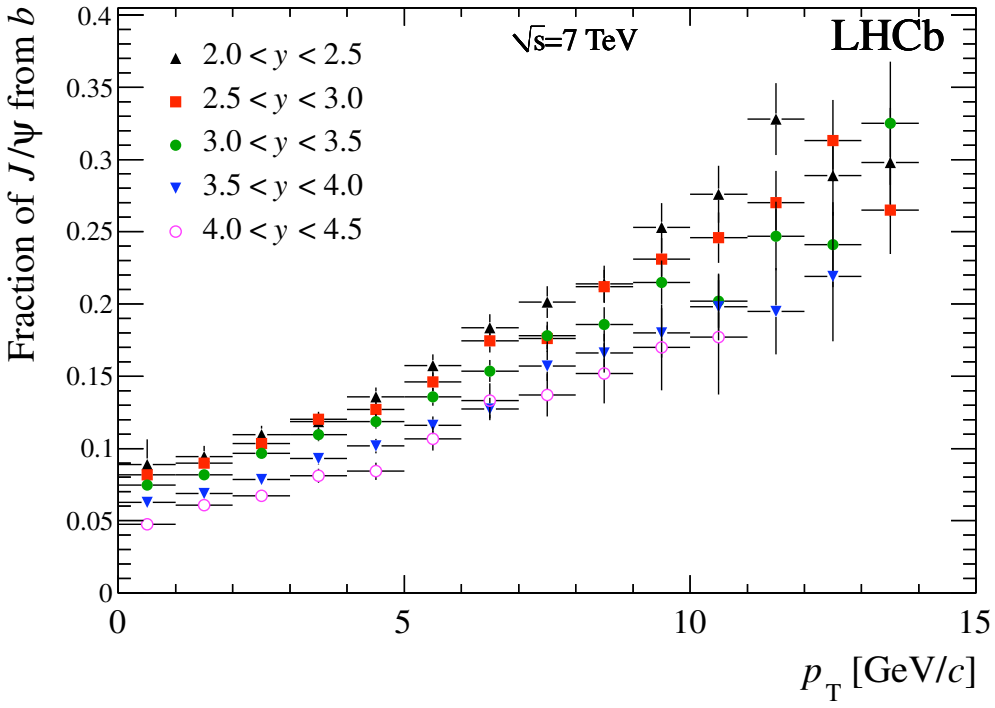

Figure 3.26 – *Fraction of* J/ψ from b, F_B, *as a function of* p_T, *in bins of rapidity.*

Table 3.13 – *Fraction of J/ψ from b (in %) in bins of the J/ψ transverse momentum and rapidity. The first uncertainty is statistical, the second systematic (uncorrelated between bins) and the third is the uncertainty due to the unknown polarisation of the* prompt *J/ψ; the central values are for unpolarised J/ψ.*

p_T (GeV/c)	$2.0 < y < 2.5$	$2.5 < y < 3.0$	$3.0 < y < 3.5$
0– 1	$8.9 \pm 1.7 \pm 0.3^{+1.2}_{-2.4}$	$8.2 \pm 0.4 \pm 0.3^{+1.5}_{-2.9}$	$7.4 \pm 0.3 \pm 0.3^{+1.3}_{-2.5}$
1– 2	$9.4 \pm 0.7 \pm 0.3^{+1.3}_{-2.4}$	$9.0 \pm 0.2 \pm 0.3^{+1.4}_{-2.7}$	$8.2 \pm 0.2 \pm 0.3^{+1.1}_{-2.1}$
2– 3	$11.0 \pm 0.5 \pm 0.4^{+1.5}_{-2.8}$	$10.3 \pm 0.2 \pm 0.4^{+1.4}_{-2.6}$	$9.7 \pm 0.2 \pm 0.3^{+1.0}_{-1.9}$
3– 4	$11.9 \pm 0.4 \pm 0.4^{+1.8}_{-3.3}$	$12.0 \pm 0.2 \pm 0.4^{+1.5}_{-2.9}$	$11.0 \pm 0.2 \pm 0.4^{+0.9}_{-1.8}$
4– 5	$13.6 \pm 0.4 \pm 0.5^{+2.1}_{-3.9}$	$12.7 \pm 0.3 \pm 0.5^{+1.6}_{-3.0}$	$11.9 \pm 0.3 \pm 0.4^{+1.0}_{-1.9}$
5– 6	$15.7 \pm 0.5 \pm 0.6^{+2.4}_{-4.3}$	$14.6 \pm 0.4 \pm 0.5^{+1.7}_{-3.2}$	$13.6 \pm 0.4 \pm 0.5^{+1.1}_{-2.1}$
6– 7	$18.4 \pm 0.7 \pm 0.7^{+2.6}_{-4.8}$	$17.5 \pm 0.5 \pm 0.6^{+1.9}_{-3.5}$	$15.4 \pm 0.5 \pm 0.6^{+1.2}_{-2.3}$
7– 8	$20.1 \pm 0.8 \pm 0.7^{+2.6}_{-4.8}$	$17.6 \pm 0.7 \pm 0.6^{+1.8}_{-3.4}$	$17.8 \pm 0.7 \pm 0.6^{+1.3}_{-2.5}$
8– 9	$21.4 \pm 1.0 \pm 0.8^{+2.6}_{-4.7}$	$21.2 \pm 0.9 \pm 0.8^{+1.9}_{-3.5}$	$18.6 \pm 1.0 \pm 0.7^{+1.4}_{-2.6}$
9–10	$25.3 \pm 1.4 \pm 0.9^{+2.8}_{-5.1}$	$23.1 \pm 1.2 \pm 0.8^{+1.8}_{-3.4}$	$21.5 \pm 1.3 \pm 0.8^{+1.3}_{-2.5}$
10–11	$27.6 \pm 1.7 \pm 1.0^{+2.9}_{-5.2}$	$24.6 \pm 1.5 \pm 0.9^{+1.8}_{-3.3}$	$20.2 \pm 1.7 \pm 0.7^{+1.3}_{-2.5}$
11–12	$32.8 \pm 2.2 \pm 1.2^{+2.9}_{-5.2}$	$27.0 \pm 2.0 \pm 1.0^{+1.8}_{-3.3}$	$24.7 \pm 2.2 \pm 0.9^{+1.3}_{-2.4}$
12–13	$28.9 \pm 2.6 \pm 1.0^{+2.6}_{-4.7}$	$31.3 \pm 2.6 \pm 1.1^{+1.9}_{-3.5}$	$24.1 \pm 2.8 \pm 0.9^{+1.3}_{-2.4}$
13–14	$29.8 \pm 3.6 \pm 1.1^{+2.6}_{-4.8}$	$26.5 \pm 2.9 \pm 1.0^{+1.5}_{-2.8}$	$32.5 \pm 4.1 \pm 1.2^{+1.5}_{-2.8}$
	$3.5 < y < 4.0$	$4.0 < y < 4.5$	
0– 1	$6.3 \pm 0.3 \pm 0.2^{+0.9}_{-1.8}$	$4.8 \pm 0.4 \pm 0.2^{+0.7}_{-1.4}$	
1– 2	$6.9 \pm 0.2 \pm 0.2^{+0.8}_{-1.5}$	$6.1 \pm 0.2 \pm 0.2^{+0.6}_{-1.2}$	
2– 3	$7.9 \pm 0.2 \pm 0.3^{+0.6}_{-1.2}$	$6.7 \pm 0.3 \pm 0.2^{+0.4}_{-0.9}$	
3– 4	$9.3 \pm 0.3 \pm 0.3^{+0.6}_{-1.1}$	$8.1 \pm 0.4 \pm 0.3^{+0.4}_{-0.9}$	
4– 5	$10.2 \pm 0.3 \pm 0.4^{+0.6}_{-1.2}$	$8.4 \pm 0.5 \pm 0.3^{+0.4}_{-0.8}$	
5– 6	$11.6 \pm 0.5 \pm 0.4^{+0.7}_{-1.4}$	$10.7 \pm 0.7 \pm 0.4^{+0.4}_{-0.9}$	
6– 7	$12.7 \pm 0.6 \pm 0.5^{+0.8}_{-1.6}$	$13.3 \pm 1.1 \pm 0.5^{+0.5}_{-1.1}$	
7– 8	$15.7 \pm 0.9 \pm 0.6^{+1.0}_{-1.9}$	$13.7 \pm 1.4 \pm 0.5^{+0.6}_{-1.2}$	
8– 9	$16.6 \pm 1.2 \pm 0.6^{+1.0}_{-2.0}$	$15.2 \pm 2.0 \pm 0.5^{+0.7}_{-1.4}$	
9–10	$18.0 \pm 1.6 \pm 0.6^{+1.1}_{-2.1}$	$17.0 \pm 2.9 \pm 0.6^{+0.9}_{-1.7}$	
10–11	$19.8 \pm 2.2 \pm 0.7^{+1.1}_{-2.1}$	$17.7 \pm 3.9 \pm 0.6^{+0.8}_{-1.6}$	
11–12	$19.5 \pm 2.9 \pm 0.8^{+1.1}_{-2.0}$		
12–13	$21.9 \pm 4.4 \pm 0.8^{+1.2}_{-2.4}$		

Table 3.14 – $\frac{d\sigma}{dy}$ *in nb for* prompt J/ψ *(assumed unpolarised) and* J/ψ from b*, integrated over* p_T*. The first uncertainty is statistical, the second one is the component of the systematic uncertainty that is correlated between bins and the third one is the uncorrelated component.*

p_T range (GeV/c)	y bin	prompt J/ψ	J/ψ from b
$0-14$	$2.0-2.5$	$5504\pm83\pm381\pm726$	$697\pm27\pm40\pm96$
$0-14$	$2.5-3.0$	$5096\pm21\pm142\pm672$	$608\pm\ 7\pm13\pm84$
$0-14$	$3.0-3.5$	$4460\pm14\pm\ 59\pm589$	$479\pm\ 5\pm\ 5\pm66$
$0-13$	$3.5-4.0$	$3508\pm12\pm\ 40\pm463$	$307\pm\ 4\pm\ 3\pm42$
$0-11$	$4.0-4.5$	$2462\pm12\pm\ 48\pm325$	$180\pm\ 4\pm\ 3\pm25$

3.5.3 Rapidity distributions

Table 3.14 and Fig. 3.27 show the y differential cross-sections $\frac{d\sigma}{dy}$ integrated over p_T, both for unpolarised prompt J/ψ and J/ψ from b. For the two production sources, the cross-sections decrease by a factor approximately equal to 2 between the central and forward regions of the LHCb acceptance.

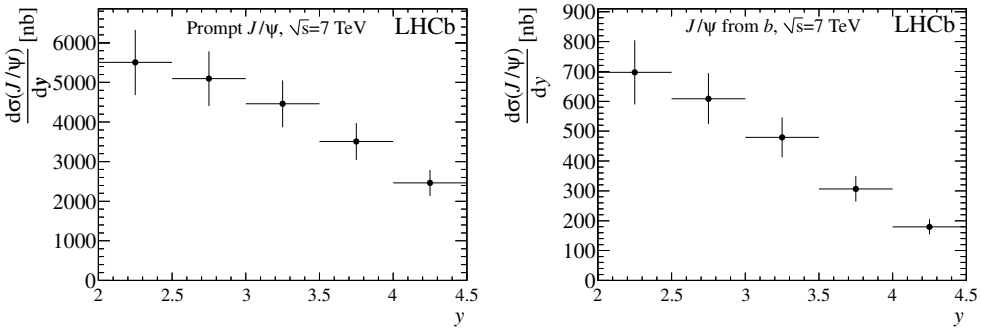

Figure 3.27 – *Differential production cross-section as a function of* y *integrated over* p_T*, for unpolarised* prompt J/ψ (left) *and* J/ψ from b (right)*. The errors are the quadratic sums of the statistical and partially-correlated systematic uncertainties.*

3.5.4 Cross-section extrapolations

Using the LHCb Monte Carlo simulation based on PYTHIA 6.4 and EvtGen [11], the measurement of J/ψ from b of Eq. (3.22) is extrapolated to the full angular acceptance

$$\sigma(pp \to b\bar{b}X) = \alpha_{4\pi} \frac{\sigma\left(J/\psi \text{ from } b,\, p_{\rm T} < 14\,\text{GeV}/c,\, 2 < y < 4.5\right)}{2\mathscr{B}(b \to J/\psi X)}, \qquad (3.24)$$

where $\alpha_{4\pi} = 5.88$ is the ratio of J/ψ from b events in the full range over the number of events in the region $2 < y < 4.5$. The results is

$$\sigma(pp \to b\bar{b}X) = 288 \pm 4 \pm 48\,\mu\text{b}\,, \qquad (3.25)$$

where the first uncertainty is statistical and the second one systematic. The systematic uncertainty includes the uncertainties on the b fractions (2%) and on $\mathscr{B}(b \to J/\psi X)$. No additional uncertainty is assigned to the extrapolation factor $\alpha_{4\pi}$ estimated from the simulation.

The above result is in excellent agreement with that obtained from b decays into $D^0\mu\nu X$ [130]: $\sigma(pp \to b\bar{b}X) = 284 \pm 20 \pm 49\,\mu\text{b}$.

3.5.5 Comparison with cross-sections from the LHCb Monte Carlo simulation

Figures 3.28 and 3.29 show the comparison between the prompt J/ψ and J/ψ from b differential cross-sections measured on data assuming no polarisation with those extracted from the LHCb Monte Carlo simulation. In general, the $p_{\rm T}$ shapes are similar but the overall normalization differs by a factor 3 for the prompt J/ψ component and a factor 2 for the J/ψ from b part, which are higher in the LHCb simulation

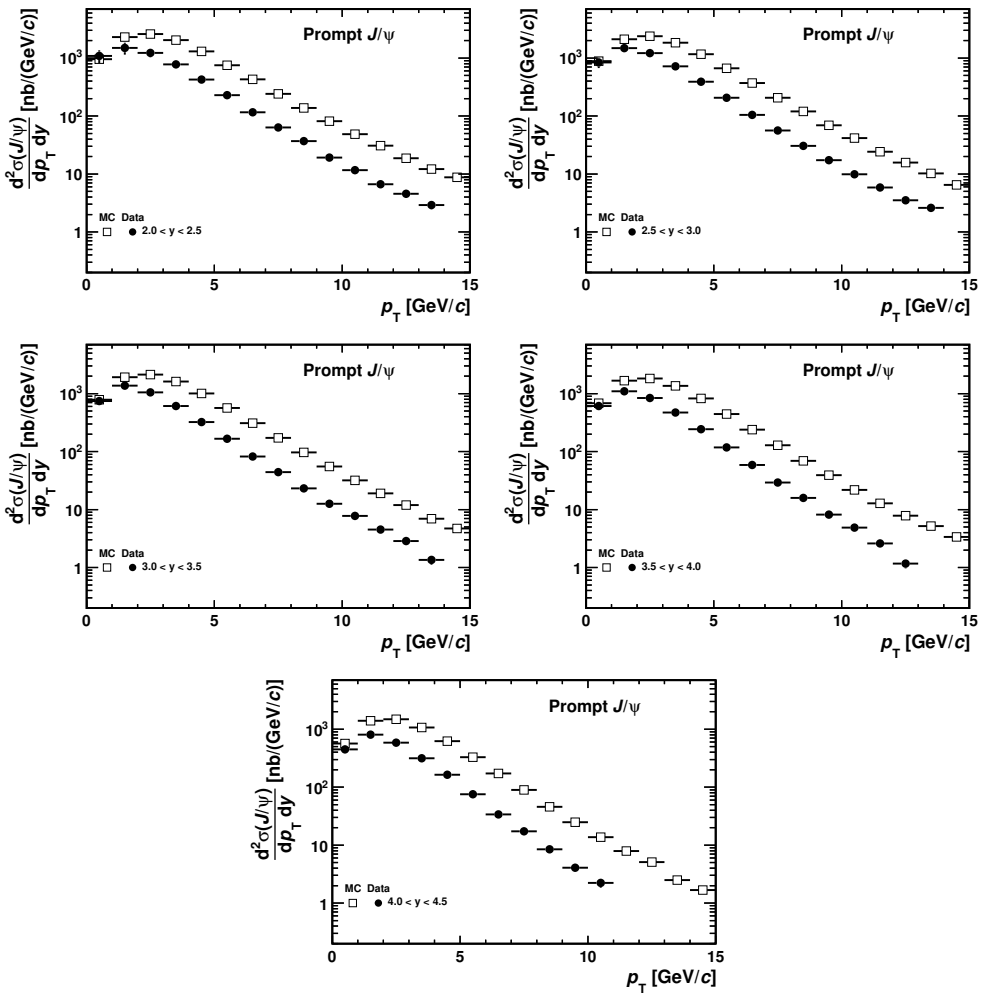

Figure 3.28 – *Differential cross-sections for* prompt J/ψ *production in data and Monte Carlo simulation as a function of* p_{T}*, in bins of rapidity.*

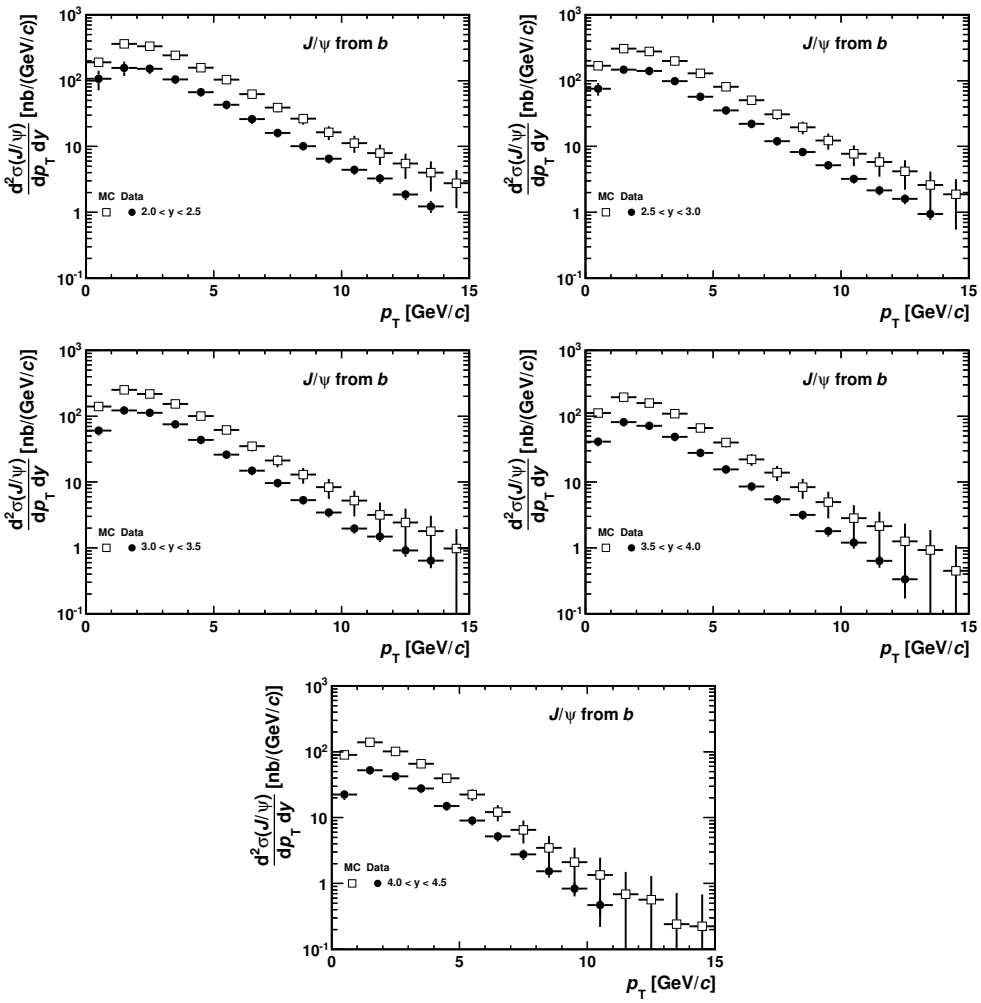

Figure 3.29 – *Differential cross-sections for J/ψ* from *b production in data and Monte Carlo simulation as a function of p_{T}, in bins of rapidity.*

3.5.6 Comparison with the results of the other LHC experiments

The J/ψ production cross-section was measured also by the ALICE [113], ATLAS [114] and the CMS [115] collaborations. The ALICE measurement used $J/\psi \to e^+e^-$ decays in the acceptance region $|y| < 0.9$ and $J/\psi \to \mu^+\mu^-$ decays in the region $2.5 < y < 4.0$ corresponding to the acceptance of their muon detectors. The measurement with the dimuon channels can be directly compared to the LHCb measurement since the acceptances overlap. However, only the inclusive production cross-section (i.e. the sum of the prompt J/ψ and J/ψ from b contribu-

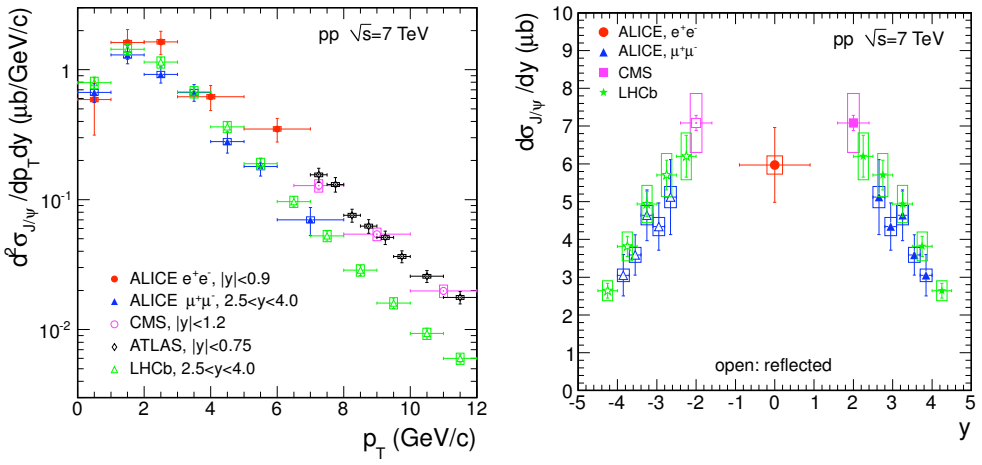

Figure 3.30 – *Inclusive J/ψ cross-sections,* Left*: $\frac{d^2\sigma}{dp_T dy}$ obtained in different rapidity ranges by the LHC experiments,* Right*: $\frac{d\sigma}{dp_T}$ from the LHC experiments. On both figures, the error bars represent the quadratic sum of the statistical and systematic errors, while the systematic uncertainties on luminosity are shown as boxes.*

tions) can be compared because the ALICE detector does not have vertexing devices in the forward acceptance region and therefore cannot separate prompt J/ψ and J/ψ from b. Fig. 3.30 shows a comparison of the inclusive J/ψ cross-section measured by ALICE and LHCb, assuming J/ψ are produced unpolarised. A good agreement is observed between the two measurements.

Prompt J/ψ and J/ψ from b production were mesured also by ATLAS and CMS, in the central region ($|y| < 2.4$) and for high p_T J/ψ (up to 70 GeV/c). Fig 3.31 show a comparison between ATLAS, CMS and LHCb of the prompt J/ψ differential cross-section (*left*) assuming prompt J/ψ are produced unpolarised, and the fraction of J/ψ from b (*right*) [131]. The measurements in similar phase space regions (around $y = 2$) are in good agreement and the combination of these analyses allows to have access to J/ψ production in a very large acceptance range.

3.5.7 Comparison with theoretical models

Figure 3.32 compares the LHCb measurement of the differential prompt J/ψ production with several recent theory predictions computed in the LHCb acceptance region:

- top, left: direct J/ψ production as calculated from NRQCD at leading order in α_s (LO, filled orange uncertainty band) [132] and next-to-leading order

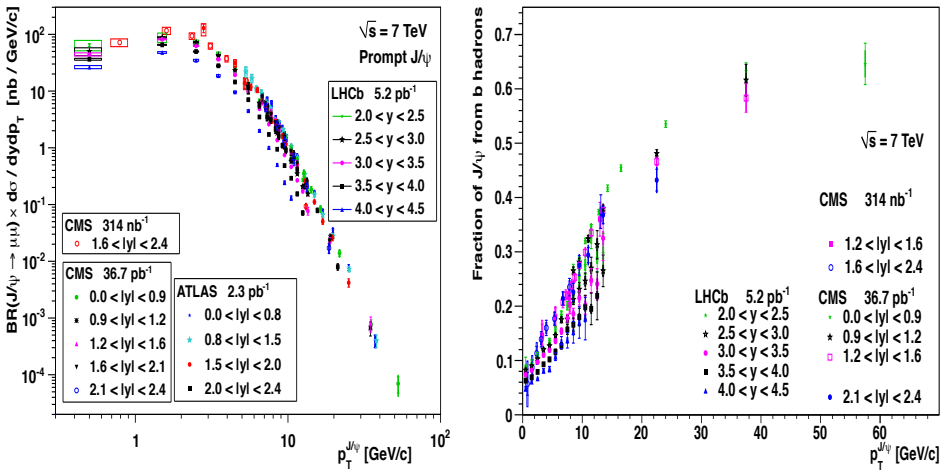

Figure 3.31 – Left*:* $\frac{\mathrm{d}^2\sigma}{\mathrm{d}p_\mathrm{T}\,\mathrm{d}y}$ *of* prompt J/ψ *obtained in different rapidity ranges by the LHC experiments,* Right*:* F_b *from the LHC experiments.*

(NLO), with colour-octet long distance matrix elements determined from HERA and Tevatron data (hashed green uncertainty band) [133], summing the colour-singlet and colour-octet contributions.

- top, right: direct production as calculated from a NNLO⋆ colour-singlet model (CSM, filled red uncertainty band) [112, 134]. The notation NNLO⋆ denotes an evaluation that is not a complete next-to-next leading order computation and that can be affected by unphysical logarithmic corrections, which are however not easily quantifiable. Direct production as calculated from NLO CSM (hashed grey uncertainty band) [109, 111] is also represented.

- bottom, left: prompt J/ψ production as calculated from NRQCD at NLO, including contributions from χ_c decays, summing the colour-singlet and colour-octet contributions [135].

- bottom, right: prompt J/ψ production as calculated from a NLO colour-evaporation model (CEM), including contributions from χ_c decays [136].

It should be noted that some of the theoretical models compute the direct J/ψ production, whereas the prompt J/ψ measurement includes J/ψ from χ_c decays and, to a smaller extent, $\psi(2S)$ decays. However, if one takes into account the feeddown contribution, which has been estimated to be of the order of 30% averaging over several experimental measurements at lower energies [137], a satisfactory agreement is found with the theoretical predictions.

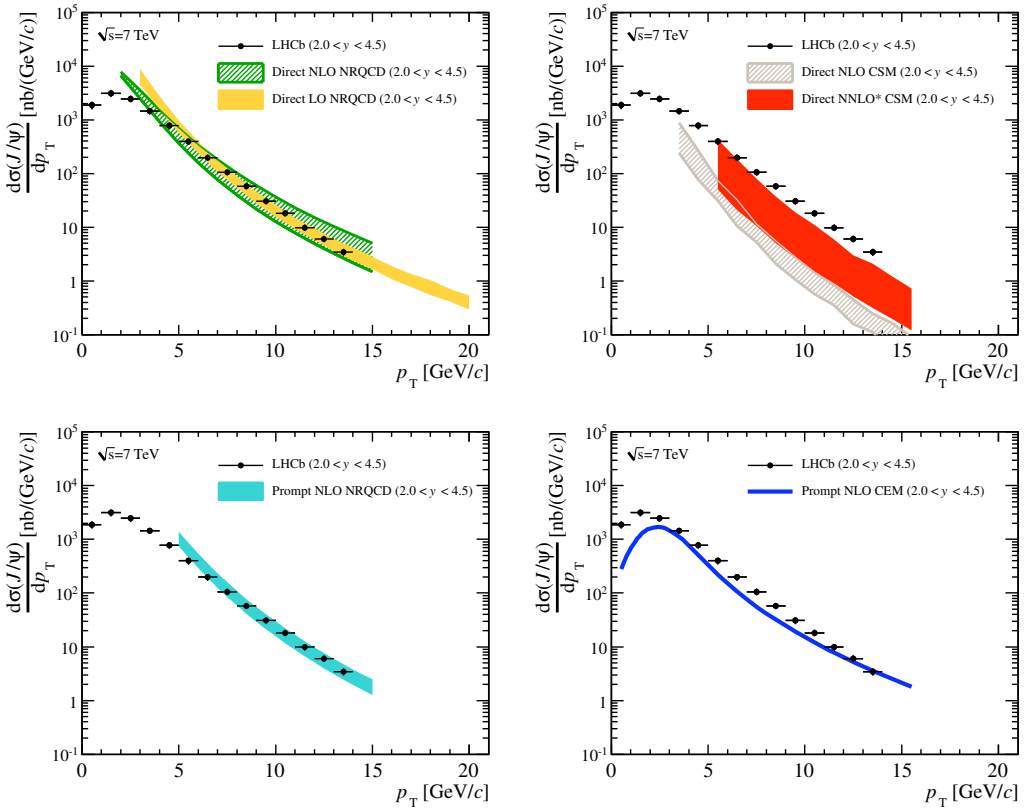

Figure 3.32 – *Comparison of the LHCb results for the differential prompt J/ψ production for unpolarised J/ψ (circles with error bars) with: (top, left) direct J/ψ production as predicted by LO and NLO NRQCD; (top, right) direct J/ψ production as predicted by NLO and NNLO⋆ CSM; (bottom, left) prompt J/ψ production as predicted by NLO NRQCD; (bottom, right) prompt J/ψ production as predicted by NLO CEM.*

The J/ψ from b measurement is compared with the cross-section obtained with a calculation based on the Fixed-Order Next-To-Leading Log (FONLL) mechanism [138–140]. This model predics in fact the production cross-section of b-quarks. The fragmentation of b-quarks into b-hadrons and the decay into a final state with a J/ψ are included to obtain the J/ψ from b cross-section. Figure 3.33 shows the comparison between the LHCb measurement and the FONLL prediction. The theoretical values are obtained using the CTEQ6.6 PDF [33] and using for the b-quark mass $m_b = 4.75\,\text{GeV}/c^2$. The uncertainty bands of Fig. 3.33 include uncertainties from the different scales used, from the values of the b-quark mass and from the PDF.

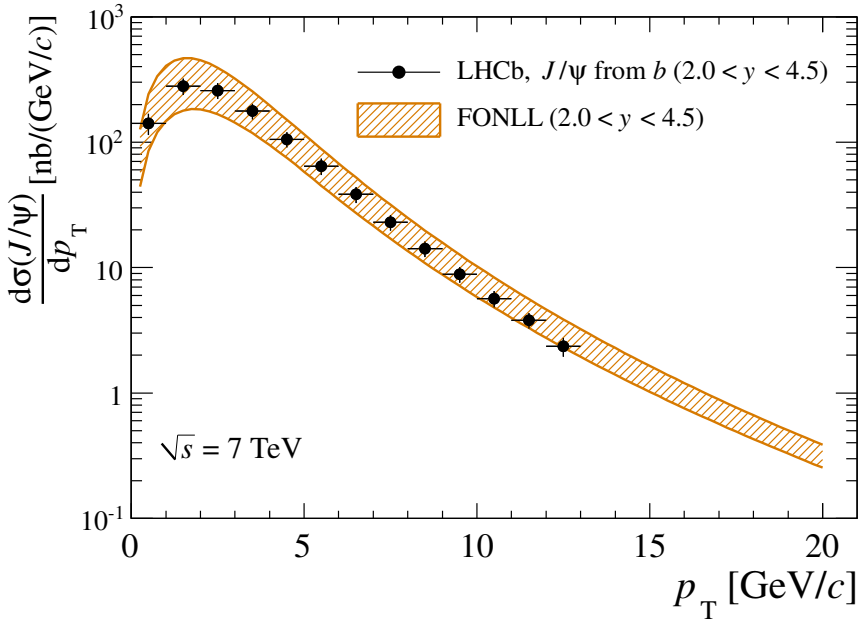

Figure 3.33 – *Comparison of the LHCb results for the differential* J/ψ from b *production with FONLL computations.*

3.6 Conclusions

The cross-section for prompt J/ψ and J/ψ from b production has been measured in the LHCb acceptance. The results are in good agreement with various theoretical models if one takes into account feeddown from excited charmonium states, proving that important theoretical progresses were made in the past years to understant quarkonium production. However, more observables are needed to distiguish between the different approaches to charmonium production. J/ψ polarization measurements may give valuable input for this but cross-section measurement of various charmonium states will also be crucial to understand the production mechanisms. Data collected by the LHCb experiment allowed to already obtain important results about $\psi(2S)$ [141] and χ_c production [142]. A lot of other measurements will follow when the size of the data sample will increase.

Conclusions

Several aspects of the LHCb experiment work has been presented in this document. All the preparations done in the past years have been validated when taking the first LHCb data, but consolidation will be needed in the future so that these tools and analyses can be continued.

The LHCb generation software has been explained. This is a flexible framework in which various generators can be plugged in. The main production generator used is the PYTHIA 6 generator, but it will be replaced progressively by the new PYTHIA 8 generator, written in C++, and which brings significant improvements to the description of hadronic collisions, in particular for diffractive events. Work has started to integrated it in LHCb and the plan is to completely replace the PYTHIA 6 Fortran generator by PYTHIA 8 in 2013. EvtGen is also a very important generator for LHCb. It has been successfully interfaced and used since several years now, and new models or functionalities will be added to it in the future. LHCb collaborators also help maintaining the software so that it will be possible to use it in the long term.

The calorimeter trigger allowed to commission the experiment, to take its first data and to perform the first analyses. The system as it was designed proved to be very robust to exploit. Small adaptations were need in particular to cope with the higher particle multiplicity seen with respect to what was foreseen. The major difficulty in running the system was to time align all data exchange between the different boards, and the situation there is still not perfect. Tests and studies how to improve this are ongoing. The other preoccupation of the next years will be to ensure that the trigger efficiency remains constant over time and over the full calorimeters.

The measurement of the J/ψ production cross-section showed that the LHCb data is of high quality and that measurements of quarkonium production in the forward region is useful to undertand their production mechanisms. This however has a cost because the size of the collected J/ψ sample is huge. In the future, preselections in the trigger will throw away low momentum prompt J/ψ in order to concentrate on higher momentum J/ψ where the statistics is lower. More importantly, reconstruction of J/ψ will allow to have access to "exotic" charmonium states, like the $X(3872)$ or the Z^+ particles that decay with a J/ψ in the final state.

This will allow the experiment to contribute to this field where many puzzles are still open.

APPENDIX A

Cabling of the L0CALO

A.1 Backplane

The ethernet cables located on the top of the calorimeters are plugged in the backplane, in RJ45 connectors located on the back of the backplane. Figure A.1 shows the function of each RJ45 connectors for ECAL Front-End Boards, HCAL Front-End Boards, PS Front-End Boards and Trigger Validation Boards. The list of all cables with their identification number and their length is given in Ref. [143].

A.2 Optical Cables

A.2.1 Patch panel in the cavern

Figure A.2 gives the position of the optical cables connected to the TVB and the SPD Control Boards in the patch panel located in the cavern, in the Q2A01 rack, behind the muon detector. The TVB and SPD Control Boards are identified by their crate and slot numbers as explained in Chapter 2.

A.2.2 Patch panel in the barrack

Figure A.3 gives the position of the optical cables in the patch pannel located in the barrack, in rack D3B01, close to the Selection Boards. The TVB and SPD Control Boards are indicated with the same convention.

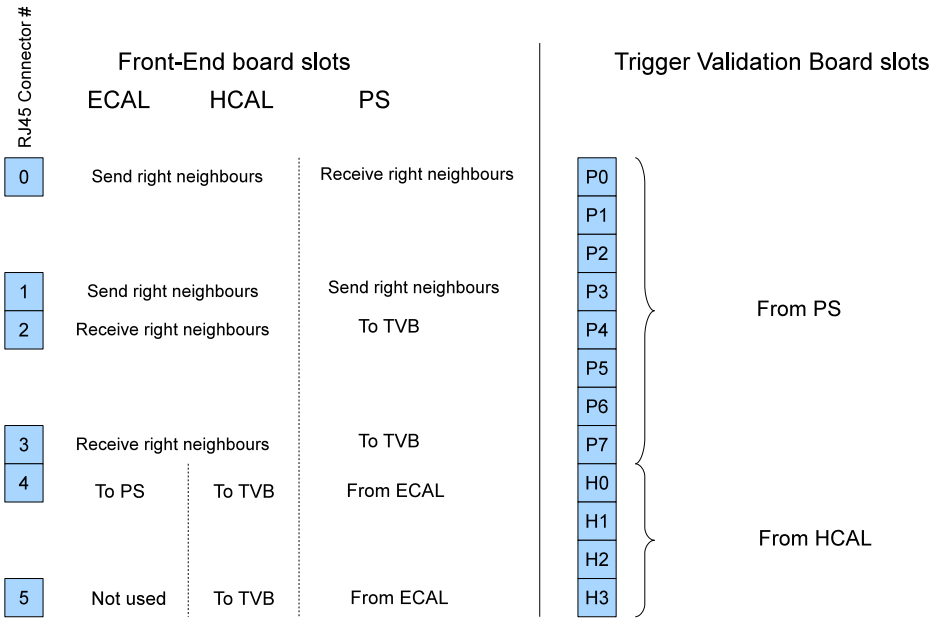

Figure A.1 – *Ethernet cable mapping in the Calorimeter backplane.*

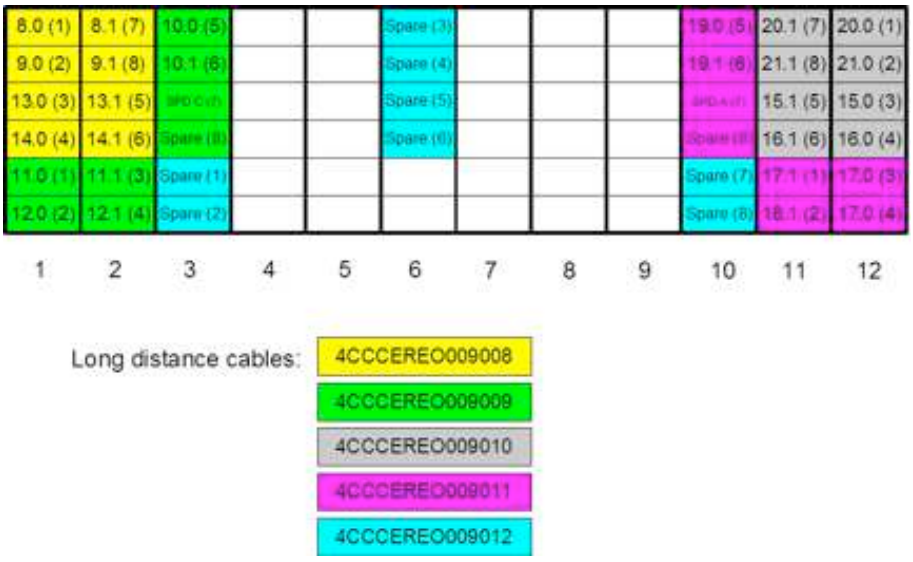

Figure A.2 – *Optical cable patch pannel (cavern).*

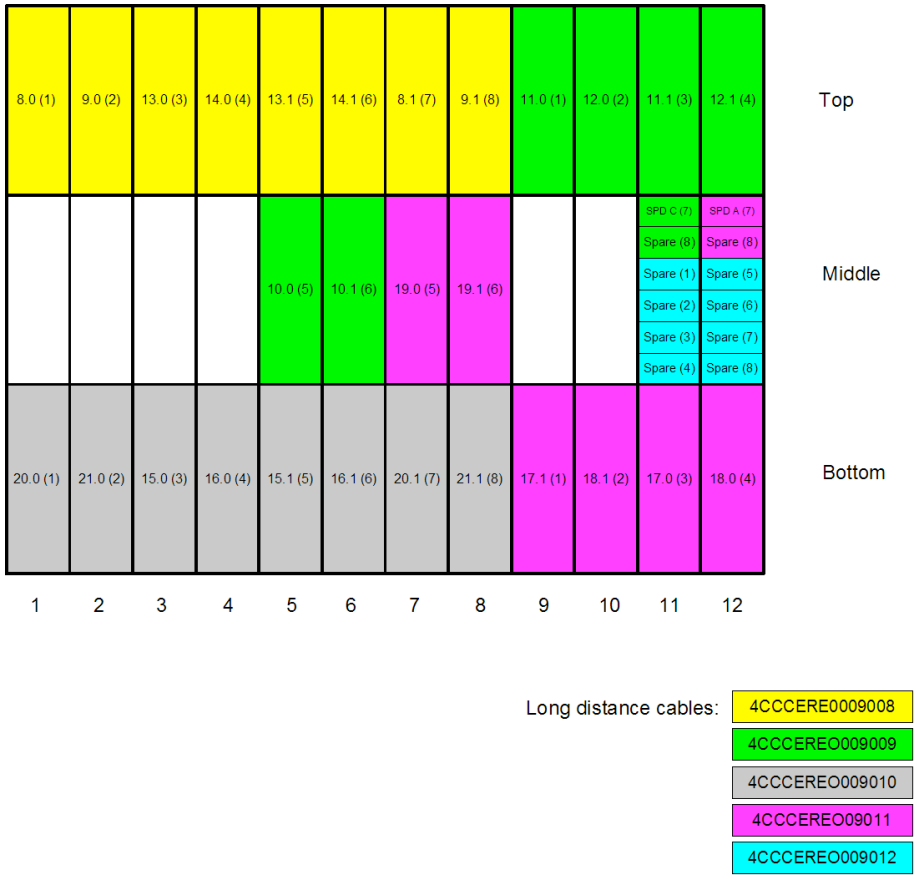

Figure A.3 – *Optical cable patch pannel (barrack).*

APPENDIX B

ECAL and HCAL Trigger FPGA configuration registers

This appendix lists the different configuration registers of the Trigger FPGA, and their interface to the LHCb experimental control system (as a PVSS Device Unit, called `FEBXCAL_TrigPGA`).

The Trigger FPGA is configured through the SPECS system, using the I^2C protocol, with the following parameters:

- **Address**: 0x53,
- I^2C **bus**: 12,
- **Mode of addressing**: with sub-address (the first byte of transferred data is the address of the register).

All registers are 16 bit long. For the I^2C transfer, the 8 most significant bits (MSB) are read and written first.

B.1 Setup Register (sub-address 0)

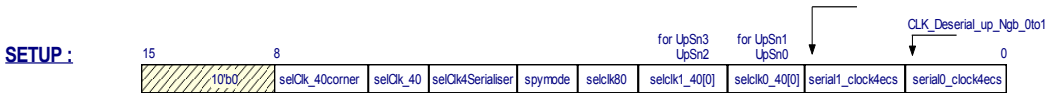

Figure B.1 – *Setup Register (sub-address 0).*

Table B.1 – *Setup register bit assignments.*

Bit	Name	Read/ Write	Description
0	`Serial0_clock4ecs`	R	Sampling of the clock transmitted by the cable 1 for right neighbours
1	`Serial1_clock4ecs`	R	Sampling of the clock transmitted by the cable 0 for right neighbours
2	`Selclk0_40`	R/W	Use falling (1) or raising (0) clock's edge to sample cable 1 right neighbour data
3	`Selclk1_40`	R/W	Use falling (1) or raising (0) clock's edge to sample cable 0 right neighbour data
4	`Selclk80`	R/W	Use falling (1) or rising (0) clock's edge to sample the input channels at 80 MHz
5	`Spymode`	R/W	When set to 1, store trigger results in spy memory
6	`SelClk4Serialiser`	R/W	Use falling (1) or rising (0) clock's edge to serialize data sent to TVB or PS FEB
7	`SelClk_40`	R/W	Use falling (1) or rising (0) clock's edge to sample top neighbour data
8	`SelClk_40corner`	R/W	Use falling (1) or rising (0) clock's edge to sample corner neighbour data

B.2 BCID Reset Register (sub-address 1)

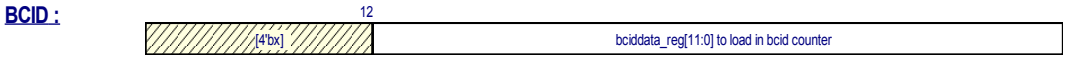

Figure B.2 – *BCID Reset Register (sub-address 1).*

Table B.2 – *BCID reset register bit assignments.*

Bit	Name	Read/ Write	Description
$0-11$	`Bciddata_reg`	R/W	Delay to apply to the BCID Reset TFC command, in number of clock cycles

B.3 Test length register (sub-address 2)

Must always be written with the value 0xFF.

B.4 Data offset register (sub-address 3)

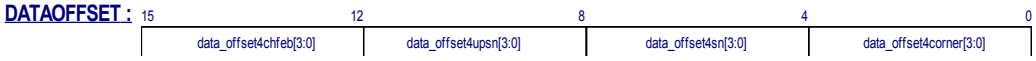

Figure B.3 – *Data offset Register (sub-address 3).*

The values stored in this register are the delays to apply to each categories of input to time align them. The value which is written is in fact $15-N$ where N is the number of clock cycles to the channel needs to be delayed ($0 < N < 15$).

Table B.3 – *Data offset (latency) register bit assignments.*

Bit	Name	Read/ Write	Description
$0-3$	`Data_offset4corner`	R/W	N for the corner neighbour
$7-4$	`Data_offset4sn`	R/W	N for the top neighbours
$11-8$	`Data_offset4upsn`	R/W	N for the right neighbours
$15-12$	`Data_offset4chfeb`	R/W	N for the 80 MHz input channels

B.5 Channel Clear Registers (sub-addresses 4, 5, 6)

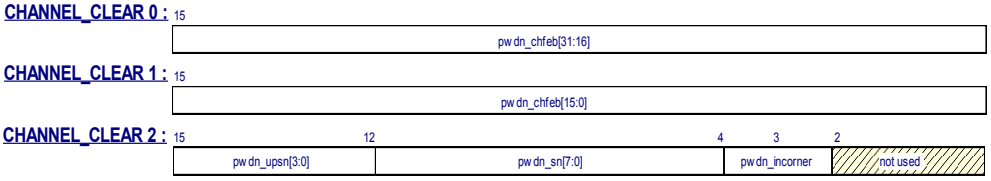

Figure B.4 – *Channel Clear Registers (sub-addresses 4, 5 and 6).*

Table B.4 – *Channel clear register bit assignments.*

Bit	Name	Read/ Write	Description
			sub-address 4
0 – 15	`Pwdn_chfeb`	R/W	Mask (0) or unmask (1) channels 16 to 31 of the input channels at 80 MHz. Bit 0 corresponds to channel `E16`, bit 15 to channel `E31`.
			sub-address 5
0 – 15	`Pwdn_chfeb`	R/W	Mask (0) or unmask (1) channels 0 to 15 of the input channels at 80 MHz. Bit 0 corresponds to channel `E0`, bit 15 to channel `E15`.
			sub-address 6
3	`Pwdn_incorner`	R/W	Mask (0) or unmask (1) the corner neighbour.
4 – 11	`Pwdn_sn`	R/W	Mask (0) or unmask (1) the top neighbours: bit 4 corresponds to `In_Sn0`, bit 11 to `In_Sn7`.
12 – 15	`Pwdn_upsn`	R/W	Mask (0) or unmask (1) the right neighbours: bit 12 corresponds to `In_Up_Sn0`, bit 15 to `In_Up_Sn3`.

B.6 Reset TrigPGA Register (sub-address 10)

Writing 1 in this register resets the Trigger FPGA.

B.7 Date ID and Serial ID registers (sub-addresses 12 and 13)

These registers store the date and the version number of the firmware loaded in the Trigger FPGA. These registers have a special feature: a random value must be written in these registers before reading them.

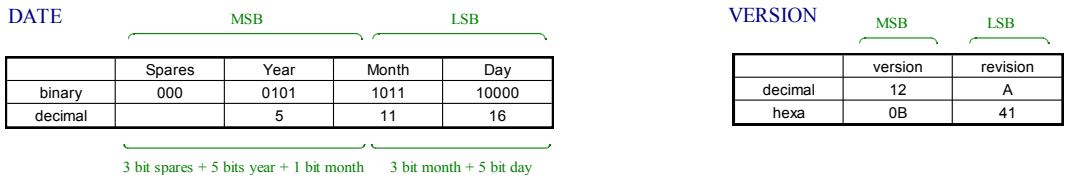

Figure B.5 – *Date and serial ID registers (sub-addresses 12 and 13).*

Table B.5 – *Date and serial ID register bit assignments.*

Bit	Name	Read/ Write	Description
			sub-address 12
0 – 4	`Day`	R	Day of the date of the firmware
5 – 8	`Month`	R	Month of the date of the firmware
9 – 12	`Year`	R	Year of the date of the firmware
			sub-address 13
0 – 7	`Revision`	R	Revision (coded in ASCII) of the firmware
8 – 15	`Version`	R	Version number of the firmware

B.8 Spy memory usage

The results of the calculation of the Trigger FPGA can be store in two "spy memories" (RAMs) containing each 256 words of 16 bits width. The filling of the RAMs starts when a Calibration Command is received from the TFC system. This command can be delayed by a programmable number of clock cycles, which is stored in the **"Test Delay Register"** at the sub-address **11**.

The positions in the RAM where to start writing or reading data (usually 0) is selected writing in the **"NTA Register"** at the sub-address **7**. Once the Calibration Command has been received, the trigger results in the RAM are accessible through two 16 bit registers at the sub-addresses **8** and **9**. After each read operation, the position at which the RAM is acccessed is incremented automatically. The format of the RAMs is shown in Fig. B.6 and in Table B.6.

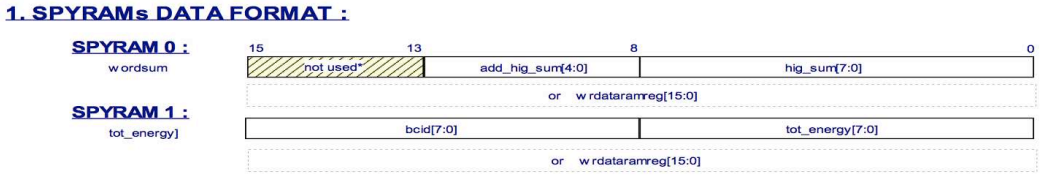

Figure B.6 – *Format of the Spy RAMs (sub-addresses 8 and 9).*

Table B.6 – *Format of the Spy RAMs.*

Bit	Name	Description
		sub-address 8
0 – 7	`Hig_sum`	Energy of the maximum energy cluster
8 – 12	`Add_hig_sum`	Address of the maximum energy cluster. The address must be decoded as `Add_hig_sum[2,1,0,4,3]`.
		sub-address 9
0 – 7	`Tot_energy`	Total energy on the board
8 – 15	`Bcid`	BCID of the event

The procedure to use the Spy memories is the following:

1. Set the "Spy mode" bit in the **"Setup Register"** to 1,
2. Set the test length to 0 in the **"Test Length Register"**,
3. Reset the Trigger FPGA, writing 1 in the **"Reset TrigPGA Register"**,
4. Set the test length to 255 in the **"Test Length Register"**,
5. Wait for the Calibration Command from the TFC,
6. Write 0 in the **"NTA Register"**,
7. Read the Spy RAMs.

B.9 PVSS Device Unit

The hardware type interfacing PVSS to the Trigger FPGA is `FebXCAL_TrigPGA` which is a member of the global hardware type `FebXCAL`. The `FebXCAL_TrigPGA` contains the following device unit registers:

- `SETUP`, of type I^2C and size 17 bytes. This PVSS register is mapped to the concatenation of the registers: **"Setup", "BCID Reset", "Test length", "Data offset", "Channel clear 0", "Channel clear 1" and "Channel clear 2"**, in this order.
- `RESET`, of type I^2C and size 2 bytes. It is mapped to the **"Reset TrigPGA"** register.
- `IDENTIFICATION`, of type I^2C and size 4 bytes. It is mapped to the concatenation of the **"Date ID" and "Serial ID"** registers.
- `NTA`, of type I^2C and size 2 bytes. It is mapped to the **"NTA"** register.
- `RAM0`, of type I^2C and size 2 bytes. It is mapped to the sub-address 8 of the Trigger FPGA.
- `RAM1`, of type I^2C and size 2 bytes. It is mapped to the sub-address 9 of the Trigger FPGA.
- `Crate`, of type integer. It indicates the crate number of the board.
- `Slot`, of type integer. It indicates the crate number of the board.

- `Status`, of type integer. It indicates the configuration state of the board, and is used by the Finite State Machine (FSM) of the LHCb configuration system.
- `Side`, of type string. It contains the location of the board of the right neighbours.
- `Top`, of type string. It contains the location of the board of the top neighbours.
- `Corner`, of type string. It contains the location of the board of the corner neighbour.

APPENDIX C

Selection Boards configuration registers

This appendix lists the different configuration registers of the Selection Boards, and their interface to the LHCb experimental control system (as a PVSS Decive Unit, called `SelectionBoard`).

The registers are 32 bit wide and are accessed through the parallel bus of the CCPC interface card. Since there are 5 Input FPGAs, the address of the registers for these FPGAs will depend on the FPGA number, N.

C.1 Input FPGAs

Table C.1 – *Registers of the Selection Board Input FPGAs.*

Bit	Description
	ResetECS (address: 0x0N200000)
0	Write 1 to reset the Spy Memory
1	Write 1 to reset the Bit Error Rate (BER) counter of Channel 1
2	Write 1 to reset the Bit Error Rate (BER) counter of Channel 2
3	Write 1 to reset the Bit Error Rate (BER) counter of Channel 3
4	Write 1 to reset the Bit Error Rate (BER) counter of Channel 4
5	Write 1 to reset the Bit Error Rate (BER) counter of Channel 5
6	Write 1 to reset the Bit Error Rate (BER) counter of Channel 6
7	Write 1 to reset the measurement of difference between the "Data Valid" and "BCID Reset" signals for Channel 1
8	Write 1 to reset the measurement of difference between the "Data Valid" and "BCID Reset" signals for Channel 1
9	Write 1 to reset the measurement of difference between the "Data Valid" and "BCID Reset" signals for Channel 1
10	Write 1 to reset the measurement of difference between the "Data Valid" and "BCID Reset" signals for Channel 1
11	Write 1 to reset the measurement of difference between the "Data Valid" and "BCID Reset" signals for Channel 1
12	Write 1 to reset the measurement of difference between the "Data Valid" and "BCID Reset" signals for Channel 1
13 – 31	Not used
	Config1ECS (address: 0x0N101000)
0 – 4	Delay of Channel 1 (up to 32 clock cycles)
5 – 9	Delay of Channel 2 (up to 32 clock cycles)
10 – 14	Delay of Channel 3 (up to 32 clock cycles)
15 – 19	Delay of Channel 4 (up to 32 clock cycles)
20 – 24	Delay of Channel 5 (up to 32 clock cycles)
25 – 29	Delay of Channel 6 (up to 32 clock cycles)
30	Write 1 to stop the flashing of the LEDs on the front pannel
31	Not used

Table C.2 – *Registers of the Selection Board Input FPGAs (cont.).*

Bit	Description
	Config2ECS (address: 0x0N102000)
0	Write 1 to mask Channel 1
1	Write 1 to mask Channel 2
2	Write 1 to mask Channel 3
3	Write 1 to mask Channel 4
4	Write 1 to mask Channel 5
5	Write 1 to mask Channel 6
6	Write 1 when asynchronous data are received
7	Write 0 to start the input data synchronization and 1 to stop it
8 – 17	Delay of the BCID reset signal[1] (up to 1024 cycles)
18 – 27	Delay of the BCID reset signal[1] (up to 1024 cycles)
28	Write 1 to detect link errors also for masked channels
29	Write 1 to start the BER test of Channel 5
30	Write 1 to start the BER test of Channel 6
31	Not used
	Config3ECS (address: 0x0N103000)
0 – 9	Delay of the BCID reset signal[1] (up to 1024 cycles)
10 – 19	Delay of the BCID reset signal[1] (up to 1024 cycles)
20	Write 1 to start the BER test of Channel 2
21	Write 1 to start the BER test of Channel 3
22	Write 1 to start the BER test of Channel 4
23	Write 1 to start the BER test of Channel 1
24 – 27	Delay to align patterns for the BER test of Channel 1
28 – 31	Delay to align patterns for the BER test of Channel 2

[1] The total BCID Reset delay is the sum of the 2 delays in Config2ECS and the 2 delays in Config3ECS.

Table C.3 – *Registers of the Selection Board Input FPGAs (cont.).*

Bit	Description
	Config4ECS (address: 0x0N104000)
0 – 3	Delay to align patterns for the BER test of Channel 3
4 – 7	Delay to align patterns for the BER test of Channel 4
8 – 11	Delay to align patterns for the BER test of Channel 5
12 – 15	Delay to align patterns for the BER test of Channel 6
16 – 31	Not used
	StatusA (address: 0x0N10A000)
0	equal to 1 if Channel 1 link is sending valid data
1	equal to 1 if Channel 1 link is in error
2	equal to 1 if Channel 2 link is sending valid data
3	equal to 1 if Channel 2 link is in error
4	equal to 1 if Channel 3 link is sending valid data
5	equal to 1 if Channel 3 link is in error
6	equal to 1 if Channel 4 link is sending valid data
7	equal to 1 if Channel 4 link is in error
8	equal to 1 if Channel 5 link is sending valid data
9	equal to 1 if Channel 5 link is in error
10	equal to 1 if Channel 6 link is sending valid data
11	equal to 1 if Channel 6 link is in error
12 – 31	not used
	StatusB (address: 0x0N10B000)
0 – 31	BER test error counter for Channel 1
	StatusC (address: 0x0N10C000)
0 – 31	BER test error counter for Channel 2
	StatusD (address: 0x0N10D000)
0 – 31	BER test error counter for Channel 3
	StatusE (address: 0x0N10E000)
0 – 31	BER test error counter for Channel 4
	StatusF (address: 0x0N10F000)
0 – 31	BER test error counter for Channel 5
	Status10ECS (address: 0x0N110000)
0 – 31	BER test error counter for Channel 6

Table C.4 – *Registers of the Selection Board Input FPGAs (cont.).*

Bit	Description
	Status11ECS (address: 0x0N111000)
0 – 11	Distance between Data Valid and BCID Reset for Channel 1
12 – 23	Number of IDLE transmitted between 2 BCID Reset for Channel 1
24 – 30	Number of Data Valid to 0 transitions between 2 BCID Reset for Channel 1
31	Equal to 1 when the above measurements are correct for Channel 1
	Status12ECS (address: 0x0N112000)
0 – 11	Distance between Data Valid and BCID Reset for Channel 2
12 – 23	Number of IDLE transmitted between 2 BCID Reset for Channel 2
24 – 30	Number of Data Valid to 0 transitions between 2 BCID Reset for Channel 2
31	Equal to 1 when the above measurements are correct for Channel 2
	Status13ECS (address: 0x0N113000)
0 – 11	Distance between Data Valid and BCID Reset for Channel 3
12 – 23	Number of IDLE transmitted between 2 BCID Reset for Channel 3
24 – 30	Number of Data Valid to 0 transitions between 2 BCID Reset for Channel 3
31	Equal to 1 when the above measurements are correct for Channel 3
	Status14ECS (address: 0x0N114000)
0 – 11	Distance between Data Valid and BCID Reset for Channel 4
12 – 23	Number of IDLE transmitted between 2 BCID Reset for Channel 4
24 – 30	Number of Data Valid to 0 transitions between 2 BCID Reset for Channel 4
31	Equal to 1 when the above measurements are correct for Channel 4
	Status15ECS (address: 0x0N115000)
0 – 11	Distance between Data Valid and BCID Reset for Channel 5
12 – 23	Number of IDLE transmitted between 2 BCID Reset for Channel 5
24 – 30	Number of Data Valid to 0 transitions between 2 BCID Reset for Channel 5
31	Equal to 1 when the above measurements are correct for Channel 5
	Status16ECS (address: 0x0N116000)
0 – 11	Distance between Data Valid and BCID Reset for Channel 6
12 – 23	Number of IDLE transmitted between 2 BCID Reset for Channel 6
24 – 30	Number of Data Valid to 0 transitions between 2 BCID Reset for Channel 6
31	Equal to 1 when the above measurements are correct for Channel 6
	Status16ECS (address: 0x0NFFFFF0)
0 – 31	Date of the firmare loaded in the FGPA (format: DDMMYYYY)

C.2 Process FPGA

Table C.5 – *Registers of the Selection Board Process FPGA.*

Bit	Description
	Config1ECS (address: 0x06101000)
0	Write 1 to send IDLE to the L0DU, 0 to send data (1st output)
1	Write 1 to send IDLE to the L0DU, 0 to send data (2nd output)
2	Write 1 to send IDLE to the TELL1, 0 to send data
3 – 14	Number of IDLE patterns to send in test mode
15	Write 1 to reset GOL of 1st output to L0DU
16	Write 1 to reset GOL of 2nd output to L0DU
17	Write 1 to reset GOL of output to TELL1
18	Write 1 to set hadron board as Slave 1
19	Write 1 to set hadron board as Slave 2
20 – 23	Not used
24	Write 1 to send test pattern between slave and master hadron boards
25 – 26	Type of test pattern: 0 for a 16 bit counter, 1 for a pattern loaded in RAM, 2 for a connectivity test pattern.
27	Write 1 to bypass the address LUT for data sent to TELL1
28 – 31	Delay to apply to data comming from slave boards (up to 16 cycles)
	Config2ECS (address: 0x06102000)
0	Write 1 to mask Channel 1 of Input FPGA 1
1	Write 1 to mask Channel 2 of Input FPGA 1
2	Write 1 to mask Channel 3 of Input FPGA 1
3	Write 1 to mask Channel 4 of Input FPGA 1
4	Write 1 to mask Channel 5 of Input FPGA 1
5	Write 1 to mask Channel 6 of Input FPGA 1
6	Write 1 to mask Channel 1 of Input FPGA 2
7	Write 1 to mask Channel 2 of Input FPGA 2
8	Write 1 to mask Channel 3 of Input FPGA 2
9	Write 1 to mask Channel 4 of Input FPGA 2
10	Write 1 to mask Channel 5 of Input FPGA 2
11	Write 1 to mask Channel 6 of Input FPGA 2
12	Write 1 to mask Channel 1 of Input FPGA 3
13	Write 1 to mask Channel 2 of Input FPGA 3
14	Write 1 to mask Channel 3 of Input FPGA 3
15	Write 1 to mask Channel 4 of Input FPGA 3
16	Write 1 to mask Channel 5 of Input FPGA 3
17	Write 1 to mask Channel 6 of Input FPGA 3

Table C.6 – *Registers of the Selection Board Process FPGA (cont.).*

Bit	Description
	Config2ECS (address: 0x06102000, cont.)
18	Write 1 to mask Channel 1 of Input FPGA 4
19	Write 1 to mask Channel 2 of Input FPGA 4
20	Write 1 to mask Channel 3 of Input FPGA 4
21	Write 1 to mask Channel 4 of Input FPGA 4
22	Write 1 to mask Channel 5 of Input FPGA 4
23	Write 1 to mask Channel 6 of Input FPGA 4
24	Write 1 to mask Channel 1 of Input FPGA 5
25	Write 1 to mask Channel 2 of Input FPGA 5
26	Write 1 to mask Channel 3 of Input FPGA 5
27	Write 1 to mask Channel 4 of Input FPGA 5
28	Write 1 to using rising edge of the clock to sample TFC signals
29	Write 1 to send test pattern to the TELL1
30	Write 1 to send test pattern to the L0DU (1^{st} output)
31	Write 1 to send test pattern to the L0DU (2^{dn} output)
	Config3ECS (address: 0x06103000)
$0-9$	Delay of the BCID reset signal (up to 1024 cycles)[2]
$10-19$	Delay of the BCID reset signal (up to 1024 cycles)[2]
$20-29$	Delay of the BCID reset signal (up to 1024 cycles)[2]
30	Not used
31	Write 1 to process data from slave boards (hadron)
	Config4ECS (address: 0x06104000)
$0-9$	Delay of the BCID reset signal (up to 1024 cycles)[2]
10	Not used
11	Write 1 to start the test pattern, 0 to stop it
$12-23$	BCID where to start sending IDLE at the end of the cycle (e.g. to send 3 IDLE, set $3561 = 3564 - 3$)

[2] The total BCID Reset delay is the sum of the 3 delays in Config3ECS and the delay in Config4ECS.

Table C.7 – *Registers of the Selection Board Process FPGA (cont.).*

Bit	Description
	Config4ECS (address: 0x06104000, cont.)
24 – 27	Not used
28 – 31	Delay for the data sent to the TELL1 (up to 16 clock cycles)
	Config8ECS (address: 0x06108000)
0 – 7	Event type sent to TELL1
8 – 17	Not used
18	Write 1 if channels 1 and 2 are duplicate
19	Write 1 if channels 3 and 4 are duplicate
20	Write 1 if channels 5 and 6 are duplicate
21	Write 1 if channels 7 and 8 are duplicate
22	Write 1 if channels 9 and 10 are duplicate
23	Write 1 if channels 11 and 12 are duplicate
24	Write 1 if channels 13 and 14 are duplicate
25	Write 1 if channels 15 and 16 are duplicate
26	Write 1 if channels 17 and 18 are duplicate
27	Write 1 if channels 19 and 20 are duplicate
28	Write 1 if channels 21 and 22 are duplicate
29	Write 1 if channels 23 and 24 are duplicate
30	Write 1 if channels 25 and 26 are duplicate
31	Write 1 if channels 27 and 28 are duplicate
	Config9ECS (address: 0x06109000)
0 – 7	Latency for the TELL1 buffer
8 – 31	Not used
	StatusA (address: 0x0610A000)
0	1 if TTC is ready
1	1 if GOL for 1st link to L0DU is ready
2	1 if GOL for 2nd link to L0DU is ready
3	1 if GOL for link to TELL1 is ready
4 – 31	Not used
	Date version firmware (address: 0x06FFFFF0)
0 – 31	Date of the firmware loaded in FPGA (format: DDMMYYYY)

C.3 Control FPGA

Table C.8 – *Registers of the Selection Board Control FPGA (cont.).*

Bit	Description
	Config1ECS (address: 0x07101000)
0 – 9	Not used
10	Write 1 to reset FPGA
11 – 13	Not used
14	Write 1 to reconfigure Input FPGA1 from PROM
15	Write 1 to reconfigure Input FPGA2 from PROM
16	Write 1 to reconfigure Input FPGA3 from PROM
17	Write 1 to reconfigure Input FPGA4 from PROM
18	Write 1 to reconfigure Input FPGA5 from PROM
19	Write 1 to reconfigure Process FPGA from PROM
20 – 31	Not used
	Date version firmware (address: 0x07FFFFF0)
0 – 31	Date of the firmware loaded in the FPGA (format: DDMMYYYY)

C.4 PVSS Device Unit

The hardware type interfacing PVSS to the Selection Board is `SelectionBoard` and contains the following device unit registers, all of type "Local parallel bus" and of size 32 bits:

- `ResetECS_UN`, mapped to address 0x0N200000, with $1 \leq N \leq 7$,
- `StatusAECS_UN`, mapped to address 0x0N10A000, with $1 \leq N \leq 7$,
- `Status11ECS_UN`, mapped to address 0x0N111000, with $1 \leq N \leq 5$,
- `Status12ECS_UN`, mapped to address 0x0N112000, with $1 \leq N \leq 5$,
- `Status13ECS_UN`, mapped to address 0x0N113000, with $1 \leq N \leq 5$,
- `Status14ECS_UN`, mapped to address 0x0N114000, with $1 \leq N \leq 5$,

- `Status15ECS_UN`, mapped to address 0x0N115000, with $1 \leq N \leq 5$,
- `Status12ECS_UN`, mapped to address 0x0N116000, with $1 \leq N \leq 5$,
- `StatusBECS_U6`, mapped to address 0x0610B000,
- `Config1ECS_UN`, mapped to address 0x0N101000, with $1 \leq N \leq 7$,
- `Config2ECS_UN`, mapped to address 0x0N102000, with $1 \leq N \leq 7$,
- `Config3ECS_UN`, mapped to address 0x0N103000, with $1 \leq N \leq 6$,
- `Config4ECS_UN`, mapped to address 0x0N104000, with $1 \leq N \leq 6$,
- `Config5ECS_U6`, mapped to address 0x06105000,
- `Config6ECS_U6`, mapped to address 0x06106000,
- `Config7ECS_U6`, mapped to address 0x06107000,
- `Config8ECS_U6`, mapped to address 0x06108000,
- `Config9ECS_U6`, mapped to address 0x06109000,
- `Config1ECS_UN`, mapped to address 0x06101000,
- `DateFirmware_UN`, mapped to address 0x0NFFFFF0, with $1 \leq N \leq 7$,

Remerciements

Je voudrais d'abord remercier Ginés Martínez, Anders Ryd et Olivier Schneider d'avoir accepté d'être rapporteurs pour ce travail, et Nora Brambilla, Olivier Callot et Achille Stocchi d'être membres du jury et de tous être venus pour la soutenance, certains de loin.

Je voudrais remercier aussi les directeurs du LAL que j'ai connus, Bernard D'Almagne, qui m'a accueilli ici, Guy Wormser et Achille Stocchi ainsi que toutes les personnes qui travaillent au LAL et qui en font un endroit où travailler est facile et agréable, et tout particulièrement le service missions que je sollicite souvent.

J'ai vécu ces années passées dans LHCb comme une aventure passionnante. Je dois beaucoup à deux personnes d'avoir pu y participer et d'avoir pu contribuer à l'acquisition et l'analyse de nos premières données: Olivier Callot et Olivier Schneider.

Olivier Callot m'a confié la responsabilité de son trigger calorimètre. Tous ceux qui ont travaillé sur ce système ont pu constater sa beauté et à quel point Olivier l'avait parfaitement conçu. L'installation et le commissioning du trigger calorimètre ont été un véritable plaisir. J'ai également eu la chance d'être au CERN au moment du commissioning global de LHCb dont Olivier était chargé et ai pu finalement simplement apprendre grâce à Olivier ce qu'était réellement une expérience de physique des particules.

Olivier Schneider m'a confié la responsabilité de l'analyse des J/ψ avec les premières données et m'a fortement soutenu dans cette activité. Nous avons finalement travaillé ensemble avec différentes formes de groupes de travail pendant 7 ans, et j'ai pu apprendre d'Olivier la rigueur et la précision indispensables pour réaliser ces mesures de section efficace absolue qui sont plus difficiles qu'elles ne paraissent, puisqu'il faut maitriser tous les détails.

Je tenais à les remercier tous les deux ici. Tous les membres de LHCb leur doivent beaucoup, mais moi certainement plus que les autres.

Merci à tous les membres du groupe LHCb au LAL, et tout d'abord à son chef, Marie-Hélène qui donne à notre groupe une ambiance de travail particulièrement agréable où tout le monde discute et s'aide, mais aussi à Sergey Barsuk, Bernard

D'Almagne, Maksym Teklishyn, Michelle Nicol, Jibo He, Frédéric Machefert, Jacques Lefrançois, Alexandra Martín Sánchez, Ioana Videau, Bernard Jean-Marie, Benoit Viaud et Olga Kochebina, tous également responsables de cette ambiance. Une petite pensée pour nos anciens étudiants, Yasmine Amhis (la date fatidique pour jouer Brahms s'approche !) et Aurélien Martens (spécialiste des paris truqués). Un grand merci à Wenbin Qian, "mon premier étudiant", pour sa curiosité sur tous les sujets et les questions allant avec qui m'ont beaucoup fait apprendre, pour son enseignement de la culture (et de la cuisine) chinoise et pour le travail que nous avons fait ensemble sur le J/ψ. Avec Alexandra, nous allons maintenant nous attaquer à la mesure de l'angle γ, qui sera aussi une aventure très intéressante.

J'ai, depuis mon arrivée dans LHCb, travaillé sur le programme de génération et de simulation de l'expérience, avec Gloria Corti. Je la remercie pour notre collaboration d'une dizaine d'années maintenant, qui a toujours été très riche en nouvelles idées et nouveaux projets. Le temps nous a souvent manqué pour mettre en oeuvre tout ce que nous avons imaginé mais j'espère qu'on pourra le faire pendant les prochaines années.

Les cartes d'électroniques du ECAL et du HCAL utilisées pour le trigger ont été réalisées au LAL, par Dominique, Christophe, Beng, Olivier, Vanessa et Daniel, avec l'aide de Jacques, Frédéric et Sergey. Les moments de rigolade dans la salle de test à Orsay ou au CERN dans la caverne ont été nombreux. Je remercie tout particulièrement Daniel Charlet et Claude Pailler pour notre travail en commun sur le SPECS. Malgré les petits défauts qu'il a pu avoir au début, je crois que nous pouvons être contents de notre petit système, en attendant les futures améliorations. La collaboration s'est ensuite étendue à d'autres groupes de LHCb lorsqu'il a fallu tester ensemble toutes les cartes du système, lors de tests communs intensifs au CERN, avec le groupe du LAPP (Cyril Drancourt, Victor Coco, Marie-Noelle Minard) pour la TVB, le groupe de Clermont pour la carte Front-End PRS (Stéphane Monteil, Eric Conte, Rémi Cornat, Valentin Niess) et la carte L0DU (Hervé Chanal, Olivier Deschamps, Régis Lefèvre, Pascal Perret), le groupe de Barcelone pour la SPD Control Board (Edu Picatoste, Xavier Vilasis, Alvaro Gaspar) et le groupe de Bologne pour les cartes de Selection (Umberto Marconi, Ignazio Lax, Gabriele Balbi, Giulio Avoni). Il a fallu ensuite installer les cartes et les nombreux cables dans la caverne, travail réalisé de main de maître par Patrick Cornebise, Michelle Quentin et Bernard Debennerot, puis intégrer le trigger calorimètre au système L0 avec l'aide précieuse de Renaud Le Gac, Pierre-Yves Duval, Julien Cogan et Clara Gaspar. Le commissioning du trigger calorimètre a demandé une présence importante voire continue pour ma part au CERN. Merci beaucoup à la petite équipe que nous mis en place: Marie-Noelle pour les nombreux scans de TVB, Marie-Hélène pour nos histogrammes du presenter, Olivier pour Orwell et le bowling, Régis pour les TCK et le tennis,

Stéphane Tjampens pour les TELL1s, Stéphane Monteil pour les nanosecondes gagnées les unes après les autres malgré mes blagues douteuses sur le PS et pour tous les autres moments passés sur et en dehors du terrain. Les souvenirs de bons moments sont nombreux. Je voudrais aussi remercier Elie Aslanides, qui a aussi été beaucoup présent au CERN aux mêmes moments que moi, pour ses nombreux conseils et sa compagnie lors des nombreux repas que nous avons pris ensemble à la cantine du CERN.

Pour l'analyse des premières données de LHCb, nous avons constitué un petit groupe pour réaliser la première mesure de section efficace de production des J/ψ. Je remercie tous ses membres pour leur aide précieuse et pour l'excellente atmosphère de travail qui s'y est développée. Je remercie tout particulièrement Monica Pepe Altarelli pour son soutien, pour la rédaction de l'article et pour sa patience devant tous les commentaires que nous avons eus. Merci beaucoup également à Giulia Manca pour son aide dans l'organisation du groupe de travail, pour son implication qui m'a beaucoup impressionné, et aussi pour avoir accepté de poursuivre les analyses du quarkonium dans LHCb. Ma participation à l'étude du quarkonium (J/ψ et B_c) doit beaucoup à ma rencontre avec Yuanning Gao. Grâce à Ioana Videau, j'ai pu démarrer une collaboration active et fructueuse avec le groupe LHCb de l'Université de Tsinghua à Pékin, et ses membres, Yuanning, Zhenwei Yang, Jibo He, Wenbin Qian, et bien d'autres. J'ai également beaucoup apprécié de rencontrer les membres de la communauté quarkonium et de pouvoir interagir avec théoriciens et expérimentateurs des expériences "concurrentes" du LHC, en particulier Jean-Philippe Lansberg, Hermine Wöhri, Carlos Lourenço, Roberta Arnaldi et Enrico Scomparin.

Enfin, je remercie Valérie, Agnès, Matthieu et Louis pour leur aide, leur patience et pour avoir fait qu'il a toujours été facile de m'absenter régulièrement au CERN.

Bibliography

[1] The LHCb Collaboration, A. A. Alves *et al.*, *The LHCb detector at the LHC*, JINST **3** (2008), S08005, doi:10.1088/1748-0221/3/08/S08005.

[2] N. Cabibbo, *Unitary symmetry and leptonic decays*, Phys. Rev. Lett. **10** (1963), 531, doi:10.1103/PhysRevLett.10.531.

[3] M. Kobayashi and T. Maskawa, *CP violation in the renormalizable theory of weak interaction*, Prog. Theor. Phys. **49** (1973), 652, doi:10.1143/PTP.49.652.

[4] The CKMfitter Collaboration, J. Charles *et al.*, *CP violation and the CKM matrix: assessing the impact of the asymmetric B factories*, Eur. Phys. J. C **41** (2005), 1, hep-ph/0406184, doi:10.1140/epjc/s2005-02169-1.

[5] The UTfit Collaboration, M. Bona *et al.*, *The 2004 UTfit collaboration report on the status of the unitarity triangle in the standard model*, JHEP **507** (2005), 28, hep-ph/0501199, doi:10.1088/1126-6708/2005/07/028.

[6] The BaBar Collaboration, B. Aubert *et al.*, *The* BaBar *detector*, Nucl. Instrum. Meth. **479** (2002), 1, hep-ex/0105044, doi:10.1016/S0168-9002(01)02012-5.

[7] The BELLE Collaboration, A. Abashian *et al.*, *The BELLE detector*, Nucl. Instrum. Meth. **479** (2002), 117, doi:10.1016/S0168-9002(01)02013-7.

[8] The LHCb Collaboration, R. Aaij *et al.*, *Measurement of the CP-violating phase ϕ_s in the decay $B_s^0 \to J/\psi\phi$*, arXiv:1112.3183 [hep-ex].

[9] The LHCb Collaboration, R. Aaij *et al.*, *Search for the rare decays $B_s^0 \to \mu^+\mu^-$ and $B^0 \to \mu^+\mu^-$*, arXiv:1112.1600 [hep-ex].

[10] The LHCb Collaboration, R. Aaij *et al.*, *Measurement of the J/ψ production in pp collisions at $\sqrt{s} = 7$ TeV*, Eur. Phys. J. C **71** (2011), 1645, arXiv:1103.0423 [hep-ex], doi:10.1140/epjc/s10052-011-1645-y.

[11] D. J. LANGE, *The EvtGen particle decay simulation package*, Nucl. Instrum. Meth. **462** (2001), 152, doi:10.1016/S0168-9002(01)00089-4.

[12] T. SJOSTRAND, S. MRENNA and P. Z. SKANDS, PYTHIA *6.4 Physics and Manual*, JHEP **0605** (2006), 026, hep-ph/0603175, doi:10.1088/1126-6708/2006/05/026.

[13] The LHCB Collaboration, R. ANTUNES NOBREGA *et al.*, *LHCb Computing Technical Design Report*, CERN-LHCC-2005-019, 2005.

[14] I. BELYAEV *et al.*, *Simulation application for the LHCb experiment*, arXiv:physics/0306035, 2003.

[15] The GEANT4 Collaboration, S. AGOSTINELLI *et al.*, *GEANT4: A simulation toolkit*, Nucl. Instrum. Meth. **506** (2003), 250, doi:10.1016/S0168-9002(03)01368-8.

[16] G. BARRAND *et al.*, *GAUDI - A software architecture and framework for building HEP data processing applications*, Comput. Phys. Commun. **140** (2001), 45, doi:10.1016/S0010-4655(01)00254-5.

[17] M. CLEMENCIC, H. DEGAUDENZI, P. MATO, S. BINET, W. LAVRIJSEN, C. LEGGETT and I. BELYAEV, *Recent Developments In The LHCb Software Framework GAUDI*, J. Phys. Conf. Ser. **219** (2010), 042006, doi:10.1088/1742-6596/219/4/042006.

[18] M. DOBBS and J. B. HANSEN, *The HepMC C++ Monte Carlo event record for High Energy Physics*, Comput. Phys. Commun. **134** (2001), 41, doi:10.1016/S0010-4655(00)00189-2.

[19] K. NAKAMURA *et al.*, *Review of Particle Physics*, J. Phys. G **37** (2010), 075021, doi:10.1088/0954-3899/37/7A/075021.

[20] T. SJOSTRAND, S. MRENNA and P. Z. SKANDS, *A Brief Introduction to* PYTHIA *8.1*, Comput. Phys. Commun. **178** (2008), 852, arXiv:0710.3820 [hep-ph], doi:10.1016/j.cpc.2008.01.036.

[21] G. CORCELLA *et al.*, *HERWIG 6.5: an event generator for Hadron Emission Reactions With Interfering Gluons (including supersymmetric processes)*, JHEP **0101** (2001), 010, hep-ph/0011363.

[22] M. BAHR *et al.*, *Herwig++ Physics and Manual*, Eur. Phys. J. C **58** (2008), 639, arXiv:0803.0883 [hep-ph], doi:10.1140/epjc/s10052-008-0798-9.

[23] T. GLEISBERG, S. HOECHE, F. KRAUSS, M. SCHONHERR, S. SCHUMANN, F. SIEGERT and J. WINTER, *Event generation with* SHERPA *1.1*, JHEP **0902** (2009), 007, arXiv:0811.4622 [hep-ph], doi:10.1088/1126-6708/2009/02/007.

[24] C. H. CHANG, C. DRIOUICHI, P. EEROLA and X. G. WU, *BCVEGPY: An Event generator for hadronic production of the B_c meson*, Comput. Phys. Commun. **159** (2004), 192, hep-ph/0309120, doi:10.1016/j.cpc.2004.02.005.

[25] M. GYULASSY and X. N. WANG, *HIJING 1.0: A Monte Carlo program for parton and particle production in high-energy hadronic and nuclear collisions*, Comput. Phys. Commun. **83** (1994), 307, nucl-th/9502021, doi:10.1016/0010-4655(94)90057-4.

[26] J. ALWALL *et al.*, *A standard format for Les Houches event files*, Comput. Phys. Commun. **176** (2007), 300, hep-ph/0609017, doi:10.1016/j.cpc.2006.11.010.

[27] P. GOLONKA and Z. WAS, *PHOTOS Monte Carlo: a precision tool for QED corrections in Z and W decays*, Eur. Phys. J. C **45** (2006), 97, hep-ph/0506026, doi:10.1140/epjc/s2005-02396-4.

[28] P. BARTALINI *et al.*, *Tuning of multiple interactions generated by* PYTHIA, LHCb-99-028.

[29] N. BROOK *et al.*, *Studies on the tuning of Minimum Bias events at LHCb*, LHCb-2005-023.

[30] The UA5 Collaboration, G.J. ALNER *et al.*, *Scaling of pseudo rapidity distributions at center-of-mass energies up to 0.9* TeV, Z. Phys. **C33** (1986), 1, doi:10.1007/BF01410446.

[31] The UA5 Collaboration, K. ALPGØARD *et al.*, *Comparison of $p\bar{p}$ and pp interactions at $\sqrt{s} = 53$ GeV*, Phys. Lett. B **112** (1982), 183, doi:10.1016/0370-2693(82)90325-2.

[32] The CDF Collaboration, F. ABE *et al.*, *Pseudorapidity distributions of charged particles produced in $\bar{p}p$ interactions at $\sqrt{s} = 630$ GeV and 1800* GeV, Phys. Rev. D **41** (1990), 2330, doi:10.1103/PhysRevD.41.2330.

[33] J. PUMPLIN, D. R. STUMP, J. HUSTON, H. L. LAI, P. M. NADOLSKY and W. K. TUNG, *New generation of parton distributions with uncertainties from global QCD analysis*, JHEP **0207** (2002), 012, hep-ph/0201195.

[34] A. MUIR, PYTHIA *minimum bias Studies and the RICH1 Spherical Mirror for the LHCb Experiment*, PhD Thesis, unpublished.

[35] The ALEPH Collaboration, R. BARATE *et al.*, *Resonant structure and flavour tagging in the $B\pi^{\pm}$ system using fully reconstructed B decays*, Phys. Lett. B **425** (1998), 215, doi:10.1016/S0370-2693(98)00180-4.

[36] The OPAL Collaboration, R. AKERS *et al.*, *Observations of $\pi - B$ charge - flavor correlations and resonant $B\pi$ and BK production*, Z. Phys. C **66** (1995), 19, doi:10.1007/BF01496577.

[37] The CDF Collaboration, A. A. AFFOLDER *et al.*, *Observation of orbitally excited B mesons in $p\bar{p}$ collisions at $\sqrt{s} = 1.8$ TeV*, Phys. Rev. D **64** (2001), 072002, doi:10.1103/PhysRevD.64.072002.

[38] The HFAG Collaboration, D. ASNER *et al.*, *Averages of b-hadron, c-hadron, and τ-lepton properties*, arXiv:1010.1589 [hep-ex], 2010.

[39] G. D. LAFFERTY, P. I. REEVES and M. R. WHALLEY, *A Compilation of inclusive particle production data in e^+e^- annihilation*, J. Phys. G **21** (1995), A1, doi:10.1088/0954-3899/21/12A/001.

[40] K. LESSNOFF, *A Study of the LHCb Experiment Sensitivity to CP Violation in Mixing and to Production Asymmetry in B_s Mesons, Using Semi-Leptonic Decays*, PhD Thesis, CERN-THESIS-2010-076.

[41] M. BARGIOTTI and V. VAGNONI, *Heavy quarkonia sector in* PYTHIA *6.324: Tuning, validation and perspectives at LHC(b)*, LHCb-2007-042.

[42] The CDF Collaboration, D. ACOSTA *et al.*, *Measurement of the J/ψ meson and $b-$hadron production cross sections in $p\bar{p}$ collisions at $\sqrt{s} = 1960$ GeV*, Phys. Rev. D **71** (2005), 032001, hep-ex/0412071, doi:10.1103/PhysRevD.71.032001.

[43] The CDF Collaboration, D. ACOSTA *et al.*, *Υ production and polarization in $p\bar{p}$ collisions at $\sqrt{s} = 1.8$ TeV*, Phys. Rev. Lett. **88** (2002), 161802, doi:10.1103/PhysRevLett.88.161802.

[44] LHCB, *DECAY.DEC file*, https://svnweb.cern.ch/trac/lhcb/export/133724/DBASE/trunk/Gen/DecFiles/dkfiles/DECAY.DEC

[45] The BABAR Collaboration, B. AUBERT *et al.*, *Study of inclusive production of charmonium mesons in B decay*, Phys. Rev. D **67** (2003), 032002, hep-ex/0207097, doi:10.1103/PhysRevD.67.032002.

[46] The CLEO Collaboration, S. ANDERSON *et al.*, *Measurements of inclusive $B \to \psi$ production*, Phys. Rev. Lett. **89** (2002), 282001, doi:10.1103/PhysRevLett.89.282001.

[47] The DELPHI Collaboration, P. ABREU *et al.*, *J/ψ production in the hadronic decays of the Z*, Phys. Lett. B **341** (1994), 109, doi:10.1016/0370-2693(94)01385-3.

[48] The L3 Collaboration, O. ADRIANI *et al.*, *χ_c production in hadronic Z decays*, Phys. Lett. B **317** (1993), 467, doi:10.1016/0370-2693(93)91026-J.

[49] The ALEPH Collaboration, D. BUSKULIC *et al.*, *Measurements of mean lifetime and branching fractions of b hadrons decaying to J/ψ*, Phys. Lett. B **295** (1992), 396, doi:10.1016/0370-2693(92)91581-S.

[50] M. R. WHALLEY and A. BUCKLEY, *LHAPDF, the Les Houches Accord PDF Interface*, http://hepforge.cedar.ac.uk/lhapdf

[51] A. RYD, private communication.

[52] The LHCB Collaboration, R. AAIJ *et al.*, *Absolute luminosity measurements with the LHCb detector at the LHC*, JHEP **7** (2012), P01010, doi:10.1088/1748-0221/7/01/P01010.

[53] O. CALLOT *et al.*, *The front-end electronics for the calorimeter triggers*, LHCb-2000-010.

[54] O. CALLOT, M. FERRO-LUZZI and P. PERRET, *Using the SPD multiplicity in the Level-0 trigger*, LHCb-2003-022.

[55] R. JACOBSSON, *Central FPGA-based Destination and Load Control in the LHCb MHz Event Readout*, LHCb-2011-023.

[56] R. JACOBBSON and B. JOST, *Timing and Fast Control*, LHCb-2001-016 (DAQ).

[57] S. BARON and M. JOOS, http://ttc.web.cern.ch/TTC/intro.html

[58] J. CHRISTIANSEN, A. MARCHIORO, P. MOREIRA and A. SANCHO, *Receiver ASIC for Timing, Trigger and Control Distribution in LHC Experiments*, IEEE Trans. Nuclear Science **43** (1996), 1773, doi:10.1109/23.507220.

[59] V. BOBILLIER and L. ROY, *Calorimeter long distance cables, patch panels and racks*, EDMS 578930, 2005.

[60] C. BEIGBEDER *et al.*, *Calorimeter ReadOut Card (CROC) design*, LHCb-2004-008.

[61] C. BEIGBEDER *et al.*, *Connections in the L0 Calorimeter trigger*, LHCb-2004-095.

[62] C. BEIGBEDER *et al.*, *Functional specification of the PGAs for the ECAL/HCAL Front-End card*, LHCb-2003-036.

[63] Y. AMHIS, *Time alignment of the electromagnetic and hadronic calorimeters, reconstruction of the* $B \to D^- \rho(770)^+$, $B_s \to D_s^- \rho(770)^+$ *and* $B_s \to D_s^- K^{*+}(892)$ *decay channels with the LHCb detector*, PhD Thesis, CERN-THESIS-2010-076, 2010.

[64] D. BRETON and D. CHARLET, *SPECS: the Serial Protocol for the Experiment Control System of LHCb*, LHCb-LHCb-2003-004.

[65] S. KOSTNER, D. BRETON, D. CHARLET, F. FONTANELLI, M. FRANK, C. GASPAR, G. HAEFELI, R. JACOBSSON *et al.*, *Generic and layered framework components for the control of a large scale data acquisition system*, IEEE Trans. Nuclear Science **55** (2008), 362, doi:10.1109/TNS.2007.913471.

[66] UM10204, I^2C*-bus specification and user manual*, http://www.mcc-us.com/i2cHowToUseIt1995.pdf

[67] ACTEL, *Axcelerator Family FPGAs*, www.actel.com/documents/AXGenDesc_DS.pdf

[68] C. BEIGBEDER *et al.*, *The trigger part of the calorimeter front-end card*, LHCb-2003-037.

[69] NATIONAL SEMICONDUCTOR, *DS90CR215/DS90CR216 data sheets*, http://www.national.com/pf/DS/DS90CR215.html#Overview

[70] FAIRCHILD SEMICONDUCTOR, *FIN1215 data sheet*, http://www.fairchildsemi.com/pf/FI/FIN1215.html

[71] AMPHENOL, *SKEWCLEAR Cable products*, http://spectra-strip.com/ecappsearch2.cfm?app=SKEWCLEAR&Nav=Skewclear&

[72] F. MACHEFERT, *LHCb calorimeter electronics. Photon identification. Calorimeter calibration.*, Habilitation à diriger des recherches, LAL, 11-38, 2011.

[73] S. MONTEIL, *Mesures de précision électrofaible*, Habilitation à diriger des recherches, LPC, HDR 280, 2009.

[74] ACTEL, *ProASIC PLUS Flash Family FPGAs*, www.actel.com/documents/PAPLUS_PB.pdf

[75] C. DRANCOURT *et al.*, *The Validation Card for the Calorimeter Triggers*, LHCb-2003-120.

[76] P. MOREIRA *et al.*, *GOL reference manual*, http://projgol.web.cern.ch/proj-gol/gol_manual.pdf

[77] AGILENT TECHNOLOGIES, *HFRB-772BH Transmitter*, http://www.avagotech.com/pages/en/fiber_optics/parallel_optics/12-channel_parallel_optics/hfbr-772bhwz/

[78] S. BOTA *et al.*, *Scintillator pad detector Front-End electronics design*, LHCb-2000-027.

[79] ULM PHOTONICS, *5 Gpbs 850 nm VCSEL chip*, http://www.ulm-photonics.com/

[80] A. BERTIN *et al.*, *The selection crates for the L0 Calorimeters trigger*, LHCb-2000-018.

[81] G. AVONI, I. LAX, G. BALBI and U. MARCONI, *Selection Crate*, https://lbtwiki.cern.ch/pub/L0/L0Caloecs/SelectionCrate.doc

[82] XILINX, *Virtex-II Pro*, http://www.xilinx.com/support/documentation/virtex-ii_pro.htm

[83] F. FONTANELLI *et al.*, *CC-PC gluecard application and user's guide*, LHCb-2003-098.

[84] TEXAS INSTRUMENT, *TLK2501*, http://www.ti.com/product/tlk2501

[85] E. ASLANIDES *et al.*, *Synchronization of optical links using the GOL with the TLK2501 or StratixGX buffers*, LHCb-2004-012.

[86] D. GASCON *et al.*, *Cards, Crates and Connections for the Calorimeters*, LHCb-2003-121.

[87] G. AVONI *et al.*, *Format specification of the LHCb L0 Calorimeters TELL1*, EDMS-845277, 2007.

[88] F. LEGGER, A. BAY, G. HAEFELI and L. LOCATELLI, *TELL1: development of a common readout board for LHCb*, LHCb-2004-100.

[89] G. HAEFELI, *ECS Interface Library User Guide*, http://lphe.epfl.ch/~ghaefeli/Release_v4.2/ECS_v4.2.doc

[90] O. CALLOT *et al.*, *Raw Data Format*, EDMS-565851, 2007.

[91] G. HAEFELI, *TELL1 VHDL framework*, http://lphe.epfl.ch/~ghaefeli/Release_v4.2/hdl_release_v4.2.zip

[92] B. BENYÓ, C. GASPAR and P. SOMOGYI, *Machine assisted histogram classification*, J. Phys.: Conf. Ser. **219** (2010), 022033, doi:10.1088/1742-6596/219/2/022033.

[93] A. MARTENS, *Towards a measurement of the angle γ of the Unitarity Triangle with the LHCb detector at the LHC (CERN): calibration of the calorimeters using an energy flow technique and first observation of the $B_s^0 \to \overline{D}^0 \overline{K}^{*0}$ decay*, PhD Thesis, LAL Orsay, 2011, LAL 11-172.

[94] J. ALBRECHT, J. BRESSIEUX, G. CARBONI, J. COGAN, S. DE CAPUA, M. FROSINI, Y. GAO, J. HE, G. LANFRANCHI, R. LE GAC, B. LIU, G. MANCA, M. NEEDHAM, M. PALUTAN, G. PASSALEVA, M. PEPE ALTARELLI, W. QIAN, P. ROBBE, G. SABATINO, E. SANTOVETTI, A. SARTI, O. SCHNEIDER, J. SERRANO and Y. ZHANG, *Updated measurement of the J/ψ production cross-section in LHCb (Kruger 2010)*, LHCb-ANA-2010-012.

[95] W. QIAN, *J/ψ production study at the LHCb experiment*, PhD Thesis, LAL Orsay, 2010, LAL 10-108.

[96] N. BRAMBILLA *et al.*, *Heavy quarkonium: progress, puzzles, and opportunities*, Eur. Phys. J. C **71** (2011), 1534, arXiv:1010.5827 [hep-ph], doi:10.1140/epjc/s10052-010-1534-9.

[97] C.-H. CHANG, *Hadronic production of J/ψ associated with a gluon*, Nucl. Phys. B **172** (1980), 425.

[98] R. BAIER and R. RUECKL, *Hadronic collisions: a quarkonium factory*, Z. Phys C **19** (1983), 251, doi:10.1007/BF01572254.

[99] The CDF Collaboration, F. ABE *et al.*, *J/ψ and $\psi(2S)$ production in $p\bar{p}$ collisions at $\sqrt{s} = 1.8\,\text{TeV}$*, Phys. Rev. Lett. **79** (1997), 572, doi:10.1103/PhysRevLett.79.572.

[100] The CDF Collaboration, F. ABE *et al.*, *Production of J/ψ mesons from χ_c meson decays in $p\bar{p}$ collisions at $\sqrt{s} = 1.8\,\text{TeV}$*, Phys. Rev. Lett. **79** (1997), 578, doi:10.1103/PhysRevLett.79.578.

[101] M. CACCIARI and M. GRECO, *J/ψ production via fragmentation at the Tevatron*, Phys. Rev. Lett. **73** (1994), 1586, hep-ph/9405241, doi:10.1103/PhysRevLett.73.1586.

[102] E. BRAATEN, M. A. DONCHESKI, S. FLEMING and M. L. MANGANO, *Fragmentation production of J/ψ and ψ' at the Tevatron*, Phys. Lett. B **333** (1994), 548, hep-ph/9405407, doi:10.1016/0370-2693(94)90182-1.

[103] G. T. BODWIN, E. BRAATEN and G. P. LEPAGE, *Rigorous QCD analysis of inclusive annihilation and production of heavy quarkonium*, Phys. Rev. D **51** (1995), 1125, hep-ph/9407339, doi:10.1103/PhysRevD.51.1125.

[104] P. L. CHO and A. K. LEIBOVICH, *Color octet quarkonia production*, Phys. Rev. D **53** (1996), 150, hep-ph/9505329, doi:10.1103/PhysRevD.53.150.

[105] P. L. CHO and A. K. LEIBOVICH, *Color octet quarkonia production 2*, Phys. Rev. D **53** (1996), 6203, hep-ph/9511315, doi:10.1103/PhysRevD.53.6203.

[106] The H1 Collaboration, C. ADLOFF *et al.*, *Inelastic Photoproduction of J/ψ Mesons at HERA*, Eur. Phys. J. C **25** (2002), 25, hep-ex/0205064, doi:10.1007/s10052-002-1009-8.

[107] The ZEUS Collaboration, S. CHEKANOV *et al.*, *Measurements of inelastic J/ψ and ψ' photoproduction at HERA*, Eur. Phys. J. C **27** (2003), 173, hep-ex/0211011, doi:10.1140/epjc/s2002-01130-2.

[108] The CDF Collaboration, A. ABULENCIA *et al.*, *Polarization of J/ψ and $\psi(2S)$ mesons in $p\bar{p}$ collisions at $\sqrt{s} = 1.96\,\text{TeV}$*, Phys. Rev. Lett. **99** (2007), 132001, arXiv:0704.0638 [hep-ex], doi:10.1103/PhysRevLett.99.132001.

[109] P. ARTOISENET, J. P. LANSBERG and F. MALTONI, *Hadroproduction of J/ψ and Υ in association with a heavy-quark pair*, Phys. Lett. B **653** (2007), 6, arXiv:0712.2770 [hep-ph], doi:10.1088/1126-6708/2008/02/102.

[110] S. P. BARANOV, *Topics in associated $J/\psi + c + \bar{c}$ production at modern colliders*, Phys. Rev. D **73** (2006), 074021, doi:10.1103/PhysRevD.73.074021.

[111] J. M. CAMPBELL, F. MALTONI and F. TRAMONTANO, *QCD corrections to J/ψ and Υ production at hadron colliders*, Phys. Rev. Lett. **98** (2007), 252002, hep-ph/0703113, doi:10.1103/PhysRevLett.98.252002.

[112] P. ARTOISENET, F. MALTONI and T. STELZER, *Automatic generation of quarkonium amplitudes in NRQCD*, JHEP **0802** (2008), 102, arXiv:0712.2770 [hep-ph], doi:10.1088/1126-6708/2008/02/102.

[113] The ALICE Collaboration, K. AAMODT *et al.*, *Rapidity and transverse momentum dependence of inclusive J/ψ production in pp collisions at $\sqrt{s} = 7$ TeV*, Phys. Lett. B **704** (2011), 442, arXiv:1105.0380 [hep-ex], doi:10.1016/j.physletb.2011.09.054.

[114] The ATLAS Collaboration, G. AAD *et al.*, *Measurement of the differential cross-sections of inclusive, prompt and non-prompt J/ψ production in proton-proton collisions at $\sqrt{s} = 7$ TeV*, Nucl. Phys. B **850** (2011), 387, arXiv:1104.3038 [hep-ex], doi:10.1016/j.nuclphysb.2011.05.015.

[115] The CMS Collaboration, S. CHATRCHYAN *et al.*, *J/ψ and $\psi(2S)$ production in pp collisions at $\sqrt{s} = 7$ TeV*, submitted to JHEP, arXiv:1111.1557 [hep-ex].

[116] E. VAN HERWIJNEN, *The LHCb trigger*, LHCb-PROC-2010-055.

[117] G. LANFRANCHI *et al.*, *The muon identification procedure of the LHCb experiment for the first data*, LHCb-PUB-2009-013.

[118] J. E. GAISER, *Charmonium spectroscopy from radiative decays of the J/ψ and ψ'*, PhD Thesis, SLAC, 1982, SLAC-R-255.

[119] T. SKWARNICKI, *A study of the radiative cascade transitions between the Υ' and Υ resonances*, PhD Thesis, DESY, 1986, DESY-F31-86-02.

[120] M. FERRO-LUZZI, *Proposal for an absolute luminosity determination in colliding beam experiments using vertex detection of beam-gas interactions*, Nucl. Instrum. Meth. **553** (2005), 388, doi:10.1016/j.nima.2005.07.010.

[121] P. FACCIOLI *et al.*, *Towards the experimental clarification of quarkonium polarization*, Eur. Phys. J. C **69** (2010), 657, arXiv:1006.2738 [hep-ph], doi:10.1140/epjc/s10052-010-1420-5.

[122] C. S. LAM and W.-K. TUNG, *A systematic approach to inclusive lepton pair production in hadronic collisions*, Phys. Rev. D **18** (1978), 2447, doi:10.1103/PhysRevD.18.2447.

[123] The ALICE Collaboration, B. ABELEV *et al.*, *J/ψ polarization in pp collisions at $\sqrt{s} = 7$ TeV*, submitted to Phys. Rev. Lett., arXiv:1111.1630 [hep-ex].

[124] H. MORATA *et al.*, *Measurement of trigger efficiencies and biases*, LHCb-2008-073.

[125] M. PIVK and F. R. LE DIBERDER, *sPlot: a statistical tool to unfold data distributions*, Nucl. Instrum. Meth. **555** (2005), 356, physics/0402083 [physics.data-an], doi:10.1016/j.nima.2005.08.106.

[126] A. SARTI *et al.*, *Calibration strategy and efficiency measurement of the muon identification procedure at LHCb*, LHCb-PUB-2010-002.

[127] The CDF Collaboration, T. AALTONEN *et al.*, *Measurement of Ratios of Fragmentation Fractions for Bottom Hadrons in $p\bar{p}$ Collisions at $\sqrt{s} =$ 1.96 TeV*, Phys. Rev. D **77** (2008), 072003, arXiv:0801.4375 [hep-ex], doi:10.1103/PhysRevD.77.072003.

[128] The LHCB Collaboration, R. AAIJ *et al.*, *Measurement of b hadron production fractions in 7 TeV pp collisions*, submitted to Phys. Rev. D, arXiv:1111.2357 [hep-ex].

[129] The LHCB Collaboration, *Central exclusive dimuon production at $\sqrt{s} =$ 7 TeV*, LHCb-CONF-2011-022.

[130] The LHCB Collaboration, R. AAIJ *et al.*, *Measurement of $\sigma(pp \to b\bar{b}X)$ at $\sqrt{s} = 7$ TeV in the forward region*, Phys. Lett. B **694** (2010), 209, arXiv:1009.2731 [hep-ex], doi:10.1016/j.physletb.2010.10.010.

[131] H. K. WOEHRI, *Quarkonium production in pp at LHC*, `http://www.univie.ac.at/vienna.seminar/2011/talks/03_Woehri.pptx`

[132] P. ARTOISENET, *Quarkonium production at the Tevatron and the LHC*, PoS **ICHEP 2010** (2010), 192.

[133] M. BUTENSCHOEN and B. A. KNIEHL, *Reconciling J/ψ production at HERA, RHIC, Tevatron, and LHC with NRQCD factorization at next-to-leading order*, Phys. Rev. Lett. **106** (2011), 022003, arXiv:1009.5662 [hep-ph], doi:10.1103/PhysRevLett.106.022003.

[134] J. P. LANSBERG, *On the mechanisms of heavy-quarkonium hadroproduction*, Eur. Phys. J. C **61** (2009), 693, arXiv:0811.4005 [hep-ph], doi:10.1140/epjc/s10052-008-0826-9.

[135] Y. Q. MA, K. WANG and K. T. CHAO, *J/ψ ($\psi(2S)$) production at Tevatron and LHC at $O(\alpha_s^4 v^4)$ in nonrelativistic QCD*, Phys. Rev. Lett. **106** (2011), 042002, arXiv:1009.3655 [hep-ph], doi:10.1103/PhysRevLett.106.042002.

[136] A. D. FRAWLEY, T. ULLRICH and R. VOGT, *Heavy flavor in heavy-ion collisions at RHIC and RHIC II*, Phys. Rept. **462** (2008), 125, arXiv:0806.1013 [nucl.ex], doi:10.1016/j.physrep.2008.04.002.

[137] P. FACCIOLI *et al.*, *Study of $\psi(2S)$ and χ_c decays as feed-down sources of J/ψ hadroproduction*, JHEP **0810** (2008), 004, arXiv:0809.2153 [hep-ph], doi:10.1088/1126-6708/2008/10/004.

[138] M. CACCIARI, M. GRECO and P. NASON, *The p_{T} spectrum in heavy-flavour hadroproduction*, JHEP **9805** (1998), 007, hep-ph/9803400.

[139] M. CACCIARI, S. FRIXIONE and P. NASON, *The p_{T} spectrum in heavy-flavor photoproduction*, JHEP **0103** (2001), 006, hep-ph/0102134.

[140] M. CACCIARI, S. FRIXIONE, M. L. MANGANO, P. NASON and G. RIDOLFI, *QCD analysis of first b cross-section data at 1.96 TeV*, JHEP **0407** (2004), 033, hep-ph/0312132, doi:10.1088/1126-6708/2004/07/033.

[141] The LHCB Collaboration, *Measurement of the $\psi(2S)$ production cross-section at $\sqrt{s} = 7$ TeV in LHCb*, LHCb-CONF-2011-026.

[142] The LHCB Collaboration, *A measurement of the cross-section ratio $\sigma(\chi_{c2})/\sigma(\chi_{c1})$ for prompt χ_c production at $\sqrt{s} = 7$ TeV in LHCb*, LHCb-CONF-2011-020.

[143] S. BARSUK *et al.*, *Liste of ethernet cables for L0Calo*, `http://`